Investigation of Iron speciation in silicate glasses and its implications for magma oceans

A DISSERTATION
SUBMITTED TO THE FACULTY OF THE GRADUATE SCHOOL
OF THE UNIVERSITY OF MINNESOTA
BY

Hongluo Zhang

IN PARTIAL FULFILLMENT OF THE REQUIREMENTS
FOR THE DEGREE OF
Doctor of Philosophy

Marc M. Hirschmann

Nov, 2015

Acknowledgements

There are many people that have earned my gratitude for their contribution to my time in graduate school.

First and foremost, I would like to express my sincere gratitude to my advisor Prof. Marc M. Hirschmann for the continuous support of my Ph.D study and related research, for his patience, motivation, immense knowledge and confidence on me. His guidance helped me in all the time of research and writing of this thesis. I could not have imagined having a better advisor and mentor for my Ph.D study.

Besides my advisor, I would like to thank the rest of my thesis committee: Prof. David Kohlstedt, Prof. Bruce Moskowitz, and Prof. Justin Revenaugh, for their insightful comments and encouragement, but also for the questions which incented me to widen my research from various perspectives.

Meanwhile, I also want to thank to Prof. Michael Walter, who gave access to his laboratory to do DAC experiments and supported my research; thank to Dr. Elizabeth Cottrell and Prof. Katie Kelley for guiding me XANES theory and measurements, and sharing good time at Advanced Phone Source.

My sincere thanks also goes to Prof. Anthony Withers, Dr. Jed Mosenfelder, and Dr. Oliver Lord, who guided me in experiments and data processing.

I also woulk like to thank Dr. Anette von der Handt, Dr. Peat A. Solheid, Dr. John Fournelle, Dr. Yingwei Fei, who gave access to the laboratory and research facilities. Without they precious support it would not be possible to conduct this research.

Many thanks to Dr. Matt Newville and Dr. Antonio Lanzirotti, who help me at Argonne National Laboratory, for guiding and supporting my measurement there. Without their professional support those measurements would not be possible performed.

I thank my fellow labmates, Dr. Celia Dalou, Dr. Lora Armstrong, Dr. Anja Rosenthal, Dr.

Paola Ardia, Dr. Haijin Xu, Prof. Fred Davis, Dr. Ben D. Stanley, Zhou Zhang, MS. Patrick Hastings, An-An Hua, Emily falksen, Jen Caseres in for the stimulating discussions, for collabrating in lab, and for all the fun we have had in the last five years. Also I thank my friends, Marzena Kohut in University of Oslo, Suzanne Birner in Stanford University, Dr. Weiwei Wang in University College London, for their supporting and help in labs.

I would like to thank all the department staff for their support during all my graduate life.

Last but not the least, I would like to thank my family: my parents and my husband for supporting me study aboard, pursue what I am interested and my life in general.

Abstract

As the most abundant multi-valent element in silicate melt, iron plays an important role in many physical and chemical respects. The ratio of Fe^{3+} and total Fe concentration, $Fe^{3+}/\Sigma Fe$, not only reflects but also establishes the redox environment in many magmatic processes. The $Fe^{3+}/\Sigma Fe$ ratio increases with oxygen fugacity, but also is affected by chemical composition, temperature and pressure. This thesis presents experimental investigations of the $Fe^{3+}/\Sigma Fe$ ratio changing with pressure in silicate melts and its implications for the redox environments of early magma ocean. Mössbauer spectrum is one of the most common methods to determine $Fe^{3+}/\Sigma Fe$ ratio in glasses. In Chapter 2, two andesitic glasses synthesized at 1 atm, 1400 °C and 3.5 GPa, 1600 °C, were examined with Mössbauer spectra collected from 47-293 K. The recoilless fractions (f) of Fe^{3+} and Fe^{2+}, can be determined from those variable-temperature Mössbauer spectra. The correction number, C, equals $\frac{f(Fe^{3+})}{f(Fe^{2+})}$, will be used to correct the $Fe^{3+}/\Sigma Fe$ ratio of andesite glasses determined through Mössbauer spectra collected at room temperature in the following studies. For 1 atm andesitic glasses equilibrated over a range of oxygen fugacities ($\log fO_2$ from -8.63 to -0.68), were examined with Fe K-edge X-ray absorption near-edge structure (XANES) and Mössbauer spectra in Chapter 3. XANES spectral features were calibrated as a function of Mössbauer derived $Fe^{3+}/\Sigma Fe$ ratios. The coordination number (CN) of Fe^{3+} and Fe^{2+} ions in andesitic glass can be calculated from observations of pre-edge centroid energies and total intensities, combined with independent constraints on $Fe^{3+}/\Sigma Fe$ ratio from spectra. The mean coordination of Fe^{2+} ions calculated this way is close to 5.5 for reduced and oxidized compositions, and this is consistent with inferences from hyperfine features of the Mössbauer spectra. The mean coordination number of Fe^{3+} inferred from XANES increases from $\sim$4.5 to $\sim$5 as andesitic glasses vary from reduced to oxidized; Mössbauer hyperfine parameters also suggest network-forming behavior of Fe^{3+}, but with higher coordination for more reduced glasses. In Chapter 4, the $Fe^{3+}/\Sigma Fe$ ratios in andesitic glasses synthesized from 1 atm to 7 GPa were examined with Mössbauer spectra. The $Fe^{3+}/\Sigma Fe$ ratios decrease as pressure increase, from 1 atm to 4 GPa, and become flatten afterwards. Those glasses were also examined with XANES spectra. Both hyperfine parameters from Mössbauer spectra and mean coordination number calculated from XANES features show that the CNs of Fe^{3+} in glasses are $\sim$5 and vary little with pressure changing, while for Fe^{2+},

the CN increases as pressure increasing. A new thermodynamic model is built to explore the relationship between oxygen fugacity and pressure and consequently, for a homogenous magma ocean, the oxidation states are more reduced at shallow part than at depth.

Contents

List of Tables

List of Figures

Chapter 1

Introduction

Iron as the most abundant multi-valent element in silicate melt, plays an important role in oxygen fugacity (fO_2) determination and in many cases can establish the fO_2 at magmatic conditions. The $Fe^{3+}/\Sigma Fe$ ratio in natural and synthetic silicate melts has been investigated for more 30 years (*Sack et al.*, 1981; *Mysen et al.*, 1985; *Mysen and Virgo*, 1986; *Christie et al.*, 1986; *Kress and Carmichael*, 1988; *Jayasuriya et al.*, 2004; *Bézos and Humler*, 2005; *O'Neill et al.*, 2006; *Wilke*, 2005; *Rossano et al.*, 2008; *Kelley and Cottrell*, 2009; *Cottrell et al.*, 2009; *Cottrell and Kelley*, 2011, 2013). The $Fe^{3+}/\Sigma Fe$ ratio increases with fO_2, but also is influenced by melt composition, temperature and pressure (*Kress and Carmichael*, 1991; *O'Neill et al.*, 2006; *Borisov and McCammon*, 2010). Of these variables, pressure effect has been least explored, and consequently the $Fe^{3+}/\Sigma Fe$ ratio in magma at high pressure is poorly constrained.

Bulk analytical techniques to determine $Fe^{3+}/\Sigma Fe$ ratio in silicate glasses include wet chemistry (*Wilson*, 1960; *Sack et al.*, 1981; *Mysen et al.*, 1985; *Christie et al.*, 1986; *Kress and Carmichael*, 1991; *Bézos and Humler*, 2005), and most commonly applied technique, Mössbauer spectroscopy (*Mysen et al.*, 1985; *Mysen and Virgo*, 1985, 1986; *Dyar et al.*, 1987; *Dingwell*, 1991; *Jayasuriya et al.*, 2004; *O'Neill et al.*, 2006; *Rossano et al.*, 2008; *Cottrell et al.*, 2009; *Borisov and McCammon*, 2010; *Righter et al.*, 2013). However, some controversy has persisted about the relative accuracies of these different techniques, and in particular, about the veracity of $Fe^{3+}/\Sigma Fe$ determined by Mössbauer spectroscopy (*Lange and Carmichael*, 1989; *Ottonello et al.*, 2001; *Righter et al.*, 2013). This thesis discusses in detail of the accuracy of $Fe^{3+}/\Sigma Fe$ determined by Mössbauer spectroscopy in Chapter 2.

Besides the bulk analytical techniques, micro analytical technique likes x-ray absorption

near edge structure (XANES) spectroscopy affords the ability to determine $Fe^{3+}/\Sigma Fe$ ratio at high spatial resolution with comparable or superior precision (*Berry et al.*, 2003; *Wilke et al.*, 2005; *Cottrell et al.*, 2009; *Cottrell and Kelley*, 2011; *Dauphas et al.*, 2014), allowing analysis of glasses from complex natural samples and from experiments. Due to determination of $Fe^{3+}/\Sigma Fe$ ratio through XANES requires calibration from materials with known $Fe^{3+}/\Sigma Fe$ ratios, this thesis presents new calibration curve for andesite glasses in Chapter 3.

This thesis also presents experimental investigations of $Fe^{3+}/\Sigma Fe$ ratio changes with pressure with known buffering conditions and andesite composition in Chapter 4. With thermodynamic calculation, the present work attempts to quantify the relationship between fO_2 and pressure with constant $Fe^{3+}/\Sigma Fe$ ratio, which can be set at depth based on equilibrium of iron and silicate melt.

A brief description of each chapter is given here.

- In **Chapter 2**, we examine in detail the temperature (47-293 K) of Mössbauer spectra for two andesitic glasses, one quenched at 1 atm, 1400 °C (VF3) and the other at 3.5 GPa, 1600 °C (M544), to evaluate the accuracy of Fe^{3+} and Fe^{2+} ratios in silicate glasses determined by Mössbauer spectroscopy. Variable-temperature Mössbauer spectra of these two glasses are used to characterize the recoilless fraction, f, by two different methods a relative method (RM) based on the temperature dependence of the ratios of Fe^{3+} and Fe^{2+} Mössbauer doublets and the second based on the temperature dependence of the center shift (CS) of the doublets. The ratio of the recoilless fractions for Fe^{3+} and Fe^{2+}, CT, can then be used to adjust the observed area of the Mössbauer doublets into the $Fe^{3+}/\Sigma Fe$ ratio in the sample. We also evaluated the contributions of non-paramagnetic components to the Fe in the glasses by determining the influence of applied magnetic field on sample magnetization. Finally, for the VF3 glass, we determined the $Fe^{3+}/\Sigma Fe$ independently by wet chemical determination of the FeO content combined with careful electron microprobe analyses of total Fe. Recoilless fractions determined with the CS method (CSM) are significantly smaller than those determined with the relative method and suggest larger corrections to room temperature $Fe^{3+}/\Sigma Fe$ ratios. However, the RM

determinations are believed to be more accurate because they depend less on the assumption of the Debye harmonic model and because they produce more nearly temperature-independent estimates of $Fe^{3+}/\Sigma Fe$ ratios. Non-linear responses of sample magnetizations to applied magnetic fields indicate that the glasses contain a small (0.4-1.1 % for VF3) superparamagnetic component that is most likely to be nanophase precipitates of $(FeMg)Fe_2O_4$ oxide, but corrections for this component have negligible influence on the total $Fe^{3+}/\Sigma Fe$ determined for the glass. For the VF3 glass, the $Fe^{3+}/\Sigma Fe$ produced by uncorrected room temperature Mössbauer spectroscopy (0.685 ± 0.014 in two standard deviation (2σ)) agrees within 3% of that determined by wet chemistry (0.666 ± 0.030 in 2σ). The $Fe^{3+}/\Sigma Fe$ corrected for recoilless fraction contributions is $0.634\pm0.078(2\sigma)$, which is 7.5% lower than the uncorrected room temperature ratio, but also agrees within 5% of wet chemical ratio. At least for this andesitic glass, the room temperature determination of $Fe^{3+}/\Sigma Fe$ is accurate within analytical uncertainty, but room temperature Mössbauer determinations of $Fe^{3+}/\Sigma Fe$ are always systematically higher compared to recoilless-fraction corrected ratios.

- **Chapter 3** presents andesitic glasses equilibrated over a range of oxygen fugacities (log fO_2 from -8.63 to -0.68) were examined with Fe K-edge X-ray absorption near-edge structure (XANES) and Mössbauer spectra. XANES spectral features were then calibrated as a function of Mössbauer-derived $Fe^{3+}/\Sigma Fe$ ratios. Additionally, both methods help characterize the local structure of iron ions in andesitic glasses. $Fe^{3+}/\Sigma Fe$ ratios were determined from Mössbauer spectroscopy collected at room temperature but corrected with recoilless fractions obtained from previously reported Mssbauer data collected on one of the glasses from 47-293 K. An empirical model was derived for the correlation between the pre-edge centroid energy and $Fe^{3+}/\Sigma Fe$ ratio for andesitic glasses. This trend is intermediate between those previously determined for rhyolitic and basaltic glasses, but and the difference with basaltic compositions may be owing chiefly to differences in calibrations for $Fe^{3+}/\Sigma Fe$ ratio determinations, rather than to intrinsic differences in the center positions as a function of $Fe^{3+}/\Sigma Fe$ ratio for mafic glasses. The ratios of intensities of pre-edge sub-peaks and $Fe^{3+}/\Sigma Fe$ ratios for andesitic, basaltic, and rhyolitic glasses plot along a common trend, indicating that these measures provide a XANES calibration for $Fe^{3+}/\Sigma Fe$ ratio that is effectively composition independent. The

coordination number of Fe^{3+} and Fe^{2+} ions in andesitic glass can be calculated from observations of pre-edge centroid energies and total intensities, combined with independent constraints on $Fe^{3+}/\Sigma Fe$ ratio from spectra. The mean coordination of Fe^{2+} ions calculated this way is close to 5.5 for reduced and oxidized compositions, and this is consistent with inferences from hyperfine features of the Mössbauer spectra. The mean coordination number of Fe^{3+} inferred from XANES increases from $\sim$4.5 to $\sim$5 as andesitic glasses vary from reduced to oxidized; Mössbauer hyperfine parameters also suggest network-forming behavior of Fe^{3+}, but with higher coordination for more reduced glasses.

- **Chapter 4** conducts experiments on the $Fe^{3+}/\Sigma Fe$ ratio of silicate melts with andesitic composition using Ru and RuO_2 redox buffer as a function of pressure from 1 atm to 7 GPa. The $Fe^{3+}/\Sigma Fe$ ratio determined by Mössbauer spectra collected at room temperature and corrected with recoilless fraction determined in Chapter 2. The hyperfine parameters show the mean coordination number of Fe^{3+} in silicate glasses is $\sim$5 and does not change with pressure, while for Fe^{2+}, the mean coordination number increases with pressure. Those feasures are consistent from the mean coordination numbers of Fe^{3+} and Fe^{2+} calculated from XANES spectra. At the same time, a new calibration curve for XANES spectra is built for 1.5-7 GPa andesite glasses. The $Fe^{3+}/\Sigma Fe$ ratio decreases as pressure increasing, which is consistent with results from *O'Neill et al.* (2006) at 1 atm-3 GPa, and becomes more flat when pressure above 5 GPa. A new thermodynamic model is built to explore how oxygen fugacity changes with pressure at constant $Fe^{3+}/\Sigma Fe$ ratio. The new model suggests that the oxidation state of a well mixed magma ocean is more reduced at shallow part than at depth.

Chapter 2

Accurate Determination of $Fe^{3+}/\Sigma Fe$ of Andesitic Glass by Mössbauer Spectroscopy

This Chapter has been published in American Minneralogist,vol. 100, pg. 1967-1977 with co-authors Peat A. Solheid, Rebecca A. Lange, Anette von der Handt, Marc M. Hirschmann, and is used in this dissertation with permission from American Minneralogist.

2.1 Introduction

The proportion of Fe^{3+} and Fe^{2+} in natural and experimental silicate glasses is one of the most important measures of the oxygen fugacity of magmatic materials, and consequently has been the subject of intensive study for more than 30 years(*Sack et al.*, 1981; *Mysen et al.*, 1985; *Mysen and Virgo*, 1986; *Christie et al.*, 1986; *Kress and Carmichael*, 1988; *Jayasuriya et al.*, 2004; *Bézos and Humler*, 2005; *O'Neill et al.*, 2006; *Wilke*, 2005; *Rossano et al.*, 2008; *Kelley and Cottrell*, 2009; *Cottrell et al.*, 2009; *Cottrell and Kelley*, 2011, 2013). Analytical techniques employed to determine $Fe^{3+}/\Sigma Fe$ in silicate glasses include wet chemistry (*Wilson*, 1960; *Sack et al.*, 1981; *Mysen et al.*, 1985; *Christie et al.*, 1986; *Kress and Carmichael*, 1991; *Bézos and Humler*, 2005), and, increasingly, XANES (*Wilke et al.*, 2001; *Berry et al.*, 2008; *Cottrell et al.*,

2009; *Kelley and Cottrell*, 2009; *Cottrell and Kelley*, 2011, 2013), but the most commonly applied technique is Mössbauer spectroscopy (*Mysen et al.*, 1985; *Mysen and Virgo*, 1985, 1986; *Dyar et al.*, 1987; *Dingwell*, 1991; *Jayasuriya et al.*, 2004; *O'Neill et al.*, 2006; *Rossano et al.*, 2008; *Cottrell et al.*, 2009; *Borisov and McCammon*, 2010; *Righter et al.*, 2013). However, some controversy has persisted about the relative accuracies of these different techniques, and in particular, about the veracity of $Fe^{3+}/\Sigma Fe$ determined by Mössbauer spectroscopy (*Lange and Carmichael*, 1989; *Ottonello et al.*, 2001; *Righter et al.*, 2013).

Recoilless interactions between ^{57}Co 14.4 keV gamma quanta and the nuclei of $^{57}Fe^{3+}$ and $^{57}Fe^{2+}$ ions occur at distinct energies and produce significant separation in Doppler-shifted velocities, potentially allowing precise quantification of $Fe^{3+}/\Sigma Fe$ in Fe-bearing materials, including silicate glasses (*McCammon and Kopylova*, 2004). However, the accuracy of such determinations depends on corrections for several effects. The most important is the relative proportion of recoilless fractions of Fe^{3+} and Fe^{2+} ions, ($f(Fe^{3+})_T$, $f(Fe^{2+})_T$), which represent the temperature-dependent fractions of 14.4 keV gamma rays interacting resonantly with the $^{57}Fe^{3+}$ and $^{57}Fe^{2+}$ ions. The absorption areas of Mössbauer doublets produced by Fe^{3+} and Fe^{2+} in an analyte ($AA(Fe^{3+})_T$, $AA(Fe^{2+})_T$) are related to the abundances of the ions ($N(Fe^{3+})_T$, $N(Fe^{2+})_T$) and the recoilless fraction of each ion, according to

$$\frac{AA(Fe^{3+})_T}{AA(Fe^{2+})_T} = C_T \frac{N(Fe^{3+})_T}{N(Fe^{2+})_T} \tag{2.1}$$

where C_T is correction number, equals $f(Fe^{3+})_T/f(Fe^{2+})_T$, and the T subscripts highlight quantities that are temperature-dependent. As the recoilless interaction depends on bond strength and is affected by lattice vibrations (*Chen and Yang*, 2007), values of f_T are usually not the same for Fe^{3+} and Fe^{2+} in minerals or glasses. Indeed, studies of silicate and oxide minerals have found values of C_T at room temperature ranging from 1.0 in biotite (*Bancroft and Brown*, 1975) to 1.4 in garnet (*Woodland and Ross II*, 1994; *Dyar et al.*, 2012), but typical values average near 1.2 (*De Grave and Van Alboom*, 1991).

Despite the demonstrated importance of recoilless fractions for $Fe^{3+}/\Sigma Fe$ determinations in silicate minerals, Mössbauer analyses of $Fe^{3+}/\Sigma Fe$ in silicate glasses are commonly conducted at room temperature without correction for recoil-free effects (*Mysen et al.*, 1985; *Dyar et al.*, 1987; *Dingwell*, 1991; *Jayasuriya et al.*, 2004; *O'Neill et al.*, 2006; *Rossano et al.*, 2008;

Cottrell et al., 2009; *Borisov and McCammon*, 2010). This simplification may be justified because some comparisons between uncorrected room temperature Mössbauer measurements and $Fe^{3+}/\Sigma Fe$ determined by other methods have found good agreement with wet chemical determinations (*Mysen et al.*, 1985; *Dingwell*, 1991; *Wilke*, 2005). *Dyar et al.* (1987) found good agreement for a basalt and an andesite, but significant discrepancies for a rhyolite, although the overall uncertainties ($\pm 6\%$) in their study are comparatively high. Also, some studies have found good agreement between room temperature and cryogenic Mössbauer analyses of glasses (*Helgason et al.*, 1989; *Jayasuriya et al.*, 2004). As recoilless fraction should be temperature-dependent (*Chen and Yang*, 2007), this implies recoilless fraction effects on Fe^{3+}/Fe^{2+} determinations at room temperature could be small.

In contrast to these encouraging results, several studies have found discrepancies in application of uncorrected room temperature Mössbauer spectra to $Fe^{3+}/\Sigma Fe$ determinations. *Lange and Carmichael* (1989) reexamined the analyses of *Mysen et al.* (1985) and concluded that they show systematic discrepancies for Fe-rich glasses. In fact, compared to wet chemical analyses, there is a systematic 6% bias to greater $Fe^{3+}/\Sigma Fe$ for all Mössbauer data presented by *Mysen et al.* (1985) and *Dingwell* (1991). Similarly, *Righter et al.* (2013) pointed out that the data of *Wilke* (2005) actually suggest systematically greater $Fe^{3+}/\Sigma Fe$ from Mössbauer spectroscopy than from wet chemical analyses. We note that the wet chemical analyses for $Fe^{3+}/\Sigma Fe$ in glasses do not always agree with other methods or with microbeam determinations, but discrepancies are thought to be owing chiefly to the effects of dissolution of microphenocrysts and are therefore applicable to natural, but not synthetic, glasses (*Bézos and Humler*, 2005; *Cottrell and Kelley*, 2011). *Mysen and Dubinsky* (2004) used a Lorentzian absorption line shape to fit their Mössbauer spectra and found an 8% difference between $Fe^{3+}/\Sigma Fe$ measured on a synthetic basalt at 298 and 150 K. Finally, *Ottonello et al.* (2001) performed a thermodynamic analysis of the Fe^{3+} and Fe^{2+} contents of a wide array of glasses as a function of bulk composition, temperature, and oxygen fugacity and found that those analyzed by Mössbauer spectroscopy had a 14% bias to greater $Fe^{3+}/\Sigma Fe$ compared to glasses determined by wet chemistry. Owing to these observations, uncertainty lingers as to the accuracy of Mössbauer determinations of $Fe^{3+}/\Sigma Fe$ in glasses.

Fe^{2+} and Fe^{3+} are predominantly paramagnetic in silicate glasses, but Mössbauer spectra of some glasses also indicate a non-paramagnetic Fe component (*Jayasuriya et al.*, 2004; *O'Neill*

et al., 2006; *Borisov and McCammon*, 2010). In some cases, non-paramagnetic features are evident as well-resolved sextets, indicating either the presence of minor ferromagnetic precipitates or unrelaxed ferromagnetic interactions between Fe^{3+} ions in the glass and incident γ rays. In other materials, the non-paramagnetic features are expressed only as a broadened absorption, and these occur owing to a super-paramagnetic phase with intermediate interactions (*Borisov and McCammon*, 2010). If these non-paramagnetic components are neglected or are too small to be quantified accurately from the Mössbauer spectra, the derived $Fe^{3+}/\Sigma Fe$ ratio may not be accurate.

To further investigate the accuracy of Mössbauer analyses of $Fe^{3+}/\Sigma Fe$ in silicate glasses, we conducted detailed low temperature Mössbauer investigations of andesitic glass. These allow us to determine directly the recoilless free fractions of Fe ions. To span glasses produced under different experimental conditions, we investigated a glass quenched from 1 atmosphere and one quenched from a high pressure device. For the low pressure glass, we also compared the results of our analysis to wet chemical determinations. Finally, because our initial results raised some questions about the structure of Fe ions in the quenched material, we also conducted magnetic susceptibility measurements to characterize non-magnetic components potentially present.

2.2 The Mössbauer Recoilless Fraction

The intensity or resonant absorption area of a particular component in a Mössbauer spectrum is determined by its recoilless fraction (f_T), which is the probability that a γ quantum will be absorbed resonantly. From both classical and quantum mechanical theories, $f(T)$ is given by

$$f(T) = e^{-k^2<x^2>} \tag{2.2}$$

where $< x^2 >$ is the temperature-dependent mean-square atomic displacement, and k is the wavenumber of the γ quantum (*Chen and Yang*, 2007). For a harmonic solid, the Debye model for the vibrational modes of the lattice (*Schroeder*, 2000), $< x^2 >$, $f(T)$ can be expressed as

$$f(T) = exp\{-\frac{3E_R}{2k_B\theta_D}[1 + 4(\frac{T}{\theta_D})^2 \int_0^{\frac{T}{\theta_D}} \frac{x}{e^x - 1} dx]\} \tag{2.3}$$

where θ_D is the Debye temperature, kB is the Boltzmann constant, ER is the recoil energy, which in turn is given by $E_R = E_\gamma/2Mc^2$, in which E_γ is the energy of the gamma rays (14.412 keV to excite ^{57}Fe), M is the mass of the absorber (^{57}Fe=56.935 amu), and c the velocity of light (c=299792458 m/s).

A popular method to quantify recoilless fractions is to calculate them via Eqn. 2.3 using Debye temperatures derived from the change of the Mössbauer center shift (CS) with temperature (*Niemantsverdriet et al.*, 1984a; *De Grave et al.*, 1985; *Dyar et al.*, 2012). The center shift (CS), which is the location of the centroid of Mössbauer peaks in velocity relative to a standard (α-iron in our case), has two components (Eqn. 2.4), the isomer shift (δ_{IS}), and the second order Doppler shift (δ_{SOD}) (*Niemantsverdriet et al.*, 1984a),

$$CS(T) = \delta_{\mathrm{IS}} + \delta_{\mathrm{SOD}}(T) \tag{2.4}$$

The isomer shift is determined by the difference of s-electron density at the nucleus between the source and the absorber, and is temperature independent, while the second-order Doppler shift is dependent of the mean-square atomic velocity difference between the source and the absorber. Because the source is kept at room temperature, δ_{SOD} varies significantly with absorber temperature and can be parameterized with a Debye model (*Pound and Rebka Jr*, 1960),

$$CS(T) = \delta_{\mathrm{IS}} - \frac{9\mathrm{k_B}T}{2\mathrm{k_B}\theta_{\mathrm{D}}}[1 + 4(\frac{T}{\theta_{\mathrm{D}}})^2 \int_0^{\frac{\theta_{\mathrm{D}}}{T}} \frac{x}{e^x - 1}dx] \tag{2.5}$$

The values of δ_{IS} and θ_{D} can be obtained from the CS of spectra measured over a range of temperatures using Eqn. 2.5, and then the recoilless fraction calculated from θ_{D} using Eqn. 2.3.

This center-shift method (CSM) for estimating recoilless fractions has been applied to Fe^{2+} and Fe^{3+} in a wide range of minerals (*De Grave and Van Alboom*, 1991) and most recently has been employed for detailed evaluation of $Fe^{3+}/\Sigma Fe$ in garnet (*Dyar et al.*, 2012) and Fe^{2+} site occupancies in pyroxenes (*Dyar et al.*, 2013). However, it may not be as accurate when applied to glasses, as the Debye model assumes harmonic behavior and therefore does not account for anharmonic contributions to atomic displacements, which are generally greater for amorphous materials (*Kieffer*, 1979). Studies comparing θ_{D} of glasses inferred from CS variations to θ_{D} determined directly from recoilless fractions deduced by other means have yielded mixed results. *Komatsu and Soga* (1980) found good agreement for a Na_2O-FeO-NiO-SiO glass, but *Oohata*

et al. (1994) found significant discrepancies for glassy V_2O_5-Fe_2O_3-P_2O_5. Thus, at least for glasses the center-shift method should be approached with caution.

A more direct method to quantify the recoilless fractions (f) is the relative method (RM) (*Chen and Yang*, 2007). For a thin sample in which the sample geometry does not change, the observed peak absorption area (AA) for each absorption are proportional to the concentration of the absorbing ion, N,

$$AA_T = f_T \mathrm{N} \tag{2.6}$$

Consequently, so long as a phase transition or change in magnetic state is not traversed, the change in absorption area with temperature is only owing to the change in recoil-free fraction. If peak areas are normalized to that observed at a particular fixed temperature (T_0), AA(T)/AA(T_0), which is equal to f(T)/ f(T_0), the ratio of recoilless-free fractions, depends only on the Debye temperature based on Eqn. 2.7

$$\frac{AA(T)}{AA(\mathrm{T_0})} = \frac{f(T)}{f(\mathrm{T_0})} = exp\{-\frac{6\mathrm{E_R}}{\mathrm{k_B}\theta_\mathrm{D}}[(\frac{T}{\theta_\mathrm{D}})^2(\int_0^{\frac{\theta_\mathrm{D}}{T}} \frac{x}{e^x-1}dx - \int_0^{\frac{\theta_\mathrm{D}}{\mathrm{T_0}}} \frac{x}{e^x-1}dx)]\} \tag{2.7}$$

Fitting the Debye temperature to values of $A(T)/A(\mathrm{T_0})$ from data collected over a range of temperatures allows calculations of the recoilless fraction at any temperature via Eqn. 2.7. Technically, application of this method to anharmonic solids is subject to the same uncertainty as the center shift method described above. However, so long as the measurements of $A(T)/A(\mathrm{T_0})$ span a significant fraction of the temperatures between 0 K and the temperature of interest (in this case, room temperature), the effect of anharmonicity on calculated absolute values of $f(T)$ will be small, as interpolation of the harmonic approximation (Eqn. 2.7) will empirically capture any anharmonic effects expressed over the range of temperatures for which data are available .

2.3 Methods

2.3.1 Sample synthesis

Two different andesitic glasses were analyzed, both with essentially the same major element composition (Table 2.1), similar to that used by *O'Neill et al.* (2006), but quenched from different conditions. One, M544, was quenched at 3.5 GPa, 1600 °C as part of the high pressure study of Chapter 4, whereas the second, VF3, was quenched at 1 atm, 1400 °C and was produced expressly for this study.

The starting materials were prepared from reagent oxides (SiO_2, Al_2O_3, Fe_2O_3, TiO_2, MgO, FeO), silicates ($CaSiO_3$, Na_2SiO_3) and stoichiometric glasses (sanidine). For M544, all iron was added as Fe_2O_3 and 30% of the Fe_2O_3 consisted of $^{57}Fe_2O_3$ (Isoflex, Inc), with the balance derived from normal reagent oxide. For VF3, similar proportions of isotopically normal FeO and Fe_2O_3 were added. Prior to weighing, the SiO_2, Al_2O_3, TiO_2, and MgO were devolatilized by heating in a furnace at 1000 °C overnight. These reagants were then weighed and mixed with the silicates and sanidine by grinding in an agate mortar under ethanol at least one hour and then devolatilized a second time by annealing at 1000 °C for 48 hrs. Finally, the Fe_2O_3, previously at 800 °C for 1 hour and for VF3, with weighed FeO were added to the silicate mix by grinding under ethanol.

For the high pressure experiment, the starting material was loaded in a 2 mm diameter Pt capsule together with a mixture of Ru and RuO_2 which produces an oxygen fugacity similar to that of the magnetite/hematite buffer (*O'Neill and Nell*, 1997). Under these conditions, loss of Fe to the Pt capsule is negligible and dissolution of RuO_2 in the silicate melt is limited to $<$100 ppm (*O'Neill et al.*, 2006). Further details of the capsule design are described in *O'Neill et al.* (2006) and Chapter 4. The experiment was performed at 3.5 GPa and 1600 °C for 4hrs in a 1000-ton Walker-style multi-anvil device with an 18/12 (octahedral edge length/WC truncation edge length) assembly (*Dasgupta et al.*, 2004). Temperature was controlled with a Type D ($W_{97}Re_3/W_{75}Re_{25}$) thermocouple that was positioned immediately above the capsule and oriented axially with respect to the heater. Pressure uncertainties are believed to be $\pm$0.3 GPa, and temperature uncertainties are believed to be $\pm$10 °C (*Dasgupta et al.*, 2004).

The VF3 glass was fused at 1400 °C for 24 hrs in a Deltech VT28 vertical gas mixing furnace in a Pt crucible with oxygen fugacity controlled using a mixture of O_2 and Ar and temperature monitored with a Type S ($Pt_{90}Rh_{10}/Pt_{100}$) thermocouple. Temperature uncertainties are

Table 2.1: Electron microprobe analyses of sample and standard glasses

	ATHO-G(11)[a]	ATHO-G[b]	BCR-2G(9)[a]	BCR-2G[b]	BIR-1G(9)[a]	BIR-1G[b]	VF3(10)[a]	M544(8)[a]
SiO_2	75.50±0.92	75.60±1.40	54.35±0.74	54.40±0.80	47.32±0.74	47.50±0.60	56.89±1.38	57.89±1.76
TiO_2	0.24±0.08	0.255±0.032	2.16±0.26	2.27±0.08	0.90±0.12	1.04±0.14	2.80±0.16	2.68±0.12
Al_2O_3	12.10±0.26	12.20±0.40	13.31±0.24	13.40±0.80	15.45±0.20	15.50±0.40	14.89±0.38	15.09±0.64
FeO*	**3.28±0.10**	**3.27±0.20**	**12.50±0.36**	**12.50±0.60**	**10.37±0.14**	**10.40±0.20**	**9.29±0.22**	**8.92±0.12**
MnO	0.10±0.02	0.11±0.010	0.20±0.02	0.19±0.02	0.17±0.04	0.19±0.02	0.06±0.02	0.03±0.04
MgO	0.11±0.02	0.10±0.02	3.73±0.18	3.56±0.18	9.95±0.22	9.40±0.20	2.26±0.08	2.24±0.08
CaO	1.78±0.04	1.70±0.06	7.20±0.12	7.06±0.22	13.39±0.24	13.30±0.40	7.60±0.10	7.40±0.08
Na_2O	3.63±0.40	3.75±0.62	3.05±0.36	3.23±0.14	1.76±0.16	1.85±0.14	4.21±0.32	4.34±0.12
K_2O	2.72±0.08	2.64±0.18	1.78±0.08	1.74±0.08	0.02±0.02	0.03±0.010	1.06±0.06	1.06±0.02
Total	99.46	99.62	98.27	98.35	99.33	99.21	99.06	99.65

Notes:Number in parentheses indicates the number of analyses averaged. FeO*:Total Iron contents.
All uncertainties are in two sigma range standard deviation (2σ)
[a]Electron microprobe analyses
[a]BIR-1G and BCR-2G reference values from *Jochum et al.* (2005) and ATHO-G reference values from *Jochum et al.* (2006).

believed to be ± 5 °C based on a thermocouple calibration which yielded 1059 °C for melting of Au, which compares to 1064 °C value given by ITS90. The VF3 glass was quenched in a few seconds by being dropped into water. Electron microprobe analysis of a section spanning the furthest and closest positions relative to the Pt hanging wire indicated that the major element concentrations of the glass are homogeneous.

2.3.2 Analytical Methods

Electron microprobe

Textures of the quenched glasses were examined by back-scattered electron (BSE) and secondary electron imaging (SEI) using the JEOL JXA-8900R electron microprobe (EPMA) at the University of Minnesota. Major element concentrations were quantified by wave-length-dispersive analysis using a 15 kV acceleration voltage, 20 nA beam current and a beam focused to 5 μm diameter. Peak and background counting times were 15 s for standard analyses and 30 s for unknown samples. Data were acquired using the following diffractometer crystals: LiF for Ti kα, LiFH for Mn kα, Fe kα, PETJ for K kα, Ca kα, and TAP for Al kα, Mg kα, Si kα, and Na kα. Mineral and glass standards from *Jarosewich et al.* (1980) were used, including basaltic glass for Mg kα, Ca kα, ilmenite for Ti kα, albite for Si kα, Al kα, Na kα, Mn-olivine for Fe kα, Mn kα, and microcline for K kα, and matrix corrections were computed with Probe for Windows software.

Besides VF3 and M544, MPI-DING glass ATHO-G (*Jochum et al.*, 2006) and USGS glasses BCR-2G and BIR-1G (*Jochum et al.*, 2005) were analyzed several glasses as secondary standards. Each of these was analyzed before VF3, between VF3 and M544 and after M544. The intensity data of standards and unknown samples, including secondary standards were checked for time dependent intensity (TDI) changes. Si kα and Na kα using a self-calibrated TDI correction and detected no TDI effect on other elements. Corrections were also applied for minor Si and Al drift that occurred during the analysis period.

Mössbauer spectroscopy

Mössbauer spectroscopy was conducted with a constant acceleration spectrometer (Web Research (currently SeeCo)) equipped with a Janis Nitrogen shielded Helium dewar at the Institute for Rock Magnetism, University of Minnesota. A ^{57}Co/Rh source and Reuter Stokes proportional Ar gas counter was employed. Data were collected over 512 channels, which were then folded to produce 256 unique channels. Calibration was relative to a pure α-Fe foil for which data were collected at room temperature (293 K). As M544 includes 3% $^{57}Fe_2O_3$, the M544 glass was crushed into fine powder with ethanol then diluted with powdered sugar, while VF3 was analyzed as a pure powdered glass. The ^{57}Fe in both samples was evenly distributed in an approximately circular mount 12.7 mm in diameter, confined by Kapton tape.

To verify the precision of the center shifts and peak areas determined at the conditions of data acquisition (collection times) at low temperature conditions, additional Mössbauer spectra were collected for sample VF3 at room temperature for durations ranging from 1 to 72 hours both at with 6 mm/s and 12 mm/s velocity scales. As shown in Figs. 2.S1 and 2.S2, both the Cente Shift (CS) of Fe^{3+} and Fe^{2+}, and the $Fe^{3+}/\Sigma Fe$ determined from peak area ratios, are consistent between 6 mm/s and 12mm/s scale and almost same when background counts exceed 0.3 X 10^6, irrespective of velocity scales, all parameters are listed in Table 2.S1. All other spectra were collected over at least one day and sufficient counts ($>$550000 cts/channel for M544 and $>$220000 cts/channel for VF3) were accumulated to get reasonable statistical error. Mössbauer thicknesses for M544 and VF3 were estimated to be 1.91 and 4.08 mg/cm^2 Fe, respectively, using the RECOIL algorithm (*Rancourt et al.*, 1993) and assuming a recoilless free fraction equal to unity.

The spectra were collected from 47 K to room temperature (298 K). A silicon diode was used as cryogenic temperature sensor. A 50 Watt constant-current-source heater, controlled by a Neocera LTC-21 temperature controller was used to adjust the sample temperature. All Mössbauer spectra were fitted with the RECOIL software package (*Lagarec and Rancourt*, 1997).

Table 2.2: Wet chemical determinations of FeO

		Measured	Accepted
USGS standards	QL	2.84	2.97[a]
	W-2a	8.1	8.34[a]
Replicates			
VF3		2.9	
VF3		2.99	
VF3		3.03	
VF3		3.02	
Average VF3		2.99	3.10[b]0.24[d]
$Fe^{3+}/\Sigma Fe$			0.666[c]$\pm$0.030[d]

[a]QL and W-2a reference values from Govindaraju(1994).
[b]Average VF3 value corrected accounting for the bias in the analyses of the USGS standards.
[c]$Fe^{3+}/\Sigma Fe$ calculated from FeO*= 9.29 wt% (2.1).
[d]Uncertainties are in two sigma range standard deviation (2σ)

Wet Chemistry

The Fe^{2+} content of VF3 was determined using the micro-colorimetric procedure, improved by *Wilson* (1960). Analyses were carried out blind at the University of Michigan. USGS standards QL and W-2a powdered rock standards (*Govindaraju*, 1994) were analyzed as part of the same procedure.

Magnetization Measurements

Magnetic hysteresis loops determining the relationship between applied magnetic field and sample magnetization (*Tauxe*, 1998) were determined at room temperature (293 K) using a Princeton Measurements Corp. vibrating sample magnetometer in the Institute for Rock Magnetism, University of Minnesota, with maximum field of 1.5 T. Sample VF3, was analyzed as a powdered glass and M544 as a powdered glass mixed with powdered sugar. Hysteresis parameters were calculated using software developed at the Institute for Rock Magnetism and described fully in (*Jackson and Solheid*, 2010).

2.4 Results

2.4.1 Wet Chemical and EMPA determinations

Electron microprobe analyses of the glasses and secondary standards established FeO*. Analyses reproduced the accepted FeO* concentrations of the standards almost perfectly with the largest discrepancy being 0.03 wt.% (Table 2.1), and so the resulting FeO* of the unknown glasses (VF3 9.29±0.22 wt.%; M544 8.92±0.12 wt.%; 2σ) are believed to have high accuracy.

Wet chemical analysis of VF3 glass was repeated 4 times, resulting in FeO of 2.99±0.12 wt%, (2σ). Analyses of USGS standards, QL and W-2a, performed at the same time resulted in FeO contents that were systematically lower than accepted values (*Govindaraju*, 1994) by 4%, and so the results of VF3 have been adjusted accordingly, to 3.10±0.24 wt%, (2σ) (2.2). We believe that the systematic discrepancy may be owing to the finely powdered standards, which were ground to grain sizes similar to the unknowns. The fine powdering results in some retention of starting material in the holding beaker. Combining the Fe^{2+} from EMPA with FeO from wet chemistry, the resulting $Fe^{3+}/\Sigma Fe$ in VF3 is 0.666±0.030 (2σ) (Table 2.2).

2.4.2 Mössbauer Spectroscopy

Mössbauer spectra of VF3 and M544 have broadened line-shapes typical of silicate glasses and can be well-accommodated by distribution fitting methods (*Rossano et al.*, 2008; *O'Neill et al.*, 2006; *Borisov and McCammon*, 2010; *Rossano et al.*, 1999; *Alberto et al.*, 1996). Spectra consist chiefly of two quadrupole doublets, one originating from paramagnetic ferric and the other from ferrous iron. There is no obvious evidence of sextets in the spectra with velocity scale up to 12 mm/s. Such sextets are commonly present in quenched mafic glasses (*Jayasuriya et al.*, 2004; *O'Neill et al.*, 2006; *Borisov and McCammon*, 2010) and are indicative of a ferromagnetic component. Thus, the Fe in the glasses is dominantly paramagnetic Fe^{2+} and Fe^{3+}. The Fe thicknesses estimated for M544 and VF3 are expected to have negligible effect on determined Mössbauer parameters, and this was verified by comparing uncorrected spectra with those corrected using the pre-analysis thickness calculation available in the RECOIL package.

Preliminary fitting of the Mössbauer data was performed by treating the spectra solely as the result of two paramagnetic doublets by assuming that the Lorentzian half widths at half maximum (L HWHM) for all sub-spectra are the same (*Lagarec and Rancourt*, 1997). Each

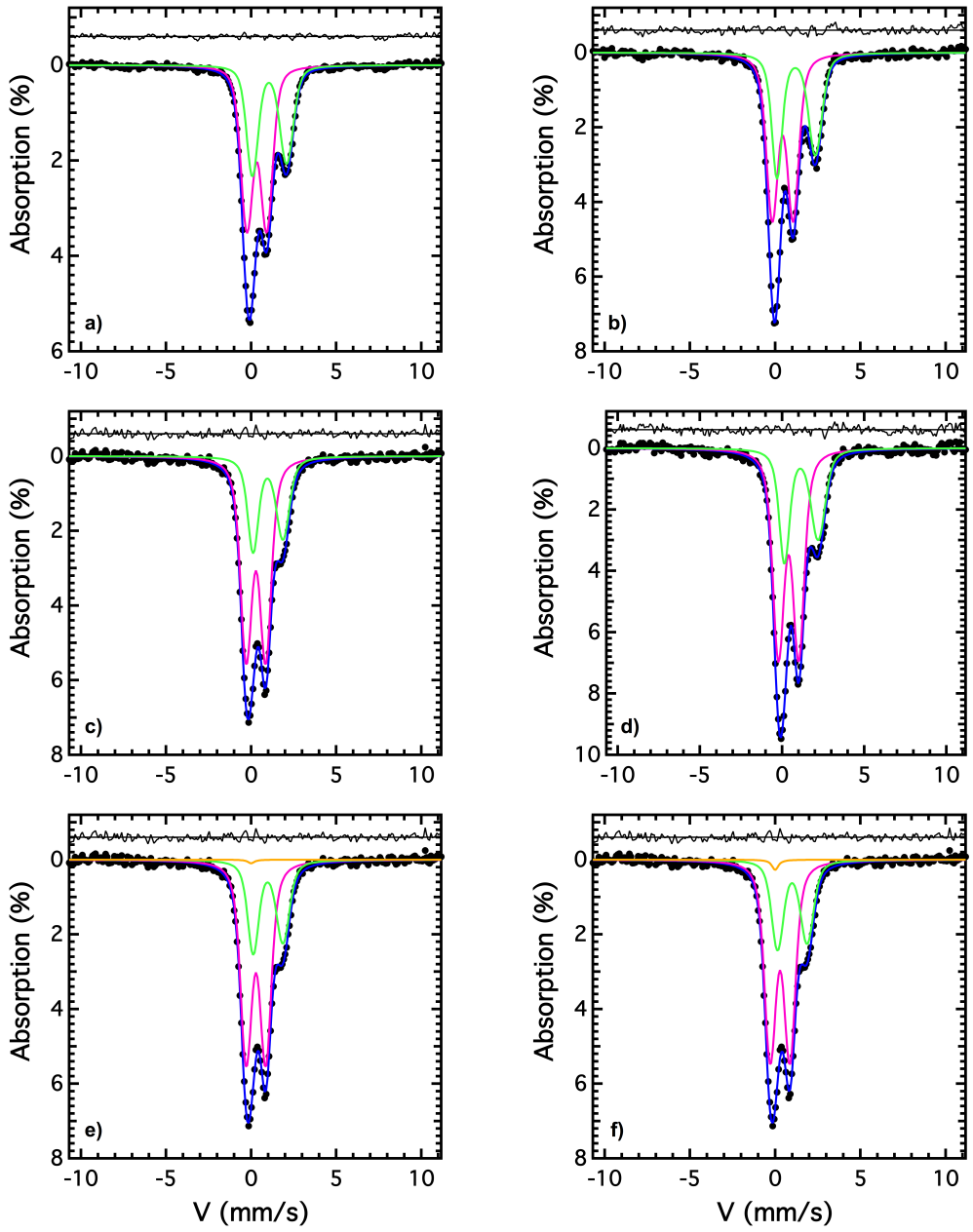

Figure 2.1: Examples of Mössbauer spectra and their fits. (a) M544 data collected at room temperature. (b) M544 data collected at 67 K. (c) VF3 data collected at room temperature. (d) VF3 data collected at 67 K. (e) VF3 data collected at room temperature fitted by assuming nanophase being Fe_3O_4. (f) VF3 data collected at room temperature fitted by assuming nanophase being $MgFe_2O_4$. For all spectra, the pink curves refer to the paramagnetic Fe^{3+} doublets, the green curves refer to the paramagnetic Fe^{2+} doublets, and the blue curves are the superposition of all the sites. For e and f, the orange curves refer to the superparamagnetic site.

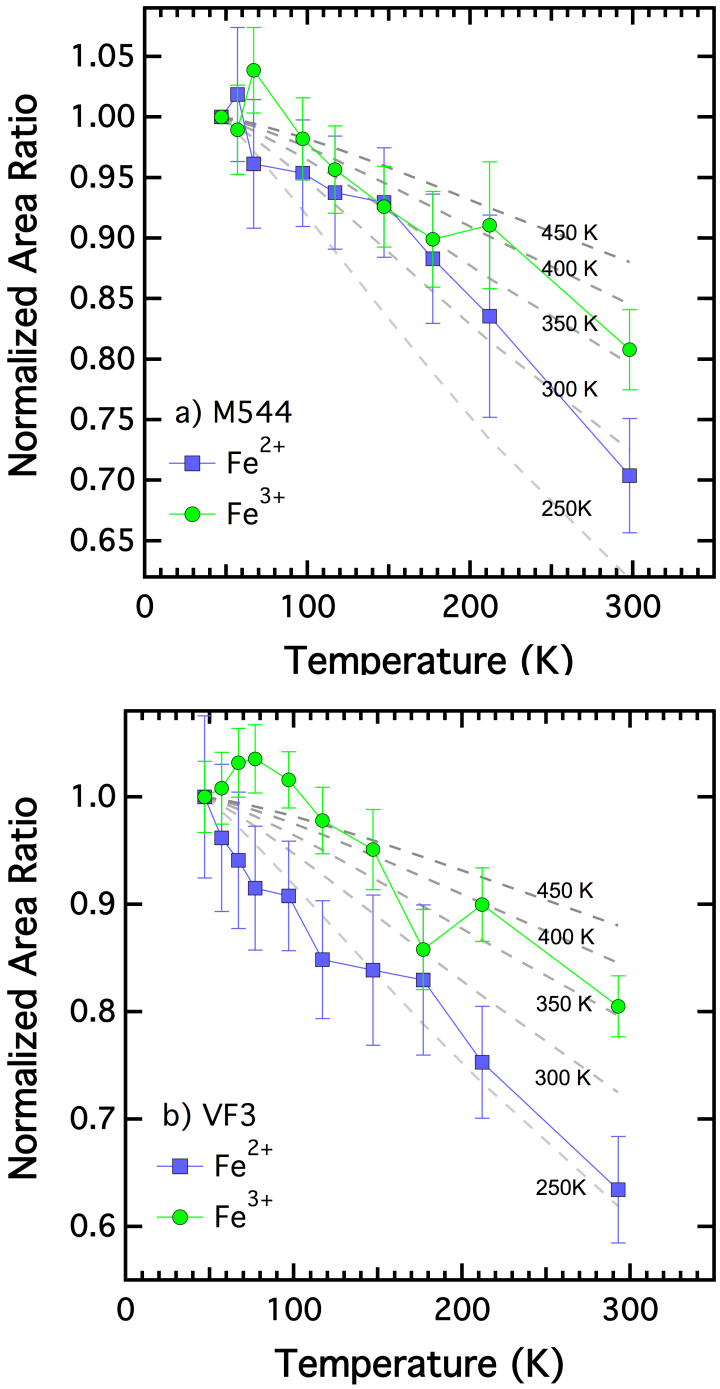

Figure 2.2: Normalized absorption areas(AA) from M544 and VF3 Mössbauer spectra fit with xVBF methods as a function of temperature. Normalized area is the background-removed AA normalized by the AA at 47K.(**a** and **b**) These show the normalized AA for M544 and VF3,respectively (normalized to AA at 47 K). Dashed curves are normalized AA at 47 K from recoilless fractions calculated at different Debye temperatures.

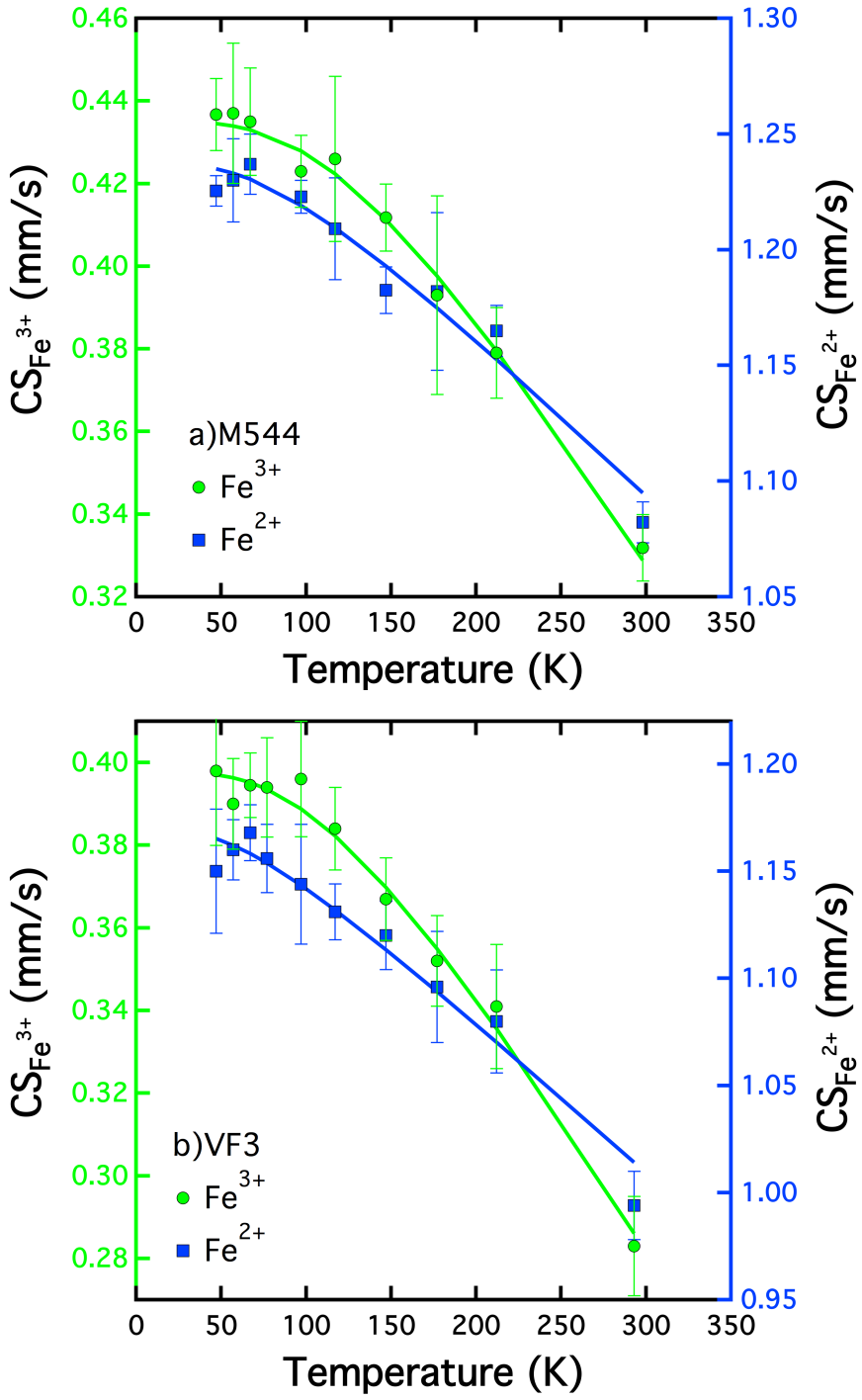

Figure 2.3: Center shift (CS) from M544 and VF3 Mossbauer spectra fit with xVBF methods. (**a** and **b**) These show the CS changes with 36 temperature in M544 and VF3, respectively. The blue (Fe^{2+}) and green curves (Fe^{3+}) are fitted from Equation 2.3.

doublet was fit with as a two dimensional (2D) distribution, whose parameters consist of the center shift (CS), the quadrupole splitting (QS), and their respective Gaussian widths, δCS and δQS, We did not consider the correlation between CS and QS for Fe^{3+}, (θ), or the correlation between the CS distribution and the QS distribution of QS (ρ), because the analysis of (*Alberto et al.*, 1996) showed that these should be effectively negligible for Fe^{3+} in silicate glasses in low concentrations (5$\sim$15 wt.% Fe2O3), (θ). The fit of the Fe^{2+} paramagnetic component considers these correlations. All the hyperfine parameters and their uncertainties were calculated based on a bootstrap method and are cataloged in Table 2.S2. The quality of these fits is characterized by reduced chi squared (χ^2) values, which are also listed in Table 2.S2 and demonstrates that the fitting is robust.

From the Mössbauer spectra collected at room temperature (Fig. 4.4a and Fig. 4.4c), for Fe^{3+} in M544, CS = 0.334 mm/s and QS = 1.166 mm/s, and for Fe^{3+} in VF3, CS = 0.283 mm/s and QS = 1.148 mm/s, whilst for Fe^{2+} in M544, CS = 1.080 mm/s and QS = 2.013 mm/s, for Fe^{2+} in VF3, CS = 0.994 mm/s and QS = 1.754 mm/s. These parameters are similar to those previously reported for silicate glasses (*O'Neill et al.*, 2006; *Alberto et al.*, 1996; *Jayasuriya et al.*, 2004; *Borisov and McCammon*, 2010). Proportions of $Fe^{3+}/\Sigma Fe$ in M544 and VF3, judged solely from the area ratios of the 293 K paramagnetic doublets are 0.6001$\pm$0.0083, 2σ, and 0.685$\pm$0.014, 2σ, respectively.

Low temperature Mössbauer spectra show features similar to those at room temperature, as illustrated at 67 K for M544 and VF3 (Fig. 4.4b and 4.4d). With increasing temperature, the relative area under the Fe^{2+} doublet diminishes compared to that of Fe^{3+} (Table 2.S2), and the normalized area ratios decrease for both Fe^{3+} and Fe^{2+} (Fig. 2.2). As the $Fe^{3+}/(Fe^{2+} + Fe^{3+})$ ratio of the sample does not change, this temperature dependence is best understood as a change in the relative recoilless fractions for Fe^{3+} and Fe^{2+}, as expected from Eqn. 2.1. Also, center shifts (CS) increase with decreasing temperature, consistent with the contributions of the second order Doppler shift (Eqns. 2.4,2.5) (Fig. 2.3). Each of these observations can be used to determine Mössbauer Debye temperatures and in turn can be used to model the relationship between temperature and recoilless fraction for these glasses.

Mössbauer Debye temperatures determined by direct measurement of the temperature dependent relative areas of the Mössbauer doublets (Eqn. 2.7) are calculated by normalizing to measurements at low temperature (47 K). Least squares analysis of normalized peak areas gives Mössbauer Debye temperatures (θ_D) of 373$\pm$39 K and 305$\pm$30 K, in 2σ, for Fe^{3+} and

Fe^{2+} respectively for M544 and 352±30 K and 269±27 K, in 2σ, respectively for VF3. Similarly, Mössbauer Debye temperatures and intrinsic isomer shifts, δIS, can be determined from a least squares fit to the CS versus temperature trends (Fig. 2.3) (Eqn. 2.5), yielding, for M544, δIS=0.576±0.026 mm/s and θ_D=506±114 K (Fe^{3+}) and δIS=1.314±0.016 mm/s and θ_D=295 ± 89 K (Fe^{2+}) and for VF3, δIS=0.524±0.016 mm/s and θ_D=466±78 K (Fe^{3+}) and δIS=1.233±0.017 mm/s and θ_D=235±114 K, all uncertainties are 2σ.

From these determinations of Mössbauer Debye temperatures and Eqn. 2.3, recoilless fractions can be calculated as a function of temperature (Table 2.S3). At 293 K, the value of C in Eqn.2.1, calculated with θ_D derived from the relative method (CRM) is 1.151±0.118 and 1.256±0.0153, for M544 and VF3 respectively. Values calculated at 293 K from CS data (CCSM) are distinctly higher: CCSM, is 1.305±0.146 for M544 and 1.762±1.188 for VF3 (Table 2.S3). Resulting calculated values of $Fe^{3+}/\Sigma Fe$, based on these values and 293 K area ratios are, for M544, 0.569 (RM) and 0.532 (CSM) and, for VF3, 0.634 (RM) and 0.552 (CSM), the rest listed in Table 2.S3 and plotted vs. temperature in Fig. 2.4.

2.4.3 Magnetic hysteresis

Measurements of sample magnetization versus applied field (hysteresis loops) reveal hysteresis in both glasses, indicating a minor ferromagnetic component (Fig. 2.5) with superparamagnetic behavior in addition to a paramagnetic component. A purely paramagnetic material would produce a simple linear relationship between applied field and magnetic moment. A small ferromagnetic contribution would saturate in lower fields (0.3 Tesla for magnetite) and typically has magnetization intensities several orders of magnitude higher than a paramagnetic material in a 1.5 Tesla field. For glass M544, the sigmoidal shape of the magnetization curves shown in Fig. 2.5a, with saturation around 500 mT are indicative of superparamagnetic behavior, as is treated Fig 2.19c in (*Tauxe*, 1998). This contrasts with the observed Mössbauer spectrum (Fig. 4.4), which shows only simple paramagnetic doublets. This seeming discrepancy is in large part owing to the admixture of sugar (which is diamagnetic) with glass in the M544 sample mount (Fig. 2.S3).

For VF3, the raw data produces a nearly linear relationship between magnetization and applied field (Fig. 2.5b), indicating very little ferromagnetic contribution to the hysteresis loop

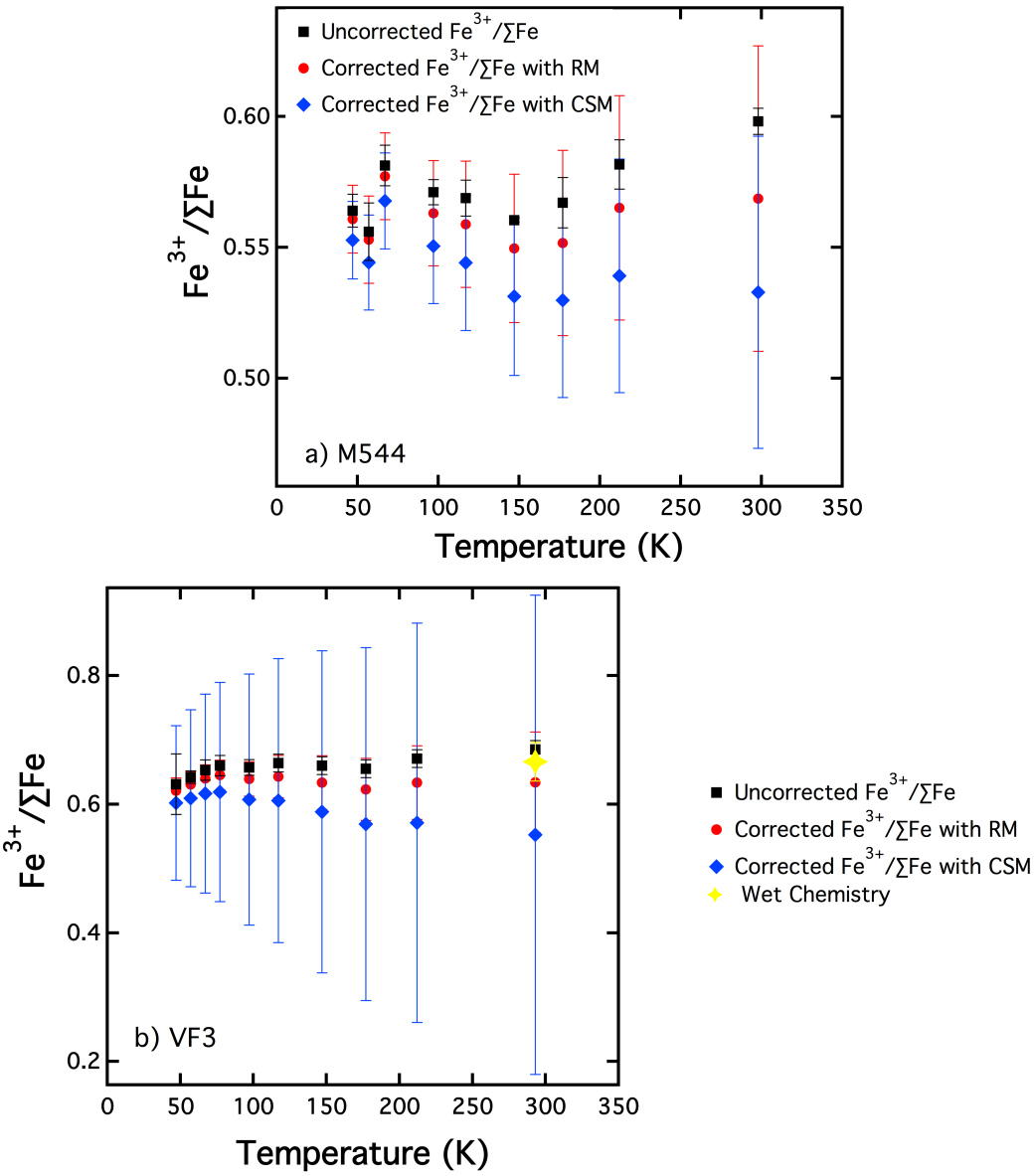

Figure 2.4: (**a** and **b**) These show $Fe^{3+}/\Sigma Fe$ ratios determined for M544 and VF3, respectively. The black squares refer to results obtained directly from uncorrected Mössbauer spectra. The red dots show $Fe^{3+}/\Sigma Fe$ ratios corrected by the relative method (RM), which is the recoilless fraction based on the Debye temperature obtained from the normalized area ratio changes with temperature, and the blue diamonds, refer to the $Fe^{3+}/\Sigma Fe$ ratios corrected by the recoilless fraction based on the Debye temperature obtained from the CS changes with temperature (CSM). For (**b**), the orange star is the $Fe^{3+}/\Sigma Fe$ ratio determined by wet chemistry and electron microprobe.

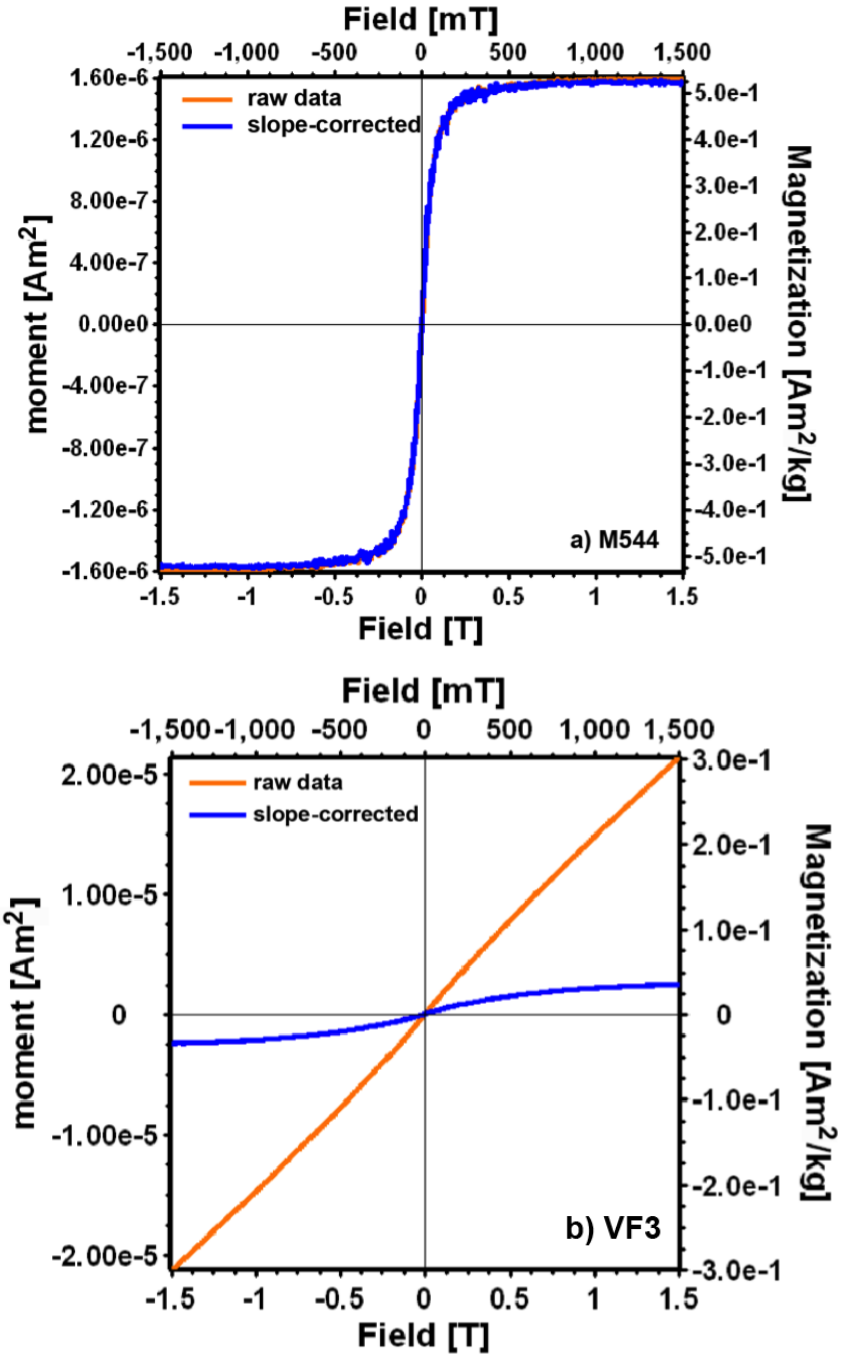

Figure 2.5: (**a** and **b**)These show the hysteresis between applied magnetic field and sample magnetization determined for M544 and VF3, respectively, both measured at 293 K. Orange curves refer to the raw data and blue curves to the slope-corrected loop, derived from a regression line subtracted through the outermost data points using the nonlinear high-field fitting at 70%. Both slope-corrected curves saturate at high field intensity, indicating superparamagnetic behavior.

(*Dunlop and Özdemir*, 2001). Yet, the small deviation from linearity, evident in the slope-corrected loop, shows that a minor superparamagnetic component is also present (*Dunlop and Özdemir*, 2001) This component is not clearly evident in the Mössbauer spectra (Fig. 4.4), presumably because it is small, but failure to account for its contribution may lead to overestimation or underestimation of the $Fe^{3+}/\Sigma Fe$ ratio determined from Mössbauer spectra, depending on the ratio of $Fe^{3+}/\Sigma Fe$ in this minor phase. Note that unrelaxed Fe^{3+} in the silicate glass cannot account for the magnetic hysteresis behavior of the sample, as the time constant of applied magnetic field is far greater than the relaxation time of isolated Fe^{3+} ions (*Chen and Yang*, 2007). Sample M544 has a stronger ferromagnetic signal, but again with near zero coercivity indicating a superparamagnetic phase.

Based on the measured saturation magnetizations (σs) (M544: 0.5235 Am^2/kg; VF3: 0.0426 Am^2/kg, Fig. 2.5), the fraction of nonparamagnetic nanophase present can be estimated provided that the identity and magnetic characteristics of the ferromagnetic nanophase are known. Although several possibilities exist, the most likely phase is a Fe-Mg ferrite (Fe_3O_4 - $MgFe_2O_4$) solid solution. For VF3, if we assume the ferromagnetic nanophase is pure Fe_3O_4, for which the saturation magnetization, σs=92 Am^2/kg (*Li et al.*, 2006), the resulting Fe in the ferromagnetic nanophase [$(Fe^{2+} + Fe^{3+})_{Fe3O4}/\sigma Fe$] is 0.0043. If we assume it is pure MgFe2O4, whose σs=33.4 Am^2/kg (*Sepelák et al.*, 2007), $Fe^{3+}{}_{MgFe_2O_4}/\sigma/Fe$ is 0.0118. Ferrite solid solutions will be intermediate between these bounds, and so the contribution of the non-paramagnetic material to $Fe^{3+}/\Sigma Fe$ of the bulk material is small but constrained.

2.5 Discussion

2.5.1 Estimating recoilless fractions from center shift versus relative methods

For both the VF3 and M544 glasses, estimates of ferric Debye temperatures are much greater from the CS method than from the relative method, while estimates of ferrous Debye temperatures from the two methods are similar, as also was observed in previous studies (*Niemantsverdriet et al.*, 1984b; *Oohata et al.*, 1994). These discrepancies are presumably owing to anharmonicity in the glasses, and the resulting inaccuracy of the Debye model. The differences in the two methods produce significant differences in recoilless fraction estimates of $Fe^{3+}/\Sigma Fe$ of the glasses (Fig. 2.4). We argue that the RM yields more accurate estimates for these glasses and that the CS method is in this case less reliable. First, as previously mentioned,

the RM is based on the effect of temperature on the areas of the observed Mössbauer doublets (Fig. 2.2), and so the Debye model functions chiefly as an empirical method to interpolate measured changes in recoilless fraction as a function of temperature. Translation of the temperature dependence of the CS to recoilless fraction is more reliant on the accuracy of the Debye theory. Second, because the $Fe^{3+}/\Sigma Fe$ of the silicate does not vary with temperature, an accurate recoilless fraction correction should produce a nearly constant ratio at all temperatures. Those determined using the CS method vary with temperature, whereas those from the RM method are more nearly temperature-independent (Fig. 2.4). Accurate values of recoilless fraction should produce the same calculated $Fe^{3+}/\Sigma Fe$ at all temperatures (Eqn. 2.1), suggesting that the values of CT calculated with the RM method are more accurate and that those calculated with the CS method overestimate recoilless effects on $Fe^{3+}/\Sigma Fe$ determinations for these andesitic glasses (Fig. 2.4).

2.5.2 Modeling nonparamagnetic effects on $Fe^{3+}/\Sigma Fe$ of the quenched glasses

Correction for recoilless effects on paramagnetic Mössbauer doublets does not address the influence of non-paramagnetic nanophases on the accuracy of room temperature Mössbauer determinations of $Fe^{3+}/\Sigma Fe$. Consequently, we refit the room temperature Mössbauer spectrum for VF3 by including superparamagnetic phase of fixed proportion based on the magnetic hysteresis loop analysis above (0.43% Fe3O4 or 1.18% $MgFe_2O_4$ for VF3, respectively). As superparamagnetic material will show six peaks at low temperature and collapse to one peak as temperature increases (*Morup and Tronc*, 1994; *Morup et al.*, 1976). To investigate whether the superparamagnetic material observed in the hysteresis measurements adds uncertainty to $Fe^{3+}/\Sigma Fe$ ratios calculated from Mössbauer spectra, we included a superparamagnetic component to the fit paramagnetic spectrum, the extra phase is expected to produce an extra single absorption peak in a magnetic site centered at CS=0 mm/s at room temperature. Because the xVBF method is applied, the Lorentzian half width at half maximum (L HWHM) for all subspectra is the same (*Lagarec and Rancourt*, 1997) and so no Gaussian width is required to fit this extra absorption peak. Resulting fits are shown in Figs. 4.4e and 4.4f, and the detailed fitting parameters are given in Table 2.S4. The resulting $Fe^{3+}/\Sigma Fe$ ratios are essentially indistinguishable regardless of whether the nanophase is assumed to be Fe_3O_4 or $MgFe_2O_4$. Specifically, the resulting $Fe^{3+}/\Sigma Fe$ ratios are 0.685 if the ferrite is pure Fe_3O_4 and 0.684 if it is $MgFe_2O_4$. These are not distinguishable from one another or from the ratio (0.685) derived by neglecting

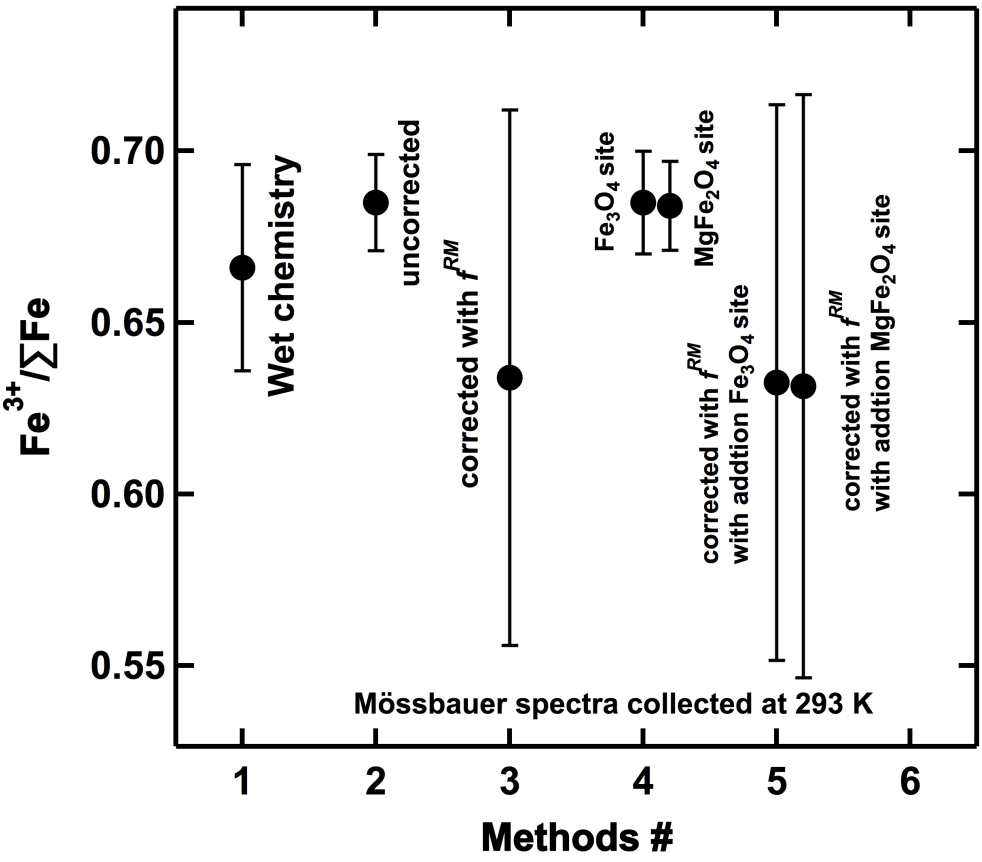

Figure 2.6: Comparison of $Fe^{3+}/\Sigma Fe$ ratios for VF3 calculated with different methods with 2 uncertainties 1 = Wet chemistry and electron microprobe. 2 = Uncorrected room temperature Mössbauer spectra. 3 = Room-temperature Mössbauer spectra corrected with recoilless fraction (f^{RM}) generated by the relative method (RM). 4 = Uncorrected room-temperature Mössbauer spectra including a fit to the nanophase assumed to be pure $MgFe_2O_4$. 4.2 = Uncorrected room-temperature Mössbauer spectra including a fit to the nanophase assumed to be pure Fe_3O_4. 5 = Room-temperature Mössbauer spectra corrected with f^{RM} and including a fit to the nanophase assumed to be pure $MgFe_2O_4$. 5.2 = Room-temperature Mossbauer spectra corrected with f^{RM} and including a fit to the nanophase assumed to be pure Fe_3O_4.

the nonparamagnetic component, indicating that the influence of the non-paramagnetic component on $Fe^{3+}/\Sigma Fe$ on this glass is small.

The $Fe^{3+}/\Sigma Fe$ ratios in the previous paragraph neglect the effects of recoilless fractions. Although the overall effect of the non-paramagnetic phase is small, for thoroughness it is appropriate to consider recoilless fractions not only for the paramagnetic doublets, as already described, but also for the nanophase oxides. For Fe_3O_4, θ_D=334$\pm$10 K for Fe^{3+} and θ_D=314$\pm$10 K for Fe^{2+} (*Sawatzky et al.*, 1969), giving recoilless fractions at room temperature (calculated from Eqn. 2.3) of $f(Fe^{3+})Fe_3O_4$=0.693 and $f(Fe^{2+})Fe_3O_4$=0.661. No similar data are available for $MgFe_2O_4$, so we assume that θ_D for Fe^{3+} is the same as in Fe_3O_4. The resulting calculated $Fe^{3+}/\Sigma Fe$ ratio for VF3 equals 0.633 or 0.632 respectively, assuming that the non-paramagnetic phase is pure Fe_3O_4 or $MgFe_2O_4$.

2.5.3 Superparamagnetism in quenched glasses

The magnetic hysteresis of the quenched glasses establish that a small fraction of the Fe is present as a superparamagnetic phase, which suggests that nanometer-scale precipitates of Fe-oxide were produced during quench of the silicate liquid. The formation of such precipitates may have been promoted by the comparatively high Fe_2O_3 content (6 wt%) of the melt. There is little reason to believe that their formation affected the $Fe^{3+}/\Sigma Fe$ of the aggregate quenched material, and so long as the nanophase is accounted for in the fitting of the spectrum, it should not compromise the accuracy of the inferred $Fe^{3+}/\Sigma Fe$ of the silicate liquid present prior to quench.

Superparamagnetic behavior has been documented in otherwise fresh natural basaltic glasses (*Pick and Tauxe*, 1994), and in Fe-rich basaltic glasses quenched in the laboratory (*Bowles et al.*, 2011) but is not generally considered to contribute to Mössbauer spectra of laboratory-quenched glasses. Non-paramagnetic components of Mössbauer spectra, including broad absorptions approximately symmetric about CS=0 mm/s as well as sextets, are a common feature in such glasses, in many cases comprising a larger fraction of the Fe than documented for VF3 or M544 (*Jayasuriya et al.*, 2004; *O'Neill et al.*, 2006; *Borisov and McCammon*, 2010; *Weigel et al.*, 2010). These non-paramagnetic components are commonly attributed to unrelaxed ferromagnetic behavior of Fe^{3+} ions in the glass, in part because of skepticism that superparamagnetic precipitates form from rapidly cooled glasses (*Weigel et al.*, 2010). Documentation of nanophase oxides from rapidly cooled glasses in this study suggests that superparamagnetic

components may be more common contributors to Mössbauer spectra of laboratory-quenched glasses than previously supposed, particularly in cases where a single symmetric peak is observed, but also in cases when non-paramagnetic features are not obvious from casual inspection of the Mössbauer results. Depending on the size and domain structure of the particles, such precipitates could also contribute to ferromagnetic sextets in Mössbauer spectra. This would be of particular concern, as such phases, presumably rich in Fe_3O_4, would contain both Fe^{2+} and Fe^{3+}, whereas normal attribution as unrelaxed ions considers them to consist solely as Fe^{3+}.

2.5.4 Wet chemical vs. Mössbauer determination of $Fe^{3+}/\Sigma Fe$

Returning to the controversy of the accuracy of FeO* ratio determined from Mössbauer spectra collected at room temperature (*Mysen et al.*, 1985; *Dingwell*, 1991; *Dyar et al.*, 1987; *Helgason et al.*, 1989; *Lange and Carmichael*, 1989; *Ottonello et al.*, 2001; *Mysen and Dubinsky*, 2004; *Jayasuriya et al.*, 2004; *Rossano et al.*, 2008; *Righter et al.*, 2013), Fig. 2.6 compares combined wet chemical/microprobe determination of $Fe^{3+}/\Sigma Fe$ for andesitic glass VF3 with different treatments of the Mössbauer spectra. In general, distinctions in $Fe^{3+}/\Sigma Fe$ ratio determined from different treatments of the Mössbauer spectra and wet chemistry are small and within 2σ analytical uncertainty envelopes. The $Fe^{3+}/\Sigma Fe$ ratio derived from temperature uncorrected for recoilless effects or for non-paramagnetic components agrees with that determined by wet chemistry with a relative difference about 3%. However, $Fe^{3+}/\Sigma Fe$ values corrected for recoilless fraction have a large uncertainties at 2σ. One possible reason for these uncertainties could be owing to insufficient constraints on the Debye temperatures, due to too few measurements made as a function of temperature (Fig. 2.2), or because of insufficient precision in peak locations and areas due to poor counting statistics. The latter may indicate that the error bands in $Fe^{3+}/\Sigma Fe$ propagated from the uncertainties in individual parameter determinations are exaggerated, as the stability of determined Mössbauer parameters as a function of counting time (Figs. 2.S1 and 2.S2) suggests that longer counting times results in smaller errors without appreciable changes in values of determined parameters. A more general factor that may apply beyond the details of data collection in this particular study is that Mössbauer spectra of glasses have comparatively broad peaks, making precise determinations of CSs and peak areas more challenging than for minerals. The former reasons indicate that high uncertainty in recoilless fractions, and therefore $Fe^{3+}/\Sigma Fe$ are specific to the conditions of this study, whereas the last reason highlights a more general challenge to application of Mössbauer spectroscopy to

$Fe^{3+}/\Sigma Fe$ determinations in glass.

2.6 Implication

Room temperature Mössbauer spectroscopy yields accurate $Fe^{3+}/\Sigma Fe$ ratios in silicate glasses within normal analytical uncertainties, but with a small systematic bias to higher values compared to wet chemical or recoilless fraction-corrected determinations. A common method for estimating recoilless fractions by measurement of the temperature dependence of the Mössbauer center-shift may not be accurate for glasses, but relative peak height methods appear to be more robust. Nanophase magnetic precipitates can form in rapidly quenched glasses and, if not accounted for properly, can bias Mössbauer-determined $Fe^{3+}/\Sigma Fe$ ratios. Therefore, accurate determination of $Fe^{3+}/\Sigma Fe$ ratios in silicate glasses by Mössbauer spectroscopy requires consideration of the recoilless fraction.

2.A Supplement material

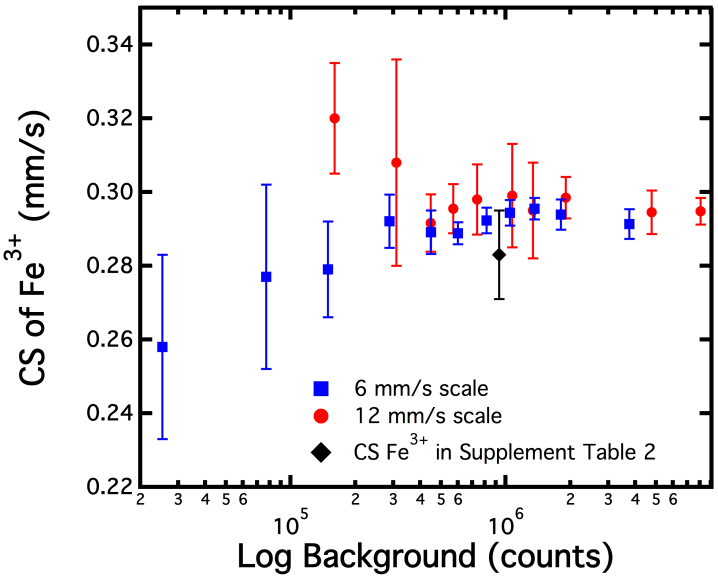

(a)

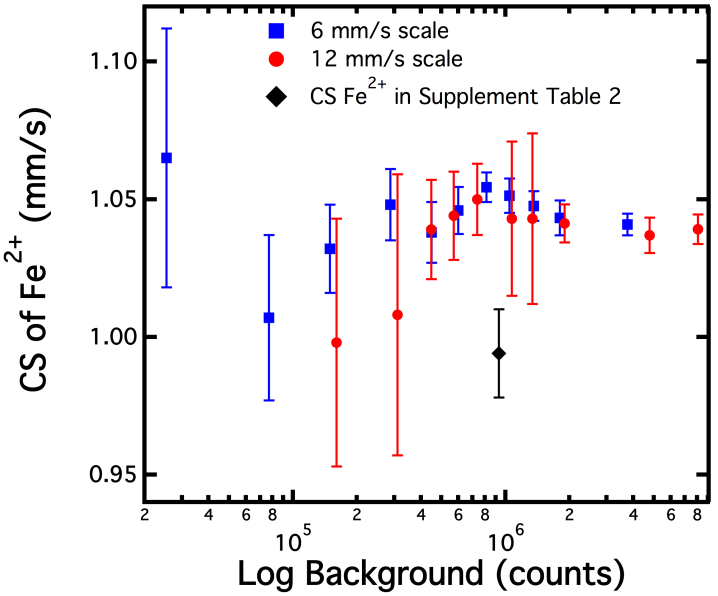

(b)

Figure 2.S1: Effect of variable Mössbauer collection time and velocity scale on Center Shifts (CS) for (a) ferric and (b) ferrous iron for sample VF3. The blue squares refer to CS obtained from Mössbauer spectra collected with 6 mm/s scale. The red dots show CS obtained from Mössbauer spectra collected with 12 mm/s scale. The black diamond refers to the room temperature data point collected with the standard methodology applied during data collection at variable temperature, as shown in Table 2.S1. All uncertainties in this figure are in 2σ.

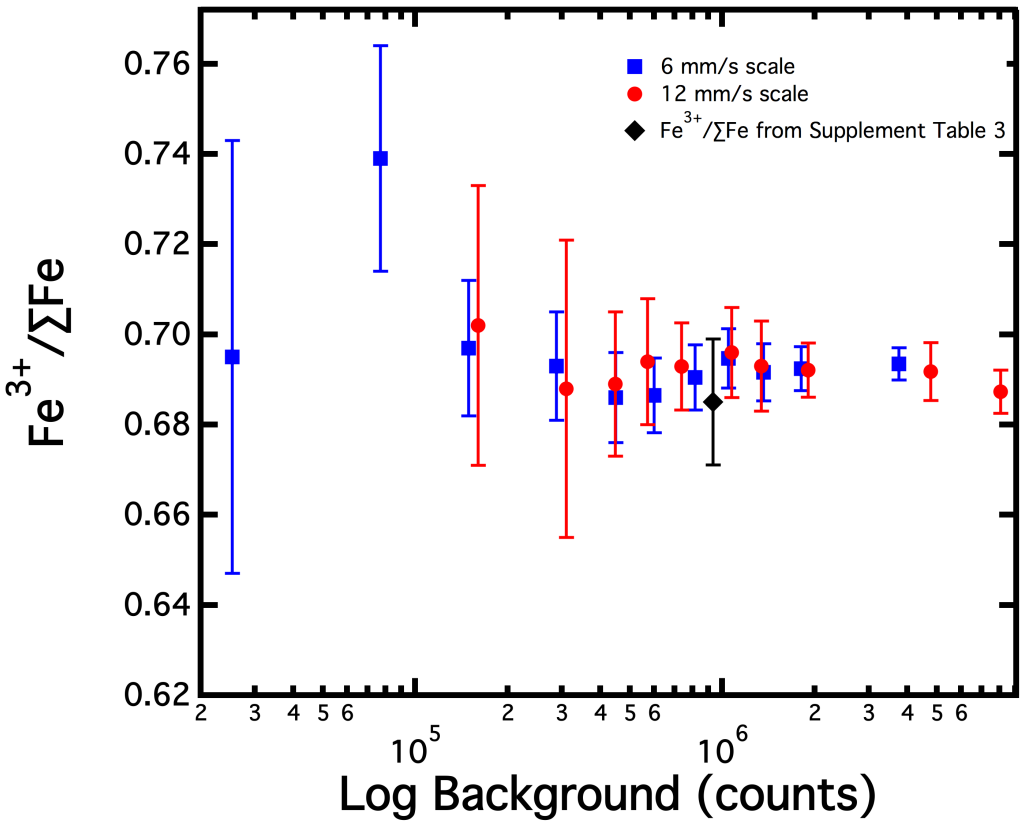

Figure 2.S2: Effect of variable Mössbauer collection time and scale on $Fe^{3+}/\Sigma Fe$ for sample VF3, with data points as described in Fig. 2.S1.

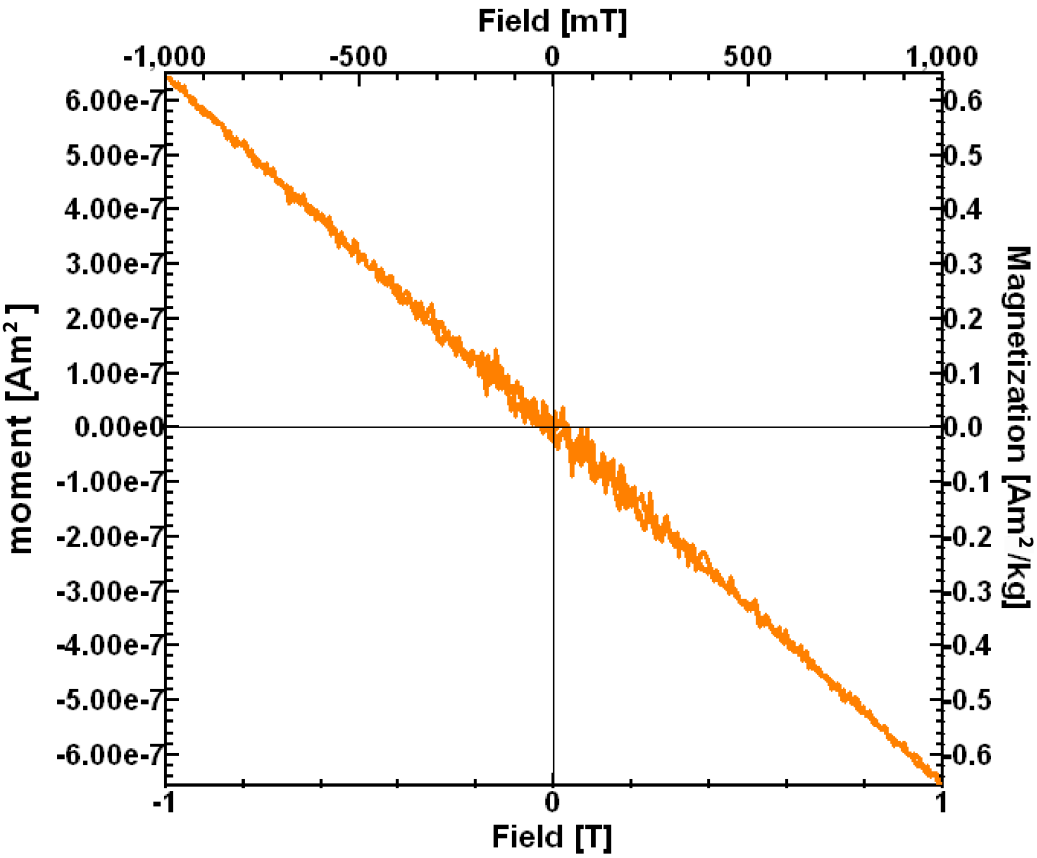

Figure 2.S3: Hysteresis between applied magnetic field and sample magnetization determined for powdered sugar.

Table 2.S1: Parameters of VF3 Mössbauer spectra collected with different scales and different duration at room temperature.

Time	CS (Fe^{2+})	δ_{CS}(Fe^{2+})	QS(Fe^{2+})	δ_{QS}(Fe^{2+})	ρ(Fe^{2+})	CS (Fe^{3+})	δ_{CS}(Fe^{3+})	QS (Fe^{3+})	δ_{QS}(Fe^{3+})
6 mm/s scale									
0.188	1.057(84)	0.04(12)	2.01(18)	0.33(33)	-0.82(87)	0.256(36)	0.002(95)	1.243(83)	0.382(61)
0.5	0.979(55)	0.15(10)	1.98(11)	0.13(16)	0.43(99)	0.290(35)	0.022(95)	1.195(56)	0.563(69)
1	1.017(56)	0.236(28)	1.88(13)	0.293(84)	0.23(29)	0.295(24)	0.000(51)	1.207(50)	0.578(14)
2	1.047(28)	0.212(30)	1.825(53)	0.262(95)	0.31(25)	0.304(15)	0.000(51)	1.198(28)	0.512(21)
3	1.020(15)	0.171(12)	1.836(24)	0.341(23)	0.432(84)	0.293(70)	0.000(38)	1.157(13)	0.478(16)
4	1.0321(86)	0.223(11)	1.854(29)	0.206(39)	0.400(79)	0.2944(79)	0.000(43)	1.182(11)	0.531(12)
5.5	1.0394(94)	0.1635(81)	1.852(19)	0.327(16)	0.421(79)	0.291(57)	0.000(38)	1.1681(87)	0.470(15)
7	1.0314(97)	0.106(22)	1.875(28)	0.436(22)	0.400(81)	0.2933(63)	0.000(42)	1.155(10)	0.505(10)
9	1.034(10)	0.220(11)	1.858(22)	0.194(34)	0.40(14)	0.3014(83)	0.000(41)	1.1616(75)	0.467(13)
12	1.0264(61)	0.2039(84)	1.852(16)	0.214(26)	0.479(72)	0.2973(46)	0.000(33)	1.1655(78)	0.4591(75)
25	1.0303(55)	0.2316(47)	1.834(13)	0.189(14)	0.394(52)	0.2945(27)	0.001(27)	1.1567(39)	0.4882(91)
12 mm/s scale									
1	0.998(45)	0.276(71)	1.991(69)	0.142(99)	-0.59(85)	0.320(15)	0.002(71)	1.108(28)	0.354(41)
2	1.008(51)	0.239(53)	1.90(12)	0.33(16)	-0.10(62)	0.308(28)	0.050(67)	1.143(50)	0.399(46)
3	1.039(18)	0.176(51)	1.861(39)	0.20(14)	0.40*	0.2916(78)	0.031(53)	1.191(16)	0.389(40)
4	1.044(16)	0.185(16)	1.861(34)	0.220(99)	0.40*	0.2955(67)	0.073(49)	1.185(16)	0.382(36)
5	1.050(13)	0.199(17)	1.861(32)	0.115(76)	0.25(40)	0.298(95)	0.000(40)	1.185(12)	0.421(13)
7	1.043(28)	0.240(48)	1.851(62)	0.116(96)	0.40(58)	0.299(14)	0.000(52)	1.174(36)	0.439(17)
9	1.043(31)	0.217(25)	1.853(76)	0.132(70)	0.62(42)	0.295(13)	0.001(41)	1.180(31)	0.425(11)
12.5	1.0412(69)	0.069(15)	1.851(17)	0.432(26)	0.40(15)	0.2985(56)	0.000(35)	1.1758(90)	0.4275(99)
31.5	1.0369(64)	0.211(16)	1.860(19)	0.130(22)	0.63(13)	0.2945(59)	0.000(35)	1.1754(90)	0.427(10)
53.5	1.0391(54)	0.208(12)	1.854(15)	0.150(17)	0.623(99)	0.2948(36)	0.000(27)	1.1731(75)	0.4102(90)

The uncertainty notation is such that, for example, 0.175(61) is equivalent to 0.175$\pm$0.061.
And uncertainties are in two sigma range standard deviation (2σ)
Time: Mssbauer spectra collection time in hours
CS: Center Shift in mm/s
δ_{CS}: Gaussian width of CS in mm/s
QS: Quadrupole splitting in mm/s
δ_{QS}: Gaussian width of QS in mm/s
ρ: correlation of δ_{QS} and δ_{QS}
*: for the VF3 Mssbauer spectra collected at 12 mm/s scale with 3 and 4 hours, ρ was fixed at 0.40

Table 2.S1: Continue

Time	χ^2	L HWHM	Background	RA(Fe^{2+})	AA(Fe^{2+})	RA(Fe^{3+})	AA(Fe^{3+})
6 mm/s scale							
0.188	0.877	0.175(61)	25358(15)	32.6(20)	866(66)	67.4(20)	1788(90)
0.5	1.097	0.2030(94)	76996(47)	27.1(36)	2150(340)	72.90(36)	5790(530)
1	0.949	0.113(29)	149297(42)	28.3(13)	4170(220)	71.7(13)	10550(410)
2	1.109	0.140(20)	287826(45)	30.2(13)	8660(480)	69.8(13)	19990(550)
3	1.057	0.160(15)	449139(77)	29.4(11)	13110(640)	70.6(11)	31460(700)
4	1.128	0.122(16)	599028(98)	29.6(11)	17070(820)	70.4(11)	40600(850)
5.5	0.939	0.168(15)	814281(79)	29.38(75)	23790(790)	70.62(75)	57180(800)
7	0.991	0.150(21)	1045800(130)	27.87(93)	28300(1000)	72.13(93)	73400(2100)
9	1.147	0.177(17)	1361180(160)	28.74(86)	38900(1400)	71.26(86)	96600(2100)
12	1.228	0.177(10)	1808490(160)	29.03(52)	52800(1100)	70.97(52)	129000(1700)
25	1.136	0.1558(94)	3757280(260)	29.05(43)	107600(2000)	70.95(43)	263000(2500)
12 mm/s scale							
1	c0.494	0.317(35)	160183(27)	29.8(31)	4700(640)	70.2(31)	11090(700)
2	0.517	0.250(40)	310318(58)	31.2(33)	9100(1200)	68.8(33)	20100(1400)
3	0.578	0.234(43)	448449(83)	31.1(16)	14410(810)	68.9(16)	31900(1400)
4	0.542	0.299(42)	570725(97)	30.6(14)	17910(960)	69.4(14)	40500(1700)
5	0.569	0.232(17)	736184(80)	30.71(97)	23270(920)	69.29(97)	52500(1200)
7	0.552	0.227(18)	1073312(96)	30.4(10)	30800(1300)	69.6(10)	70600(1500)
9	0.549	0.2311(99)	1340091(92)	30.7(10)	39000(1700)	69.3(10)	88100(1800)
12.5	0.556	0.228(10)	1903489(83)	30.79(60)	55200(1400)	69.21(60)	124000(1600)
31.5	0.658	0.232(12)	4773590(190)	30.82(64)	139800(3600)	69.18(64)	313900(4500)
53.5	0.887	0.2392(71)	8072960(210)	31.27(48)	240900(4900)	68.73(48)	529400(5100)

The uncertainty notation is such that, for example, 25358(15) is equivalent to 25358$\pm$15
And uncertainties are in two sigma range standard deviation (2σ)
χ^2: Chi square — L HWHM: Lorentzian half width at half maximum in mm/s
T: Temperature in K — Background: in counts
AA: Absorption area in countsmm/s — RA: Relative sub-spectra areas

Table 2.S2: Mössbauer fitting parameters

T	CS(Fe^{2+})	δ_{CS}(Fe^{2+})	QS(Fe^{2+})	δ_{QS}(Fe^{2+})	ρ(Fe2+)	CS(Fe^{3+})	δ_{CS}(Fe^{3+})	QS(Fe^{3+})	δ_{QS}(Fe^{3+})
M544									
47	1.223(21)	0.169(20)	2.239(48)	0.357(39)	0.41(17)	0.439(21)	0.105(16)	1.213(37)	0.384(18)
57	1.228(20)	0.210(20)	2.230(44)	0.262(52)	0.40(17)	0.438(20)	0.076(24)	1.215(33)	0.386(19)
67	1.232(12)	0.184(13)	2.249(33)	0.317(35)	0.40(11)	0.439(11)	0.115(21)	1.229(16)	0.398(24)
97	1.221(10)	0.144(17)	2.210(20)	0.422(26)	0.41(10)	0.425(10)	0.106(18)	1.227(16)	0.398(19)
117	1.206(12)	0.231(18)	2.213(24)	0.218(34)	0.41(17)	0.428(13)	0.110(22)	1.195(26)	0.393(25)
147	1.179(27)	0.228(21)	2.175(62)	0.277(41)	0.40(22)	0.414(23)	0.055(44)	1.189(43)	0.421(23)
177	1.180(20)	0.163(20)	2.138(39)	0.441(32)	0.40(15)	0.394(13)	0.097(23)	1.203(27)	0.402(22)
212	1.150(21)	0.275(23)	2.114(81)	0.220(89)	0.40(27)	0.385(28)	0.128(39)	1.195(39)	0.491(40)
293	1.080(11)	0.272(10)	2.013(34)	0.156(27)	0.38(13)	0.334(12)	0.108(15)	1.166(17)	0.494(13)
VF3									
47	1.150(29)	0.219(25)	2.034(56)	0.242(73)	0.44(29)	0.398(18)	0.090(17)	1.257(33)	0.346(18)
57	1.160(14)	0.230(15)	2.023(41)	0.246(42)	0.40(18)	0.390(11)	0.090(26)	1.250(12)	0.386(24)
67	1.168(13)	0.186(17)	2.050(27)	0.374(34)	0.45(15)	0.3945(78)	0.085(17)	1.237(14)	0.412(14)
77	1.156(16)	0.157(18)	2.019(28)	0.323(35)	0.44(13)	0.394(12)	0.089(22)	1.225(12)	0.328(24)
97	1.144(28)	0.241(21)	2.018(51)	0.179(64)	0.40(22)	0.396(14)	0.001(45)	1.227(27)	0.426(14)
117	1.131(13)	0.236(20)	1.998(33)	0.155(46)	0.41(25)	0.384(10)	0.062(31)	1.217(16)	0.410(19)
147	1.120(16)	0.194(19)	1.961(36)	0.265(46)	0.41(18)	0.367(10)	0.086(28)	1.209(15)	0.340(28)
177	1.096(26)	0.171(23)	1.927(42)	0.349(44)	0.5(19)	0.352(11)	0.061(24)	1.209(19)	0.358(17)
212	1.080(24)	0.197(42)	1.894(42)	0.189(97)	0.49(41)	0.341(15)	0.063(38)	1.198(24)	0.339(30)
293	0.994(16)	0.225(23)	1.754(37)	0.155(60)	0.49(28)	0.283(12)	0.087(23)	1.148(18)	0.405(20)

The uncertainty notation is such that, for example, 0.204(15) is equivalent to 0.204$\pm$0.015.
And uncertainties are in two sigma range standard deviation (2σ)
T: Temperature in K
CS: Center Shift in mm/s
δ_{CS}: Gaussian width of CS in mm/s
QS: Quadrupole splitting in mm/s;
δ_{CS}: Gaussian width of QS in mm/s
ρ: correlation of δ_{CS} and δ_{QS}
*: for the VF3 Mssbauer spectra collected at 177 K, the L HWHM was fixed at 0.250 mm/s.

Table 2.S2: Continue

T	χ^2	L HWHM	Background	RA(Fe^{2+})	AA(Fe^{2+})	RA(Fe^{3+})	AA(Fe^{3+})
			M544				
47	0.783	0.204(15)	1303330(150)	43.3(11)	89500(3400)	56.7(11)	117000(3100)
57	0.777	0.211(18)	1318270(110)	44.0(12)	92200(3700)	56.0(12)	117100(3000)
67	0.822	0.222(19)	1469490(130)	41.5(11)	97000(3600)	58.5(11)	137000(3200)
97	0.911	0.201(21)	2576030(190)	42.62(75)	168700(3700)	57.38(75)	227100(4800)
117	0.711	0.202(21)	1135410(110)	42.83(91)	73100(2000)	57.17(91)	97500(2400)
147	0.67	0.211(20)	1471380(130)	43.43(78)	93900(2300)	56.57(78)	122300(2500)
177	0.742	0.200(23)	1230347(100)	42.9(12)	74600(2800)	57.1(12)	99300(2900)
212	0.731	0.256(28)	1218430(150)	41.2(21)	69900(5200)	58.8(21)	99600(4500)
293	0.762	0.186(10)	5764070(260)	39.99(83)	278600(7800)	60.01(83)	418000(8300)
			VF3				
47	0.541	0.262(14)	541460(80)	36.9(14)	44900(2400)	63.1(14)	76800(1800)
57	0.608	0.225(16)	532837(83)	35.8(12)	42500(2000)	64.2(12)	76200(1800)
67	0.464	0.239(15)	434524(60)	34.7(10)	33900(1400)	65.3(10)	63600(1300)
77	0.535	0.260(18)	511304(75)	34.05(88)	38800(1300)	65.95(88)	75100(1500)
97	0.605	0.234(16)	533547(57)	34.31(47)	40160(710)	65.69(47)	76890(810)
117	0.664	0.222(21)	506043(90)	33.62(96)	35600(1300)	66.38(96)	70200(1500)
147	0.698	0.245(24)	472994(88)	34.0(16)	32900(2100)	66.0(16)	63800(2000)
177	0.701	0.250*	491374(68)	34.5(16)	33800(2200)	65.5(16)	59800(2200)
212	0.625	0.256(22)	470929(62)	32.9(12)	29400(1300)	67.1(12)	60100(1800)
293	0.556	0.232(19)	931880(88)	31.5(14)	49000(2800)	68.5(14)	106400(2800)

The uncertainty notation is such that, for example, 1303330(150) is equivalent to 1303330$\pm$150.
And uncertainties are in two sigma range standard deviation (2σ)
χ^2: Chi square — L HWHM: Lorentzian half width at half maximum in mm/s
T: Temperature in K — Background: in counts
AA: Absorption area in countsmm/s — RA: Relative sub-spectra areas

Table 2.S3: Calculated recoilless fractions and correction numbers for Mössbauer spectra

T	$f^{RM}(Fe^{2+})$	$f^{RM}(Fe^{3+})$	C^{RM}	$f^{CRM}(Fe^{2+})$	$f^{CRM}(Fe^{3+})$	C^{CRM}
M544						
47	0.880(14)	0.905(12)	1.028(21)	0.880(14)	0.931(17)	1.058(26)
57	0.873(16)	0.901(12)	1.032(23)	0.873(16)	0.929(18)	1.064(28)
67	0.865(18)	0.896(14)	1.036(26)	0.865(18)	0.927(20)	1.072(32)
97	0.838(24)	0.879(18)	1.049(36)	0.838(24)	0.919(25)	1.097(43)
117	0.818(28)	0.866(20)	1.059(44)	0.818(27)	0.913(29)	1.115(51)
147	0.788(34)	0.846(26)	1.074(55)	0.788(33)	0.902(35)	1.145(65)
177	0.757(38)	0.824(30)	1.089(67)	0.757(38)	0.890(41)	1.176(80)
212	0.722(44)	0.799(34)	1.107(82)	0.722(43)	0.876(47)	1.213(98)
293	0.645(54)	0.742(44)	1.151(118)	0.645(54)	0.842(63)	1.305(146)
VF3						
47	0.860(17)	0.898(10)	1.044(23)	0.818(160)	0.925(14)	1.131(224)
57	0.850(19)	0.893(11)	1.051(27)	0.802(180)	0.923(15)	1.150(259)
67	0.840(21)	0.888(12)	1.057(31)	0.786(196)	0.920(16)	1.170(293)
77	0.828(24)	0.882(14)	1.065(35)	0.769(210)	0.917(17)	1.192(327)
97	0.804(29)	0.869(16)	1.080(44)	0.736(235)	0.910(20)	1.238(399)
117	0.779(34)	0.854(19)	1.097(54)	0.702(257)	0.903(24)	1.285(468)
147	0.740(40)	0.831(23)	1.122(69)	0.654(277)	0.890(29)	1.360(577)
177	0.703(46)	0.807(27)	1.148(85)	0.609(292)	0.876(34)	1.437(691)
212	0.660(52)	0.779(31)	1.180(104)	0.561(304)	0.859(40)	1.531(831)
293	0.570(62)	0.716(39)	1.256(153)	0.465(312)	0.820(52)	1.762(1188)

The uncertainty notation is such that, for example, 0.880(14) is equivalent to 0.8800.014.
And uncertainties are in two sigma range standard deviation (2σ)
T: Temperature in K
f: recoilless fraction — C: $f(Fe^{3+})/f(Fe^{2+})$
RM: relative method — CSM: center shift method

Table 2.S4: Mössbauer parameters of VF3 for fit with nanophase oxide

	nanophase	Fe_3O_4	$MgFe_2O_4$
	χ^2	0.557	0.554
	L HWHM	0.230(22)	0.224(28)
paramagnetic sites	CS(Fe^{2+})	0.998(26)	1.006(38)
	δ_{CS}(Fe^{2+})	0.232(35)	0.245(53)
	QS(Fe^{2+})	1.775(58)	1.736(11)
	δ_{QS}(Fe^{2+})	0.15(10)	0.15(21)
	ρ (Fe^{2+})	0.42(50)	0.26(56)
	RA(Fe^{2+})	31.6(11)	31.6(17)
	CS(Fe^{3+})	0.283(16)	0.285(18)
	δ_{CS}(Fe^{3+})	0.089(30)	0.094(32)
	QS(Fe^{3+})	1.151(30)	1.157(49)
	δ_{QS}(Fe^{3+})	0.406(26)	0.411(31)
	RA(Fe^{3+})	68.0(11)	67.2(17)
magnetic site	RA	0.438(12)	1.182(40)

The uncertainty notation is such that, for example, 0.998(26)
is equivalent to 0.998 ± 0.026
And uncertainties are in two sigma range standard deviation (2σ)
L HWHM: Lorentzian half width at half maximum in mm/s
CS: Center Shift in mm/s
δ_{CS}:Gaussion width of CS in mm/s
QS:Quadrupole splitting in mm/s
δ_{QS}: Gaussion width of CS in mm/s
ρ: corellation of δ_{CS} and δ_{QS}
RA:Relative sub-spectral areas

Chapter 3

Structural environment of iron and accurate determination of $Fe^{3+}/\Sigma Fe$ ratio in andesitic glass by XANES and Mössbauer spectroscopy

This Chapter will submit to Chemical geology, with co-authors Marc M. Hirschmann, Elizabeth Cottrell, Matt Newville and Antonio Lanzirotti.

3.1 Introduction

The oxidation state of iron in silicate melts has an important influence on the chemical and physical properties of natural magmas (*Sack et al.*, 1981; *Virgo and Mysen*, 1985; *Christie et al.*, 1986; *Dingwell et al.*, 1988; *Kress and Carmichael*, 1991; *Jayasuriya et al.*, 2004; *Bézos and Humler*, 2005; *Wilke*, 2005; *O'Neill et al.*, 2006; *Cottrell et al.*, 2009; *Borisov and McCammon*, 2010; *Cottrell and Kelley*, 2011, 2013). With appropriate thermodynamic calibration, the proportion of ferric and ferrous iron, expressed as $Fe^{3+}/\Sigma Fe$, can be directly related to the oxygen fugacity (fO_2) of magmatic source regions, and therefore is a probe of the conditions in Earths interior (*Arculus*, 1985; *Christie et al.*, 1986; *Wood et al.*, 1990; *Kress and Carmichael*, 1991; *Lécuyer and Ricard*, 1999; *Jayasuriya et al.*, 2004; *Bézos and Humler*, 2005). $Fe^{3+}/\Sigma Fe$ also

influences the compositions of crystallizing phases, and so influences the chemical trends produced by fractional crystallization (*Osborn*, 1959; *Hill and Roeder*, 1974).

A variety of analytical techniques are used to determine $Fe^{3+}/\Sigma Fe$ in minerals and glasses. Wet chemical determinations, including colorimetry, and Mössbauer spectroscopy are perhaps the best established (*Wilson*, 1960; *Mysen et al.*, 1985; *Virgo and Mysen*, 1985; *Lange and Carmichael*, 1989; *Kress and Carmichael*, 1991; *Bézos and Humler*, 2005; *Dyar et al.*, 2006; *Rossano et al.*, 2008; *Dyar et al.*, 2012), but micro X-ray absorption near edge structure (μ-XANES) spectroscopy affords the ability to determine $Fe^{3+}/\Sigma Fe$ at high spatial resolution with comparable or superior precision (*Berry et al.*, 2003; *Wilke et al.*, 2005; *Cottrell et al.*, 2009; *Cottrell and Kelley*, 2011; *Dauphas et al.*, 2014), allowing analysis of glasses from complex natural samples and from experiments. μ-XANES is sensitive to valence and bonding environments of analyzed ions, but requires calibration from materials with known $Fe^{3+}/\Sigma Fe$ ratios. Calibrations between standards established by wet chemical or Mössbauer methods and -XANES have been determined for a range of natural glass compositions, including basalt (*Botcharnikov et al.*, 2005; *Wilke et al.*, 2005; *Cottrell et al.*, 2009; *Cottrell and Kelley*, 2011; *Dauphas et al.*, 2014), andesite (*Dauphas et al.*, 2014), dacite (*Dauphas et al.*, 2014), rhyolite (*Cottrell et al.*, 2009; *Cottrell and Kelley*, 2011; *Dauphas et al.*, 2014), and hyplotonalite and hyplogranite (*Wilke et al.*, 2006). These calibrations typically are based on the center position of the pre-edge absorption peak for Fe^{3+} and Fe^{2+}, which provides the most precise measure of $Fe^{3+}/\Sigma Fe$ (*Cottrell et al.*, 2009), though the centroid energy depends on the energy position of first derivative peak of -Fe foil been set up between facilities. In this paper we present Mössbauer and μ-XANES data for a suite of andesitic glasses and use them to establish a new calibration curve that is composition independent.

Mössbauer spectroscopy and μ-XANES are also useful for investigating the local structural environments of iron ions in silicate glasses. Because both Fe^{3+} and Fe^{2+} have the potential to behave as either network forming or network-modifying ions (*Fox et al.*, 1982; *Mysen et al.*, 1982; *Virgo et al.*, 1982, 1983; *Virgo and Mysen*, 1985; *Rossano et al.*, 2000; *Mysen*, 2006)characterization of the average coordination state of Fe^{2+} and Fe^{3+} provides useful insight into the effects of melt composition and pressure on the thermodynamic and transport properties of silicate liquids (*Mysen and Richet*, 2005). Previous studies employing a range of spectroscopic methods and molecular dynamics calculations have concluded that at low pressure Fe^{2+} and Fe^{3+} in natural and synthetic analog glasses and melts take on a variety of coordination states.

In this paper we add to these observations, with new constraints on the coordination of Fe^{2+} and Fe^{3+} in andesitic glasses.

3.2 Method

3.2.1 Starting materials

The starting material for this project consists of a synthetic andesite similar in composition to that used by *O'Neill et al.* (2006) and *Zhang et al.* (2015), and was prepared from reagent oxides (SiO_2, Al_2O_3, Fe_2O_3, TiO_2, MgO), silicates ($CaSiO_3$,Na_2SiO_3) and stoichiometric sanidine glass. The Fe_2O_3 consisted of 90 wt% normal reagent oxide and 10 wt% $^{57}Fe_2O_3$ (Isoflex, Inc). Prior to weighing, the SiO_2, Al_2O_3, TiO_2, and MgO were devolatilized by heating overnight in a furnace at 1000 °C, until the weight stabilized. These reagants were then weighed and mixed with the silicates and sanidine by grinding under ethanol for at least one hour, until the grinding sound diminished and then again devolatilized by firing at 1000 °C for 48 hrs. Finally, the Fe_2O_3, which were themselves dried at 800 °C for 1 hour and then weighed, with $^{57}Fe_2O_3$ were mixed in by grinding under ethanol.

3.2.2 High temperature experiments

Andesitic melts were equilibrated at 1 atm and 1350 °C for 24 hours in a Deltech VT28 vertical gas mixing rapid-quench furnace, with temperature measured by a Type S ($Pt_{90}Rh_{10}/Pt_{100}$) thermocouple. Temperature uncertainties are believed to be ±4 °C, as judged from gold melting calibrations (1059 °C). Oxygen fugacity (fO_2) was controlled with CO_2/CO, O_2/CO_2 or air and measured with $SIRO_2$ C700+ Solid Zirconia Electrolyte Oxygen Sensor. The Oxygen Sensor was calibrated against the Ni-NiO buffer (*Huebner and Sato*, 1970) and the reference gas was air.

Except for experiment VF85, which used 0.005" diameter Re wire, experiments used Pt wire loops (0.005 inch diameter), which were pre-equilibrated with the starting material by loading approximately 30 mg of oxides powder mixture, bonded by PVA on the loops and holding them at the experimental temperature and fO_2. The loops were then cleaned in HF and

reloaded with starting material, with the experiment then repeated. Electron microprobe analyses on each quenched glass verified that this procedure prevented detectable Fe loss during the experiment (Table 3.S1). Andesitic glasses were equilibrated at 1350 °C in flowing CO/CO_2 for 24 h when $\log fO_2$ <-3.2 (∼QFM+3.5), and in CO_2/O_2 or air for more oxidized conditions. This duration was judged sufficient to completely equilibrate Fe speciation with the gas mix based on previous studies (*Kilinc et al.*, 1983; *Roskosz et al.*, 2008; *Knipping et al.*, 2015). All experimental conditions were listed in Table 3.1.

Some experiments (VF30-VF59), whose oxygen fugacity were measured before experiments, were quenched by being removed from the furnace and put into cold water within seconds, and others (VF66-VF88), whose oxygen fugacity were monitored during the experiments, were rapidly drop quenched into a water bath by vaporizing the Pt hang wire. Although the structure of the glass likely is not identical to that of the liquid from which it was quenched, at cooling rates typical of drop quench (<100°C/second) from 1 atmosphere furnaces (*Dyar et al.*, 1987) both the $Fe^{3+}/\Sigma Fe$ and the key structural features such as Fe-O coordination characteristic of the molten liquid are likely only slightly changed from that in the glass (*Wilke et al.*, 2007; *Cottrell and Kelley*, 2011). All glasses were carefully separated from the Pt loops (or Re loop for VF85). From each experiment, several glass chips were removed and doubly polished for optical examination, XANES, and electron microprobe analyses, while the remainder was ground to powder for Mössbauer spectroscopy.

3.2.3 Analytical Methods

Electron Microprobe

Textures of polished sections from experiments were examined by back-scattered electron (BSE) and secondary electron imaging (SEI) using the JEOL JXA8900R EMPA at the University of Minnesota. Major element concentrations of quenched glasses were determined by wave-length-dispersive EMPA, using 15 kV acceleration voltage and 20 nA beam current and ZAF data reduction with software supplied by JEOL (Table 3.S1). A focused beam (5 m diameter) was employed, with counting times of 20 s for elements and 10 s for the synthetized Mg_2SiO_4 for Mg kα, anorthite for Ca kα, ilmenite for Ti kα, Fe kα, albite for Si kα, Na kα, and microcline for Al kα, K kα, and matrix corrections were computed with Probe for Windows

Table 3.1: Experimental conditions* and $Fe^{3+}/\Sigma Fe$ ratios determined from Mössbauer spectroscopy

Sample Name	**wire**	**Air flow**	**logfO2**	**$Fe^{3+}/\Sigma Fe$ *100 (xVBF)$^{\psi}$**	**$Fe^{3+}/\Sigma Fe$ *100 (LMA)$^{\psi}$**	**$Fe^{3+}/\Sigma Fe$ *100 (xVBF) corrected with C$^{\#}$**	**Predicted$^{\&}$ $Fe^{3+}/\Sigma Fe$ *100**
VF30	Pt	air	-0.68	83.50(0.60)	84.92(1.86)	80.12(0.60)	74.3
VF35	Pt	CO_2/CO	-8.07	8.04(0.49)	8.30(1.50)	6.51(0.49)	8.74
VF49	Pt	CO_2/CO	-8.63	12.94(0.47)	13.21(2.50)	10.58(0.47)	6.95
VF50	Pt	CO_2/CO	-6.52	13.98(0.50)	16.32(2.50)	11.45(0.50)	16.73
VF53	Pt	CO_2/O_2	-1.3	73.17(0.35)	79.68(2.10)	68.47(0.35)	68.06
VF54	Pt	CO_2/CO	-5.15	34.38(0.39)	35.10(2.10)	29.44(0.39)	26.87
VF59	Pt	pure CO_2	-3.18	49.25(0.27)	52.05(1.60)	43.59(0.27)	47.58
VF66	Pt	CO_2/CO	-4.94	35.01(0.25)	35.52(2.00)	30.02(0.25)	28.55
VF68	Pt	CO_2/CO	-5.72	24.83(0.43)	24.85(2.30)	20.82(0.43)	21.96
VF70	Pt	CO_2/CO	-6.27	21.69(0.35)	20.71(1.80)	18.07(0.35)	17.4
VF74	Pt	CO_2/O_2	-2.06	65.20(0.38)	66.60(2.31)	59.87(0.38)	59.81
VF75	Pt	CO_2/O_2	-2.27	62.43(0.25)	65.69(1.70)	56.95(0.25)	57.52
VF81	Pt	CO_2/CO	-6.98	13.00(0.70)	13.19(3.40)	10.63(0.70)	13.79
VF83	Pt	CO_2/CO	-3.76	39.30(0.60)	40.53(1.90)	34.01(0.60)	40.75
VF85	Re	CO_2/CO	-8.24	9.10(1.40)	6.87(1.60)	7.38(1.40)	8.15
VF87	Pt	air	-0.68	78.41(0.21)	77.53(2.36)	74.30(0.21)	73.48
VF88	Pt	CO_2/CO	-6.26	19.40(0.24)	17.67(2.10)	16.08(0.24)	17.74

Uncertainties are in 1σ.

*All experiments were performed at 1350 C

$^{\psi}$Mössbauer spectra collected at room temperature were fitted with Extended Voigt-based Fitting (xVBF) and Lorentzian Multiplet Analysis (LMA).

$^{\#}$equals $(Fe^{3+}/\Sigma Fe)/[(Fe^{3+}/\Sigma Fe)+ C*(1-Fe^{3+}/\Sigma Fe)]$, where $Fe^{3+}/\Sigma Fe$ is the ratio inferred from the relative areas of doublets from Mössbauer spectra collected from room temperature and C is the correction (1.256) for recoilless fraction for andesitic glass quenched at ambient pressure (*Zhang et al.*, 2015).

$^{\&}$Predicted from the model of *Kress and Carmichael* (1991), using the observed composition of each glass (Table 3.S1).

software.

During microprobe analyses, MPI-DING glass ATHO-G (*Jochum et al.*, 2006) was analyzed as a secondary standard, and this was examined before and after analyses of unknown samples, as well as in between each 5 or 6 unknown samples. The x-ray intensities of standards, secondary standards and unknown samples were checked for time dependent (TDI) changes. Na kα counts were corrected with TDI using a self-calibrated correction; no TDI effect was observed for other elements.

Mössbauer Spectroscopy

Mössbauer spectra were collected using a constant acceleration Ranger spectrometer at the Institute for Rock Magnetism, University of Minnesota, and the measurements were carried out with a ^{57}Co/Rh source and a pure Fe foil calibrant at room temperature (293 K). Data were collected over 512 channels, which were then folded to produce 256 unique channels. All spectra were collected over at least one day and until sufficient (>1,200,000 counts / channel) were accumulated to minimize statistical error. Sample mounts consisted of powdered glass mixed with powdered sugar evenly distributed in an approximately circular shape of diameter 12.7 mm. The absorber thicknesses were adjusted for an absorber density of $\sim$2 mg/cm^2 Fe.

All Mössbauer spectra were fitted using the RECOIL software package (*Lagarec and Rancourt*, 1998) with a 2D distribution Extended Voigt-based Fitting (xVBF) method described in detail by *Zhang et al.* (2015). Detailed considerations of precision and accuracy, including accounting for the effect of recoilless fraction, are introduced briefly here. Lorentzian half widths at half maximum (L HWHM) is assumed to be the same for all sub-spectra of Mössbauer spectra with the xVBF method (*Lagarec and Rancourt*, 1997). Each doublet was fit with as a 2D distribution, whose parameters consist of the center shift (CS), the quadrupole splitting (QS), and their respective Gaussian widths, σ_{CS} and σ_{QS}. The correlation (ρ) between the CS distribution and QS distribution was assumed to be 0 for Fe^{3+} (*Alberto et al.*, 1996) and variable for Fe^{2+}. All hyperfine parameters and their uncertainties, in 1σ, were calculated based on a bootstrap method and are cataloged in Table 3.S2. The quality of these fits is characterized by reduced chi squared (χ^2) values, which are also listed in Table 3.S2. Irrespective of fitting method, resolving precise $Fe^{3+}/\Sigma Fe$ from Mössbauer spectra is challenging for samples with $Fe^{3+}/\Sigma Fe$ below $\sim$15 %, as has also been reported previously (*Dyar et al.*, 1987; *Rossano et al.*, 1999; *Berry et al.*, 2003; *Botcharnikov et al.*, 2005; *Wilke et al.*, 2005; *Cottrell et al.*, 2009). This

challenge is not alleviated by shape-independent distribution analysis, and the inclusion of additional doublets did not improve model fit statistics, as also found by *Cottrell et al.* (2009) and so all xVBF fits employ only one site each for the ferrous and ferric components. However, to aid reasonable fits for reduced glasses, we use the Gaussian width of the ferric quadrupole splitting, δ_{QS}, as a parameter marker. If fits to δ_{QS} fell below the range of 0.4$\sim$0.6, we fixed the value to 0.4 and the Gaussian width of ferric center shift, δ_{CS}, to 0 (Table 3.S2). This is because all fits for more oxidized spectra, which have three distinguishable peaks and so better constraints on the Fe^{3+} doublets, have δ_{QS} between 0.4$\sim$0.6 and values of δ_{CS} near zero, as also found by *Alberto et al.* (1996).

Besides the shape-independent distribution analysis described above, we also constructed a second set of fits using the Lorentzian Multiplet Analysis (LMA) in RECOIL software package (*Lagarec and Rancourt*, 1998) for all andesitic glasses. One or more symmetric doublets of Lorentzian shape were used to fit Mössbauer spectra. All hyperfine parameters and their uncertainties, in 1σ, were calculated based on a bootstrap method and are cataloged in Table 3.S3. The quality of these fits is characterized by reduced chi squared (χ^2) values, which are also listed in Table 3.S3. The $Fe^{3+}/\Sigma Fe$ ratios determined from LMA are listed in Table 3.1. For samples with $Fe^{3+}/\Sigma Fe$ ratios $<$0.15, we use the same approach as (*Wilke et al.*, 2005) adding ferrous iron doublets and observing the change in the χ^2 statistic. Best fits incorporated 5 ferrous doublets for the reduced andesitic glasses (Table 3.S3).

Both approaches' extract similar $Fe^{3+}/\Sigma Fe$ ratios (Fig. 3.1, Table 3.1). Zhang et al. (2015), using a composition identical to that employed in the present study, demonstrated that recoilless fractions for Fe^{3+} and Fe^{2+} ($f(Fe^{3+})$ and $f(Fe^{2+})$) in andesitic glasses are unequal at room temperature, and using low temperature analyses as well as comparison to wet chemical determinations, established a factor C ($f(Fe^{3+})/f(Fe^{2+})$) of 1.256$\pm$0.153 that should be applied to room temperature Mössbauer analyses of $Fe^{3+}/\Sigma Fe$ ratio in andesitic glasses according to the relation:

$$Fe^{3+}/\Sigma Fe_{\text{Corrected}} = \frac{Fe^{3+}/\Sigma Fe}{Fe^{3+}/\Sigma Fe + C(1 - Fe^{3+}/\Sigma Fe)} \tag{3.1}$$

The $Fe^{3+}/\Sigma Fe$ ratios of glasses determined from xVBF and then corrected with C are listed in Table 3.1 and are similar to the ratios predicted from the model of *Kress and Carmichael* (1991) based on the temperature and fO_2, from which they were quenched as well as the major

element composition of the andesitic glasses (Fig. 3.2, Table 3.1).

X-ray absorption near edge structure (XANES)

Fe K-edge XANES spectra were collected at station X26A (bending magnet) of the National Synchrotron Light Source (NSLS), Brookhaven national lab (BNL) in one session and at beamline 13-IDE at the Advanced Photon Source (APS), Argonne National Lab (ANL) in two sessions. A minimum of 3 spectra was collected on each andesitic glass, each time on a fresh spot.

NSLS operates at 2.8 GeV and 300 mA, and the spot size on sample was 95 m. Energy selection was achieved with a silicon monochromator channel-cut along Si (311), as *Cottrell et al.* (2009) highlighted how, for some optical configurations, the (311) cut can provide significant improvement in energy resolution as compared to monochromators made along (111). A Huber 410 rotational stage with a 20:1 gear reducer that provides about 510-5 degrees rotator resolution was used to mount the crystal holder/translation assembly. All spectra were collected in fluorescence mode with 9 and 13 element Ge array detectors (Canberra) utilizing digital spectrometers (XIA). 7112.0 eV was set up as the first derivative peak for Fe foil (*Ruffoni and Pettifer*, 2006), which defined the energy calibration for the system. Spectra were recorded with four energy regions previously defined by *Cottrell et al.* (2009). At X26A, the monochromator energy drifts with time and glass LW_0 (centroid $\equiv$ 7112.3 eV, *Cottrell et al.*, 2009) was used to correct for both centroid energy drift and center position for Fe^{3+} and Fe^{2+} drift.

APS operates at 7 GeV and 85-101 mA. The spot size on sample was 2×2 μm or 2525 μm and the flux rate is $5\text{-}20\times10^{10}$ photons/sec. Energy selection was achieved with silicon channel-cut monochromators with Si (311). The Sample was mounted hanging down vertically from the rotational stage. To detect the x-ray fluorescence signal, a Vortex ME4 silicon-drift diode array detector array was used, coupled to a high-speed digital spectrometer system (XIA XMAP). The first derivative peak of Fe foil set up at 7110.7 eV (*Kraft et al.*, 1996), defining the energy calibration for the system. Spectra were recorded from 7020 to 7312 eV with four regions: 5 eV steps from 7020 to 7105 eV with 1 s dwell; 0.1 eV steps from 7106 to 7118 eV, over the pre-edge energy range with 3 s dwell; 1.0 eV steos from 7118 to 7120 eV with a 2 s dwell, 2.0 eV steps from 7120 to 7312 eV at 1 s dwell. Spectra of the LW_0 reference glass (*Cottrell et al.*, 2009) were collected every 2$\sim$3 hours to trace the monochromator energy

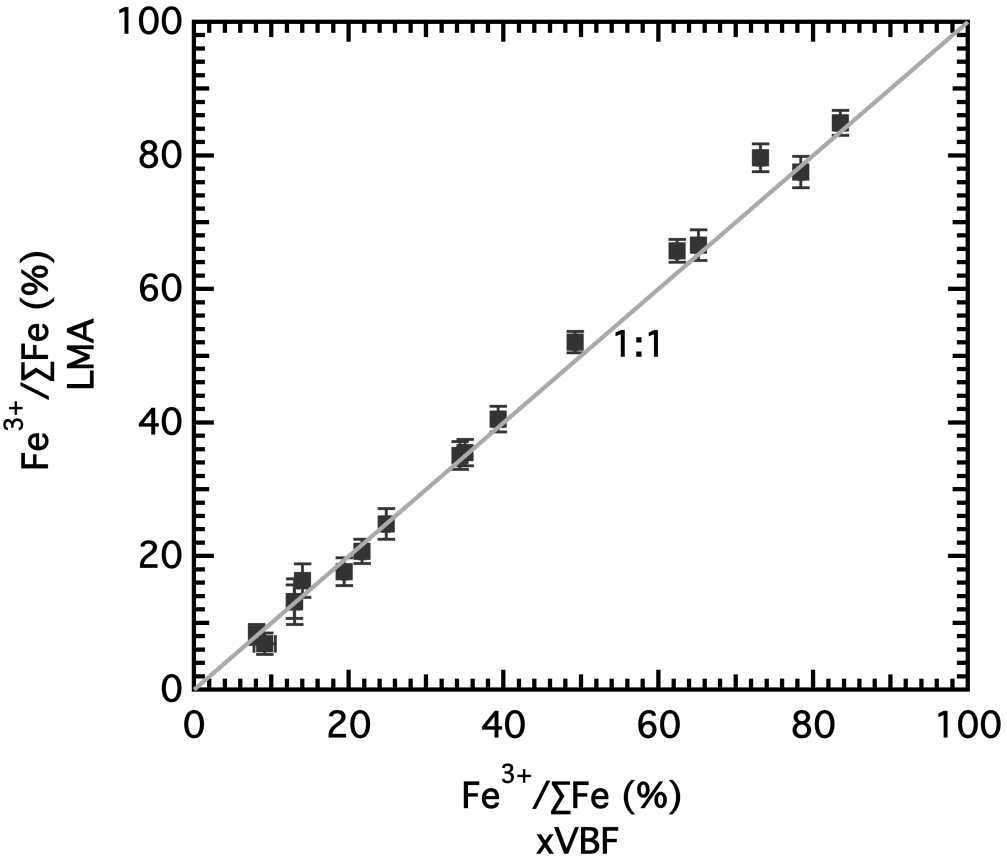

Figure 3.1: Comparison between $Fe^{3+}/\Sigma Fe$ obtained for andesitic glasses from uncorrected Mssbauer spectra collected at room temperature using the extended Voigt-Based Fitting (xVBF) and Lorentzian Multiplet Analysis (LMA) fit methods, both calculated from RECOIL software (*Lagarec and Rancourt*, 1998) using methods described in the text. The two methods give similar results, though the LMA fits yield on average slightly higher $Fe^{3+}/\Sigma Fe$. The results of the xVBF fits are used in the remaining portion of the text.

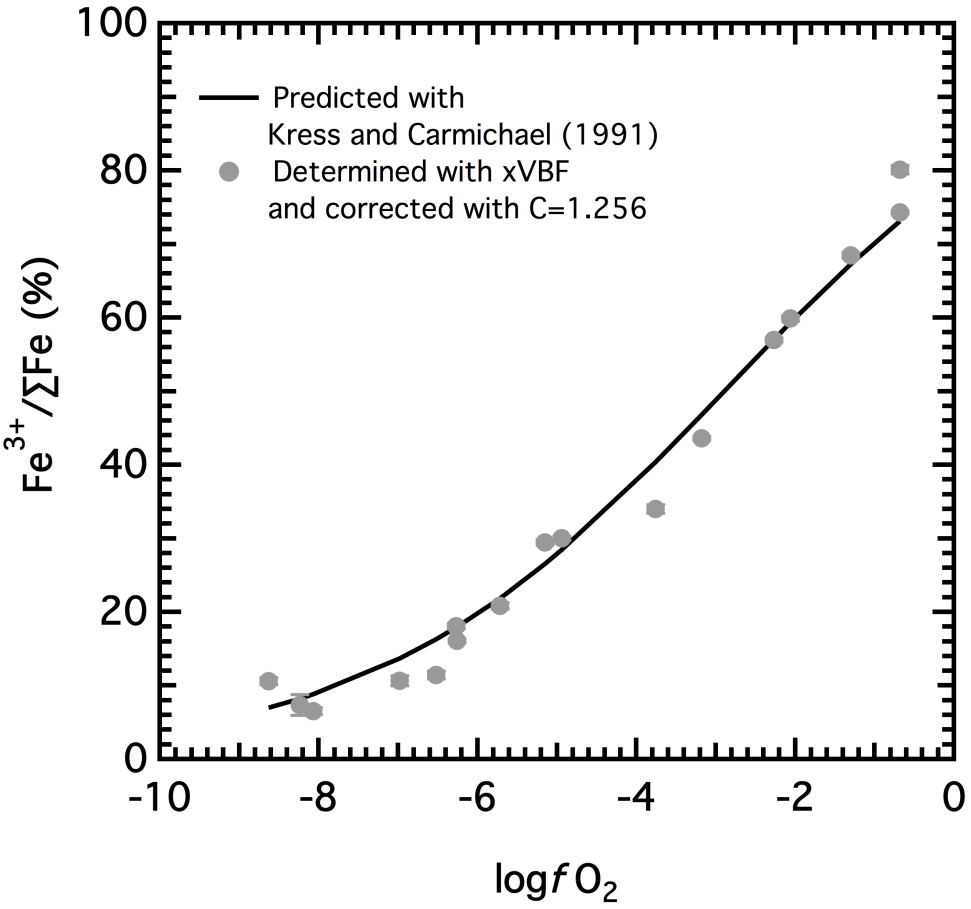

Figure 3.2: Variations in $Fe^{3+}/\Sigma Fe$ in quenched andesitic glasses with oxygen fugacity determined by the solid zirconia electrolyte oxygen sensor in the gas mixing furnace at 1350 °C. Solid dots represent $Fe^{3+}/\Sigma Fe$ ratios obtained from Mössbauer spectra collected at room temperature using xVBF fit methods and corrected with C=1.256 (*Zhang et al.*, 2015). Black line is $Fe^{3+}/\Sigma Fe$ calculated with eqn. (7) from *Kress and Carmichael* (1991) using the T, fO_2, and averaged major element glass composition.

drift with time. Across two sessions, one in which the x-ray beam was operated with top-up mode and the other which was operated in 324 bunch mode, the centroid energy of LW_0 was consistent with average values of 7111.954±0.018 eV for top-up mode and 7111.925±0.005 eV for 324 bunch mode. To compare andesitic glass data collected at APS to that collected at NSLS, all APS spectra were corrected with a standard energy for LW_0 ≡ 7112.3 eV (*Cottrell et al.*, 2009). Center positions of pre-edge sub-peaks of Fe^{3+} and Fe^{2+} were corrected with the same ratio based on the centroid energy correction. The drift corrected centroid energies are reproducible from facility to facility and session to session with precision similar to that within a single session.

All XANES spectra were fit using the methods described by *Cottrell et al.* (2009) and are only briefly introduced here. As the mass of the absorber is different for each analysis point, spectra were normalized using the average absorption coefficient of the edge-step region from 7200 to 7312 eV. All parameters for the pre-edge features were extracted by simultaneously fitting the baseline, which consists of a linear function with a positive slope and a damped harmonic oscillator (DHO) function, and two Gaussian functions to describe pre-edge peaks. The fit of the pre-edge region, from 7110 eV to 7118 eV was performed using Interactive Data Language (IDL) software and the MPFIT set of routines for robust least-squares minimization (*Markwardt*, 2008). All parameters resolved from fit with correction were listed in Table 3.S4.

With fluorescence detection, self-absorption becomes a factor when the penetration depth into the sample is dominated by the absorbing atom, in this case iron. Self-absorption attenuates X-rays, modifying the intensities of pre-edge and other components of the XANES spectrum. Spectra were corrected for self-absorption using the FLUO algorithm *Haskel* (1999) embedded in Athena software package written by *Ravel and Newville* (2005). After correction, total integrated intensities of the pre-edge decreased and the intensity ratios and centroid energies were little affected, consistent with previous studies of self-absorption on Fe-XANES spectra in silicate glasses (*Botcharnikov et al.*, 2005; *Cottrell et al.*, 2009).

3.3 Results

3.3.1 EMPA determinations

Electron microprobe analyses of the glasses and secondary standards established FeO* (Table 3.1). The resulting FeO* of the unknown glasses have high precision (generally ± 1 % relative) and are believed to have high accuracy because analyses reproduced the accepted FeO* concentrations of secondary standards, with discrepancies of no more than 0.1 wt.% (Table 3.S1). FeO* concentrations of glasses range from 8.2 to 10.2 wt%, with average deviations compared of the nominal starting composition (9.4 wt% FeO*) of 5% relative and a maximum of 13% indicating that Fe gains or losses from/to the Pt hanging wires was minimal. Apart from FeO*, SiO_2, and Na_2O, all the glasses have the same major element chemical composition within analytical uncertainty (Table 3.S1), indicating that melts were compositionally homogeneous.

3.3.2 Mössbauer Spectroscopy

Mössbauer spectra consist of two quadrupole doublets, one each originating from paramagnetic ferric and ferrous iron. No obvious sextets at 12 mm/s, as would arise from ferromagnetic Fe, are evident. All hyperfine parameters obtained from Mssbauer spectral fits (Table 3.S2 and Table 3.S3), are similar to those previously reported for silicate glasses (*Mysen et al.*, 1985; *Alberto et al.*, 1996; *Jayasuriya et al.*, 2004; *Botcharnikov et al.*, 2005; *O'Neill et al.*, 2006; *Zhang et al.*, 2015).

The Mössbauer spectra have broadened line-shapes typical of silicate glasses, with examples showed in Fig. 3.S1, and these can be well-accommodated by distribution fitting methods (*Alberto et al.*, 1996; *Rossano et al.*, 1999; *O'Neill et al.*, 2006; *Rossano et al.*, 2008; *Borisov and McCammon*, 2010; *Zhang et al.*, 2015). *Wilke et al.* (2002) argued that relative to conventional fitting with Lorentzian doublets, the improvement of a shape-independent distribution analysis for determination of $Fe^{3+}/\Sigma Fe$ is negligible. As shown in Fig. 3.1, the two fit methods produce $Fe^{3+}/\Sigma Fe$ that are consistent within uncertainty, although the average ratio is displaced to slightly higher values with LMA, with the average $Fe^{3+}/\Sigma Fe$ of all measurements 0.022 ± 0.020 greater. As xVBF methods are thought to better-describe the internal structure of glass (*Alberto et al.*, 1996; *Rossano et al.*, 1999, 2008) and produce smaller statistical errors

(Table 3.S2), for the rest of paper, we present $Fe^{3+}/\Sigma Fe$ resulting from xVBF fits.

Hyperfine parameters (CS and QS) obtained from xVBF and LMA are plotted versus $Fe^{3+}/\Sigma Fe$ *100 resolved from xVBF in Figs. 3.3 and Fig. 3.4. For LMA methods when Fe^{3+} or Fe^{2+} has more than one site, subspectra area weighted CS and QS are used. Overall, hyperfine parameters obtained from the two fit methods show similar values and trends with increasing $Fe^{3+}/\Sigma Fe$, but determinations from xVBF show less variability, must notably for QS (Fe^{3+}), and are therefore possibly more accurate. CS (Fe^{3+}) decreases with increasing $Fe^{3+}/\Sigma Fe$ (Fig. 3.3a). However, QS (Fe^{3+}) varies little with increasing $Fe^{3+}/\Sigma Fe$ (Fig 3.4a). CS (Fe^{2+}) and QS (Fe^{2+}) change little with increasing $Fe^{3+}/\Sigma Fe$ (Fig. 3.3b and Fig. 3.4b), indicting that the nearest neighbor environment of Fe^{2+} does not change significantly from 8.04% to 83.5% Fe^{3+}.

3.3.3 XANES spectra

XANES spectra also provide information on the coordination and bonding of iron in the silicate glasses. In particular, the pre-edge region (position I in Fig. 3.5a) is attributed to the 1s→3d transition, the energy of main absorption (position II in Fig. 3.5a) is produced by a 1s→4p electron transition (*PennerHahn*, 2005). Smooth variations of these features are observed with changes in Fe oxidation state (Fig 3.5a, 3.5b), including shifts to higher energy of the main absorption (Fig. 3.5a, position II), and changes in the intensity, shape, and centroid energy of the pre-edge feature (Fig. 3.5a Position I, Fig. 3.5b). We focus our attention on the pre-edge feature, as it provides the most easily quantifiable constraints.

For the suite of andesitic glasses, the pre-edge region consists of two sub-peaks, which can be attributed to Fe^{2+} ions (center near 7111.9 eV) and Fe^{3+} ions (center near 7113.5 eV), respectively. Features of the pre-edge change systematically with the $Fe^{3+}/\Sigma Fe$ in the glass, as illustrated in Fig. 3.5c, which shows baseline-subtracted pre-edge spectra for glasses with a representative range of $Fe^{3+}/\Sigma Fe$ ratios. The ferrous and ferric peak height intensities grow and diminish in normalized absorbance as oxidation state changes. The ferrous center positions, $E_0(Fe^{2+})$, shift downwards by 0.2 eV as $Fe^{3+}/\Sigma Fe$ varies from 0.84 to 0.08 (Fig. 3.6a), whilst, the ferric center positions, $E_0(Fe^{3+})$, increase by 0.3 eV (Fig. 3.6b). We fit these variations to quadratic functions, which are listed in Table 3.2. Area-weighted centroid positions, also known as centroid energies, can be calculated from individual peak areas ($I(Fe^{3+})$ and $I(Fe^{2+})$), and

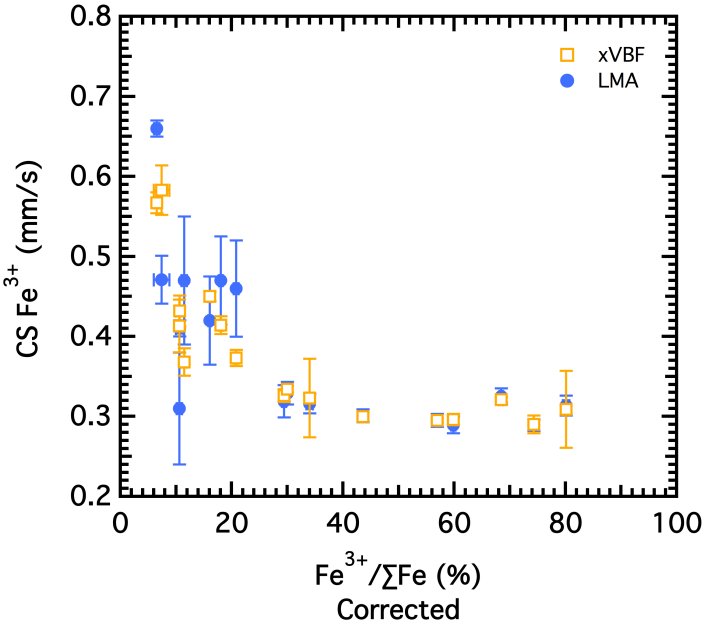

(a)

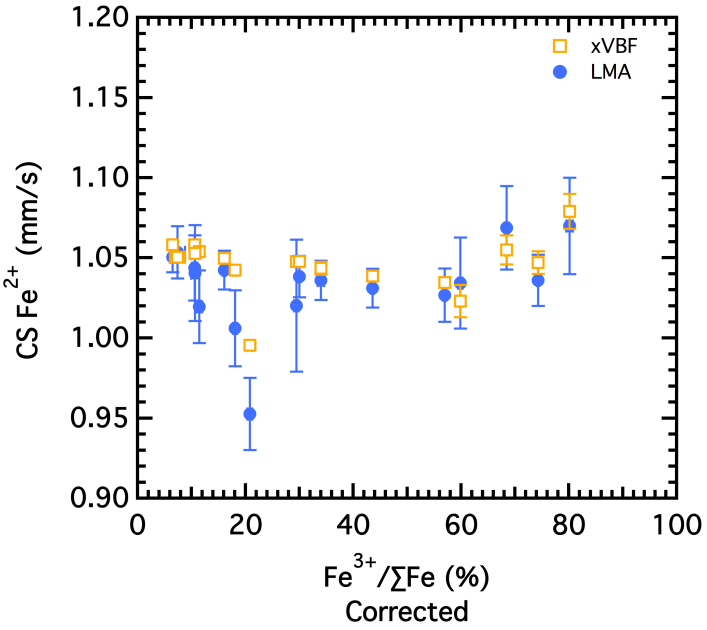

(b)

Figure 3.3: Mössbauer Center Shift (CS) of paramagnetic doublets for of a) Fe^{3+} and b) Fe^{2+} from xVBF and LMA fits of spectra from andesitic glasses collected at room temperature as a function of Fe^{3+} based on recoilless-fraction corrected room temperature Mössbauer spectra with xVBF fits.

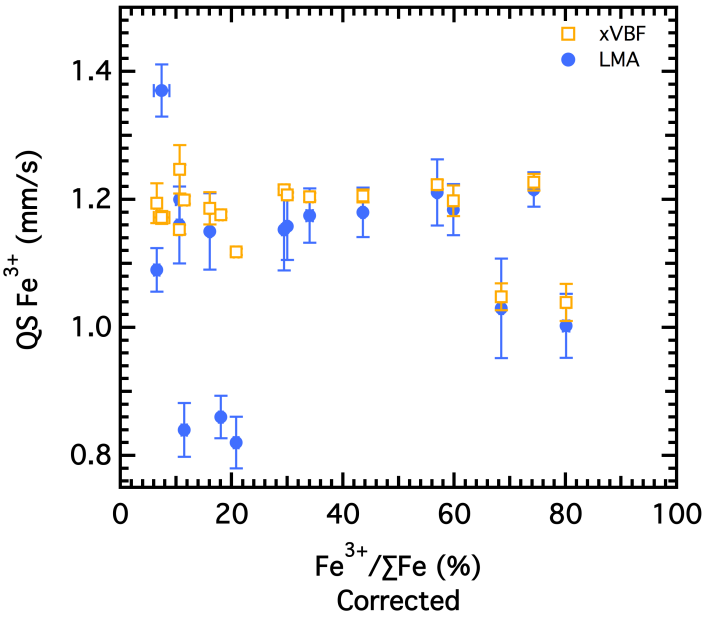

(a)

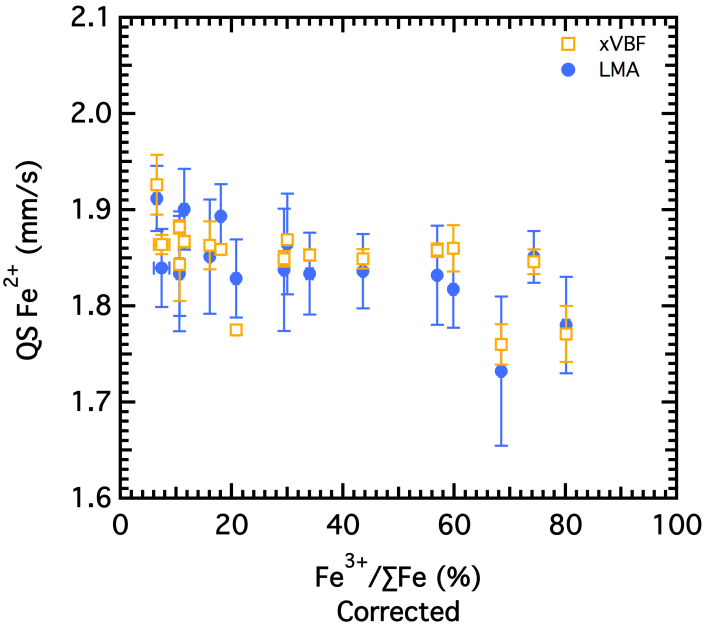

(b)

Figure 3.4: Quadrupole splitting (QS) of paramagnetic doublets for of a) Fe^{3+} and b) Fe^{2+} from xVBF and LMA fits of spectra from andesitic glasses collected at room temperature as a function of $Fe^{3+}/\Sigma Fe$ based on recoilless-fraction corrected room temperature Mössbauer spectra with xVBF fits.

center positions ($E_0(Fe^{3+})$ and $E_0(Fe^{2+})$) according to

$$\text{Centroid Energy} = \frac{I(Fe^{3+})E_0(Fe^{3+}) + I(Fe^{2+})E_0(Fe^{2+})}{I(Fe^{3+}) + I(Fe^{2+})} \quad (3.2)$$

Variations in the centroid energy with $Fe^{3+}/\Sigma Fe$ and associated errors are shown in Fig. 3.7.

Several features of the pre-edge shape produce trends that can be empirically related to quantitative determination of $Fe^{3+}/\Sigma Fe$ in andesitic glasses directly from XANES spectra, as has been previously explored for other silicate glasses (*Berry et al.*, 2003; *Botcharnikov et al.*, 2005; *Wilke et al.*, 2005; *Métrich et al.*, 2006; *Cottrell et al.*, 2009; *Dauphas et al.*, 2014; *Knipping et al.*, 2015). For andesitic glasses ranging from $Fe^{3+}/\Sigma Fe$ of 0.06 to 0.80, centroid energies increase from 7112.092 to 7113.404 (Fig. 3.7). Similarly, baseline-subtracted pre-edge integrated intensity ratios ($I(Fe^{3+})/I(Fe^{2+})$, and $I(Fe^{3+})/[I(Fe^{3+})+I(Fe^{2+})]$) increase systematically with $Fe^{3+}/\Sigma Fe$ (Fig. 3.8). Uncertainties, established by replicate analyses of at least 3 separate spots on each sample are typically 0.01 and 0.02 eV for centroid energies measured at NSLS and APS, respectively. Uncertainties in area ratios vary from 0.005 to 0.67 for $I(Fe^{3+})/I(Fe^{2+})$, and 0.001 to 0.049 for $I(Fe^{3+})/[I(Fe^{3+})+I(Fe^{2+})]$, respectively, with greater values (up to 10% and 9% relative) associated with larger ($I(Fe^{3+})/I(Fe^{2+})$ and $I(Fe^{3+})/[I(Fe^{3+})+I(Fe^{2+})]$ ratios, separately. Application of these features to $Fe^{3+}/\Sigma Fe$ is explored further in the Section 3.4.

The total integrated intensity of the pre-edge peaks, normalized to that for the k edge (Fig. 3.9) provides information about the average coordination of Fe ions in the silicate structure, with larger normalized total integrated intensities associated with lower coordination states and greater $Fe^{3+}/\Sigma Fe$ ratios. (e.g., *Wilke et al.*, 2001). Among the andesitic glasses, normalized pre-edge intensities range from 0.1 for the more reduced glasses up to 0.18 for those more oxidized (Table 3.3). Quantitative interpretations of coordination are examined in the Section 3.4.

3.4 Discussion

3.4.1 Determination of $Fe^{3+}/\Sigma Fe$ by XANES

Variations in XANES pre-edge features with $Fe^{3+}/\Sigma Fe$ can be calibrated to produce empirical quantitative measures of the oxidation state of Fe in silicate glasses (*Berry et al.*, 2003;

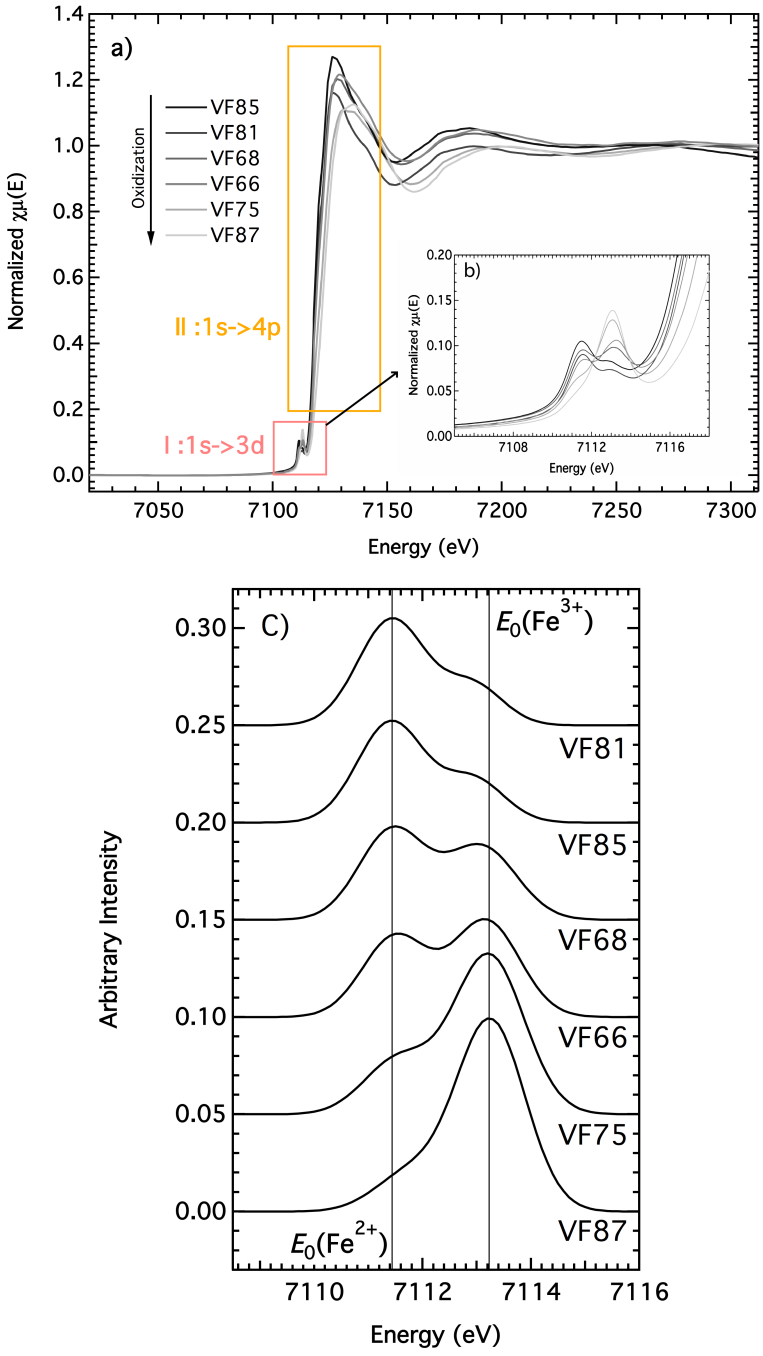

Figure 3.5: Examples of XANES spectra from 6 andesitic glasses collected at APS with $Fe^{3+}/\Sigma Fe$ ranging from 0.08 to 0.78. a) Edge-step normalized full XANES spectra. b) A magnified view of the pre-edge. c) Iron 1s→3d pre-edge transition, baseline-subtracted and drift-corrected. Spectra are vertically offset for clarity.

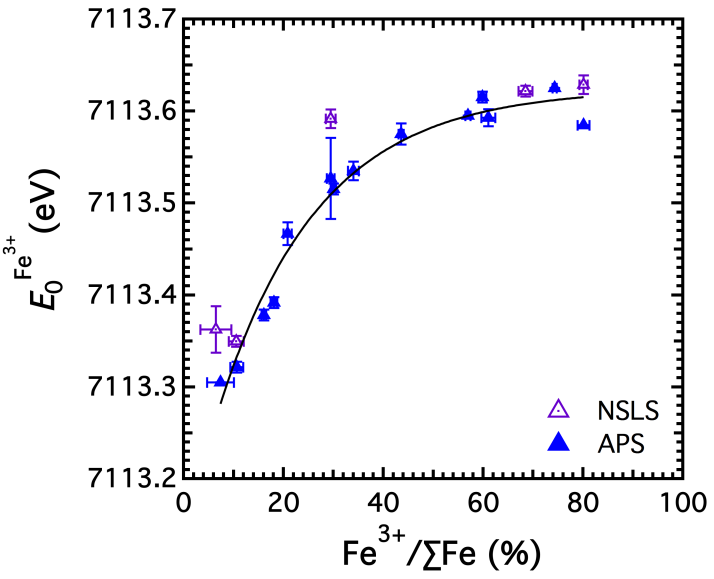

(a)

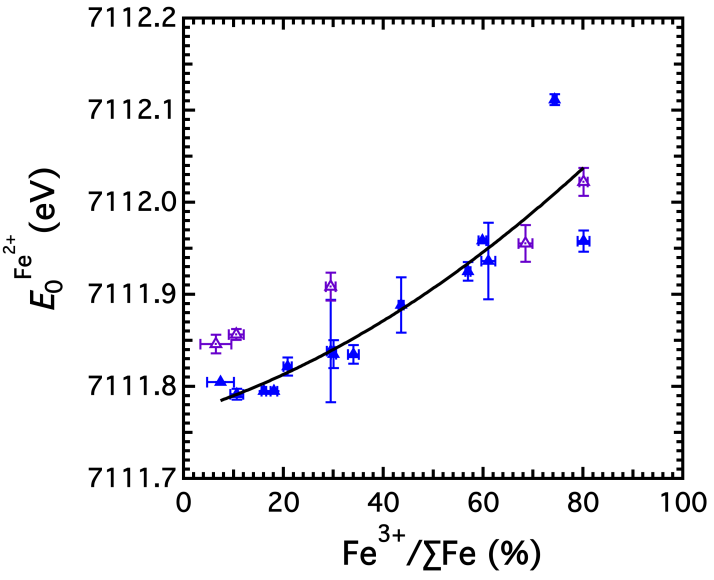

(b)

Figure 3.6: Center position (E_0) of XANES pre-edge features attributable to Fe^{2+} (a) and Fe^{3+} (b) of andesitic glasses vary as a function of $Fe^{3+}/\Sigma Fe$ as determined from recoilless-fraction-corrected room temperature Mössbauer spectra. The purple and yellow triangles represent XANES spectra collected at NSLS, and APS respectively. Uncertainties of XANES energies and $Fe^{3+}/\Sigma Fe$ equal 1σ standard deviation. The curves in (a) and (b) are least squares best fit curves, with coefficients listed in Table 3.2, and allow extrapolation of E_0 values to hypothetical compositions with pure Fe^{2+} and Fe^{3+}.

Table 3.2: Regression coefficients for least-squares fits with error estimates for the center positions (E_0) of the pre-edge XANES attributable to Fe^{2+} and Fe^{3+}

	Coefficients		
	a	**b**	**c**
E_0(**Fe**$^{3+}$)*	7113.625±0.015	-0.4939±0.0329	0.0494±0.0007
E_0(**Fe**$^{2+}$)$^{\#}$	7111.771±0.038	0.00017±0.00217	2.04E-05±2.47E-05

*:$E_0(Fe^{3+})$=**a**+**b***$(Fe^{3+}/\Sigma Fe)$ +**c***$(Fe^{3+}/\Sigma Fe)^2$

$^{\#}$:$E_0(Fe^{2+})$=**a**+**b***exp(-**c***$(Fe^{3+}/\Sigma Fe)$)

Table 3.3: Parameters from step-edge normalized XANES spectra

Sample Name	**Corrected$^{\&}$ Centroid (eV)**	**I(Fe^{3+})+I(Fe^{2+})***	**I(Fe^{3+})/I(Fe^{2+})***	**I(Fe^{3+})/ [I(Fe^{2+}) +I(Fe^{3+})]***
		APS		
VF3	7113.265(0.007)	0.172(0.004)	4.064(0.236)	0.802(0.009)
VF30	7113.369(0.019)	0.181(0.003)	6.579(0.670)	0.867(0.012)
VF54	7112.749(0.035)	0.156(0.010)	1.193(0.277)	0.539(0.049)
VF59	7112.999(0.009)	0.165(0.012)	1.930(0.092)	0.658(0.011)
VF66	7112.782(0.016)	0.140(0.001)	1.294(0.068)	0.564(0.013)
VF68	7112.568(0.010)	0.131(0.004)	0.830(0.024)	0.454(0.007)
VF70	7112.393(0.002)	0.114(0.001)	0.599(0.005)	0.375(0.002)
VF74	7113.226(0.013)	0.179(0.001)	3.259(0.097)	0.765(0.005)
VF75	7113.175(0.001)	0.179(0.001)	2.974(0.023)	0.748(0.001)
VF81	7112.218(0.001)	0.111(0.001)	0.387(0.007)	0.279(0.003)
VF83	7112.833(0.007)	0.154(0.017)	1.423(0.011)	0.587(0.002)
VF85	7112.174(0.008)	0.113(0.001)	0.326(0.009)	0.246(0.005)
VF87	7113.386(0.003)	0.187(0.002)	5.341(0.103)	0.842(0.003)
VF88	7112.350(0.006)	0.120(0.002)	0.539(0.008)	0.350(0.003)
		NSLS		
VF30	7113.404(0.018)	0.164(0.007)	6.204(0.623)	0.861(0.012)
VF35	7112.146(0.005)	0.096(0.001)	0.247(0.017)	0.198(0.011)
VF49	7112.092(0.015)	0.102(0.001)	0.187(0.012)	0.158(0.009)
VF53	7113.308(0.021)	0.148(0.004)	4.321(0.352)	0.812(0.012)
VF54	7112.736(0.011)	0.132(0.003)	0.968(0.041)	0.492(0.011)

$^{\&}$Centroid energy corrected for drift based on LW_0≡7112.3 eV (*Cottrell et al.*, 2009)

*I: Integrated pre-edge intensity

APS: Advanced Photon Source

NSLS: National Synchrotron Light Source

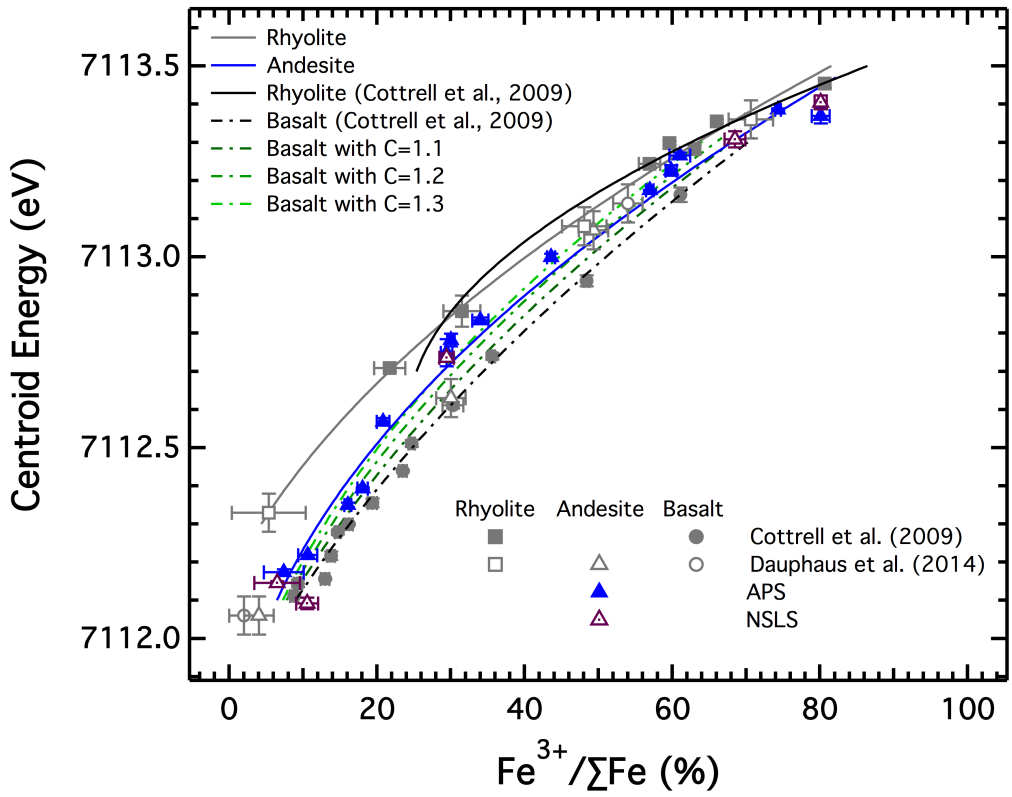

Figure 3.7: XANES pre-edge centroid energies as a function $Fe^{3+}/\Sigma Fe$ for andesitic glasses collected at NSLS and APS. The triangles represent andesitic glasses from this study and from *Dauphas et al.* (2014), both of which are plotted against $Fe^{3+}/\Sigma Fe$ determined from room temperature Mössbauer spectra corrected for recoilless fraction using the C factor of 1.256 from *Zhang et al.* (2015) (see text). The curve through these data is an empirical best fit to these andesite data (excluding the most reduced glass from *Dauphas et al.* (2014), which has a large uncertainty). The squares, and dots represent rhyolitic glasses, and basaltic glasses separately from *Cottrell et al.* (2009) and *Dauphas et al.* (2014). $Fe^{3+}/\Sigma Fe$ ratios of rhyolites determined with room temperature Mssbauer spectra are corrected with a C factor of 1.124, determined from comparison between RT Mssbauer and wet chemical determinations from *Cottrell et al.* (2009). $Fe^{3+}/\Sigma Fe$ ratios of basalts are plotted with values obtained from room temperature Mssbauer spectra owing to the uncertain correction value. Dashed and solid black curves represent basalt and rhyolite calibration curves respectively from *Cottrell et al.* (2009). A new rhyolite calibration (solid gray curve) is applied based on all rhyolite glasses in the plot. Three more basalt calibration curves are calculated based on C factor of 1.1, 1.2 and 1.3. All uncertainties are 1 standard deviation. All plotted data, with corrections, are listed in Table 3.S5; coefficients to the new curves in this plot are given in Table 3.4.

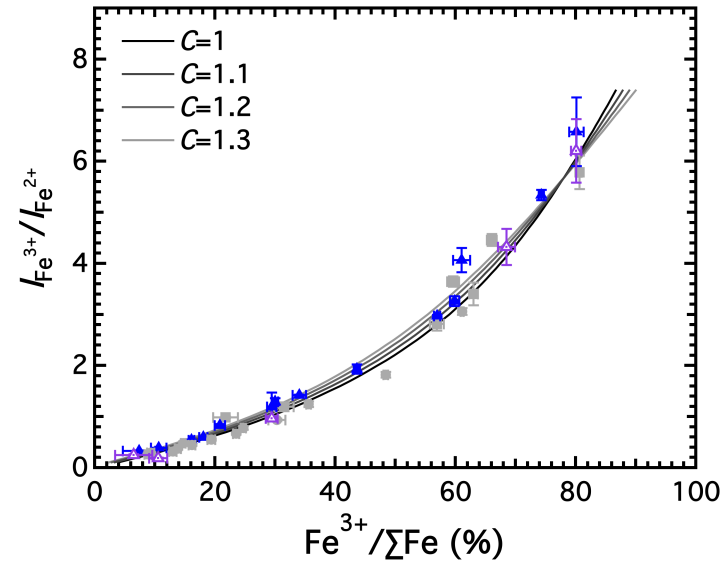

(a)

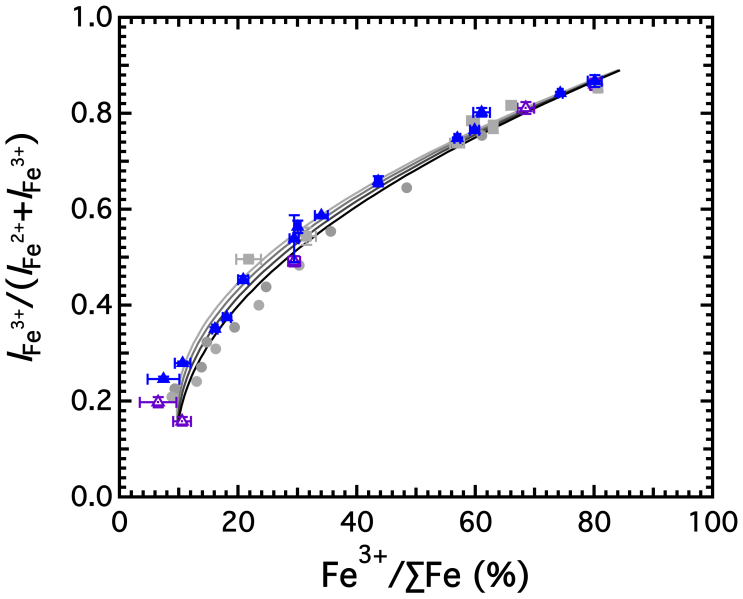

(b)

Figure 3.8: The ratio of Gaussian component integrated XANES pre-edge intensity (a) $I(Fe^{3+})/I(Fe^{2+})$ and (b) $I(Fe^{3+})/[I(Fe^{3+}) + I(Fe^{2+})]$ as a function of $Fe^{3+}/\Sigma Fe$, after *Wilke et al.* (2005) and *Cottrell et al.* (2009). $Fe^{3+}/\Sigma Fe$ ratios of rhyolites, andesites are corrected as described in Fig. 3.7 and basalts are not corrected and listed in Table 3.1 and Table 3.S5. Symbols are applied same as Fig 3.7. All uncertainties are 1 standard deviation. New calibration curves of are applied for all three compositions with $Fe^{3+}/\Sigma Fe$ of basalts plotted for different C factors of 1, 1.1, 1.2 and 1.3.

Botcharnikov et al., 2005; *Wilke et al.*, 2005; *Métrich et al.*, 2006; *Cottrell et al.*, 2009; *Dauphas et al.*, 2014; *Knipping et al.*, 2015). The most widely-used such parameterization uses the centroid energy. For glasses in this study, $Fe^{3+}/\Sigma Fe$ was calculated from room temperature Mössbauer spectra, corrected for the effects of recoil-free fraction based on a low temperature Mössbauer study on identical glass composition (*Zhang et al.*, 2015). The accuracy of this correction is well-demonstrated by the good correspondence between $Fe^{3+}/\Sigma Fe$ determined in this way and the predictions of *Kress and Carmichael* (1991) (Fig. 3.2).

Prior to comparison between the present results and those previously analyzed glasses of various compositions, it is important to consider possible systematic biases owing to different methods of establishing $Fe^{3+}/\Sigma Fe$. In contrast, most of the glasses from the studies of *Cottrell et al.* (2009) and *Dauphas et al.* (2014) were characterized by Mössbauer measurements that were not corrected for these effects, though some of the rhyolites used by *Cottrell et al.* (2009) were characterized by wet chemical methods. The accuracy of uncorrected room temperature (RT) Mössbauer measurements of $Fe^{3+}/\Sigma Fe$ has long been debated. This history was reviewed in detail by *Zhang et al.* (2015), but two key considerations are that theoretical arguments based on bond strength (*Chen and Yang*, 2007) make clear that RT Mössbauer should overestimate $Fe^{3+}/\Sigma Fe$, as is known to be true based on measurements of recoilless fractions from a wide spectrum of Fe-bearing minerals (*De Grave and Van Alboom*, 1991), and that key studies that are generally cited to suggest that RT Mössbauer yields accurate $Fe^{3+}/\Sigma Fe$ within analytical uncertainty for silicate glasses (*Mysen and Virgo*, 1985; *Dingwell*, 1991; *Wilke*, 2005) show systematic biases to higher $Fe^{3+}/\Sigma Fe$ (*Lange and Carmichael*, 1989; *Righter et al.*, 2013; *Zhang et al.*, 2015). Only *Partzsch et al.* (2004) observed the opposite trend, finding that wet chemical analyses yielded higher Fe^{3+} than Mössbauer analyses of glasses quenched from similar conditions, but in their study individual experiments were not analyzed by multiple methods. Similarly, *Jayasuriya et al.* (2004) showed that $Fe^{3+}/\Sigma Fe$ in synthetic basaltic glasses calculated from RT Mössbauer gave similar results to $Fe^{3+}/\Sigma Fe$ calculated from Mössbauer spectra taken at 4.2 K, but both their RT and low temperature spectra are complicated by strong non-paramagnetic components, which introduce ambiguity to quantification of $Fe^{3+}/\Sigma Fe$ (*Zhang et al.*, 2015). Thus, the following comparisons consider the possibility that previous calibrations of XANES for Fe oxidation state of glasses may be biased to exaggerated to elevated $Fe^{3+}/\Sigma Fe$.

Previous studies have noted that the relationship between pre-edge centroid energy and

$Fe^{3+}/\Sigma Fe$ can depend on glass composition, and most notably that trends for rhyolite are distinct from those for less silicic natural glass compositions (*Cottrell et al.*, 2009; *Dauphas et al.*, 2014). Consequently, the previous data most similar to those in the present study are three andesitic glasses analysed by RT Mössbauer and XANES spectroscopy by *Dauphas et al.* (2014). If we adjust their $Fe^{3+}/\Sigma Fe$ ratios determined at RT for recoil-free fraction effects by the same factor as that determined for the andesites in the present study (Table 3.S5), two of the three glasses have variations in centroid energy and $Fe^{3+}/\Sigma Fe$ that are similar to those from the present study (Fig. 3.7). The third, equilibrated at IW, does not have a well-resolved $Fe^{3+}/\Sigma Fe$ ratio from the Mössbauer spectrum. Combining the recoil-free fraction-corrected Mössbauer determinations with the centroid energies for the suite of andesitic glasses from this study as well as the two additional constraints from Dauphas et al. (2014) allows regression of a function

$$Fe^{3+}/\Sigma Fe = a + b * (x - d) + c * (x - d)^2 \tag{3.3}$$

for quantitative prediction of $Fe^{3+}/\Sigma Fe$ (Table 3.4).

For rhyolites, the relation between centroid energy and $Fe^{3+}/\Sigma Fe$ is anchored chiefly from the XANES data of *Cottrell et al.* (2009), for which Fe oxidation states were determined principally by wet chemical analyses (*Moore et al.*, 1995). Exceptions include one glass, 568_2, from *Cottrell et al.* (2009) and the 3 samples analyzed by *Dauphas et al.* (2014), for which only RT Mössbauer data are available. These four samples can be adjusted by a factor derived by comparison of wet chemical *Moore et al.* (1995) and RT Mössbauer results (*Cottrell et al.*, 2009) for samples DT_46 and DT_39, which indicate a factor, C, equal to 1.124±0.035. The resulting centroid versus $Fe^{3+}/\Sigma Fe$ trend for rhyolites (Table 3.S5, Fig. 3.7) remains distinct from that derived for andesitic glasses, which could be owing to differences in Fe-O bond strengths in the two glass compositions, as suggested by *Dauphas et al.* (2014).

Centroid versus $Fe^{3+}/\Sigma Fe$ trends for basalt are established chiefly from RT Mössbauer spectroscopy and at this time we do not have an unambiguous constraint on how these should be corrected for recoilless fraction. Fig. 3.7 shows the basalt trend from data of *Cottrell et al.* (2009) in which the original RT Mössbauer determinations were modified with values of C of 1.1, 1.2, and 1.3. With values between 1.2 and 1.3, similar to that applied here (1.256) to the andesitic glasses based on *Zhang et al.* (2015), the basalt and andesite trends are more nearly coincident. Thus, much or all of the offset between basalt and andesite could be owing to the

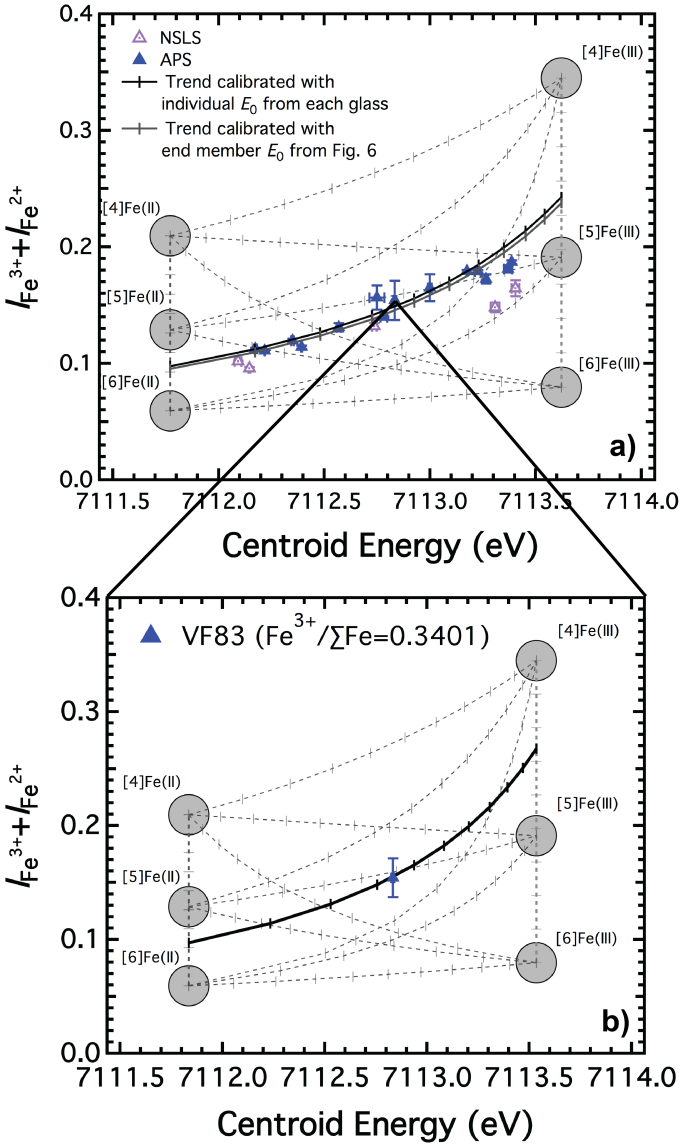

Figure 3.9: Pre-edge parameters of a) all andesitic glasses and b) VF83 plotted in the variogram after *Wilke et al.* (2001). Grey fields designate pre-edge parameters for the Fe coordination and oxidation state indicated. Dashed lines between fields indicate the variation of pre-edge parameters assuming binary mixtures of a) respective end-members, determined from center position of Fe^{3+} and Fe^{2+} (Fig. 3.6) and b) energy positions of Fe^{3+} and Fe^{2+} from VF83. Ticks on curves refer to the percentage of mixtures with a) the average coordination number of Fe^{2+} and Fe^{3+} for all andesitic glasses and b) coordination number of Fe^{2+} and Fe^{3+} for VF83.

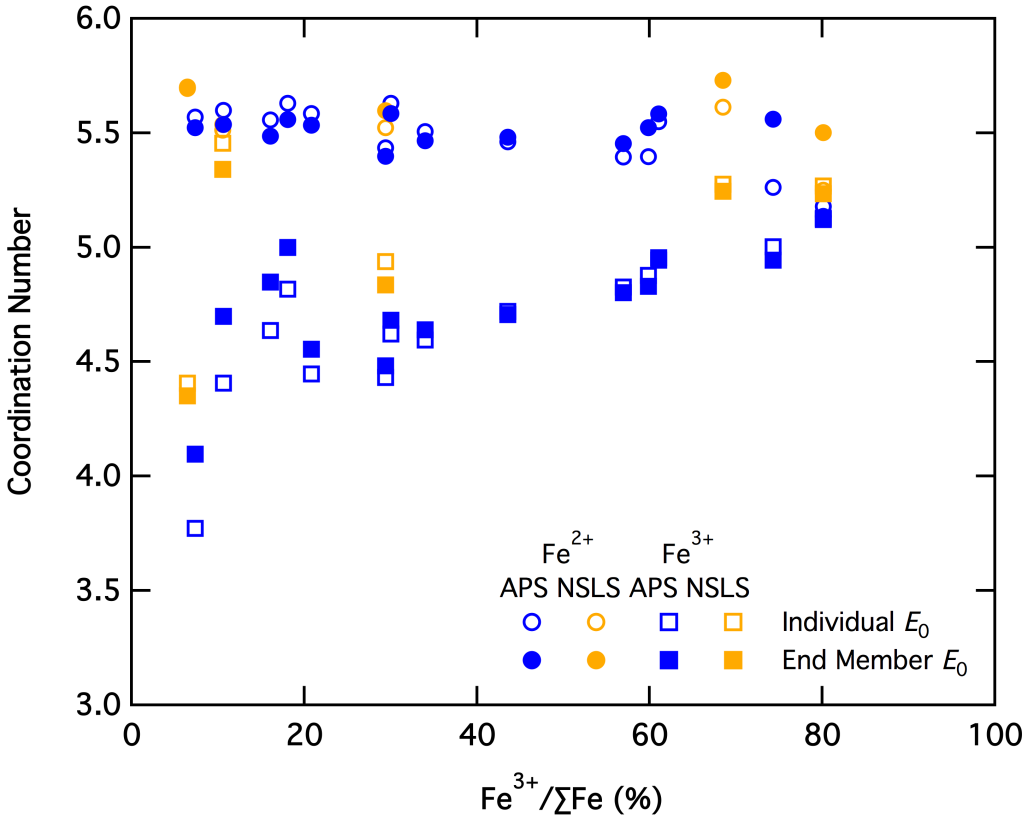

Figure 3.10: Coordination number of Fe^{3+} and Fe^{2+} calculated based on the XANES pre-edge intensities and $Fe^{3+}/\Sigma Fe$. CN(Fe^{2+}) calculated with individual E_0, = 5.49±0.14; CN(Fe^{3+}) calculated with individual E_0, = 4.77±0.39; CN(Fe^{2+}) calculated with end member E_0 = 5.52±0.12; CN(Fe^{3+}) calculated with end member E_0 = 4.81±0.31

Table 3.4: Regression coefficients from least-squares fits with error estimates for $Fe^{3+}/\Sigma Fe$ calibration curves from XANES pre-edge fratures.

x*		Coefficients			
		a	**b**	**c**	**d**
Centroid Energy$^{\#}$	Rhyolite	17.8188±3.1682	-2.6657±7.7448	51.0927±4.6651	7112.33
	Andesite	6.2885±0.2655	23.1409±1.4366	23.1663±1.1703	7112.092
	Basalt with C=1$^{@}$	9.4221±0.2839	34.0051±1.4332	14.4706±1.2569	7112.112
	Basalt with C=1.1$^{@}$	8.699±0.2839	30.6326±1.4332	16.2446±1.2569	7112.112
	Basalt with C=1.2$^{@}$	8.091±0.2839	27.6918±1.4332	17.6539±0.1.2569	7112.112
	Basalt with C=1.3$^{@}$	7.5721±0.2839	25.1161±1.4332	18.77±0.1.2569	7112.112
$\frac{I(Fe^{3+})}{I(Fe^{3+})+I(Fe^{2+})}$ $^{\&}$	Basalt with C=1$^{@}$	87.097±1.1896	-87.0399±1.0402	0.3492±0.0106	
	Basalt with C=1.1$^{@}$	87.9272±1.2362	-87.8909±1.0851	0.3409±0.0105	
	Basalt with C=1.2$^{@}$	88.6772±1.2791	-88.6604±1.1264	0.3338±0.0104	
	Basalt with C=1.3$^{@}$	89.3597±1.3186	-89.3609±1.1648	0.3276±0.0104	
$\frac{I(Fe^{3+})}{I(Fe^{2+})}$ ^{v}	Basalt with C=1	55.4285±3.0698	4.3284±0.4615	-55.2023±2.7574	-0.5880±0.0400
	Basalt with C=1.1$^{@}$	50.7104±2.9053	5.108±0.442	-51.0215±2.593	-0.6022±0.0427
	Basalt with C=1.2$^{@}$	46.1907±2.7092	5.8533±0.4184	-46.9435±2.3973	-0.6208±0.0458
	Basalt with C=1.3$^{@}$	41.8742±2.4912	6.565±0.3918	-42.9981±2.1803	-0.6443±0.0492

All data used for fitting are listed in Table 3.S5

*:x is the quantity measured from XANES.

$^{\#}$:$Fe^{3+}/\Sigma Fe$ =**a**+**b***(x - **d**) +**c***(x - **d**)^2

$^{\&}$:$Fe^{3+}/\Sigma Fe$ =**a**+**b***exp(-**c***x)

^{v}:$Fe^{3+}/\Sigma Fe$ =**a**+**b***x+**c***exp(**d***x)

$^{@}$:$Fe^{3+}/\Sigma Fe$ values of basalt are adjusted for recoilless fration with the specified values of C based on Eqn. 3.1 in the text.

absence of a recoil-free fraction correction for the basalt Mössbauer data. Data for basalts from *Wilke et al.* (2005) can be corrected with a factor of C of 1.29 and eqn. (3.1), based on comparison between RT Mössbauer and wet chemical analyses for four samples analysed in that study. These data show greater scatter, owing in part to much lower analytical precision for centroid determinations as compared to more recent determinations, but generally agree with the trends established for basalts by *Cottrell et al.* (2009) and for andesites in this study. Within the uncertainties of analytical precision and, at this time, imperfectly constrained corrections of $Fe^{3+}/\Sigma Fe$, the XANES centroid trends for basalts are not distinguishable from those of andesites.

The ratios of the intensities of the different sub-peaks of the pre-edge, ($I(Fe^{3+})/I(Fe^{2+})$, and $I(Fe^{3+})/[I(Fe^{3+})+I(Fe^{2+})]$), are also potential quantitative measures of $Fe^{3+}/\Sigma Fe$. The two ratios are complementary, as the former is more sensitive to changes in $Fe^{3+}/\Sigma Fe$ for oxidized compositions and the latter for more reduced compositions (Fig. 3.8). The relationship between integrated pre-edge intensity ratios and $Fe^{3+}/\Sigma Fe$ from basalts, rhyolites (*Cottrell et al.*, 2009) and andesites (this study), can be modeled with an exponential function (Table 3.4, Fig. 3.8) and either can be used to determine the oxidation state of glasses. Intensity ratios are insensitive to energy drift, which facilitates more readily than centroids comparison of observations from studies at different beamlines. Perhaps more importantly, in contrast to centroids, intensity ratios for different glass compositions have essentially the same correspondence to $Fe^{3+}/\Sigma Fe$, and so provide a compositionally-independent method of $Fe^{3+}/\Sigma Fe$ determination. Thus, although centroid-based calibrations have greater precision and are preferred in XANES analyses of glasses for which compositions can be closely matched to existing standard calibrations, peak-area ratios are more suitable for evaluation of $Fe^{3+}/\Sigma Fe$ in silicate glasses for which specific compositions have not yet been calibrated.

3.4.2 Bonding and coordination of Fe in andesitic glasses

Variations in XANES pre-edge integrated intensity and centroid energy can be interpreted in terms of the coordination of Fe^{2+} and Fe^{3+} in silicate glasses according to the variogram first introduced by *Wilke et al.* (2001) (Fig. 3.9). Total integrated intensities ($I(Fe^{3+})+I(Fe^{2+})$), increase together with centroid energies along a trend consistent with average coordination of Fe^{2+} and Fe^{3+} that are approximately 5-fold (Figure 3.9a). This result is similar to that found

by *Wilke et al.* (2005) for basaltic glasses. We note, of course that the average coordination is only semi-quantitative, as the variogram is a generalization based on integrated pre-edge intensities typical of various Fe-rich minerals (*Wilke et al.*, 2001) and cannot distinguish between absolute coordination and a mixture of a range of 4-, 5-, and 6-fold coordination (*Wilke et al.*, 2005).

To examine the apparent coordination of Fe ions in greater detail, we can calculate average coordination of Fe^{2+} and Fe^{3+} in each glass based on the integrated intensities of the observed glasses as well as those assumed for the 4-, 5-, and 6-fold coordination states of each ion from *Wilke et al.* (2001) together with values of $E_0(Fe^{2+})$ and $E_0(Fe^{3+})$ appropriate for each composition (Fig. 3.9b), and the $Fe^{3+}/\Sigma Fe$. This approach differs slightly from the variogram methodology in Fig. 3.9a, which assumes a single value of $E_0(Fe^{2+})$ and $E_0(Fe^{3+})$ for all compositions. Fig. 3.10 shows average coordination calculated with both approaches, and the quantitative difference between the two is small. Calculated average coordination of Fe^{2+} is consistently near 5.5, or decreasing slightly for more oxidized glasses, whereas that for Fe^{3+} is near 4.5 for reduced glasses and closer to 5 for more oxidized glasses. Thus, these calculations suggest Fe^{2+} is more nearly a network modifying ion for both reduced and oxidized glasses, whereas Fe^{3+} is closer to a network forming ion for reduced glasses, where its abundance is low, and becomes more network-modifying as its abundance increases.

Hyperfine parameter values obtained from Mössbauer spectra provide information on the next-nearest neighbor environment of iron in minerals (*Dyar et al.*, 2006; *Chen and Yang*, 2007). The center shift is sensitive to bonding parameters such as coordination and co-valency, and quadrupole splitting is sensitive to changes in the distortion of the iron coordination environment (*Dyar and Schaefer*, 2004; *Dyar et al.*, 2006; *Chen and Yang*, 2007). Values of CS for Fe^{2+} for the andesitic glasses are close to 1.05 (Fig. 3.3b), similar to values found in previous studies of mafic glasses (*Dyar*, 1985; *Mysen and Virgo*, 1985; *Botcharnikov et al.*, 2005) and suggesting Fe^{2+}-O coordination close to 6-fold (*Dyar*, 1985), consistent with results from XANES. CS values for Fe^{3+} are more variable, with values between 0.45 and 0.6 for glasses with low $Fe^{3+}/\Sigma Fe$, and 0.3 for glasses above 30% $Fe^{3+}/\Sigma Fe$. This trend of decreasing CS with increasing $Fe^{3+}/\Sigma Fe$ for reduced glasses has been observed previously for a variety of natural and synthetic silicate melt compositions, and has been attributed to decreasing Fe^{3+}-O coordination in glasses quenched from more oxidized conditions (*Mysen et al.*, 1985; *Virgo and Mysen*, 1985; *Dingwell and Virgo*, 1987; *Dingwell*, 1991; *Jayasuriya et al.*, 2004; *Partzsch*

et al., 2004; *Mysen*, 2006; *Volovetskii et al.*, 2012). This, however, is the opposite from the inferences from XANES for the andesitic glasses in this study, which suggest increased coordination of Fe3+ for more oxidized glasses (Fig. 3.10). Also, whereas some previous studies found changes in Fe^{3+} quadrupole splittings that correlate positively with observed shifts in Fe^{3+} CS (*Jayasuriya et al.*, 2004; *Volovetskii et al.*, 2012), others found Fe^{3+} QSs have negative correlations (*Mysen et al.*, 1985; *Virgo and Mysen*, 1985; *Dingwell*, 1991) and still others found Fe^{3+} QS to be nearly constant (*Partzsch et al.*, 2004; *Mysen*, 2006; this study). This lack of consistency suggests that artifacts could affect these variations in hyperfine features of Fe^{3+}. As noted above, fitting of Fe^{3+} hyperfine parameters in reduced glasses is challenging, as the Fe^{3+} doublet is largely obscured by the Fe^{2+} doublet, and there are consequently possibly unavoidable covariances between the resolved parameters for Fe^{2+} and Fe^{3+} for these glasses.

In summary, the Mössbauer and XANES measurements on andesitic glasses show that Fe^{2+} has a higher average coordination with oxygen than Fe^{3+}, and this is broadly consistent with previous spectroscopic studies. It is also consistent with measurements of viscosities, which indicate that oxidized glasses are more polymerized than their reduced equivalents (e.g., *Dingwell and Virgo*, 1987). The spectroscopy suggests that Fe^{2+} is a network modifier with consistent melt structure from reduced to oxidized glasses, whereas Mössbauer and XANES indicate conflicting variations in Fe^{3+} structure with fO_2.

3.5 Conclusion

The first detailed calibration for determination of $Fe^{3+}/\Sigma Fe$ ratio for andesitic glasses by XANES has been derived from a suite of samples spanning 8 to 84% $Fe^{3+}/\Sigma Fe$, with ratios determined from recoilless fraction-corrected room temperature Mssbauer spectroscopy. Variations in the centroid energy of XANES pre-edge features produce the most precise calibration. The centroid versus $Fe^{3+}/\Sigma Fe$ ratio trend is intermediate between those previously derived for basalts and rhyolites (*Cottrell et al.*, 2009; *Dauphas et al.*, 2014) from facilities from which centroid energies can be compared directly. The distinction between andesitic and basaltic glasses may derive in part from the methods used to calibrate $Fe^{3+}/\Sigma Fe$ ratio in the basaltic standards. Alternative calibrations for $Fe^{3+}/\Sigma Fe$ ratio based on the relative intensities of pre-edge sub-peak features show less dependence on composition, and this provides a potential facility-, standard- and composition independent methodology to determine $Fe^{3+}/\Sigma Fe$ ratio. XANES

and Mössbauer spectra on andesitic glasses confirm previous spectroscopic studies indicated that Fe^{2+} is a network modifying cation in natural silicate glasses, whereas Fe^{3+} is more similar to a network forming ion. However, in detail XANES and Mössbauer show conflicting trends of Fe^{3+} coordination with changing bulk $Fe^{3+}/\Sigma Fe$; XANES indicates increasing average coordination in more oxidizing glasses, whereas Mössbauer indicates that Fe^{3+} in the most reduced glasses has higher coordination. The origin of this conflict is not known, though it may relate to the indirect basis of coordination assignments in XANES, which is based chiefly by analogy to XANES spectra in minerals.

3.A Supplement material

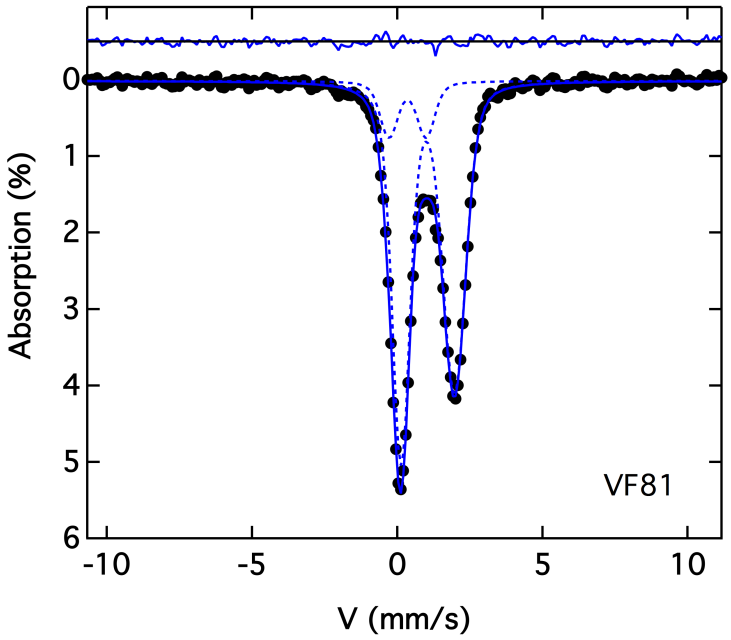

(a)

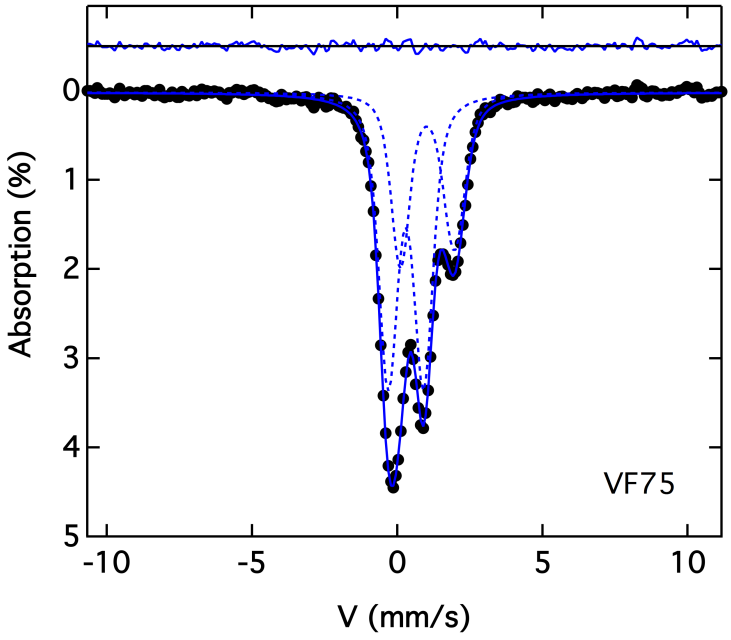

(b)

Figure 3.S1: Mössbauer spectra examples, a) VF81, with undistinguished Fe^{3+} doublets; b) is from VF75, with three distinguished peaks

Table 3.S1: Electron microprobe analyses of sample and standard glasses

Sample Name	SiO_2	TiO_2	Al_2O_3	FeO*	MgO	CaO	Na_2O	K_2O	TOTAL
VF30	59.24±0.14	2.88±0.10	14.36±0.08	9.13±0.09	2.00±0.02	7.31±0.07	4.50±0.13	1.13±0.02	100.56±0.31
VF35	60.30±0.32	2.91±0.11	14.66±0.07	9.12±0.07	2.06±0.02	7.38±0.05	3.38±0.17	1.10±0.01	100.92±0.14
VF49	60.25±0.11	2.95±0.14	14.62±0.09	8.19±0.08	2.17±0.03	7.70±0.06	3.07±0.07	1.00±0.02	99.95±0.25
VF50	59.55±0.16	3.08±0.14	14.90±0.07	8.49±0.09	2.26±0.03	7.85±0.05	3.73±0.09	1.01±0.02	100.86±0.20
VF53	59.03±0.12	2.86±0.13	14.55±0.07	9.44±0.09	2.06±0.03	7.36±0.07	4.21±0.10	1.08±0.02	100.59±0.32
VF54	59.38±0.17	2.80±0.11	14.54±0.08	9.46±0.09	2.04±0.04	7.32±0.08	3.92±0.12	1.08±0.03	100.53±0.30
VF59	59.66±0.54	2.76±0.13	14.43±0.14	9.36±0.08	2.05±0.04	7.18±0.06	4.16±0.11	1.10±0.02	100.70±0.56
VF66	58.38±0.20	2.90±0.10	14.42±0.21	10.20±0.10	2.09±0.03	7.41±0.08	3.83±0.12	1.05±0.02	100.28±0.25
VF68	59.13±0.13	2.85±0.12	14.70±0.10	9.57±0.13	2.05±0.03	7.29±0.07	3.80±0.12	1.09±0.03	100.50±0.21
VF70	58.01±0.26	2.84±0.14	14.31±0.12	9.98±0.10	2.10±0.03	7.37±0.03	3.77±0.12	1.03±0.02	99.50±0.42
VF74	58.73±0.36	2.83±0.18	14.61±0.11	9.65±0.06	2.06±0.02	7.31±0.06	4.02±0.10	1.08±0.03	100.28±0.58
VF75	58.79±0.14	2.83±0.09	14.48±0.05	9.73±0.08	2.08±0.03	7.38±0.05	3.97±0.13	1.08±0.02	100.34±0.19
VF81	59.81±0.11	3.00±0.12	14.46±0.08	8.56±0.07	2.15±0.02	7.72±0.07	3.37±0.1	1.02±0.02	100.10±0.20
VF83	58.57±0.27	2.90±0.13	14.06±0.09	9.97±0.05	2.06±0.02	7.41±0.05	3.87±0.12	1.03±0.01	99.87±0.39
VF85	59.15±0.13	2.86±0.07	14.40±0.07	9.92±0.12	2.12±0.04	7.49±0.07	3.53±0.10	1.03±0.02	100.48±0.28
VF87	58.72±0.17	2.90±0.09	14.34±0.08	9.85±0.09	2.07±0.02	7.44±0.05	4.07±0.16	0.92±0.02	100.31±0.32
VF88	60.18±0.30	2.81±0.11	14.45±0.06	9.57±0.15	2.04±0.04	7.25±0.11	3.55±0.11	0.90±0.02	100.75±0.26
ATHO	77.19±0.52	0.23±0.03	11.45±0.21	3.17±0.04	0.09±0.01	1.71±0.03	3.29±0.33	2.69±0.02	99.82±0.70
ATHO^r	75.60±1.40	0.26±0.03	12.20±0.40	3.27±0.20	0.10±0.02	1.70±0.06	3.75±0.62	2.64±0.18	99.62

Notes: r: ATHO-G reference values from *Jochum et al.* (2006).
FeO*:Total Iron contents.
All uncertainties are in one sigma range standard deviation (1σ)

Table 3.S2: Mössbauer fitting parameters from extended Voigt-based Fitting (xVBF) method

Sample Name	χ^2	Background	L HWHM	Fe^{3+}				Fe^{2+}				
				CS	δ_{CS}	QS	δ_{QS}	ρ	CS	δ_{CS}	QS	δ_{QS}
VF30	0.63	3609670(70)	0.283(6)	0.309(48)	0(23)	1.039(8)	0.473(8)	0.43(12)	1.079(11)	0.156(27)	1.771(29)	0.300(6)
VF35	3.01	12550900(185)	0.118(5)	0.567(13)	0(23)	1.194(22)	0.380(26)	0.15(1)	1.058(2)	0.248(1)	1.926(31)	0.326(5)
VF49	1.02	7480850(160)	0.144(6)	0.413(33)	0*	1.153(40)	0.4*	0.29(5)	1.058(3)	0.238(4)	1.882(7)	0.298(10)
VF50	1.24	25667830(375)	0.121(8)	0.368(17)	0*	1.199(28)	0.4*	0.30(2)	1.054(3)	0.237(4)	1.867(6)	0.321(11)
VF53	0.52	5342130(60)	0.203(7)	0.321(3)	0(30)	1.048(7)	0.489(8)	0.24(9)	1.055(9)	0.178(8)	1.760(21)	0.343(15)
VF54	0.61	7608690(125)	0.132(4)	0.326(8)	0(27)	1.215(9)	0.572(8)	0.19(2)	1.048(3)	0.236(2)	1.849(8)	0.388(6)
VF59	0.58	2918710(55)	0.198(7)	0.300(5)	0(32)	1.205(4)	0.451(12)	0.36(49)	1.039(3)	0.245(5)	1.849(10)	0.190(11)
VF66	0.70	5370860(70)	0.165(5)	0.334(4)	0(25)	1.207(5)	0.498(6)	0.24(2)	1.048(2)	0.239(2)	1.869(4)	0.254(7)
VF68	0.70	3944210(85)	0.161(3)	0.373(10)	0(30)	1.118(8)	0.524(12)	0.21(2)	0.995(2)	0.213(2)	1.775(5)	0.282(5)
VF70	0.90	36972320(190)	0.164(2)	0.414(11)	0(30)	1.176(10)	0.613(9)	0.19(11)	1.042(1)	0.249(1)	1.859(5)	0.315(3)
VF74	0.63	4440270(85)	0.225(5)	0.296(7)	0(22)	1.198(14)	0.525(7)	0.11(25)	1.023(10)	0.289(8)	1.860(24)	0.040(6)
VF75	0.62	4987620(80)	0.222(5)	0.295(3)	0(19)	1.223(3)	0.427(5)	0.23(4)	1.035(3)	0.159(4)	1.858(7)	0.347(8)
VF81	0.62	3497200(80)	0.176(8)	0.432(19)	0*	1.247(28)	0.4*	0.31(2)	1.053(3)	0.228(3)	1.843(38)	0.283(10)
VF83	0.77	3784470(80)	0.210(5)	0.323(49)	0(23)	1.204(7)	0.453(8)	0.27(3)	1.044(4)	0.229(3)	1.853(6)	0.205(15)
VF85	0.72	3505810(60)	0.168(3)	0.583(31)	0(33)	1.172(17)	0.326(32)	0.26(2)	1.051(2)	0.109(6)	1.864(10)	0.508(7)
VF87	1.24	3507520(50)	0.247(3)	0.290(11)	0(18)	1.227(3)	0.406(4)	0*	1.047(7)	0.238(6)	1.846(13)	0.163(33)
VF88	0.70	2458090(70)	0.196(7)	0.450(6)	0(6)	1.186(30)	0.500(8)	0.19(30)	1.050(3)	0.222(3)	1.863(25)	0.265(10)

The uncertainty notation is such that, for example, 0.283(6) is equivalent to 0.283±0.006 and are one sigma standard deviation (1σ).

χ^2: Chi square — Background: Background in counts

L HWHM: Lorentzian half width at half maximum in mm/s

CS: Center shift in mm/s — QS: Quadrupole splitting in mm/s;

δ_{CS}: Gaussian width of CS in mm/s — δ_{QS}: Gaussian width of QS in mm/s

ρ: correlation of δ_{CS} and δ_{QS} — *: parameter was fixed as indicated;

Table 3.S3: Mössbauer fitting parameters from Lorentzian Multiplet Analysis (LMA)

Sample Name	χ^2*	CS*	QS*	L HWHM*	Site Populations (%)
VF30	0.81	0.309(13)	1.450(55)	0.322(21)	29.0(55)
		0.316(12)	0.771(47)	0.371(14)	56.0(55)
		1.070(30)	1.780(50)	0.391(24)	15.1(10)
VF35	4.13	0.66(10)	1.090(160)	0.310(49)	8.3(15)
		1.018(12)	1.234(43)	0.235(18)	20.5(21)
		1.040(9)	1.647(31)	0.172(17)	22.2(22)
		1.053(7)	1.986(22)	0.135(13)	16.8(17)
		1.067(9)	2.313(32)	0.143(18)	17.5(20)
		1.089(10)	2.694(41)	0.180(15)	14.7(22)
VF49	1.52	0.310(70)	1.160(120)	0.320(60)	13.2(25)
		0.977(26)	1.140(75)	0.238(27)	17.3(48)
		1.010(19)	2.230(55)	0.217(18)	27.4(40)
		1.034(15)	1.660(60)	0.227(29)	29.4(44)
		1.231(28)	2.330(50)	0.190(32)	12.6(33)
VF50	1.67	0.470(80)	0.840(100)	0.360(55)	16.3(25)
		0.751(25)	1.930(50)	0.200(18)	20.2(19)
		0.928(27)	0.960(65)	0.149(29)	5.7(27)
		1.077(25)	2.188(35)	0.171(27)	20.7(30)
		1.104(17)	1.697(33)	0.187(20)	26.4(16)
		1.258(26)	2.296(50)	0.158(28)	10.6(32)
VF53	0.79	0.325(10)	1.030(18)	0.384(12)	79.6(21)
		1.037(30)	1.420(85)	0.254(46)	10.4(28)
		1.102(22)	2.060(70)	0.207(38)	9.9(24)
VF54	1.25	0.319(20)	1.153(41)	0.349(20)	35.1(21)
		0.780(55)	1.750(60)	0.286(34)	24.0(55)
		1.148(36)	1.670(70)	0.228(30)	24.0(60)
		1.180(29)	2.200(60)	0.210(27)	16.9(47)
VF59	1.24	0.301(8)	1.180(16)	0.356(13)	52.0(16)
		0.998(13)	1.538(43)	0.311(15)	25.2(27)
		1.068(11)	2.167(34)	0.269(22)	22.7(25)
VF66	3.34	0.329(14)	1.158(26)	0.352(19)	35.8(20)
		1.007(13)	1.540(55)	0.292(15)	31.0(60)
		1.067(13)	2.160(50)	0.276(24)	34.0(60)
VF68	2.63	0.460(60)	0.820(95)	0.390(55)	24.8(23)
		0.799(24)	1.805(40)	0.288(19)	39.0(55)
		1.119(21)	1.854(41)	0.262(20)	36.0(55)
VF70	14.08	0.470(55)	0.860(110)	0.420(50)	20.9(18)
		0.836(28)	1.861(38)	0.311(22)	42.0(55)
		1.194(19)	1.929(28)	0.286(16)	38.0(55)

Table 3.S3: Continue

Sample Name	χ^2*	CS*	QS*	L HWHM*	Site Populations (%)
VF74	0.94	0.285(9)	1.027(41)	0.344(19)	51.3(44)
		0.304(15)	1.710(50)	0.252(20)	15.3(36)
		0.841(29)	1.753(46)	0.293(44)	15.0(32)
		1.192(28)	1.870(35)	0.304(24)	18.4(34)
VF75	1.56	0.295(8)	1.211(16)	0.365(11)	65.7(17)
		1.004(16)	1.670(50)	0.337(16)	24.2(28)
		1.081(18)	2.220(55)	0.221(40)	10.1(29)
VF81	1.07	0.41(10)	1.200(120)	0.340(55)	13.2(34)
		0.912(48)	1.470(70)	0.265(39)	24.0(50)
		0.972(22)	2.000(50)	0.250(24)	40.0(50)
		1.295(25)	1.963(45)	0.234(17)	22.9(49)
VF83	2.10	0.316(12)	1.175(25)	0.363(19)	40.5(19)
		1.009(14)	1.581(45)	0.325(16)	34.4(45)
		1.073(10)	2.180(39)	0.270(23)	25.1(38)
VF85	1.91	0.471(30)	1.370(55)	0.211(34)	6.9(16)
		0.839(19)	1.590(50)	0.237(36)	20.7(47)
		1.113(18)	2.297(43)	0.242(24)	26.9(48)
		1.115(14)	1.684(35)	0.264(14)	46.0(55)
VF87	1.31	0.283(10)	1.576(49)	0.285(18)	30.0(50)
		0.293(5)	0.987(32)	0.302(10)	47.3(50)
		1.036(16)	1.851(27)	0.402(16)	22.4(9)
VF88	1.96	0.420(55)	1.150(90)	0.349(39)	17.6(21)
		1.011(11)	1.500(65)	0.295(18)	37.0(65)
		1.068(13)	2.140(55)	0.292(18)	45.0(65)

And uncertainties are in one sigma range standard deviation (1σ) and present in the same way in Table 3.S2.

*All items are the same shortening and units as Table 3.S2 noted,

Table 3.S4: Fit parameters for step-edge normalized XANES pre-edge spectra

Sample	Fe^{2+}				Fe^{3+}			
Name	Intensity*	FWHM	Height	Corrected E_0^{ψ}	Intensity	FWHM	Height	Corrected E_0^{ψ}
APS								
VF3	0.034(0.002)	1.475(0.043)	0.0217(0.0007)	7111.936(0.042)	0.138(0.004)	1.605(0.036)	0.0810(0.0012)	7113.593(0.009)
VF30	0.024(0.003)	1.424(0.073)	0.0159(0.0009)	7111.958(0.012)	0.157(0.002)	1.635(0.014)	0.0903(0.0006)	7113.585(0.000)
VF54	0.072(0.004)	1.500(0.067)	0.0449(0.0009)	7111.838(0.056)	0.085(0.014)	1.553(0.187)	0.0510(0.0021)	7113.527(0.044)
VF59	0.056(0.002)	1.519(0.019)	0.0348(0.0018)	7111.888(0.030)	0.109(0.009)	1.528(0.050)	0.0668(0.0037)	7113.575(0.012)
VF66	0.061(0.002)	1.411(0.032)	0.0406(0.0012)	7111.835(0.015)	0.079(0.002)	1.494(0.059)	0.0496(0.0012)	7113.515(0.006)
VF68	0.072(0.002)	1.454(0.024)	0.0463(0.0010)	7111.822(0.010)	0.059(0.002)	1.507(0.022)	0.0371(0.0010)	7113.467(0.012)
VF70	0.071(0.001)	1.426(0.007)	0.0470(0.0004)	7111.795(0.000)	0.043(0.000)	1.431(0.013)	0.0281(0.0004)	7113.392(0.006)
VF74	0.042(0.001)	1.518(0.013)	0.0260(0.0009)	7111.958(0.000)	0.137(0.001)	1.546(0.009)	0.0832(0.0006)	7113.615(0.006)
VF75	0.045(0.000)	1.489(0.002)	0.0284(0.0000)	7111.925(0.010)	0.134(0.001)	1.533(0.006)	0.0822(0.0003)	7113.595(0.000)
VF81	0.080(0.000)	1.449(0.004)	0.0518(0.0001)	7111.792(0.006)	0.031(0.001)	1.320(0.012)	0.0220(0.0002)	7113.322(0.006)
VF83	0.064(0.007)	1.453(0.012)	0.0411(0.0041)	7111.835(0.010)	0.091(0.010)	1.517(0.015)	0.0560(0.0058)	7113.535(0.010)
VF85	0.085(0.000)	1.465(0.004)	0.0544(0.0002)	7111.805(0.000)	0.028(0.001)	1.271(0.023)	0.0205(0.0002)	7113.305(0.000)
VF87	0.029(0.001)	1.475(0.012)	0.0188(0.0003)	7112.112(0.006)	0.157(0.001)	1.506(0.005)	0.0982(0.0010)	7113.625(0.000)
VF88	0.078(0.001)	1.438(0.007)	0.0507(0.0007)	7111.795(0.000)	0.042(0.001)	1.413(0.007)	0.0278(0.0003)	7113.378(0.006)
NSLS								
VF30	0.023(0.003)	1.464(0.070)	0.0147(0.0011)	7112.022(0.015)	0.141(0.004)	1.681(0.011)	0.0790(0.0019)	7113.629(0.010)
VF35	0.077(0.002)	1.622(0.019)	0.0445(0.0005)	7111.846(0.010)	0.019(0.001)	1.235(0.028)	0.0144(0.0003)	7113.362(0.025)
VF49	0.086(0.001)	1.640(0.017)	0.0492(0.0001)	7111.857(0.006)	0.016(0.001)	1.152(0.033)	0.0131(0.0004)	7113.350(0.006)
VF53	0.028(0.001)	1.463(0.039)	0.0179(0.0003)	7111.955(0.020)	0.120(0.005)	1.675(0.018)	0.0675(0.0026)	7113.622(0.006)
VF54	0.067(0.002)	1.603(0.021)	0.0393(0.0007)	7111.909(0.015)	0.065(0.002)	1.492(0.030)	0.0409(0.0005)	7113.592(0.010)

$^{\psi}$Correction ratio is based on measured LW_ 0 centroid energy and defined LW_ 0$\equiv$7112.3 (*Cottrell et al.*, 2009).

*Integrated pre-edge intensity FWHM: full width at half maximum

APS: Advanced Photon Source NSLS: National Synchrotron Light Source

Table 3.S5: Data Summary

	Sample name	Drift correctted centroid energy	$\frac{I(Fe^{3+})}{I(Fe^{2+})}$	$\frac{I(Fe^{3+})}{I(Fe^{2+})+I(Fe^{3+})}$	$Fe^{3+}/\Sigma Fe$ Wet Chem	$Fe^{3+}/\Sigma Fe$ Mössbauer	C	$Fe^{3+}/\Sigma Fe$ (%) corrected
MORB[&]	All_-15	7112.144(0.010)	0.294(0.010)	0.226(0.006)	n.d.	0.093(0.0060)		9.3(0.60)
	All_-05	7112.217(0.011)	0.372(0.018)	0.271(0.010)	n.d.	0.138(0.0050)		13.8(0.50)
	All_0	7112.279(0.006)	0.478(0.033)	0.323(0.017)	n.d.	0.147(0.0038)		14.7(0.38)
	All_05	7112.355(0.011)	0.550(0.019)	0.354(0.008)	n.d.	0.194(0.0063)		19.4(0.63)
	All_15	7112.511(0.009)	0.780(0.033)	0.438(0.010)	n.d.	0.247(0.0044)		24.7(0.44)
	All_25	7112.740(0.009)	1.243(0.056)	0.554(0.007)	n.d.	0.356(0.0038)		35.6(0.38)
	All_35	7112.937(0.014)	1.822(0.056)	0.645(0.007)	n.d.	0.484(0.0040)		48.4(0.40)
	All_45	7113.163(0.019)	3.060(0.066)	0.754(0.004)	n.d.	0.611(0.0026)	1	61.1(0.26)
Hawaii[&]	LW_-20	7112.112(0.003)	0.265(0.007)	0.209(0.005)	n.d.	0.088(0.0053)		8.8(0.53)
	LW_-10	7112.156(0.002)	0.318(0.014)	0.241(0.008)	n.d.	0.130(0.0058)		13.0(0.58)
	LW_0	7112.299(0.002)	0.447(0.013)	0.309(0.006)	n.d.	0.162(0.0055)		16.2(0.55)
	LW_10	7112.439(0.002)	0.666(0.019)	0.400(0.007)	n.d.	0.235(0.0053)		23.5(0.53)
	LW_20	7112.611(0.008)	0.934(0.024)	0.483(0.006)	n.d.	0.303(0.0140)		30.3(1.40)
Tholeiitic Basalt[v]	IW	7112.06(0.05)	n.d.	n.d.	n.d.	<0.02		2*
	AIR	7113.14(0.05)	n.d.	n.d.	n.d.	0.54(0.02)		54(2)
Rhyolite[&]	568_2	7112.709(0.010)	0.985(0.017)	0.496(0.004)	n.d.	0.238(0.0210)	1.124(0.035)[@]	21.75(2.10)
	DT_46[#]	7113.244(0.010)	2.817(0.132)	0.738(0.009)	0.569(0.0117)[#]	0.600(0.0146)		56.9(1.17)[#]
	DT_39[#]	7112.858(0.041)	1.191(0.085)	0.544(0.018)	0.315(0.0159)[#]	0.320(0.0250)		31.5(1.59)[#]
	H2O_63[#]	7113.298(0.005)	3.645(0.100)	0.785(0.005)	0.596(0.0100)[#]	n.d.	1	59.6(1.00)[#]
	DT_29[#]	7113.454(0.011)	5.786(0.327)	0.853(0.007)	0.806(0.0034)[#]	n.d.		80.6(0.34)[#]
	DT_31[#]	7113.282(0.011)	3.401(0.222)	0.772(0.013)	0.630(0.0073)[#]	n.d.		63.0(0.73)[#]
	DT_18[#]	7113.355(0.005)	4.458(0.116)	0.817(0.004)	0.660(0.0080)[#]	n.d.		66.0(0.80)[#]
Rhyolite[v]	IW	7112.33(0.05)	n.d.	n.d.	n.d.	0.06(0.05)		5.37(5)
	INT	7113.08(0.05)	n.d.	n.d.	n.d.	0.51(0.03)	1.124(0.035)[@]	48.08(3)
	AIR	7113.36(0.05)	n.d.	n.d.	n.d.	0.73(0.03)		70.64(3)
Andesite	IW	7112.06(0.05)	n.d.	n.d.	n.d.	<0.05		4.02*
	INT	7112.63(0.05)	n.d.	n.d.	n.d.	0.35(0.02)	1.256(0.153)[Q]	30.01(2)
	AIR	7113.07(0.05)	n.d.	n.d.	n.d.	0.55(0.02)		49.32(2)

*number listed is only for reference, not counting into fitting

[&]*Cottrell et al.*, 2009

[v]*Dauphas et al.*, 2014

[#]$Fe^{3+}/\Sigma Fe$ determined by wet chemistry in the study of *Moore et al.* (1995), and uncertainties are calculated based on error provided

[@]Correction number determined by Fe^{3+}/Fe^{2+} difference of wet chemistry results and mssbauer results of DT_46 and DT_39.

[Q]*Zhang et al.*, 2015

Chapter 4

Effect of pressure on $Fe^{3+}/\Sigma Fe$ in a mafic magma and consequences for magma ocean redox gradients

This Chapter will submit to Chemical Geology with co-authors Marc M. Hirschmann, Anthony Withers

4.1 Introduction

Owing to its importance to the chemical and physical properties of magmas, the relative concentration of Fe^{2+} and Fe^{3+} in natural and synthetic silicate liquids has received broad attention for at least 30 years (*Sack et al.*, 1981; *Mysen and Virgo*, 1985; *Christie et al.*, 1986; *Dingwell et al.*, 1988; *Lange and Carmichael*, 1989; *Kress and Carmichael*, 1991; *Jayasuriya et al.*, 2004; *Bézos and Humler*, 2005; *O'Neill et al.*, 2006; *Borisov and McCammon*, 2010; *Cottrell and Kelley*, 2011). In natural silicate melts, Fe is commonly the most abundant element with multiple oxidation states, and so the ratio of Fe^{3+} to total Fe, $Fe^{3+}/\Sigma Fe$, not only reflects but in many cases can establish the oxygen fugacity, fO_2 at magmatic conditions. $Fe^{3+}/\Sigma Fe$ ratio increases with fO_2, but also is influenced by melt composition, temperature, and pressure (*Kress and Carmichael*, 1991; *O'Neill et al.*, 2006; *Borisov and McCammon*, 2010). Of these variables, the effect of pressure has been least explored, and consequently Fe^{2+}-Fe^{3+} redox

relationships in magmas at high pressures are poorly constrained.

A pressure dependence to the $Fe^{3+}/\Sigma Fe$ ratio in silicate liquids arises owing to differences in partial molar volumes of Fe_2O_3 and FeO (*Rivers and Carmichael*, 1987; *Kress and Carmichael*, 1991; *Liu and Lange*, 2006; *O'Neill et al.*, 2006). As a consequence, compression or decompression of magmas with fixed $Fe^{3+}/\Sigma Fe$ can create variations in fO_2. For example, *Kress and Carmichael* (1991) and *O'Neill et al.* (2006) noted that basalts ascending from a shallow mantle source become more reduced compared to solid oxide buffers such as quartz-fayalite-magnetite (QFM). Magma oceans represent another environment in which changes in pressure can produce shifts in fO_2 relative to standard buffers. *Hirschmann* (2012) emphasized that redox gradients in magma oceans with fixed $Fe^{3+}/\Sigma Fe$ ratio may control the redox state and mass of early planetary atmospheres. Understanding oxygen fugacity gradients in magma oceans is the chief motivation for the present high pressure experimental study of the influence of pressure on $Fe^{3+}/\Sigma Fe$ ratio in magmas.

4.1.1 Magma oceans and fO_2 gradients

Magma oceans represent a pivotal stage in the chemical and dynamical evolution of terrestrial planets. Reactions between silicate magmas and transiting core-forming metal establish geochemical partitioning between the nascent mantle and core (*Righter*, 2003; *Rubie et al.*, 2003; *Wade and Wood*, 2005; *Rubie et al.*, 2011; *Rubie and Jacobson*, 2015) and large-scale planetary degassing from magma oceans and associated silicate-vapor equilibration creates massive primitive atmospheres (*Matsui and Abe*, 1986; *Zahnle et al.*, 2007; *Elkins-Tanton*, 2008; *Hamada et al.*, 2013). The characters of early atmospheres, in turn, control the time scale of crystallization of magma oceans and therefore have important effects on early planetary evolution (*Abe and Matsui*, 1986; *Elkins-Tanton*, 2008; *Hamada et al.*, 2013).

Oxygen fugacity is an important parameter influencing the composition and mass of atmospheres overlying planetary magma oceans because it controls the relative proportions of oxidized (H_2O, CO_2) and reduced (H_2, CO) species in a high temperature magmatic vapor, and because differential solubility of these species (*Pawley et al.*, 1992; *Hirschmann*, 2012; *Wetzel et al.*, 2013; *Chi et al.*, 2014; *Stanley et al.*, 2014; *Armstrong et al.*, 2015) affects the proportion of volatiles sequestered in the magma ocean (*Hirschmann*, 2012). Further, oxygen fugacity prevailing during silicate-metal separation in magma oceans determines the fraction of atomophile elements (H,C,N) sequestered in the core (*Stevenson*, 1977; *Ohtani et al.*, 2005; *Roskosz et al.*,

2006; *Dasgupta et al.*, 2013) and thereby removed from possible liberation to the atmosphere.

Where silicate in magma oceans reacts with Fe-rich metal, the oxygen fugacity is set by the reaction

$$\mathrm{Fe} + \frac{1}{2}\mathrm{O_2} = \mathrm{FeO_{melt}} \tag{4.1}$$

Such reactions can occur at any depth, and associated pressure and temperature, where metal and silicate equilibrate, but considerations from dynamic models and from siderophile elements establish that the mean pressure of metal-silicate equilibration in the early Earth was high (>25 GPa) (*Li and Agee*, 1996; *Rubie et al.*, 2003; *Chabot et al.*, 2005; *Rubie et al.*, 2011; *Rubie and Jacobson*, 2015). In contrast, silicate melts and overlying atmosphere react at low pressure and the oxygen fugacity may be different at high and low pressure if the magma ocean is well mixed and has a similar $Fe^{3+}/\Sigma Fe$ over a range of depths (*Hirschmann*, 2012). *Righter and Ghiorso* (2012a) also noted that the pressure of metal-silicate equilibration can influence oxygen fugacities.

4.1.2 Effect of pressure on $Fe^{3+}/\Sigma Fe$ ratio in silicate melts

Studies focused on 1 bar relations have elucidated the combined effects of fO_2, temperature, and silicate melt composition on the $Fe^{3+}/\Sigma Fe$ ratio of both natural and synthetic silicate liquids (*Sack et al.*, 1981; *Kilinc et al.*, 1983; *Kress and Carmichael*, 1988; *Helgason et al.*, 1989; *Jayasuriya et al.*, 2004; *Partzsch et al.*, 2004; *Borisov and McCammon*, 2010). The effect of pressure has been investigated indirectly through low pressure measurements of FeO and Fe_2O_3 volumetric properties (*Lange and Carmichael*, 1987; *Rivers and Carmichael*, 1987; *Dingwell et al.*, 1988; *Kress and Carmichael*, 1991). Direct studies of the effect of pressure include determinations of $Fe^{3+}/\Sigma Fe$ ratios of silicate glasses quenched from high pressure experiments (*Mysen and Virgo*, 1985; *O'Neill et al.*, 2006).

Low pressure measurements of partial molar volumes, thermal expansivities, and compressibilities (*Lange and Carmichael*, 1987; *Rivers and Carmichael*, 1987; *Kress and Carmichael*, 1991) allow calculation of the influence of pressure on the fO_2 of magmas with fixed $Fe^{3+}/\Sigma Fe$ ratio (*Kress and Carmichael*, 1991). Owing to a smaller molar volume/atom of FeO compared to Fe_2O_3, compression stabilizes FeO, resulting in higher fO_2 at fixed $Fe^{3+}/\Sigma Fe$ ratio. The same, of course, is true for oxide-oxide or metal-oxide buffers such as QFM or iron-wüstite (IW), but the effect is more pronounced in melts, such that a basalt with fixed $Fe^{3+}/\Sigma Fe$ ratio

becomes more oxidized relative to QFM or IW with increased pressure (*Kress and Carmichael*, 1991).

Mysen and Virgo (1985) performed experiments up to 4 GPa and found $Fe^{3+}/\Sigma Fe$ ratios in Na_2O-FeO-Fe_2O_3-SiO_2 liquids to diminish dramatically with increasing pressure according to a trend that is far greater than that predicted by the thermodynamically-derived model of *Kress and Carmichael* (1991). However, oxygen fugacity was not buffered directly in these experiments. *O'Neill et al.* (2006) quenched glasses from andesitic melts annealed at 1400 °C and buffered by the coexistence of Ru and RuO_2 (*O'Neill and Nell*, 1997). With increasing pressure, observed $Fe^{3+}/\Sigma Fe$ diminished from 0.80 at 0.4 GPa to 0.71 at 3 GPa. *O'Neill et al.* (2006) coupled their results to the 1 bar relationship calibrated by *Jayasuriya et al.* (2004) to formulate an equation of state which predicts a pressure dependence to $Fe^{3+}/\Sigma Fe$ ratio that is qualitatively similar to the model formulated by *Kress and Carmichael* (1991).

The effect of pressure on $Fe^{3+}/\Sigma Fe$-fO_2 relations in silicate melts is linked to the coordination of Fe^{2+} and Fe^{3+} ions. For mafic silicate melts at low pressure, the average coordination of Fe^{2+} is usually close to V (*Wilke et al.*, 2005, 2006, 2007) and for the andesitic glass investigated in this study, XANES and Mössbauer spectroscopy suggest that it is near 5.5 (Chapter 3). Fe^{3+} apparently takes on multiple coordination states at low pressure, with IV being most common, but some evidence for V and VI as well (*Wilke et al.*, 2006; *Giuli et al.*, 2011) and for the andesite composition investigated here, Mssbauer and XANES investigations are consistent with average coordination close to 5 (Chapter 3). With increasing pressure, more highly coordinated geometries are favored. For example, in situ X-ray diffraction of molten fayalite shows that mean coordination of Fe^{2+} increases from 4.2±0.2 at ambient pressure to 7.2±0.3 at 7.5 GPa (*Sanloup et al.*, 2013). Pressure should also favor increases in Fe^{3+} coordination, as the partial molar volume of VI-coordinated Fe^{3+} in silicate melts is 25% smaller than that of IV Fe^{3+} (*Liu and Lange*, 2006). We are not aware of any in situ studies pertaining to the coordination of Fe^{3+} in high pressure melts, but Mössbauer investigations of Na_2O-Fe_2O_3-SiO_2 glasses quenched from 0-4 GPa may be consistent with gradual increases in Fe^{3+} coordination (*Brearly*, 1990). However, the changes also may be attributable to shifts in bond angles, similar to those that are chiefly responsible for the anelastic compression effects observed for (MAS, CAS) glasses *Allwardt et al.* (2005). At pressures beginning around 8-10 GPa, Fe^{3+} is stabilized in high coordination environments in minerals such as garnet, wadsleyite, and (MgFe)SiO_3 perovskite (*ONeill et al.*, 1993; *McCammon*, 1997; *Frost et al.*, 2004; *Rohrbach et al.*, 2007), and

so it is reasonable to speculate that this may also occur in silicate melts (*Hirschmann*, 2012).

To further understand the influence of pressure on the relationship between $Fe^{3+}/\Sigma Fe$ ratio and oxygen fugacity, we have quenched glasses from a range of pressures up to 7 GPa and analyzed them by Mössbauer and XANES spectroscopy. We apply the results to understanding gradients in oxygen fugacity in a well-mixed column of magma and the consequences for the compositions and masses atmospheres associated with magma oceans on terrestrial planets.

4.1.3 Effect of quenching on observed $Fe^{3+}/\Sigma Fe$ ratios and glass structure

An important question is whether the glasses quenched under experimental conditions record the $Fe^{3+}/\Sigma Fe$ ratios and melt structure established at high temperature and high pressure. Many studies have documented the comparatively rapid migration of redox fronts through amorphous silicates exposed to strong gradients in oxygen fugacity (e.g., *Cooper et al.*, 1996; *Gaillard et al.*, 2002, 2003a,b). However, these considerations likely do not apply to the present experiments because (a) the quenching rate is too high and because, (b) unlike quenching from 1 atmosphere, the mechanism of quench in high pressure experiments does not involve exposure to a gradient in fO_2.

The quench rates in the piston cylinder and multianvil devices at Minnesota range from 125 K/s to 340 K/s (Fig. 4.1), resulting in cooling through the glass transition ($\sim$1000 K, *Neuville et al.*, 1993) in 2-6 seconds. These are comparable to the fastest cooling rate imposed by *Dyar et al.* (1987), who observed no measurable differences in $Fe^{3+}/\Sigma Fe$ ratios for basalt or andesite quenched from 1 atmosphere furnaces at rates of 300 K/s and 70 K/s. The quench rates in the present study are also more rapid than the range (150 K/s, $>$2.5 K/s and $<$0.02 K/s) imposed by *Wilke et al.* (2002) across the glass transition for a hydrous Fe-bearing haplotonalite. They observed shifts in $Fe^{3+}/\Sigma Fe$ ratio only for the slowest quenching rate explored, suggesting that $Fe^{3+}/\Sigma Fe$ ratio is preserved during quenching ($>$2.5 K/s) that is comparatively slow compared to the present study. We note, however, the experiments of *Wilke et al.* (2002) were not buffered, and it is not clear whether variations in $Fe^{3+}/\Sigma Fe$ ratio between samples are owing to cooling rates or other effects.

A related question is whether the structural features of the quenched glass, such as the coordination state of the Fe^{2+} and Fe^{3+} ions, represent those present in the liquid. Indeed, some features of high pressure liquids are not quenched in recovered glasses (*Williams and Jeanloz*, 1988), but those chiefly responsible for melt densification, such as metal-oxygen coordination

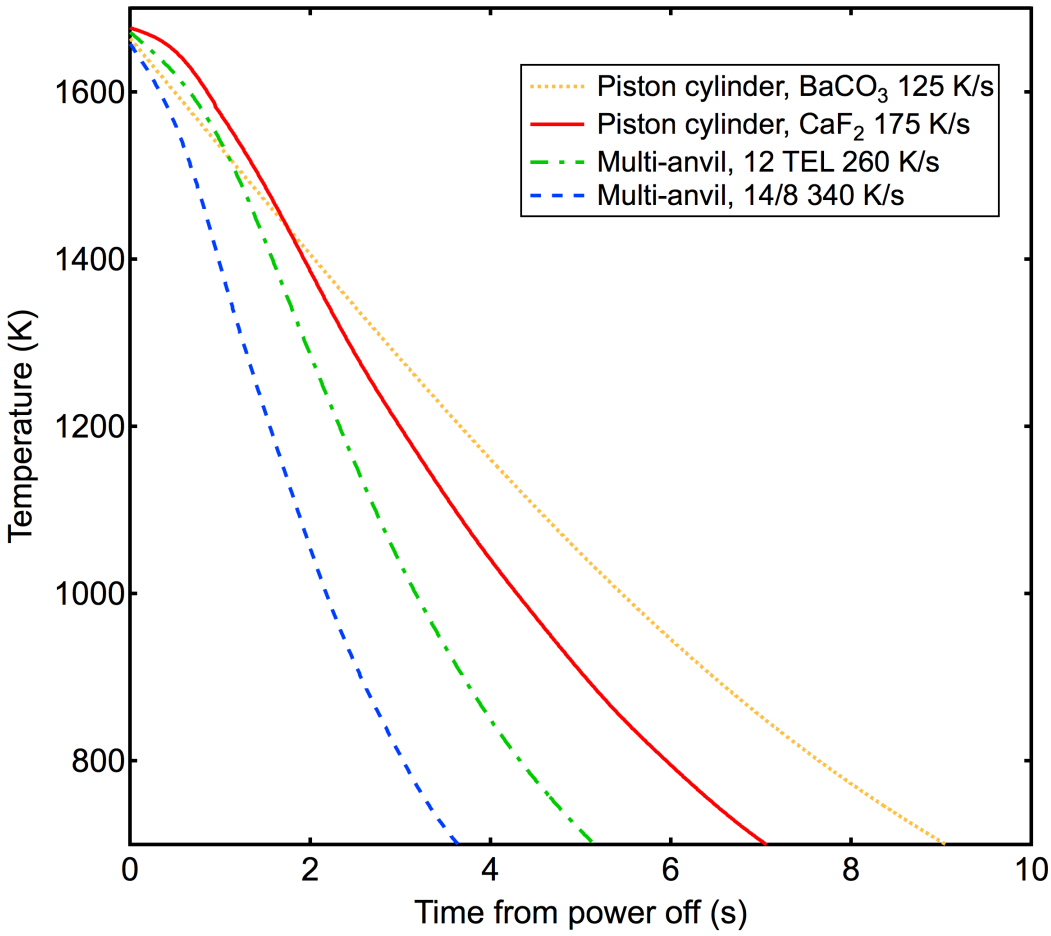

Figure 4.1: Temperature-time relations recorded at the thermocouple during quenching for the solid media devices at the University of Minnesota. Mean quench rates are 340 °C (multianvil 14/8 assembly), 260 °C (multianvil 18/12 assembly), 175 °C (piston cylinder, CaF_2 pressure cell), and 125 °C/s (piston cylinder, $BaCO_3$ cell)

and bond angles, may be preserved (*Allwardt et al.*, 2005). Judging from Mössbauer center shifts and quadrupole splittings, *Dyar et al.* (1987) found no appreciable structural differences in Fe^{2+} and Fe^{3+} environments between andesitic glasses quenched at 300 and 70 K/s, but did detect differences for a third glass quenched at a slow, poorly quantified rate, and between basalt glasses quenched at variable rates. *Wilke et al.* (2002) and *Rossano et al.* (2008) found similar center shifts and quadrupole splittings for haplotonalite glasses quenched rapidly and slowly, but observed considerable line narrowing for those quenched at $<$0.02 K/s, likely owing to formation of nanocrystalline Fe-oxides (*Wilke et al.*, 2006). Thus, some structural features of rapidly quenched glasses may be indicative of high temperature high pressure melt structure, but such features should be interpreted with care.

Studies showing rapid change in $Fe^{3+}/\Sigma Fe$ ratio in silicate melts (*Cooper et al.*, 1996; *Gaillard et al.*, 2002, 2003a,b), invariably involve exposing the melt to a strong redox gradient. This is also true for studies of $Fe^{3+}/\Sigma Fe$ ratio changes on quench when the experiments are conducted at ambient pressure. For example, melts quenched from 1 atmosphere furnaces in air, gas (Ar-H_2), or a brine (e.g., *Dyar et al.*, 1987). Large redox gradients are not present during quenching from high pressure solid media apparatuses, as cooling occurs in a nearly isochemical environment by conduction to the large thermal mass of water-cooled carbide. Even if such gradients were imposed on the experimental charge, their penetration into the melts would be minimal at the quench rates of solid media devices. For example, the most rapid diffusion is associated with the migration of hydrogen, which according to the rate law of (*Gaillard et al.*, 2003b) should penetrate less than 1 micron at 1400 °C over the 2-6 seconds required for glass quenching in multianvil or piston cylinder devices (Fig. 4.1). We conclude that quench modification of $Fe^{3+}/\Sigma Fe$ ratio owing to reaction with the surrounding environment is not likely to be relevant to glasses quenched in solid media devices.

Additionally, $Fe^{3+}/\Sigma Fe$ ratios of quenched glasses may differ from those of their precursor liquids if redox reactions with other dissolved heterovalent species occur during cooling through the glass transition. For example, *Berry et al.* (2006) found that Cr^{2+} present in basaltic melts oxidized to Cr^{3+} during quenching owing to a reaction between Cr and Fe ions, Cr^{2+}+Fe^{3+} $\longrightarrow$$Cr^{3+}$+$Fe^{2+}$. Such reactions would therefore also affect $Fe^{3+}/\Sigma Fe$ ratios of glasses. This problem should be considered carefully if materials contain appreciable concentrations of elements that may change valence over the span of oxidation states to be investigated (e.g., Cr, V,

Mn, S), but these were excluded from our starting materials. Some amount of C in experimental glasses is unavoidable, but we do not expect this to be a major problem because changes in valence of dissolved C occur only under conditions at or below stabilization of graphite (e.g., *Stanley et al.*, 2014), which are much more reducing than the oxidizing conditions in the present study.

4.2 Methods

The starting material for the this project consists of a synthetic andesite (Table 4.S1) similar in composition to that used by *O'Neill et al.* (2006), and was prepared from reagent oxides (SiO_2, Al_2O_3, Fe_2O_3, TiO_2, MgO), silicates ($CaSiO_3$,Na_2SiO_3) and stoichiometric glasses (sanidine). The Fe_2O_3 consisted of 70% normal reagent oxide and 30% $^{57}Fe_2O_3$ (Isoflex, Inc). Prior to weighing, the SiO_2, Al_2O_3, TiO_2, and MgO were devolatilized by heating in a furnace at 1000 °C overnight, until the weight stabilized. These reagents were then weighed and mixed by grinding in an agate mortar and pestle under ethanol for at least one hour until the grinding sound vanished and then again devolatilized by firing at 1000 °C for 48 hrs. Finally, the Fe_2O_3 sources, which had been dried at 800 °C for 1 hour and then weighed, were mixed in by grinding under ethanol. All the starting materials were stored in a vacuum oven.

Experiments were conducted in 2 or 3 mm diameter Pt capsules, which were sealed by welding (Table 4.1). All capsules were packed with 80% silicate starting material and 20% of a mixture consisting of equal proportions Ru and RuO_2 and loaded as layers on both the bottom and top of the capsule, producing a sandwich arrangement (Fig. 4.2). Ru/RuO_2 buffers the oxygen fugacity, imposing conditions close to that of the magnetite/hematite buffer (*O'Neill and Nell*, 1997), which is sufficiently oxidizing that loss of Fe to the Pt capsule is negligible. RuO_2 has negligible solubility in andesitic melt ($<$100 ppm) (*O'Neill et al.*, 2006).

4.2.1 Experimental Apparatus

A single experiment (VF1) using a sealed 2mm Pt capsule with Ru+RuO_2 buffer at top and bottom was conducted in a Deltech VT28 vertical gas mixing furnace, at 1400 °C and 1 atm, as measured by a Type S ($Pt_{90}Rh_{10}$/Pt_{100}) thermocouple, and lasting 4 hrs (Table 4.1). Temperature uncertainties are believed to be $\pm$5 °C based on calibration against Au melting, which was

Table 4.1: Experimental Conditions

NO.	T (^{o}C)	P (GPa)	D (hrs)	Themo-couple Type	Capsule Diameter	Pressure Apparatus	Iron valence
Time Series							
A839	1400	1.5	1	D	3	PC	3+
A840	1400	1.5	4	D	3	PC	3+
A841	1400	1.5	24	D	3	PC	3+
A843	1400	1.5	24	D	3	PC	2+
A844	1400	1.5	4	D	3	PC	2+
A846	1400	1.5	1	D	3	PC	2+
A848	1400	1.5	24	D	3	PC	2+
A853	1400	1.5	12.5	D	3	PC	3+
A855	1400	1.5	24	D	3	PC	3+
A857	1400	1.5	0.167	D	3	PC	3+
A860	1400	1.5	0.167	D	3	PC	2+
A862	1400	1.5	0.167	D	3	PC	3+
A863	1400	1.5	12	D	3	PC	2+
Variable Pressure Series							
A867	1500	1.5	4	D	2	PC	3+
A888	1400	3	4	D	2	PC	3+
A896	1400	2	4	D	2	PC	3+
A944	1500	3	4	D	2	PC	3+
A945	1500	2	4	D	2	PC	3+
A952	1500	2.5	4	D	2	PC	3+
B388	1400	2.5	4	D	2	PC	3+
B402	1400	1.5	4	D	2	PC	3+
M535	1600	4	4	D	2	MA	3+
M537	1600	5	4	D	2	MA	3+
M540	1600	3	4	D	2	MA	3+
M543	1600	4.5	4	D	2	MA	3+
M544	1600	3.5	4	D	2	MA	3+
M559	1750	7	0.2	D	2	MA	3+
M562	1750	6	0.2	D	2	MA	3+
M563	1750	5	0.2	D	2	MA	3+
M572	1750	6.5	0.2	D	2	MA	3+
M601	1750	5.5	0.2	B	2	MA	3+
VF1	1400	0.0001	4	S	2	VF	3+

PC: Piston Cylinder MA: Multi Anvil VF: Vertical Furnace

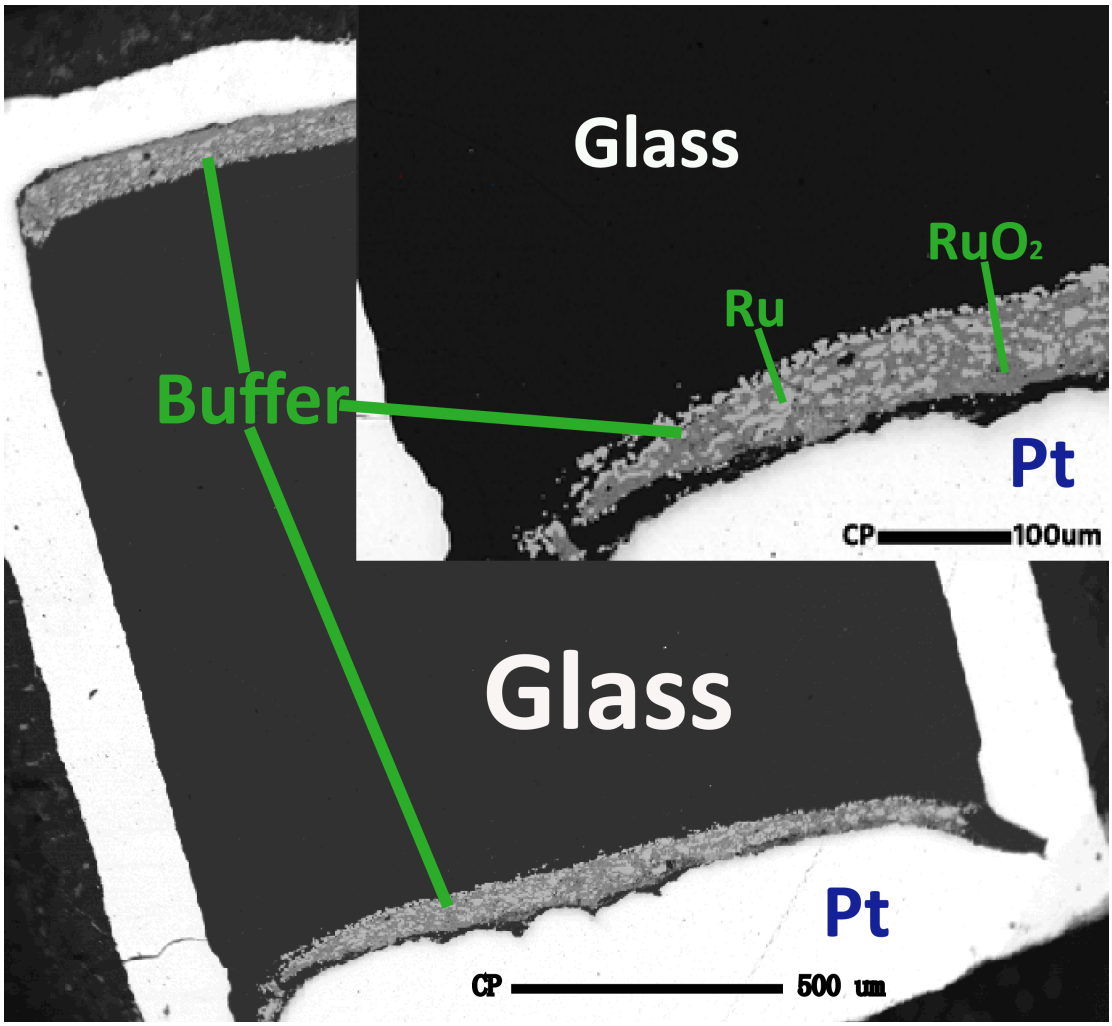

Figure 4.2: Back-scattered electron image of sample M537, which was performed at 5 GPa, 1600 °C, is an example shows the both Ru and RuO_2 phases coexist with andesite glass in a Pt capsule. All other samples have same capsule structure.

observed at a thermocouple reading of 1059 °C. The VF1 glass was quenched by being put into cold water within seconds.

Experiments up to 3 GPa were performed in a half-inch, end-loaded piston cylinder (PC) apparatus, using the assembly and the temperature and pressure calibrations documented by *Xirouchakis et al.* (2001). Temperature was measured by Type B ($Pt_{70}Rh_{30}/Pt_{94}Rh_6$) or Type D ($W_{97}Re_3/W_{75}Re_{25}$) thermocouples (Table 4.1). Experiments from 3.5 -7 GPa were performed in a 1000-ton Walker-style multi-anvil device (MA) with an 18/12 (octahedral edge length/WC truncation edge length) assembly described and calibrated by *Dasgupta et al.* (2004). Temperature was controlled with a Type D ($W_{97}Re_3/W_{75}Re_{25}$) thermocouple positioned immediately above the capsule and oriented axially with respect to the heater. Pressure uncertainties are believed to be $\pm$0.3 GPa, and temperature uncertainties are believed to be $\pm$10 °C (*Dasgupta et al.*, 2004). For both piston cylinder and multi-anvil experiments, durations were 4 hours at temperatures of 1400-1600 °C and 12 minutes at 1750 °C (Table 4.1). Several glass chips were removed from each experiment and double-sided polished for optical examination, XANES, and electron microprobe analyses, while the remainder was ground to powder and mixed with sugar for Mössbauer spectroscopy.

Previous investigations of the approach to Fe^{2+}-Fe^{3+} equilibrium in silicate liquids includes the study of *Thornber et al.* (1980) and *Kilinc et al.* (1983) who showed, 5 hours is sufficient for the $Fe^{3+}/\Sigma Fe$ ratio to reach steady state at 1200 °C for a basalt and 1350 °C for an andesite, respectively. Five hours was also sufficient for $Fe^{3+}/\Sigma Fe$ ratio in supercooled melts of a pyroxene composition to reach steady-state at 650$\pm$50 °C (*Magnien et al.*, 2004). To determine appropriate experimental times for our specific composition with the Ru+RuO_2 buffer, we conducted a time series of reversal experiments at 1400 °C and 1.5 GPa (Table 4.1). In addition to the starting mixture, for which all Fe is initially Fe^{3+}, we also employed a reduced version of the starting mixture in which the initial Fe was nearly entirely Fe^{2+}. This latter mixture was prepared in a 1 atmosphere gas mixing horizontal furnace in an Fe doped Pt crucible with CO_2/CO at QFM-1, 1000 °C for 12 hrs. As shown in Fig. 4.3, the $Fe^{3+}/\Sigma Fe$ ratio of the quenched glass converges to a constant ratio after 2 hours, with most of the change towards equilibrium occurring within 10 mins. Based on this result, we conducted experiments between 1400 and 1600 °C for 4 hours. In order to prevent multi-anvil failures, experiments at 1750 °C were conducted for only 12 minutes, but considering the much faster reaction expected at hotter conditions and the results from 10 minutes at 1400 °C (Fig. 4.3) the high temperature

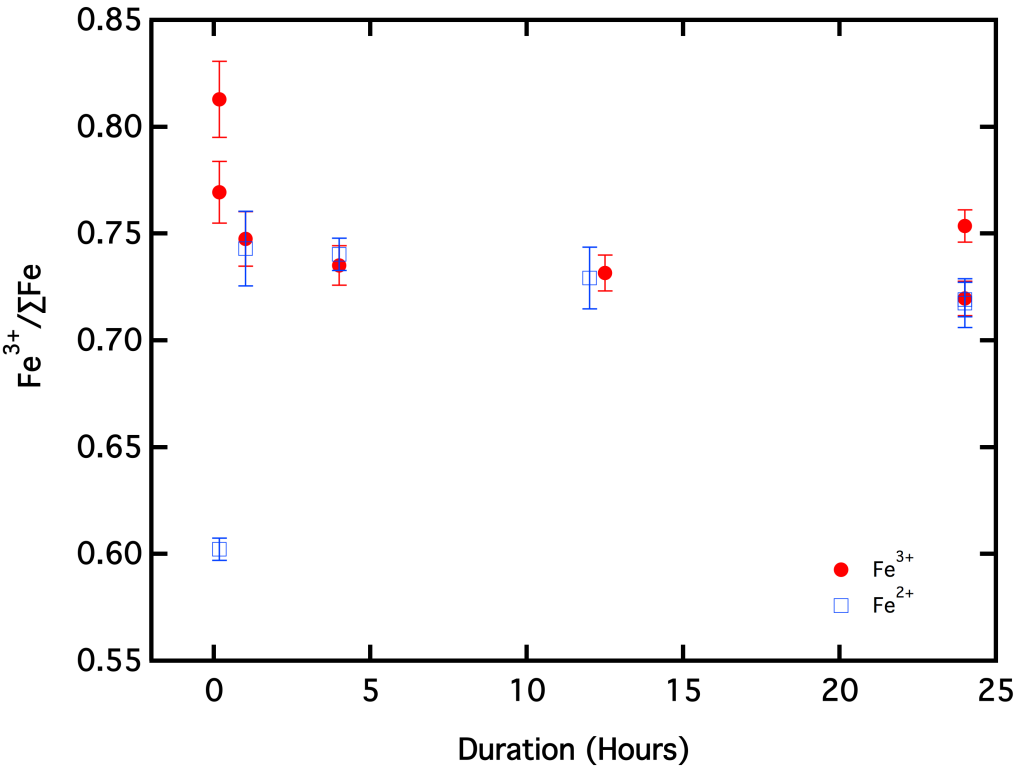

Figure 4.3: Average $Fe^{3+}/\Sigma Fe$ ratios obtained from Mssbauer spectra with different fit processors and collected with different scale at room temperature change with experimental duration. Red dots and blue squares refer to starting materials from oxides mixture contain pure ferric iron and was reduced with gas mix furnace at IW+1, 1000 °C for 12 hrs.

experiments likely also approached equilibrium.

4.2.2 Analytical Methods

Electron Microprobe

Quenched glasses were examined by powder X-ray diffraction (XRD) to verify that they consisted only of amorphous silicate. Experimental textures were also examined by back-scattered electron (BSE) and secondary electron imaging (SEI) on using the JEOL JXA8900R EMPA at the University of Minnesota according to procedures detailed in *Zhang et al.* (2015). Major element concentrations of quenched glasses were determined by wave-length-dispersive EMPA and listed in Table **??**. MPI-DING glass, ATHO-G *Jochum et al.* (2006) and USGS

glasses BCR-2G and BIR-1G *Jochum et al.* (2005) were analyzed as secondary standards before and after each sample analysis session, as well as interspersed between each 4 or 5 samples individual sample analyses; this procedure ensured that the electron beam was stable. The intensity data of standards, secondary standards and unknown samples were checked for time dependent intensity (TDI) changes and values for Si kα and Na kα were corrected using a self-calibrated function; no TDI effect was detected for other elements.

Mössbauer Spectroscopy

Mössbauer spectra were collected using a constant acceleration Ranger spectrometer at the Institute for Rock Magnetism, University of Minnesota, and the measurements were carried out with a ^{57}Co/Rh source and a pure Fe foil calibrant at room temperature (293 K). Data were collected over 512 channels, which were then folded to produce 256 unique channels. All spectra were collected over at least one day and until sufficient ($>$1000,000 counts / channel) were accumulated to minimize statistical error. Sample mounts consisted of powdered glass mixed with powdered sugar evenly distributed in an approximately circular shape of diameter 12.7 mm. The absorber thickness were adjusted for an absorber density of $\sim$2 mg/cm^2 Fe.

All spectra have broadened line-shapes typical of silicate glasses and were fitted using distribution methods (*Alberto et al.*, 1996; *Rossano et al.*, 1999; *O'Neill et al.*, 2006; *Rossano et al.*, 2008; *Borisov and McCammon*, 2010; *Zhang et al.*, 2015). All Mössbauer spectra were fitted with a 2D distribution Extended Voigt based fitting (xVBF) method with the RECOIL software package (*Lagarec and Rancourt*, 1997) and hyperfine parameters with their 1 uncertainties are listed in Tables 4.S2, 4.S3 and 4.S4.

Most of Mössbauer spectra we collected consist chiefly of two quadrupole doublets, one each originating from paramagnetic ferric and ferrous iron. For those spectra (like Fig. 4.4a), there is no obvious evidence of sextets at 12 mm/s. Thus, the Fe ions in those glasses are dominated by paramagnetic Fe^{2+} and Fe^{3+} and the fit process is the same as that described in *Zhang et al.* (2015). Each doublet was fit as a 2D distribution, whose parameters consist of the center shift (CS), the quadrupole splitting (QS), and their respective Gaussian widths, δ_{CS} and δ_{QS} (Table 4.S4). Ferric δ_{CS} and the correlation between the δ_{CS} and δ_{QS} (ρ) are assumed to be 0, because the analysis of *Alberto et al.* (1996) showed that these should be effectively negligible for Fe^{3+} in silicate glasses in low concentrations (5 15 wt.% Fe_2O_3). The fit of the Fe^{2+} paramagnetic component considers these correlations.

The spectra of 4 of 32 glasses include, in addition to the paramagnetic doublets, an obvious sextet (Fig. 4.4b). Such sextets are commonly present in quenched mafic glasses (*Jayasuriya et al.*, 2004; *O'Neill et al.*, 2006; *Borisov and McCammon*, 2010) and are indicative of a ferromagnetic component. Thus we use the same fit philosophy for paramagmetic sites and for magnetic sextet site, parameters including CS, QS, hyperfine magnetic field (H) and its Gaussian width ($delta_{\mathrm{H}}$) are used (Table 4.S3 and Table 4.S4).

Additionally, spectra for 14 of the 32 glasses, in addition to the paramagnetic doublets, display a broadened magnetic absorption (Fig. 4.4c and 4.4d), which could owing to a superparamagnetic component observed previously in similar glasses based on magnetic susceptibility measurements (*Zhang et al.*, 2015). For some of those samples from time series, both 12 mm/s and 20 mm/s scale Mössbauer spectra were collected to ensure full accounting for all Fe components in the quenched material (Fig. 4.S1, Table 4.S2, Table 4.S3). All spectra were fitted in two ways: In the first, we fit the magnetic site with a CS value, its Gaussian width (δ_{CS}), QS and the strength of the hyperfine magnetic field (H) (Figs 4.4c, 4.S1a, 4.S1c, and Table 4.S2). In the second the sextets were fit using values for the CS, QS, hyperfine magnetic field (H) and its Gaussian width (δ_{H}) (Figs. 4.4d, 4.S1b, 4.S1d, and Table 4.S3). Resulting $Fe^{3+}/\Sigma Fe$ ratios for glasses from the time series (Table 4.S2 and Table 4.S3) do not vary with data collection using different velocity scales. We can use these glasses to monitor the influence of the magnetic site on the fits by plotting the resulting $Fe^{3+}/\Sigma Fe$ on the area proportion of each spectra that is in the magnetic sub-site (P_M). When PP_M $<35\%$, the fit results are consistent between the two fit methods, but in cases where P_M is $>35\%$, the difference between two fit methods is noticeable (Fig. 4.S2). For variable pressure series glasses, none of them have P_M fractions$>35\%$ and we chose the second fitting method (Table 4.S4).

X-ray absorption near edge structure (XANES)

Fe K-edge XANES spectra of glass chips were collected at station X26A of the National Synchrotron Light Source (NSLS), Brookhaven national lab (BNL) using a 95 m spot and at beamline 13-IDE at the Advanced Photon Source (APS), Argonne National Lab (ANL) using 2×2 m or 25×25 m spots. A minimum of 3 spectra were collected on each andesitic glass. All spectra were collected in fluorescence mode. 7112 eV and 7110.7 eV were set up as the first derivative peak for Fe foil at NSLS and APS, respectively, which defined the energy calibration for the system. Spectra were recorded with four energy regions previously defined by *Cottrell*

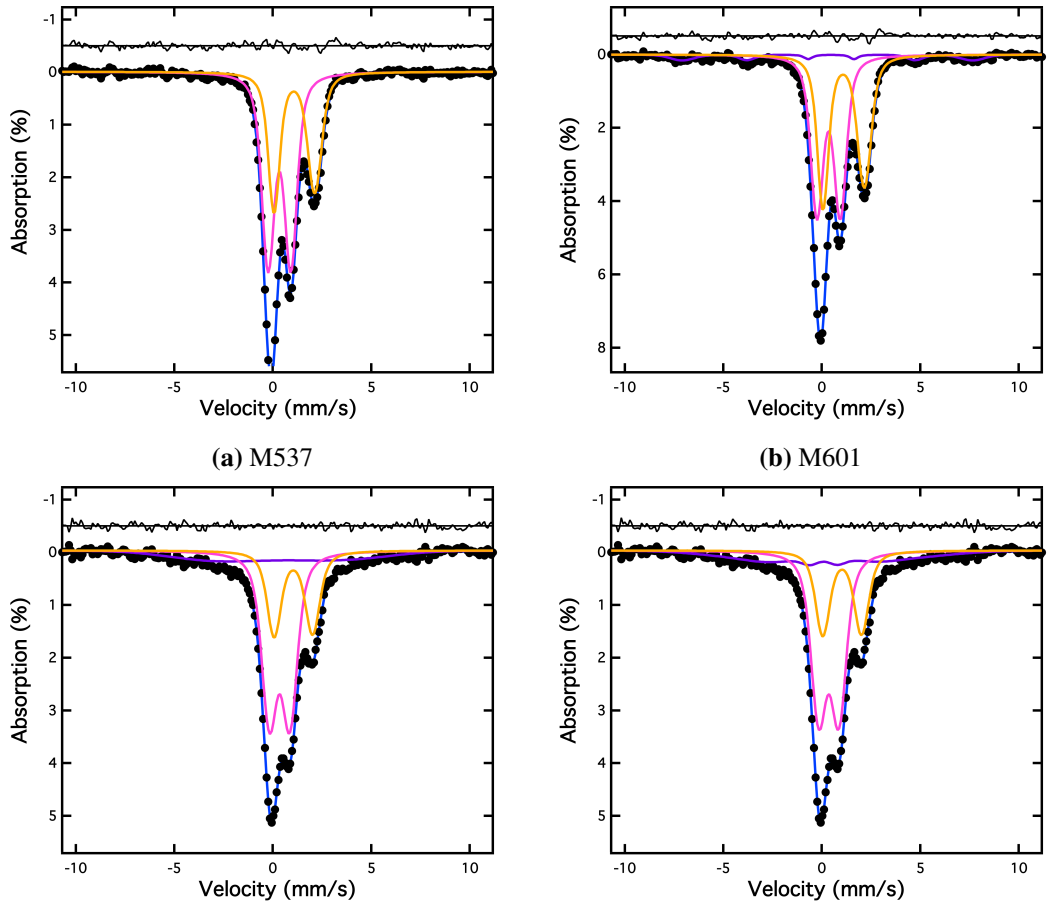

(a) M537 **(b)** M601

(c) B402 **(d)** B402

Figure 4.4: Examples of Mössbauer spectra and their fits. a) M537 fitted with only paramagnetic sites b) M601 fitted with paramagnetic sites and a sextet magnetic site; c) B402 fitted with paramagnetic sites and a broaden magnetic site; d) B402 fitted with paramagnetic sites and a sextet magnetic site. For all spectra, the pink curves refer to the paramagnetic Fe^{3+} doublets, the orange curves refer to the paramagnetic Fe^{2+} doublets, and the blue curves are the superposition of all the sites. For b), c) and d), the purple curves refer to the magnetic site.

et al. (2009) and Zhang et al. (in prep.) for NSLS and APS, respectively. At both X26A and 13IDE, the monochromated beam energy drifts with time and so measurements of glass LW_0 (7112.3 eV, *Cottrell et al.*, 2009), repeated after every 2 or 3 hours, were used to correct measured features, including the pre-edge centroid energy as well as the positions of the sub-features attributed to Fe^{3+} and Fe^{2+}. A more complete account of spectral collection and fitting details is given in Chapter 3. All corrected parameters resolved from fits are listed in Table 4.S5.

4.3 Results

4.3.1 Major element compositions of glasses

Electron microprobe analyses indicate all quenched glasses have similar compositions close to that of the original andesite. The average and 1 standard deviations of the 32 analyzed glasses are 57.55±0.55 wt% SiO_2, 2.65±0.09 wt% TiO_2, 15.16±0.13 wt% Al_2O_3, 2.25±0.09 wt% MgO, 7.54±0.13 wt% CaO, 1.01±0.04 wt% K_2O, 8.81±0.21 wt% FeO*, 4.65±0.20 wt% Na_2O (Table 4.S1).

4.3.2 $Fe^{3+}/\Sigma Fe$ ratio determinations from Mössbauer Spectroscopy

Proportions of Fe^{3+} and Fe^{2+} are calculated from the areas of their sub-spectra, which are listed in Table S2, S3 and S4. For andesitic glasses of the same compositions as those studied here, *Zhang et al.* (2015) showed that the relative abundances of Fe^{3+} and Fe^{2+} in quenched glasses must be corrected for the effects of recoilless fractions according to a correction number C, in which the ratio of Fe^{3+} and Fe^{2+} ions in a sample, $\frac{N(Fe^{3+})}{N(Fe^{2+})}$, is related to the areas of the associated paramagnetic doublets $\frac{AA(Fe^{3+})}{AA(Fe^{2+})}$,

$$\frac{AA(Fe^{3+})}{AA(Fe^{2+})} = C\frac{N(Fe^{3+})}{N(Fe^{2+})} \tag{4.2}$$

Zhang et al. (2015) found values of C of 1.151±0.118 and 1.256±0.153, respectively, for glass quenched from high and ambient pressures, presumably owing to different structures and densities of these glasses, and so we apply these former value for all the glasses in this study except for the lone ambient pressure glass, VF1, for which we apply the latter value. The uncorrectedand corrected $Fe^{3+}/\Sigma Fe$ ratios of quenched glasses are listed in Table 4.2.

Table 4.2: $Fe^{3+}/\Sigma Fe$ ratios determined from Mössbauer spectra collected at room temperature

No.	$Fe^{3+}/\Sigma Fe$ *	C#	Correctted $Fe^{3+}/\Sigma Fe$ &
A867	68.80(3.00)		65.70(3.00)
A888	68.20(0.77)		65.08(0.77)
A896	70.10(0.54)		67.07(0.54)
A944	63.73(0.43)		60.42(0.43)
A945	65.28(0.31)		62.03(0.31)
A952	65.78(0.48)		62.55(0.48)
B388	68.19(0.39)		65.06(0.39)
B402	73.23(3.13)		70.38(3.13)
M535	59.50(0.57)	1.151(0.118)#	56.07(0.57)
M537	59.30(0.67)		55.87(0.67)
M540	61.12(0.57)		57.73(0.57)
M543	60.88(0.56)		57.48(0.56)
M544	60.01(0.51)		56.59(0.51)
M559	53.52(0.66)		50.01(0.66)
M562	54.10(0.66)		50.59(0.66)
M563	56.76(0.99)		53.28(0.99)
M572	52.50(0.88)		48.99(0.88)
M601	55.49(0.88)		52.00(0.88)
VF1	75.30(0.63)	1.256(0.153)#	70.82(0.62)

Uncertainties are in one sigma standard deviation (1σ)
*$Fe^{3+}/\Sigma Fe$ obtained from Mssbauer spectra collected at room temperature
#Correction Number from Zhang et al. (2015)
&$Fe^{3+}/\Sigma Fe$ corrected with C through equation
$(Fe^{3+}/\Sigma Fe)_{corrected} = (Fe^{3+}/\Sigma Fe) / [(Fe^{3+}/\Sigma Fe) + C*(1-Fe^{3+}/\Sigma Fe)]$

Values $Fe^{3+}/\Sigma Fe$ ratios of andesite liquids buffered by Ru-RuO_2 decreases as pressure increases (Fig. 4.5), as previously observed by *O'Neill et al.* (2006). Three experiments, all at 1400 °C, were performed at the same conditions as experiments by *O'Neill et al.* (2006) and these allow direct comparison of experimental and analytical results between the two studies. At 1.5 GPa, experiment B402, has the same $Fe^{3+}/\Sigma Fe$ ratio within uncertainty, 73.23±3.13 (Table 4.2) as the correlative experiment from *O'Neill et al.* (2006) (73.4±1.0). in *O'Neill et al.* (2006). However those at 2 GPa (A896), and 3 GPa (A888) have slightly different $Fe^{3+}/\Sigma Fe$ ratios from the analogous experiments performed by *O'Neill et al.* (2006) (70.10±0.54 vs. 72.1 at 2 GPa and 68.20±0.77 vs. 70.8 at 3 GPa, respectively). These differences may reflect problems with precision when sextets are present in the spectra, as is the case that sextets exist in all

spectra from *O'Neill et al.* (2006), while we observed sextet exists in B402 spectra, not A896 and A888 (Table 4.S4).

4.3.3 XANES spectra of andesitic glasses

Fe kα XANES spectra can reflect electron transitions, oxidation state and coordination information. Features of the XANES pre-edge can be calibrated to give quantitative $Fe^{3+}/\Sigma Fe$ of silicate glasses (*Berry et al.*, 2003; *Wilke et al.*, 2005; *Botcharnikov et al.*, 2005; *O'Neill et al.*, 2006; *Cottrell et al.*, 2009; *Cottrell and Kelley*, 2011; *Dauphas et al.*, 2014; Chapter 3), but because the pre-edge also depends on bonding characteristics such as Fe-O coordination (*Wilke et al.*, 2005; Chapter 3), calibrations based on glasses quenched from low pressure are not necessarily applicable to glasses quenched from high pressure. Consequently, the XANES spectra collected in this study can be used to infer the effects of pressure on typical bonding environments of Fe^{2+} and Fe^{3+} in quenched andesitic glasses. Relationships between pre-edge spectral features and $Fe^{3+}/\Sigma Fe$ can also be interpreted with the aid of Mössbauer spectra also collected on these glasses.

Representative XANES pre-edge spectra are presented in Fig. 4.6. Deconvolution of the pre-edge into centroids and relative areas of sub-peaks attributable to Fe^{2+} and Fe^{3+} was calculated according to the methods of *Cottrell et al.* (2009), and fit parameters are listed in Table 4.S5.

Spectra for samples collected at both NSLS and APS give the same centroid positions, which are the weighted energies of the entire pre-edge, area within 1 sigma standard deviation (Fig. 4.S3 , Table 4.S5). For glasses quenched from 1.5 to 7 GPa and $Fe^{3+}/\Sigma Fe$ ratios determined from Mössbauer spectroscopy ranging from 0.49 to 0.71, the averaged Centroid Energy varies from 7113.085 to 7113.338 (Table 4.3).

Integrated pre-edge intensity ratios, $\frac{I(Fe^{3+})}{I(Fe^{2+})}$, from pre-edge XANES spectra collected at NSLS are systematically smaller by 0.4 than those collected at APS (Fig. 4.S4 , Table 4.S5). Although these differences are similar to the analytical uncertainties for individual determinations, in Fig. 4.7, we use only the $\frac{I(Fe^{3+})}{I(Fe^{2+})}$ acquired at APS, owing to most of the data for low pressure andesitic glasses (Zhang et al. in prep) were acquired only at APS Trends of $\frac{I(Fe^{3+})}{I(Fe^{2+})}$ versus $Fe^{3+}/\Sigma Fe$, determined from Mössbauer spectroscopy, are distinct for high pressure and ambient pressure andesitic glasses (Fig. 4.7). The high pressure intensity ratios are described

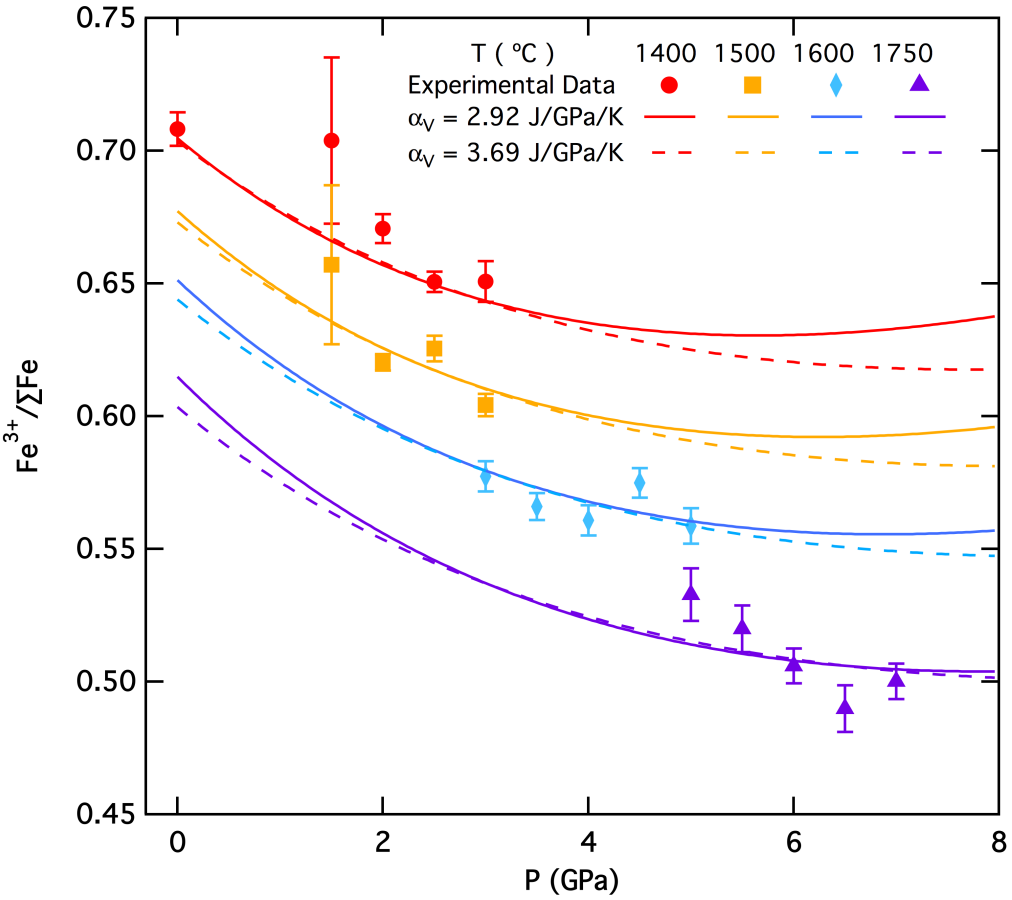

Figure 4.5: $Fe^{3+}/\Sigma Fe$ changes with pressure. Different colors and markers refer to different temperature. The curved is the thermodynamic fit with Eqn 11 based on ideal silicate solution with different Ferrous thermal expansion values, 2.92 from *Lange and Carmichael* (1987) and 3.69 from *Guo et al.* (2014). Fit coefficients are listed in Table 4.4.

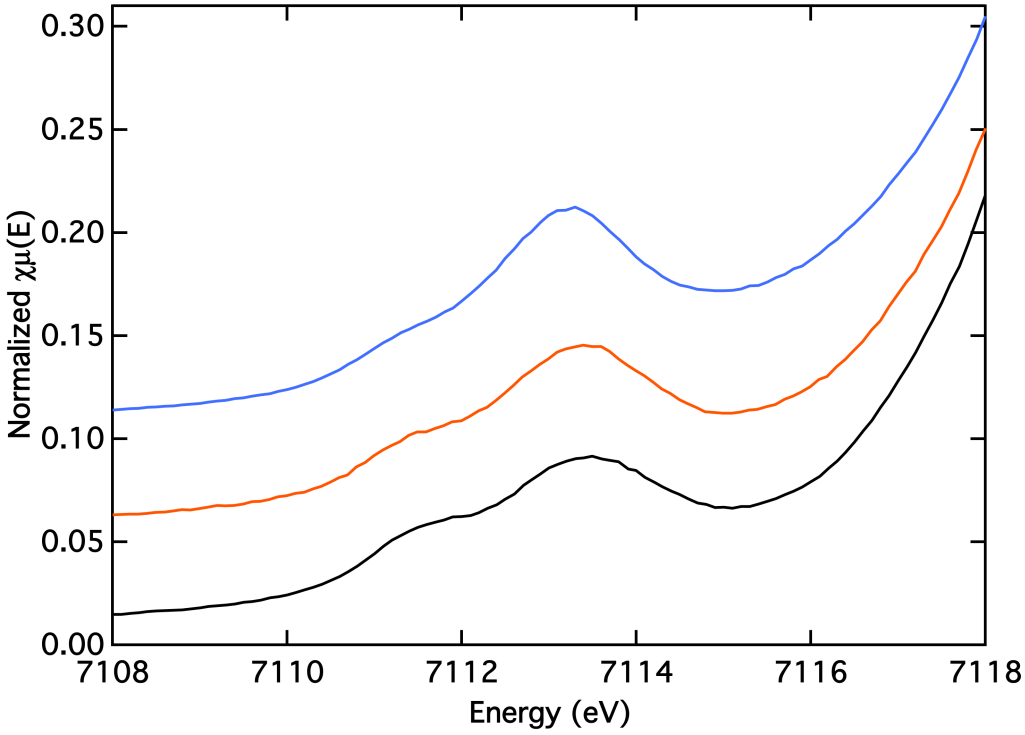

Figure 4.6: Examples of XANES pre-edge spectra. Spectra are vertically offset 0.05 for clarity

Table 4.3: Parameters obtained from XANES spectra

No.	APS				NSLS			
	I(Fe^{3+})+I(Fe^{2+})*	$\frac{I(Fe^{3+})}{I(Fe^{2+})}$*	$\frac{I(Fe^{3+})}{I(Fe^{3+})+I(Fe^{2+})}$*	**Centroid Energy (eV)**	**I(Fe^{3+})+I(Fe^{2+})***	$\frac{I(Fe^{3+})}{I(Fe^{2+})}$*	$\frac{I(Fe^{3+})}{I(Fe^{3+})+I(Fe^{2+})}$*	**Centroid Energy (eV)**
A867	0.1447(0.0055)	4.557(0.378)	0.819(0.013)	7113.205(0.016)	0.1459(0.0011)	4.363(0.394)	0.813(0.014)	7113.238(0.014)
A888	n.a.#				n.a.#			
A896	0.1441(0.0026)	4.493(0.227)	0.818(0.008)	7113.233(0.007)	0.1522(0.0015)	4.250(0.195)	0.809(0.007)	7113.230(0.010)
A944	0.1370(0.0072)	4.038(0.194)	0.801(0.008)	7113.197(0.005)	0.1399(0.0035)	3.656(0.122)	0.785(0.006)	7113.197(0.019)
A945	0.1354(0.0018)	4.270(0.075)	0.810(0.003)	7113.201(0.004)	0.1415(0.0055)	3.677(0.314)	0.785(0.015)	7113.184(0.010)
A952	0.1361(0.0051)	4.343(0.114)	0.813(0.004)	7113.195(0.009)	0.1547(0.0026)	4.057(0.090)	0.802(0.004)	7113.211(0.001)
B388	0.1389(0.0017)	4.763(0.145)	0.826(0.004)	7113.245(0.002)	0.1452(0.0044)	4.111(0.651)	0.802(0.024)	7113.244(0.013)
B402	0.1395(0.0022)	4.779(0.178)	0.827(0.005)	7113.229(0.008)	0.1467(0.0039)	4.211(0.254)	0.808(0.009)	7113.241(0.009)
M535	n.a.#				n.a.#			
M537	0.1360(0.0020)	3.792(0.231)	0.791(0.010)	7113.168(0.006)	n.a.#			
M540	0.1482(0.0050)	3.472(0.358)	0.775(0.018)	7113.143(0.014)	0.1345(0.0031)	2.868(0.183)	0.741(0.012)	7113.116(0.018)
M543	0.1260(0.0031)	3.876(0.043)	0.795(0.002)	7113.162(0.010)	0.1395(0.0007)	3.298(0.205)	0.767(0.011)	7113.137(0.014)
M544	0.1100(0.0053)	2.899(0.881)	0.735(0.059)	7113.165(0.036)	0.1001(0.0022)	2.945(0.348)	0.745(0.022)	7113.198(0.015)
M559	0.1364(0.0061)	4.536(0.573)	0.818(0.020)	7113.194(0.035)	n.a.#			
M562	0.1313(0.0117)	3.715(0.232)	0.787(0.011)	7113.131(0.019)	0.1290(0.0025)	3.681(0.190)	0.786(0.009)	7113.128(0.004)
M563	n.a.#				n.a.#			
M572	0.1114(0.0026)	3.612(0.160)	0.783(0.008)	7113.099(0.007)	0.1132(0.0027)	3.442(0.316)	0.774(0.016)	7113.071(0.009)
M601	0.1179(0.0014)	3.376(0.028)	0.771(0.001)	7113.092(0.005)	n.a.#			
VF1	0.1680(0.0065)	5.137(0.133)	0.837(0.004)	7113.338(0.005)	n.a.#			

Uncertainties are in one sigma standard deviation (1σ)

APS: Advanced Photon Source

NSLS: National Synchrotron Light Source

*Intergrated pre-edge intensity

#Results not available

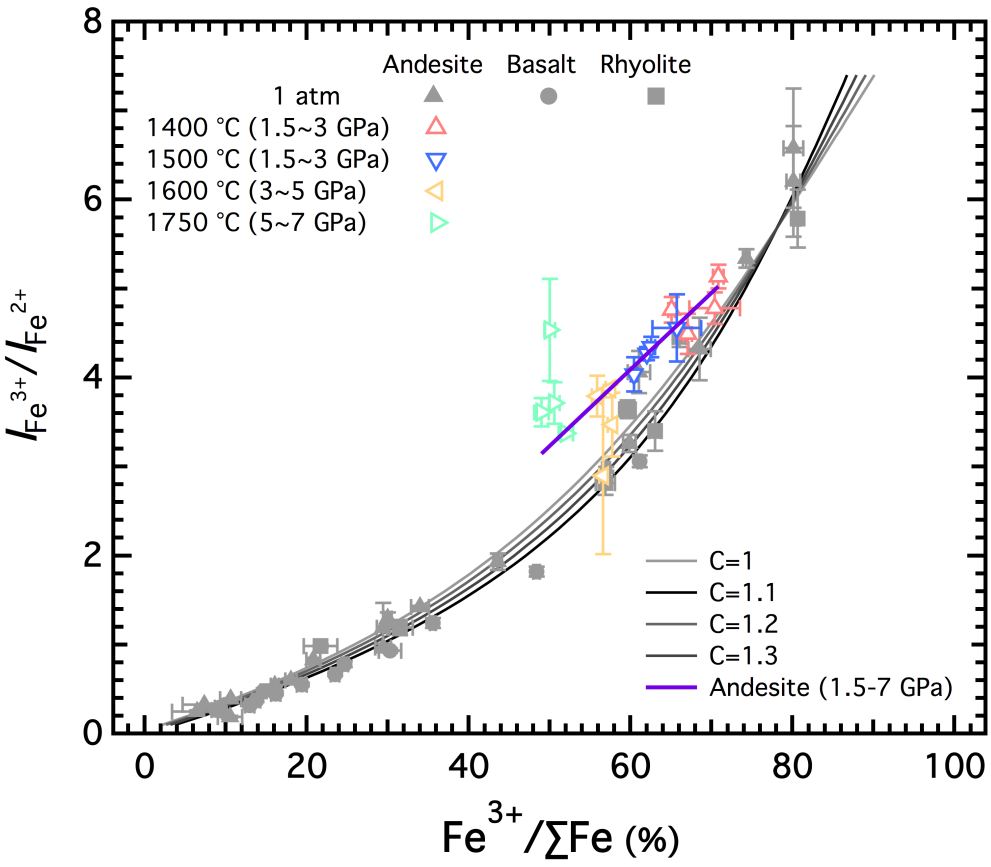

Figure 4.7: Integrated pre-edge intensity ratios ($\frac{I(Fe^{3+})}{I(Fe^{2+})}$) vs. $Fe^{3+}/\Sigma Fe$ (%) after Chapter 3. 1 atm basalt and rhyolite data from *Cottrell et al.* (2009) and 1 atm andesite data from Zhang et al., (in prep.). Grey curves are the best fit of glasses synthesized at 1 atm with all three compositions and $Fe^{3+}/\Sigma Fe$ ratio of basalt obtained from Mssbauer spectra collected at room temperature corrected with correction number C= 1, 1.1, 1.2, 1.3. More details are described in Chapter 3. The purple line is the best fit with andesite glasses synthesized at 1.5-7 GPa.

by the function

$$\frac{I(Fe^{3+})}{I(Fe^{2+})} = (-1.0740.228) + (0.0861040.00408) \times (\frac{Fe^{3+}}{\Sigma Fe} \times 100) \quad (4.3)$$

which gives an r^2 of 0.94.

4.4 Discussion

4.4.1 Local environments of Fe^{3+} and Fe^{2+} in silicate glasses

With increasing pressure, changes in the bonding environments of Fe^{2+} and Fe^{3+} of quenched glasses can be characterized from both Mössbauer spectroscopy and XANES. Quenchable compression mechanisms in silicate glasses include both steric effects and changes in mean cation-oxygen coordination numbers (CN) (*Allwardt et al.*, 2005).

For Mössbauer spectroscopy, the relationship between hyperfine parameters CS and QS and CNs for Fe^{3+} and Fe^{2+} ions is well established for minerals (*Dyar et al.*, 2006), but interpretation for glasses is somewhat more complex, in part because ions can reside in a population of environments, rather than in discrete sites with a unique coordinatation (*Wilke et al.*, 2005; Chapter 3). Parameters generated from Mössbauer spectra of silicate glasses constrain average coordination.

Values of center shifts and quadrupole splittings of Fe^{3+} and Fe^{2+} in andesitic glasses as a function of pressure are shown in Fig 4.8. CSs of Fe^{3+} vary little from 1.5 to 7 GPa, with values chiefly near 0.341$\pm$0.010 mm/s, though the low pressure (0.1 MPa) glass, VF1, is lower (0.297$\pm$0.007). Values of QSs also fail to show a discernable trend, with most near 1.172 mm/s. For Fe^{2+}, CS increases 0.05 mm/s from 1.5 GPa to 5 GPa then is nearly constant at 1.10 mm/s between 5 and 7 GPa, whereas QS increases linearly with pressure up to 7 GPa from 1.820 to 2.213 mm/s. These patterns suggest that for these comparatively oxidized glasses (all with $Fe^{3+}/\Sigma Fe$ >0.5), the average coordination number for Fe^{3+} is close to 5 (*Dyar*, 1985; Chapter 3) and shows little change from 1 atm to 7 GPa, but that the average coordination number of Fe^{2+} increases slightly, from between 5 and 6 (*Dyar*, 1985; *Dyar et al.*, 2006). The marked increase in QS for Fe^{2+}, which is more pronounced than the CS shift, likely suggests that additional compression of Fe^{2+}-O polyhedra occurs owing to changes in O-Fe^{2+}-O bond angles resulting in less-symmetric Fe^{2+} sites.

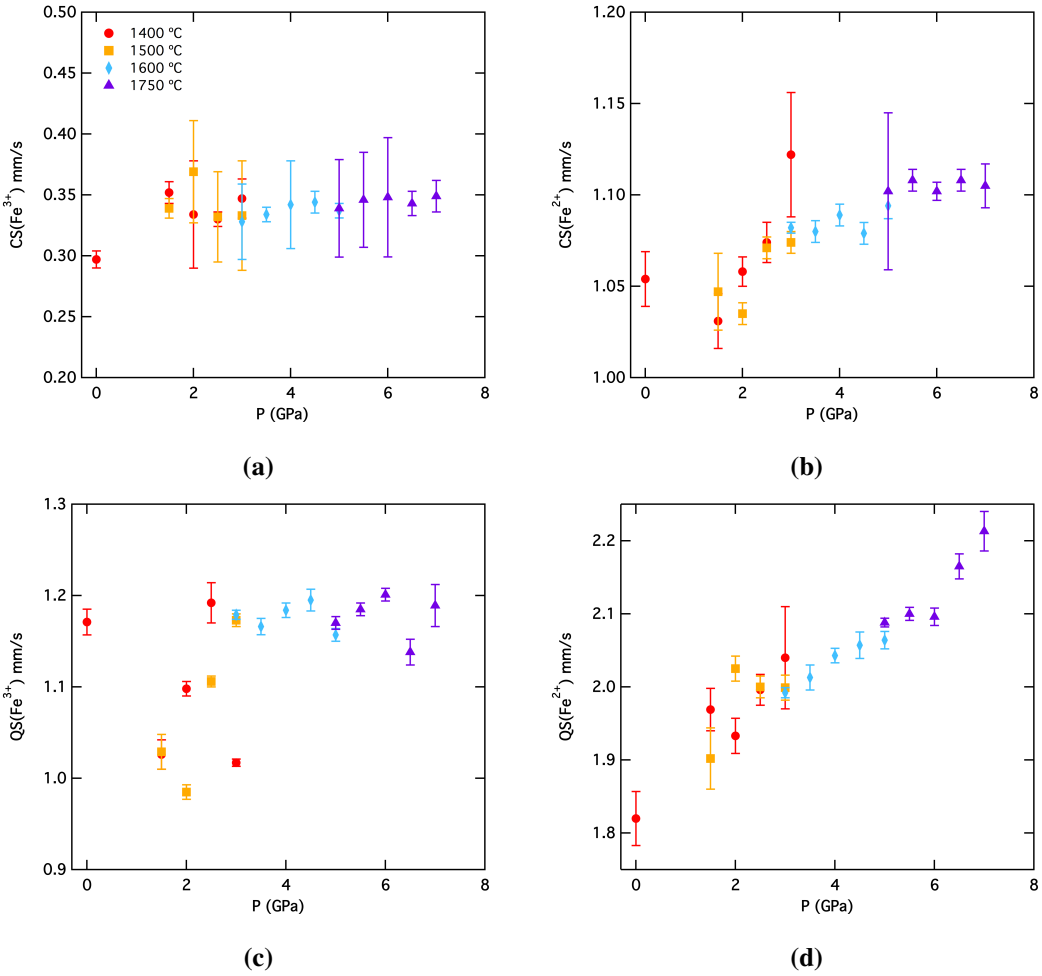

Figure 4.8: The ferrous and ferric center shift (CS) and Quadrupole splitting (QS) of various pressure series glasses change with pressure. Different colors and makers indicate different temperature.

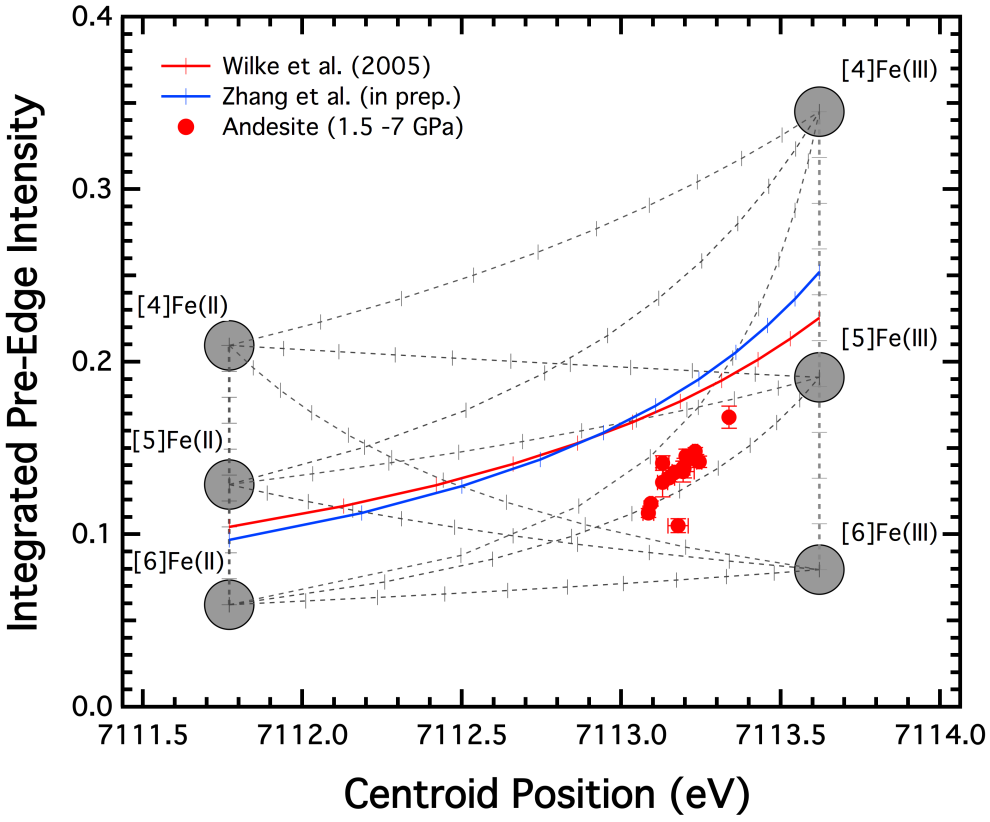

Figure 4.9: Pre-edge parameters of andesitic glasses synthesized at 1.5-7 GPa plotted in the variogram after *Wilke et al.* (2001) and Chapter 3. Grey fields designate pre-edge parameters for the Fe coordination and oxidation state indicated. Blue and red solid lines between fields indicate the variation of pre-edge parameters assuming binary mixtures of respective end-members intensity determined by *Wilke* (2005) for 1 atm basalt and Chapter 3 for 1 atm andesite. Ticks on curves refer to the percentage of mixtures.

XANES pre-edge spectra also contain constraints on the effects of pressure on Fe^{2+} and Fe^{3+} site geometries. Estimates of Fe ion geometries can be calculated from the variogram approach of *Wilke et al.* (2005), which compares simultaneously the pre-edge centroid positions and integrated intensities to those of minerals with Fe in known oxidation state and CN. As shown in Fig. 4.9, the diminished integrated intensities with increasing pressure reflect an increase in CN in andesitic glasses. A similar conclusion can be drawn by comparison between the low integrated intensities of the high pressure glasses and those for andesitic and basaltic glasses quenched from low pressure from Chapter 3 and *Wilke et al.* (2005), respectively. Quantitative estimates of mean coordination numbers of Fe^{3+} and Fe^{2+} can be calculated from the approach of Chapter 3, which combines the XANES pre-edge characteristics with by $Fe^{3+}/\Sigma Fe$ determined from Mössbauer analyses (Fig. 4.10). Mean CN for Fe^{3+} are 5.22±0.14 (APS) and 5.25±0.13 (NSLS), with no discernable pressure variation, whilst the mean coordination number of Fe^{2+} increases from 5.5 to 6.2 over the pressure range explored. Thus, the results from Mössbauer and XANES spectroscopies agree that at modest pressure, compression of Fe^{3+} in andesitic silicate liquid is not accompanies by significant geometric changes, but that Fe^{2+} compression is facilitated by significant increases in mean coordination and, possibly, bond geometries. This latter result is in qualitative agreement though not as pronounced as the results of *Sanloup et al.* (2013) for fayalite liquid, who found an increase in Fe^{2+} CN from 4.8 to 7.2 from ambient pressure up to 7.5 GPa.

4.4.2 Effect of pressure on $Fe^{3+}/\Sigma Fe$

The reaction governing homogeneous iron redox equilibrium in a silicate melt is

$$^{\text{FeO}}_{\text{magma}} + \frac{1}{4}\text{O}_2 = ^{\text{FeO}_{1.5}}_{\text{magma}} \tag{4.4}$$

which is governed by the thermodynamic properties of Fe oxides in silicate melts according to the relation:

$$\frac{-\Delta G^0_{(T,P)}(4.4)}{\text{R}T} = \ln\frac{X^{\text{magma}}_{\text{FeO}_{1.5}}}{X^{\text{magma}}_{\text{FeO}}} + \ln\frac{\gamma^{\text{magma}}_{\text{FeO}_{1.5}}}{\gamma^{\text{magma}}_{\text{FeO}}} - \frac{1}{4}\ln f\text{O}_2 \tag{4.5}$$

where $\delta G^0_{(T,P)}(4.4)$ is the free energy change of reaction (4.4) at the temperature (T) and pressure (P) of interest, and Xs and γs are, respectively, the mole fractions and activity coefficients

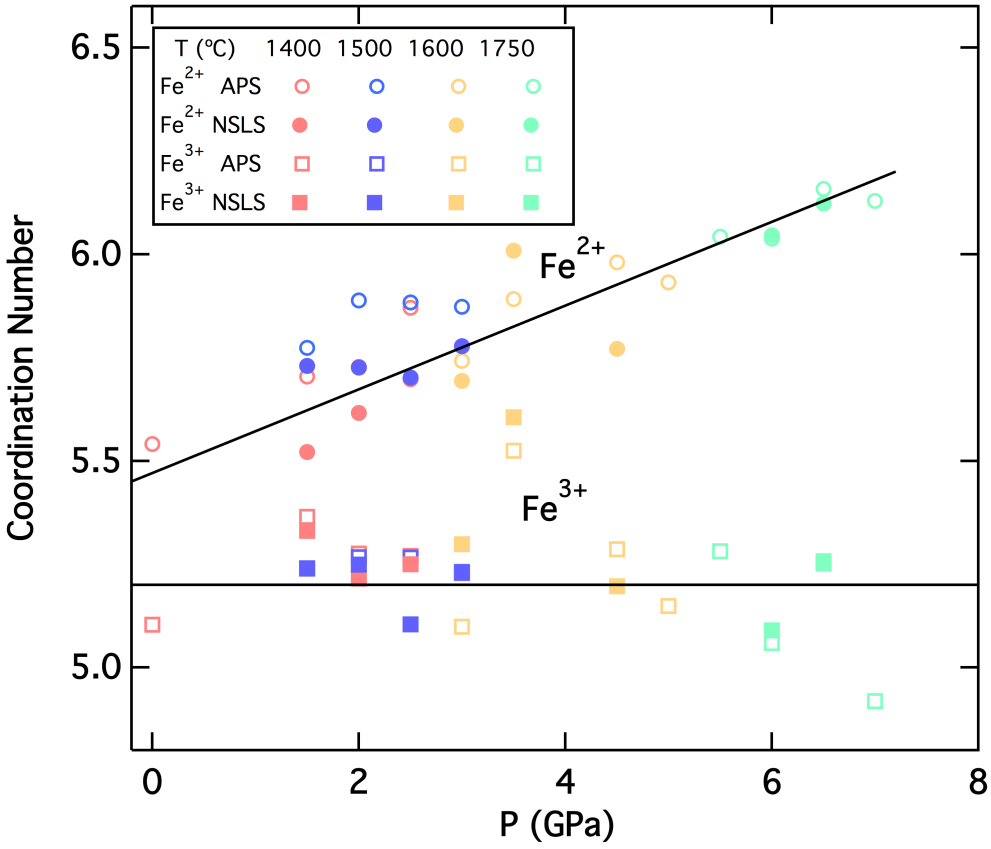

Figure 4.10: Coordination numbers of Fe^{2+} and Fe^{3+} that calculated according to Chapter 3 change with pressure.

of the Fe-oxide components, and R is the gas constant. Because the difference in molar partial volumes between $FeO_{1.5}$ and FeO, $\Delta V_{\text{magma}(T,P)}$ is non-zero (*Mo et al.*, 1982; *Lange and Carmichael*, 1987; *Liu and Lange*, 2006), this relationship is pressure dependent and can be expressed as

$$\Delta G^0_{(T,P)}(4.4) = \Delta G^0_{(T,1\text{ bar})}(4.4) + \int_{1\text{ bar}}^{P} \Delta \bar{V}_{\text{magma}(T,P)}(4.4)\mathrm{d}P \tag{4.6}$$

The $Fe^{3+}/\Sigma Fe$ ratios of glasses described in this paper resolved from Mössbauer spectroscopy are plotted as a function pressure along different isotherms in Fig. 4.5. Accounting for the observed changes in $Fe^{3+}/\Sigma Fe$ using Eqn. 4.6 requires first accounting for the fO_2 fixed by the Ru+RuO_2 buffer, which changes with pressure and temperature according to the expression:

$$\log_{10} fO_2(\text{Ru+RuO}_2) = -\frac{16953}{T} + 17.98 - 2.660\log_{10}T + 0.0562\frac{P}{T} \tag{4.7}$$

where T is in K and P is in GPa (*O'Neill and Nell*, 1997).

To model the volumes of Fe-oxides as a function of pressure, we apply the Murnaghan equation of state in the form suggested by *Holland and Powell* (2001).

$$V_{(T,P)} = V_{(T,1\text{ bar})}[1 + P(\frac{\kappa'}{\kappa})]^{-\frac{1}{\kappa'}} \tag{4.8}$$

where κ is the bulk modulus, and κ' its pressure derivative. We assume a value of 4 for κ'; although this value comes chiefly from its applicability to crystalline oxides and silicates, the available evidence on silicate melts indicates that it is not inappropriate (*Rigden et al.*, 1989; *Miller et al.*, 1991; *Campbell et al.*, 2009). Rearranging and integrating Eqns. 4.6 and 4.8 leads to

$$\int_{1\text{ bar}}^{P} \bar{V}_{(1673\text{ K},P)}\mathrm{d}P = \frac{(\bar{V}_{(1673\text{ K, 1 bar})}\kappa}{\kappa' - 1}[(1 + \frac{\kappa' P}{\kappa})^{1-\frac{1}{\kappa'}} - 1] \tag{4.9}$$

The spectroscopic results discussed in Section 4.4.1 indicate that coordination and bonding of ferric iron in andesitic liquids does not change appreciably over the pressures investigated, so applicable equation of state parameters are possibly well-constrained by low pressure measurements. We take the $\bar{V}_{(T,1\text{ bar})}$ of $FeO_{1.5}$ in silicate melts to be 20170+4.54(T-1673) J/GPa (*Lange and Carmichael*, 1987) and κ of 16.6 GPa (*Kress and Carmichael*, 1991). *Liu and*

Lange (2006) give an updated partial molar volume of $FeO_{1.5}$ of 20760 J/GPa, but with a negligible thermal expansion is negligible and so we choose to retain the older parameters from (*Lange and Carmichael*, 1987). We consider two alternative values of the $\bar{V}_{(T,1\text{ bar})}$ for FeO, 2.92 J/GPa/K from *Lange and Carmichael* (1987) and 3.69 J/GPa/K from *Guo et al.* (2014). The values of $\bar{V}_{(T,1\text{ bar})}$ and κ for FeO is then fit from the experimental data in Fig. 4.5. We note that the temperature span of our data is insufficient to extract meaningful independent constraints on the thermal expansion term for Fe^{2+}.

Rearranging Eqns. (4.5) and (4.6) yields

$$\ln\frac{X^{\text{magma}}_{\text{FeO}_{1.5}}}{X^{\text{magma}}_{\text{FeO}}} = \frac{1}{4}\ln f\text{O}_2 - \ln\frac{\gamma^{\text{magma}}_{\text{FeO}_{1.5}}}{\gamma^{\text{magma}}_{\text{FeO}}} + \frac{-\Delta G^0_{(T,1\text{ bar})}(4.4)}{\text{R}T} + \frac{-\int_{1\text{ bar}}^{P}\Delta\bar{V}_{\text{magma}}(4.4)\text{d}P}{\text{R}T} \quad (4.10)$$

We treat -$\ln\frac{\gamma^{\text{magma}}_{\text{FeO}_{1.5}}}{\gamma^{\text{magma}}_{\text{FeO}}}$ and -$\Delta G^0_{(T,1\text{ bar})}(4.4)$ as refinable parameters. Using a weighted Levenberg-Marquardt algorithm to values of $\ln\frac{X^{\text{magma}}_{\text{FeO}_{1.5}}}{X^{\text{magma}}_{\text{FeO}}}$ as a function of pressure and temperature produces the relation

$$\begin{aligned}\ln&\frac{X^{\text{magma}}_{\text{FeO}_{1.5}}}{X^{\text{magma}}_{\text{FeO}}}\\ &= \frac{1}{4}\ln f\text{O}_2 + a + \frac{b}{\text{R}T}\\ &\quad - [20170 + 4.54\times(T-1673)]\times\frac{16.6}{3}\times\frac{(1+0.241P)^{0.75}-1}{\text{R}T}\\ &\quad + [c + \alpha_V\times(T-1673)]\times\frac{4}{3d}\times\frac{(1+d\times P)^{0.75}-1}{\text{R}T}\end{aligned} \quad (4.11)$$

where α_V is the thermal expansion. The resulting trends of $Fe^{3+}/\Sigma Fe$ ratios are compared to the experimental data in Fig. 4.5. Similar fit results are obtained from different α_V values (Table 4.4, Fig. 4.5), showing the limited constrains on α_V.

In theory, thermodynamic fit can be improved with a compositionally dependent model for non-ideal mixing, eqution of state more sophisticated than the Murnaghan equation, and direct constraints on κ' values for $FeO_{1.5}$ and FeO. But these more advanced considerations cannot be constrained within the limited span of T, P, and $Fe^{3+}/\Sigma Fe$ of the experimental data available in Fig. 4.5.

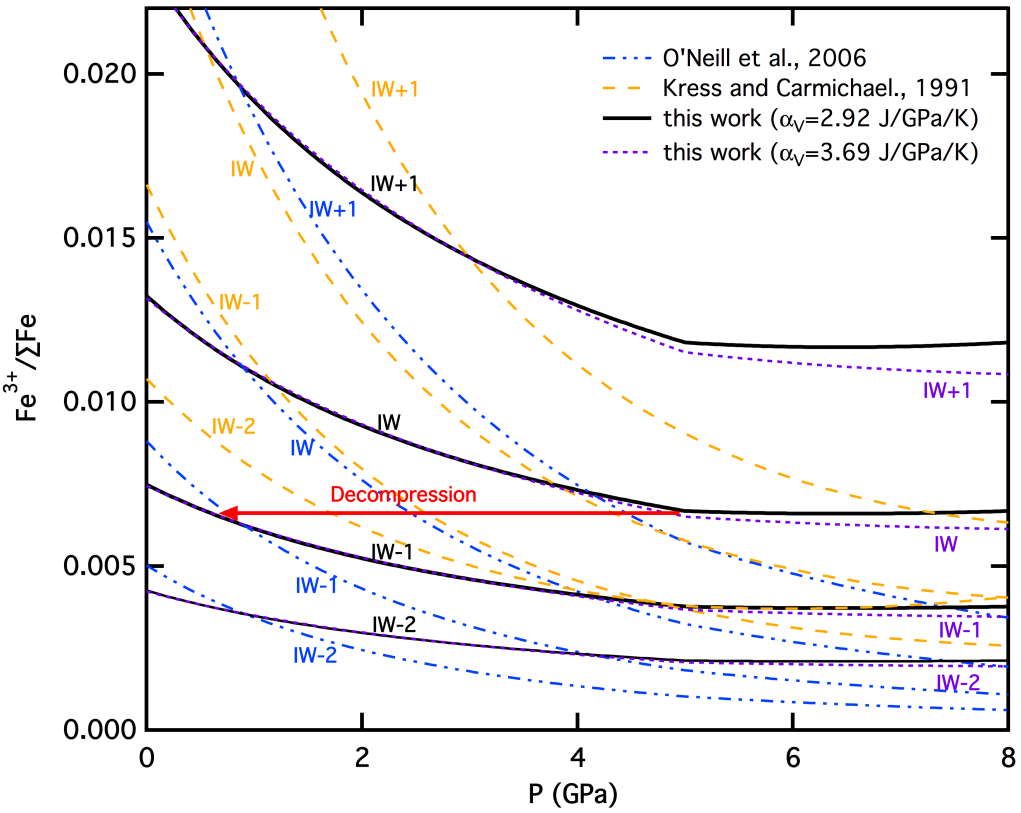

Figure 4.11: $Fe^{3+}/\Sigma Fe$ of silicate melts as a function of pressure at oxygen fugacities fixed relative to the iron-wüstite (IW) buffer (calculated with Eqn. 4.13) after *Hirschmann* (2012) with bulk silicate earth composition (*McDonough and Sun*, 1995) at 1400 °C. Trends are calculated from the models obtained from this work, *Kress and Carmichael* (1991) (their Eq. 7) and *O'Neill et al.* (2006). As illustrated by the red arrow, decompression at fixed values of $Fe^{3+}/\Sigma Fe$ leads to reduction relative to the IW buffer. Quantitative differences between the models are likely because of small amount of Fe^{3+} present at these reducing conditions and because all models are extrapolated from data obtained under more oxidizing conditions.

4.4.3 Redox-pressure relations in a magma column

Iron-wüstite is an important reference redox buffer to evaluate the relative oxidation state of a reduced magma close to equilibrium with Fe-rich alloy. Experimental calibrations of the fO_2 defined by the coexistence of crystalline Fe and FeO include low pressure (e.g., *O'Neill*, 1988) and high pressure (*Campbell et al.*, 2009; *Fischer et al.*, 2011) studies. Unfortunately, because of the change in stoichiometry of wüstite, from non-stoichiomtric ($Fe_{1-x}O$, x>0), at low pressure to nearly pure FeO above ∼5 GPa (*McCammon and Liu*, 1984), low pressure and high pressure calibrations are inconsistent, differing by more than 0.5 log units (Fig. 4.S5). An ideal parameterization of the IW buffer would incorporate internally consistent estimates of the 100 kPa free energy of formation of wüstite (*O'Neill*, 1988), the equilibrium stoichiometry as a function of pressure, temperature, and fO_2 (*McCammon and Liu*, 1984), and the respective equations of state of the solid phases, including their dependence on stoichiometry (*Campbell et al.*, 2009; *Fischer et al.*, 2011). In the absence of such a comprehensive analysis, a reasonable approximation is to assume that below 5 GPa, the high pressure buffer defined by *Campbell et al.* (2009) is offset as a linear function of pressure so that it matches the function given by *O'Neill* (1988) at 100 kPa. Thus, above 5 GPa, we use the relation proposed by *Campbell et al.* (2009); below 5 GPa, we use the relation given by *O'Neill* (1988), with the pressure derivative derived from the volumes of Fe and $Fe_{1-x}O$ at 100 kPa (*Huebner and Sato*, 1970)

$$\log fO_2(\text{O'Neill-Huebner}) = -\frac{28777.89}{T} + 14.0572 - 2.039 \times \log T + 550\frac{(P - 0.0001)}{T} \tag{4.12}$$

where T is in K, and P is in GPa, but with a linear pressure adjustment such that the function matches that of *Campbell et al.* (2009) at 5 GPa.

$$\begin{aligned} &\log fO_2(\text{IW}) \\ &\quad = \log fO_2(\text{O'Neill-Huebner}) \times (1 - 0.2P) \\ &\qquad + 0.2P \times \log fO_2(\text{Campbell}), \\ &\qquad 0 < P < 5\text{GPa} \end{aligned} \tag{4.13}$$

The relationship between these functions for IW is illustrated in Fig 4.S5.

The new thermodynamic model (Eqn. 4.11) and Eqn. 4.13 can be used to calculate the relationship between $Fe^{3+}/\Sigma Fe$ in melts, pressure and fO_2 relative to the IW buffer at 1400

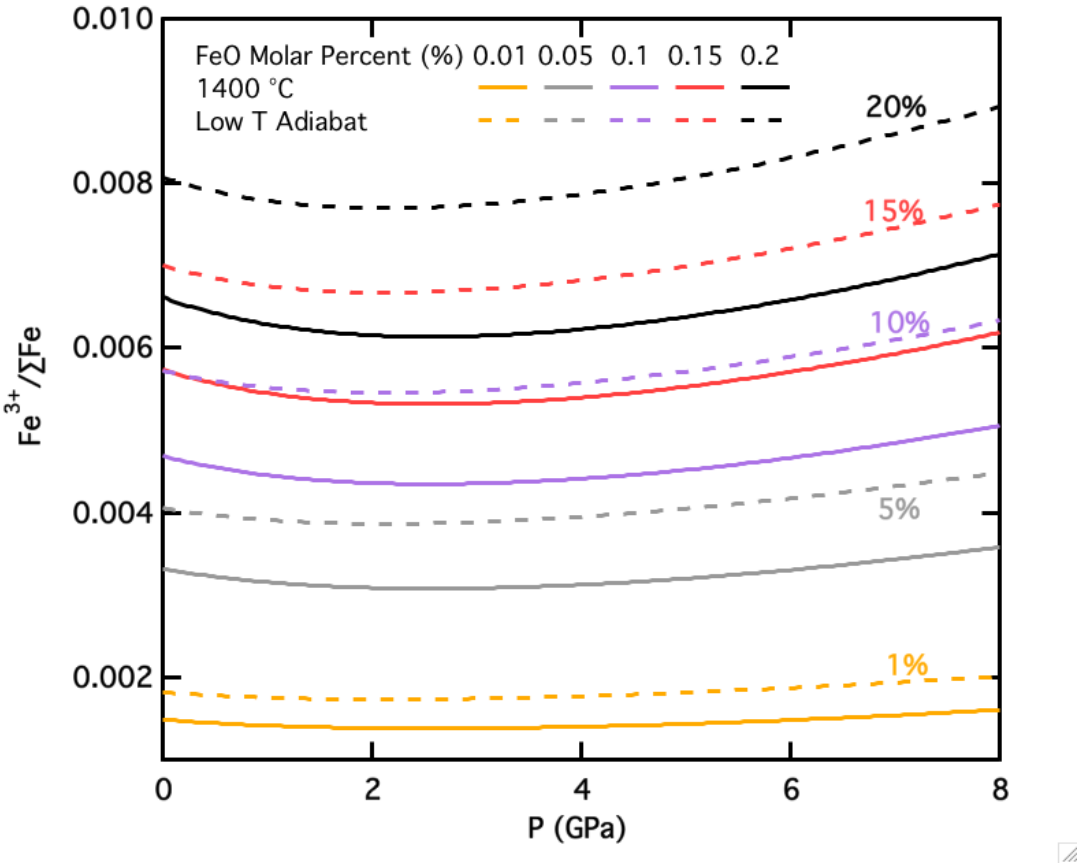

Figure 4.12: $Fe^{3+}/\Sigma Fe$ of silicate melts as a function of pressure at oxygen fugacities fixed relative to the iron$FeO_{\text{silicate melt}}$ (IW*), which is calculated with Eqn. 4.16, with different FeO molar percent in silicate liquid along isotherm or adiabat (*Stixrude et al.*, 2009). Trends are calculated from the models obtained from this work with first group parameters (Table 4.4).

°C (Fig. 4.11). For melts with constant $Fe^{3+}/\Sigma Fe$ self-compression of magma leads to oxidation relative to the IW buffer, as also suggested by the thermodynamic models of *Kress and Carmichael* (1991) and *O'Neill et al.* (2006), but the revised model shows a smaller dependence below 5 GPa. Above 5 GPa, the new model indicates that changes in pressure at constant fO_2 relative to IW produce little change in $Fe^{3+}/\Sigma Fe$, suggesting small changes in fO_2 for compression or decompression of an isochemical melt.

The relationship in Fig. 4.11 indicates that modest pressures (e.g., starting < 8 GPa) decompression of an isochemical magma ocean (e.g., constant $Fe^{3+}/\Sigma Fe$) leads to reduction relative to the IW buffer. This relationship applies to a column of magma that is metal-free, in which the only influence on ΔIW is the pressure dependence of $Fe^{3+}/\Sigma Fe$, and in this case a shallow magma ocean would be more reduced near its surface than at depth. However, as emphasized by *Righter and Ghiorso* (2012a,b), another effect to be considered when magma is in equilibrium with Fe-rich alloy is the difference of fO_2 between the metal-oxide (IW) buffer and the similar buffer in which metal coexists with FeO-bearing silicate liquid. Because the partial molar volume of FeO in the liquid is different from that of FeO in crystalline oxide, the pressure dependences of the two are distinct (*Righter and Ghiorso*, 2012a,b). To distinguish the two, we define the effective buffer reaction IW*, which is defined by the reaction

$$\mathrm{Fe_{metal}} + \frac{1}{2}O_2 = \mathrm{FeO_{silicate\ liquid}} \tag{4.14}$$

We evaluate the fO_2 defined by IW* by rearranging the relations evaluated by *Medard et al.* (2008).

$$\log fO_2 = \frac{2}{\ln 10}\left(\ln\frac{X_{\mathrm{FeO}}^{\mathrm{melt}}}{X_{\mathrm{Fe}}^{\mathrm{alloy}}} + \ln\frac{\gamma_{\mathrm{FeO}}^{\mathrm{melt}}}{\gamma_{\mathrm{Fe}}^{\mathrm{alloy}}} - \ln K\right) \tag{4.15}$$

and

$$\begin{aligned} \ln K &= a + \frac{b}{T} - \frac{\int_{100\mathrm{kPa}}^{P}\Delta V(4.1)\mathrm{d}P}{\mathrm{R}T} \\ &= -5.779 + \frac{28056}{T} - \frac{\int_{100\mathrm{kPa}}^{P}\Delta V(4.1)\mathrm{d}P}{\mathrm{R}T} \end{aligned} \tag{4.16}$$

Following *Holzheid et al.* (1997), the activity coefficient for FeO in silicate liquid is assumed to be unity, and in the following calculations, we consider pure Fe alloy, so both $\gamma_{\mathrm{Fe}}^{\mathrm{alloy}}$ and $X_{\mathrm{Fe}}^{\mathrm{alloy}}$ are also unity. The Murnaghan equation of state is used to describe the volume integral, (e.g., Eqn. 4.8). With the volume of γ-Fe at 100 kPa assumed to be 7554.347+0.527×(T-1661) J/GPa (*Kaufman et al.*, 1963), with a bulk modulus of κ=133 GPa (*Campbell et al.*, 2009) and κ'=5 (*Funamori et al.*, 1996). Consideration of molten, rather than crystalline Fe, would have only a small effect on the calculations, and would not affect any of the trends or conclusions. As discussed in Section 4.4.2, two alternative fits with different assumed values of the thermal expansion of FeO, each listed in Table 4.4, yield similar results, so for the following discussion, we only use the first group of parameters in Table 4.4 for FeO. Consequently, the oxygen fugacity of iron coexisting with FeO in silicate melt can be calculated from,

$$\begin{aligned}\log f\mathrm{O}_2 &= \frac{2}{\ln 10} \\ &\times \Big(\ln X_{\mathrm{FeO}}^{\mathrm{melt}} + 5.779 - \frac{28056}{T} \\ &+ 1.4676 \times [15316 + 2.92(T - 1673.15)] \times \frac{[(1 + 0.10927P)^{0}.75 - 1]}{T} \\ &- 3.9992 \times [7554.347 + 0.527(T - 1661)] \times \frac{[(1 + 0.037593P)^{0}.8 - 1]}{T}\Big)\end{aligned} \tag{4.17}$$

The oxygen fugacity defined by IW* for the case of a (metastable) peridotitic melt in equilibrium with Fe metal at 1400 °C as a function of pressure is plotted in Fig. 4.S5. Owing to the greater volume of FeO in silicate melts, IW* becomes more oxidized with increasing pressure relative to IW.

The effect of pressure on variations compared to IW of a column of magma will be influenced by the relationship between $Fe^{3+}/\Sigma Fe$ on ΔIW (e.g. Fig. 4.11) and the progressive offset between IW and IW* (Fig. 4.S5). The $f\mathrm{O}_2$ buffered by isochemical (constant FeO*) melts coexisting with alloy (e.g., IW*) increases with FeO concentration (Fig. 4.12). Further, with increasing pressure, the increase in $f\mathrm{O}_2$ for IW* relative to IW means that melts in equilibrium with alloy have enhanced $Fe^{3+}/\Sigma Fe$. Thus, the distinction between Figs. 4.11 and 4.12 is that the former is calculated for an Fe-free column of magma and $f\mathrm{O}_2$ is affected only by the relationship between $Fe^{3+}/\Sigma Fe$ and melt, whereas the latter assumes metal is present at every depth, and $f\mathrm{O}_2$ is affected by reaction between FeO in the melt and metal. This calculation

Table 4.4: Thermodynamic fit parameters for Eqn. 4.11

α_V	$2.92^{\#}$	3.69*
a	-6.1388±0.128	-6.389±0.131
b	12426±214	12836±222
c	15316±208	15512±210
d	0.10927±0.0187	0.14757±0.0205
$\kappa^{\&}$	36.61	27.11
$\kappa^{@}$	30.3^{v}	21.1*
χ^2	87.76	82.73

α_V: Thermal expansion, in J/GPa/K.
$^{\#}$: from Lange and Carmichael (1987)
*: from Guo et al. (2014)
$^{\&}$: Bulk modulus, which is calculated using equation κ=4/d
$^{@}$:Bulk modulus from reference
^{v}: from Kress and Carmichael (1991)
Uncertainties are in one sigma standard deviation (1σ)

shows that at high pressures, melts of a given FeO content that are in equilibrium with metal are more oxidized and have higher $Fe^{3+}/\Sigma Fe$ than melts equilibrated with metal at lower pressure.

4.4.4 Applications to redox gradients in magma oceans

The parameterization of $Fe^{3+}/\Sigma Fe$ as a function of T,P, and fO_2 can be applied to the problem of redox gradients in magma oceans (*Hirschmann*, 2012; *Righter and Ghiorso*, 2012a). In a magma ocean, the mean depth of metal-silicate equilibrium occurs at high pressure (e.g., $>$25 GPa for Earth, *Li and Agee*, 1996; *Chabot et al.*, 2005; *Corgne et al.*, 2008; *Kegler et al.*, 2008) and, to a first approximation, one can consider that the region above this depth is well-mixed, and therefore homogeneous in $Fe^{3+}/\Sigma Fe$ ratio (*Hirschmann*, 2012). Thus, the fO_2 variations with depth can be evaluated from a vertical column of the magma ocean assumed homogeneous and metal-free except at its base, where the fO_2 relative to IW depends on the pressure of metal-silicate equilibration, and the $Fe^{3+}/\Sigma Fe$ ratio through the magma column by the depth metal-silicate liquid equilibration.

These calculations can be applied to redox gradients in magma oceans applicable to the early differentiation of terrestrial planets and moons (Fig. 4.13). For magma oceans on small

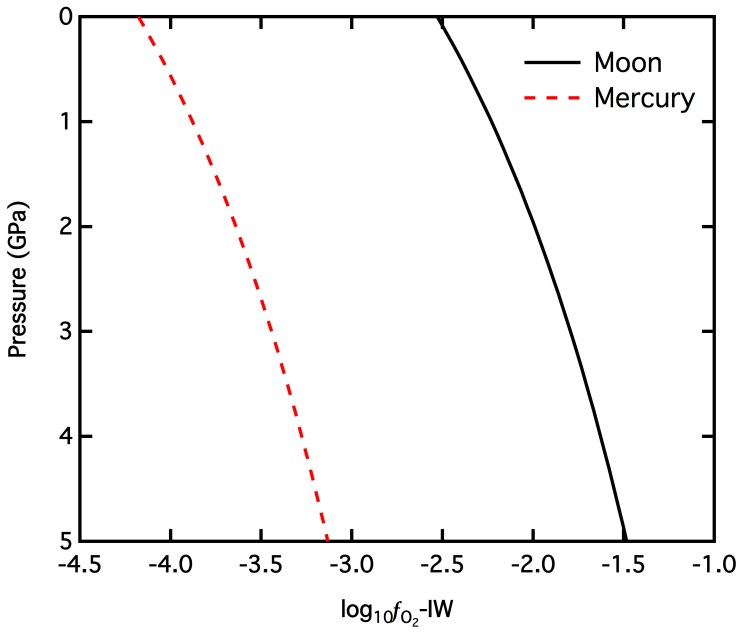

(a)

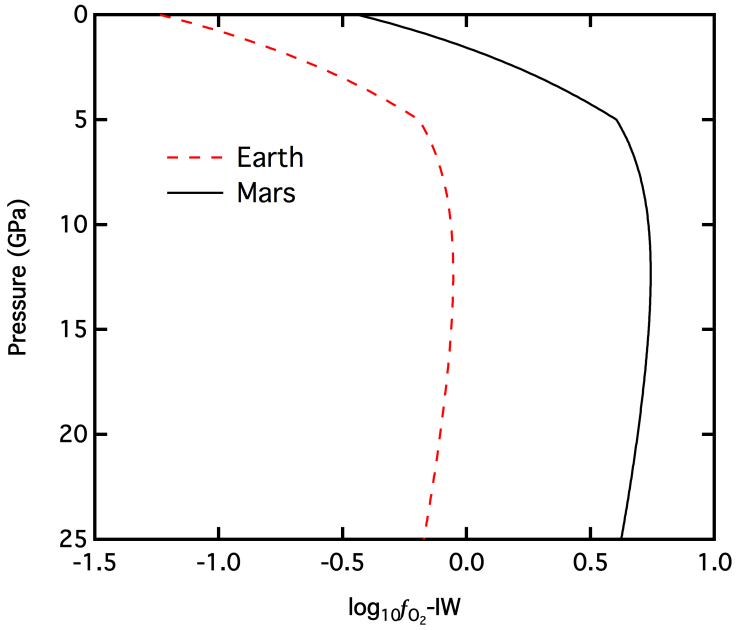

(b)

Figure 4.13: Oxygen fugacity of silicate melts relative to IW (a, b) with bulk silicate composition for Moon (*Elardo et al.*, 2011), Mercury *Robinson and Taylor* (2001), Earth (*McDonough and Sun*, 1995), and Mars (*Bertka and Fei*, 1997) as a function of pressure at $Fe^{3+}/\Sigma Fe$ fixed at depth (5 GPa for Moon and Mercury, 25 GPa for Earth and Mars), with equilibrium between iron and silicate melt (Eqn. 4.16). Trends are calculated from the models obtained from this work with first group parameters (Table 4.4) along adiabat (*Stixrude et al.*, 2009)

bodies such as Mercury and the Moon, the fO_2 at the magma ocean base is comparatively reduced, owing to the low pressure prevailing at the magma ocean base, and about 1 log unit more reduced at the surface. The difference between the calculated trends for Mercury and the Moon is related to the different FeO contents of the silicate melts (3 wt.% for Mercury, 9.37 wt.% for the Moon, from *Robinson and Taylor* (2001) and *Elardo et al.* (2011)). On larger bodies, such as Mars or the Earth, the pressure at the base of the magma ocean can be higher and consequently the fO2 relative to IW set at the base is significantly more oxidized (Fig. 4.13). Our calculations for both Mars and the Earth assume 25 GPa at the base of the magma ocean, though this is a minimum pressure for Earth (*Li and Agee*, 1996; *Chabot et al.*, 2005; *Corgne et al.*, 2008; *Kegler et al.*, 2008). Conditions at the surface of the magma ocean are approximately 1 order of magnitude more reduced than at the base, chiefly owing to effects at low pressure.

We emphasize that the calculations above 8 GPa are extrapolations based on lower pressure experimental data. Our experimental and spectroscopic data indicate notable densification of Fe^{2+}-O components in the magma over this pressure range, but no appreciable change in coordination of Fe^{3+}-O polyhedra (Figs. 4.8,4.10). Our expectation, based on the increase in coordination of Fe^{3+} in minerals with pressure (e.g., *Frost and McCammon*, 2008), as well as the general trend of increase in coordination of cations in silicate melts with pressure (e.g., *Ghiorso*, 2004), is that Fe^{3+}-O coordination in silicate melts increases at some as-yet unknown pressure above 8 GPa, eventually leading to stabilization Fe^{3+} and increase in $Fe^{3+}/\Sigma Fe$ in silicate melts in equilibrium with metal alloy (*Hirschmann*, 2012). If this occurs, then near-surface conditions could be highly oxidizing for deep magma oceans on Earth or Mars.

Further, it should be clear from the discussion that the calculations applied to magma oceans still have considerable uncertainties owing to lack of detailed information about the thermodynamics of FeO and Fe_2O_3 in silicate melts at high pressure. For example, the offset between IW and IW* calculated in this work is different from that calculated by *Righter and Ghiorso* (2012b), who found a smaller difference and lower pressure sensitivity for the offset between IW and IW*. Although the equation of state of *Ghiorso* (2004), which was employed by *Righter and Ghiorso* (2012b), is more sophisticated and based on higher pressure constraints for the behavior of FeO than that used here, it shows very significant sensitivity to melt composition (compare *Righter and Ghiorso* (2012a)and *Righter and Ghiorso* (2012b)), highlighting the significant uncertainty in all equations of state. Thus, the fO_2 set by equilibration with metal in deep magma oceans requires further experimental and theoretical refinement.

4.A Supplement material

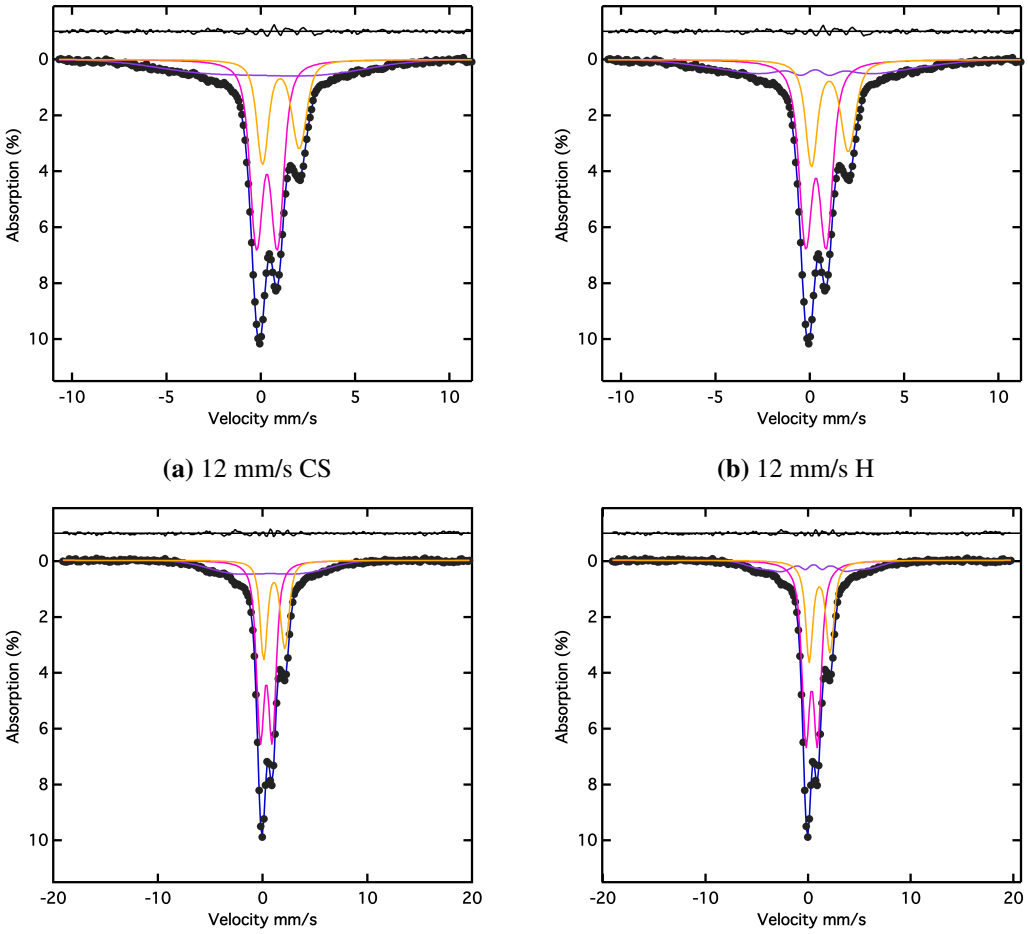

(a) 12 mm/s CS

(b) 12 mm/s H

(c) 20 mm/s CS

(d) 20 mm/s H

Figure 4.S1: Example of Mössbauer spectra, A848, collected at different velocity scale with different fit methods. a) collected at 12 mm/s scale and fitted with paramagnetic sites and a broaden magnetic site; b) collected at 12 mm/s scale and fitted with paramagnetic sites and a sextet magnetic site; c) collected at 20 mm/s scale and fitted with paramagnetic sites and a broaden magnetic site; d) collected at 20 mm/s scale and fitted with paramagnetic sites and a sextet magnetic site. For all spectra, the red curves refer to the paramagnetic Fe^{3+} doublets, the yellow curves refer to the paramagnetic Fe^{2+} doublets, the purple curves refer to the magnetic site, and the blue curves are the superposition of all the sites.

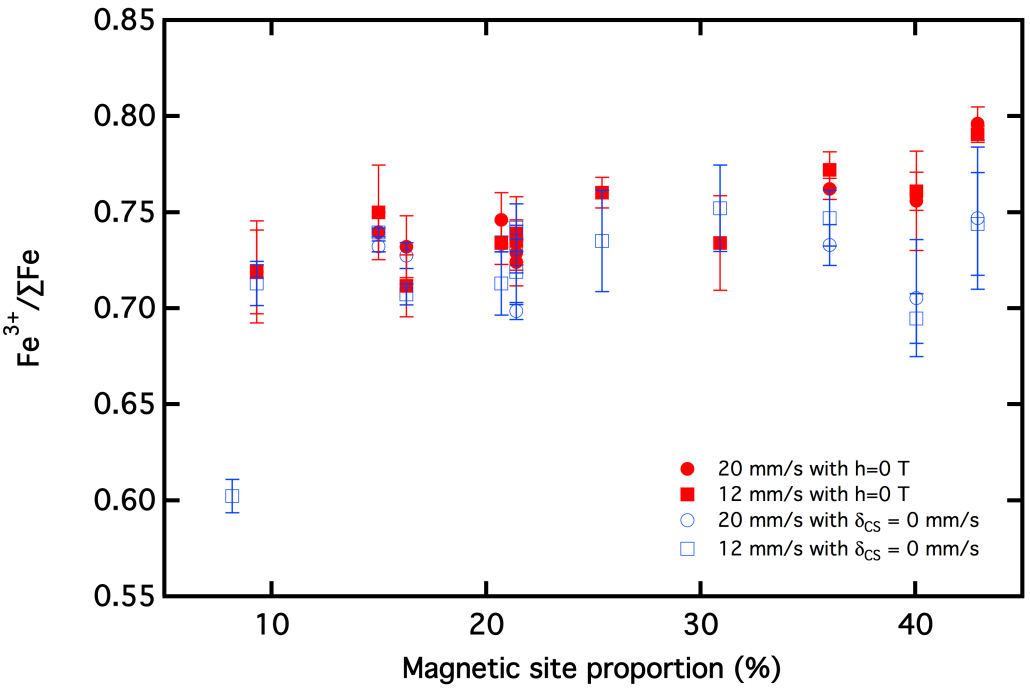

Figure 4.S2: $Fe^{3+}/\Sigma Fe$ changes with magnetic site area resulting from 12 mm/s scale Mössbauer spectra fitted with Hyperfine field (H) Gaussian width equals 0. Round and Square symbols refer to the velocity scale of Mössbauer spectra; solid red symbols refer to Mössbauer spectra were fitted Hyperfine field (H) Gaussian width equals 0 and empty blue symbols refer to Mössbauer spectra were fitted Center Shift (CS) Gaussian width equals 0. Unicertainties are in one sigma standard deviation(1σ).

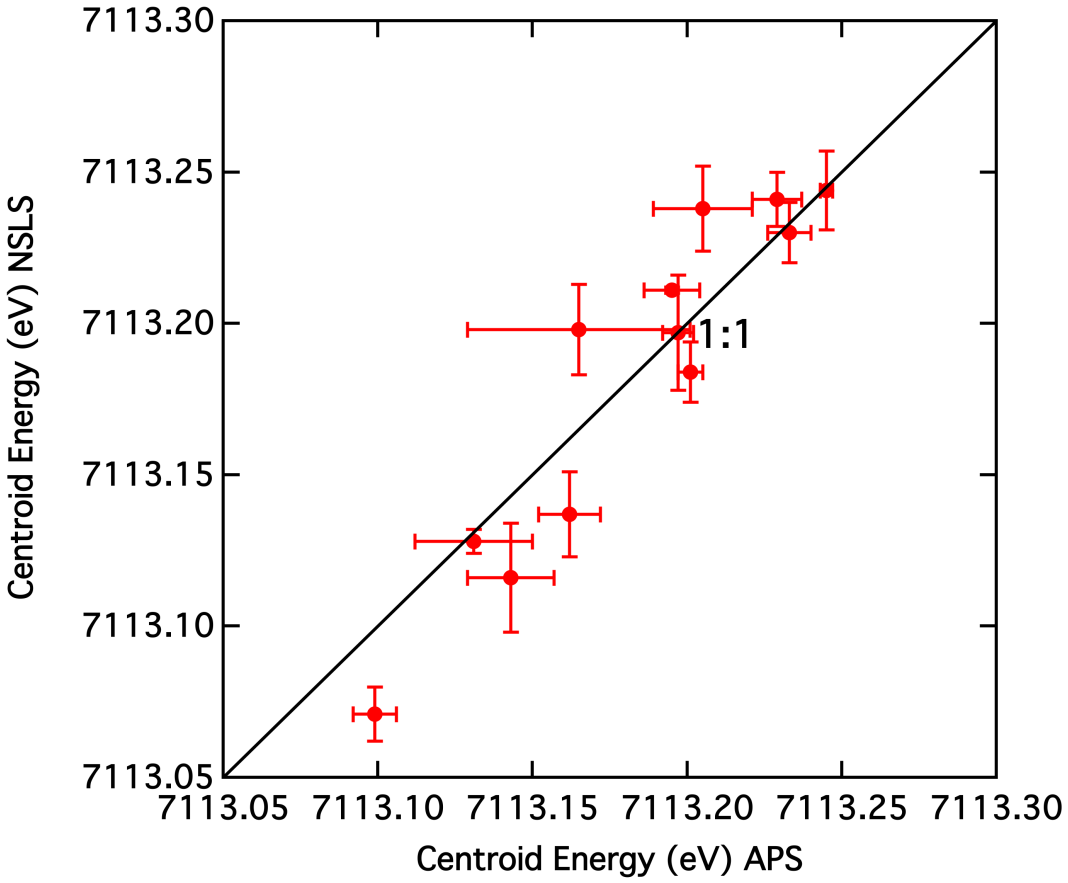

Figure 4.S3: Compare Centroid Energies obtained from XANES pre-edge spectra collected at APS and NSLS. The black line is 1:1 line. Unicertainties are in one sigma standard deviation(1σ).

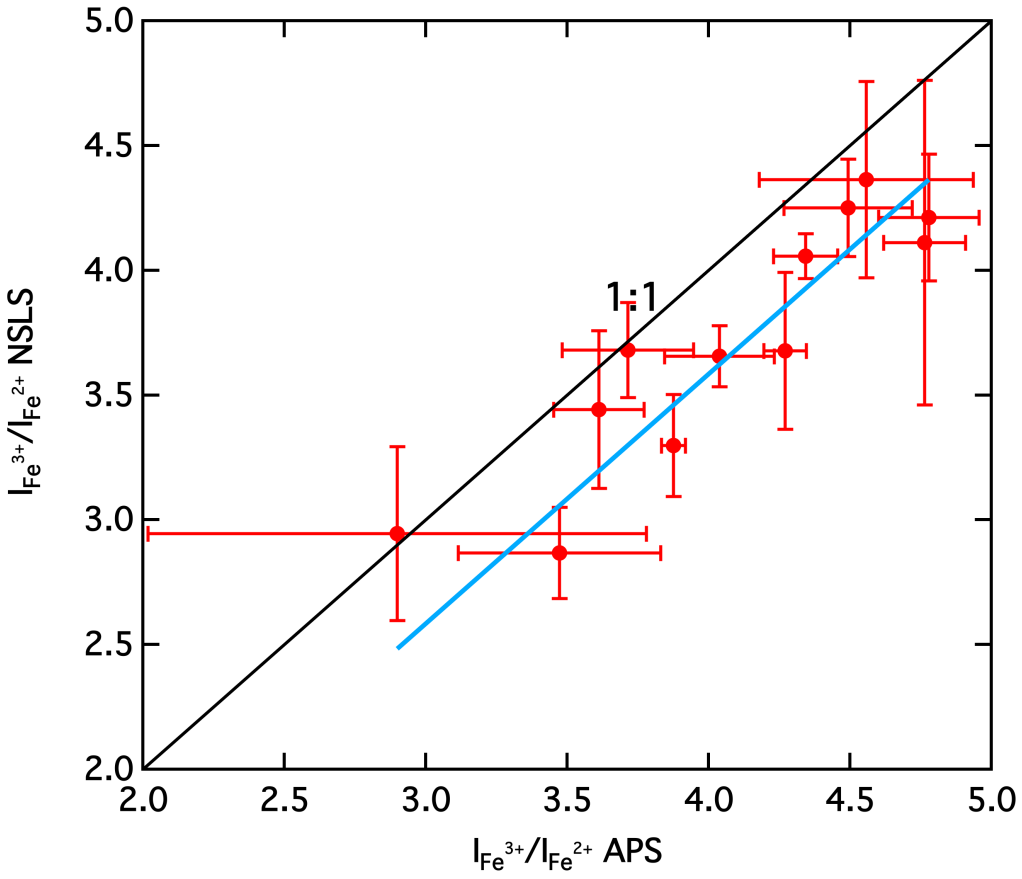

Figure 4.S4: Compare integrated pre-edge intensities obtained from XANES pre-edge spectra collected at APS and NSLS. The black line is 1:1 line. Unicertainties are in one sigma standard deviation(1σ).

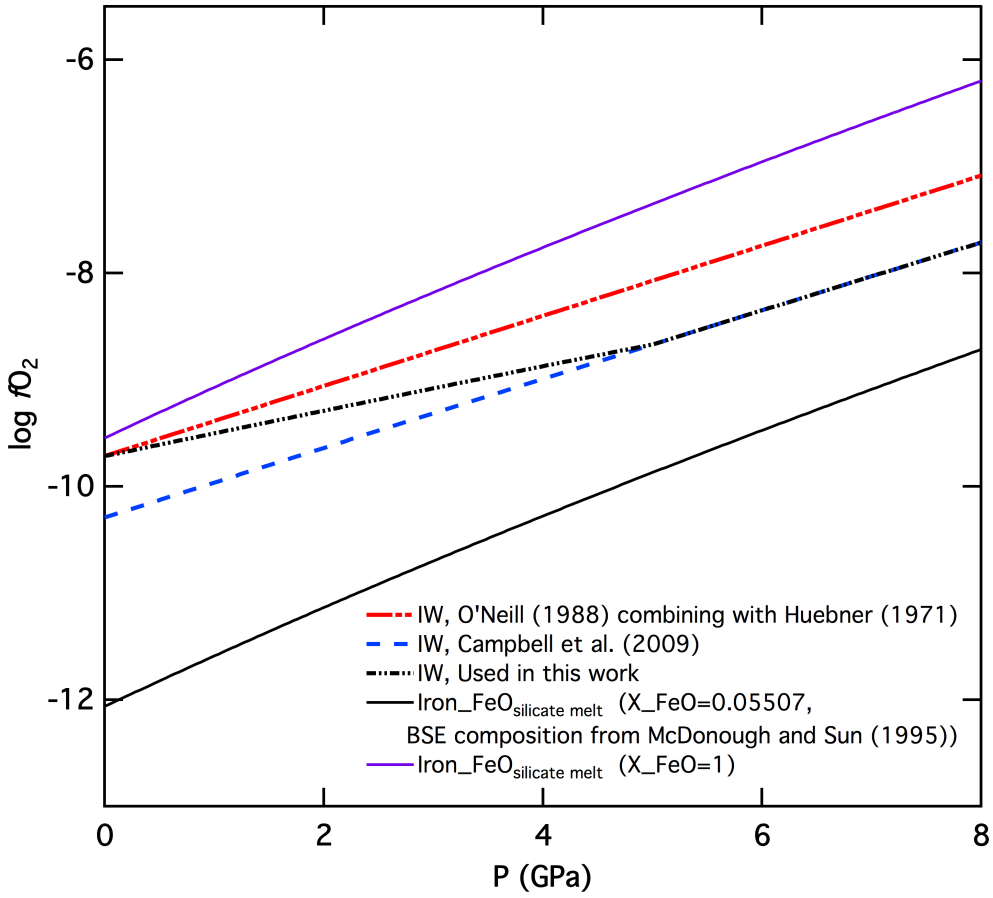

Figure 4.S5: $\log fO_2$ of Iron-Wüstite (IW) buffer and Iron-FeO$_{\text{silicate melt}}$ (IW*) changes with pressure at 1400 °C. For $\log fO_2$ of IW, the dash red curve is calculated from *O'Neill* (1988) and *Huebner and Sato* (1970) with Eqn. 4.12; the dash blue burve is calculated from *Campbell et al.* (2009); the dash black curve is calculated with combined Eqn. 4.13 from *O'Neill* (1988), **?** and *Campbell et al.* (2009) below 5 GPa, and from *Campbell et al.* (2009) above 5 GPa. The solid curves are for $\log fO_2$ of IW*, the purple one is assumed its FeO liquid and the black one is assumed that silicate melt is bulk silicate Earth composition from *McDonough and Sun* (1995) with 0.055 molar% FeO.

Table 4.S1: Electron microprobe analyses of sample

NO.	SiO_2	TiO_2	Al_2O_3	FeO	MgO	CaO	K_2O	Na_2O	Total
A839	57.87±0.25	2.79±0.11	15.46±0.05	8.80±0.07	2.29±0.02	7.64±0.06	1.02±0.02	4.65±0.09	100.53
A840	58.07±0.42	2.59±0.07	15.45±0.09	8.85±0.05	2.24±0.02	7.71±0.05	1.00±0.01	4.67±0.10	100.58
A841	57.56±0.30	2.64±0.07	15.23±0.08	8.67±0.06	2.24±0.03	7.60±0.06	1.03±0.02	4.62±0.10	99.58
A843	58.38±0.17	2.62±0.06	15.33±0.06	8.79±0.06	2.25±0.02	7.58±0.04	1.03±0.01	4.68±0.11	100.66
A844	58.11±0.32	2.58±0.08	15.29±0.11	8.15±0.05	2.2±0.03	7.49±0.06	1.02±0.02	4.62±0.08	99.46
A846	57.39±0.33	2.66±0.08	15.09±0.10	9.20±0.16	2.32±0.05	7.77±0.09	0.97±0.02	4.54±0.11	99.95
A848	57.46±0.26	2.62±0.06	15.12±0.09	8.82±0.07	2.25±0.02	7.60±0.04	1.00±0.02	4.57±0.06	99.45
A853	57.54±0.19	2.57±0.08	15.14±0.06	8.87±0.05	2.27±0.02	7.62±0.06	1.01±0.02	4.62±0.08	99.63
A855	57.93±0.12	2.58±0.12	15.28±0.05	8.9±0.05	2.27±0.02	7.66±0.05	1.01±0.01	4.64±0.08	100.25
A857	57.59±0.15	2.77±0.10	15.24±0.06	8.97±0.07	2.21±0.03	7.53±0.05	1.00±0.02	4.44±0.09	99.74
A860	58.54±0.11	2.75±0.15	15.27±0.04	8.70±0.01	2.10±0.01	7.28±0.04	1.02±0.01	4.89±0.24	100.56
A862	56.85±0.29	2.72±0.09	15.13±0.07	9.14±0.06	2.21±0.02	7.53±0.05	1.01±0.02	4.50±0.09	99.09
A863	56.99±0.13	2.56±0.09	15.03±0.04	8.78±0.03	2.20±0.03	7.46±0.06	1.01±0.01	4.36±0.11	98.39
A867	56.88±0.251	2.74±0.08	15.18±0.09	8.89±0.07	2.46±0.02	7.59±0.05	1.00±0.02	4.70±0.09	100.9
A888	58.61±0.78	2.88±0.20	14.99±0.15	8.35±0.29	1.89±0.24	7.07±0.49	1.14±0.08	4.34±0.15	99.28
A896	57.36±0.15	2.73±0.05	15.08±0.07	9.07±0.06	2.29±0.02	7.57±0.03	1.01±0.02	4.65±0.08	99.75
A944	57.77±0.30	2.56±0.07	15.22±0.06	8.91±0.06	2.27±0.02	7.62±0.05	1.02±0.02	4.77±0.13	100.14
A945	57.78±0.13	2.63±0.06	15.10±0.07	8.8±0.07	2.24±0.02	7.62±0.06	1.02±0.01	4.56±0.08	99.75
A952	57.54±0.17	2.54±0.07	15.17±0.05	8.86±0.07	2.27±0.02	7.56±0.05	1.01±0.02	4.71±0.06	99.67
B388	57.38±0.29	2.75±0.08	15.16±0.09	8.89±0.04	2.46±0.02	7.6±0.05	1.00±0.01	4.70±0.09	99.94
B402	56.99±0.14	2.74±0.10	15.08±0.07	9.08±0.07	2.3±0.02	7.62±0.06	1.01±0.02	4.60±0.12	99.43
M535	56.92±0.16	2.68±0.04	15.05±0.13	8.82±0.06	2.27±0.02	7.61±0.05	0.97±0.01	4.69±0.10	99.00
M537	56.98±0.13	2.46±0.08	15.16±0.07	8.74±0.06	2.25±0.02	7.45±0.05	1.00±0.02	5.00±0.10	99.04
M540	57.44±0.24	2.63±0.07	15.3±0.06	8.86±0.07	2.25±0.02	7.53±0.04	1.01±0.02	4.70±0.06	99.71
M543	57.39±0.15	2.57±0.07	15.23±0.06	8.95±0.06	2.26±0.02	7.62±0.06	1.02±0.03	4.61±0.09	99.65
M544	57.89±0.88	2.68±0.06	15.09±0.32	8.92±0.06	2.24±0.04	7.40±0.04	1.06±0.01	4.34±0.06	99.66
M559	57.09±0.19	2.65±0.09	14.97±0.06	8.59±0.08	2.26±0.02	7.46±0.06	1.01±0.02	4.97±0.09	99.00
M562	57.58±0.17	2.7±0.05	14.94±0.05	8.78±0.07	2.26±0.02	7.51±0.06	1.05±0.02	4.64±0.08	99.46
M563	57.67±0.31	2.69±0.09	14.91±0.08	9.00±0.09	2.17±0.05	7.58±0.15	0.87±0.06	4.14±0.18	99.04
M572	56.43±0.12	2.62±0.07	14.99±0.03	8.72±0.09	2.23±0.02	7.42±0.02	0.97±0.01	4.64±0.11	98.01
M601	56.93±0.19	2.51±0.08	15.13±0.07	8.68±0.05	2.26±0.03	7.50±0..05	1.01±0.02	5.01±0.10	99.03
VF1	58.63±0.45	2.48±0.08	15.27±0.14	8.47±0.07	2.2±0.02	7.44±0.05	1.07±0.02	5.12±1.15	100.69

Table 4.S2: Mössbauer Hyperfine Parameters assumed with h(T)=0

No.	L HWHM	Paramagnetic sites							
		CS(Fe^{3+})	**QS(Fe^{3+})**	**δ_{QS} (Fe^{3+})**	**CS(Fe^{2+})**	**δ_{CS} (Fe^{2+})**	**QS(Fe^{2+})**	**δ_{QS} (Fe^{2+})**	ρ
12 mm/s scale									
A839	0.144(0.006)	0.330(0.004)	1.096(0.007)	0.592(0.005)	1.072(0.005)	0.225(0.004)	1.883(0.010)	0.456(0.008)	0.22(0.04)
A840	0.278(0.020)	0.314(0.005)	1.053(0.008)	0.452(0.012)	1.043(0.006)	0.161(0.011)	1.864(0.012)	0.341(0.021)	0.49(0.07)
A841	0.229(0.018)	0.352(0.008)	1.058(0.015)	0.542(0.010)	1.023(0.010)	0.299(0.016)	1.927(0.022)	0.000(0.048)	0.40(0.05)
A843	0.267(0.048)	0.336(0.015)	1.059(0.033)	0.382(0.030)	1.066(0.040)	0.145(0.046)	1.910(0.060)	0.280(0.090)	0.53(0.24)
A844	0.305(0.039)	0.344(0.018)	1.021(0.035)	0.468(0.017)	1.047(0.047)	0.218(0.049)	1.970(0.080)	0.032(0.031)	0.40(0.06)
A846	0.276(0.046)	0.337(0.017)	1.060(0.036)	0.493(0.022)	1.071(0.043)	0.214(0.034)	1.930(0.070)	0.270(0.090)	0.28(0.14)
A848	0.244(0.019)	0.323(0.005)	1.108(0.008)	0.392(0.015)	1.067(0.005)	0.196(0.012)	1.945(0.014)	0.223(0.025)	0.42(0.10)
A853	0.279(0.030)	0.327(0.014)	1.086(0.029)	0.403(0.019)	1.057(0.027)	0.153(0.029)	1.961(0.047)	0.310(0.060)	0.40(0.17)
A855	0.315(0.033)	0.326(0.009)	1.084(0.019)	0.346(0.022)	1.064(0.022)	0.131(0.024)	1.962(0.030)	0.262(0.048)	0.44(0.12)
A857	0.149(0.017)	0.356(0.011)	1.085(0.021)	0.536(0.011)	1.058(0.014)	0.261(0.010)	1.982(0.028)	0.265(0.030)	0.21(0.08)
A862	0.277(0.017)	0.367(0.006)	1.037(0.012)	0.425(0.010)	1.034(0.009)	0.150(0.010)	2.012(0.018)	0.301(0.019)	0.40(0.08)
A863	0.160(0.023)	0.350(0.017)	1.036(0.034)	0.494(0.013)	1.033(0.024)	0.262(0.019)	1.974(0.037)	0.346(0.046)	0.31(0.12)
A867	0.219(0.011)	0.334(0.004)	1.039(0.007)	0.474(0.008)	1.058(0.048)	0.230(0.008)	1.891(0.010)	0.155(0.013)	0.56(0.09)
B402	0.279(0.015)	0.343(0.006)	1.040(0.011)	0.483(0.009)	1.044(0.009)	0.219(0.011)	1.953(0.020)	0.041(0.020)	0.42(0.37)
20 mm/s scale									
A840	0.268(0.010)	0.333(0.041)	1.091(0.003)	0.517(0.010)	1.086(0.006)	0.256(0.009)	1.933(0.018)	0.137(0.012)	0.68(0.10)
A841	0.257(0.015)	0.344(0.010)	1.136(0.020)	0.492(0.008)	1.076(0.017)	0.188(0.012)	1.990(0.290)	0.382(0.023)	0.29(0.08)
A843	0.270(0.037)	0.339(0.013)	1.063(0.024)	0.432(0.026)	1.068(0.020)	0.181(0.023)	1.909(0.044)	0.230(0.050)	0.47(0.22)
A844	0.277(0.021)	0.344(0.011)	1.089(0.019)	0.367(0.026)	1.088(0.017)	0.052(0.018)	1.960(0.035)	0.500(0.037)	0.59(0.30)
A848	0.292(0.032)	0.346(0.015)	1.138(0.022)	0.387(0.028)	1.108(0.021)	0.197(0.023)	2.015(0.043)	0.210(0.060)	0.36(0.23)
A853	0.306(0.018)	0.348(0.009)	1.127(0.024)	0.425(0.023)	1.100(0.020)	0.144(0.022)	2.010(0.440)	0.303(0.044)	0.32(0.18)
A855	0.299(0.032)	0.347(0.013)	1.136(0.025)	0.439(0.022)	1.118(0.026)	0.174(0.026)	2.019(0.046)	0.280(0.006)	0.31(0.14)
A857	0.151(0.027)	0.372(0.025)	1.158(0.042)	0.563(0.018)	1.111(0..027)	0.313(0.026)	2.102(0.049)	0.090(0.060)	0.58(0.37)
A863	0.194(0.041)	0.364(0.031)	0.910(0.007)	0.474(0.041)	0.946(0.043)	0.302(0.034)	2.010(0.070)	0.300(0.009)	0.44(0.21)

Uncertainties are in one sigma standard deviation (1σ)

CS: Center shift in mm/s

QS: Quadrupole splitting in mm/s;

δ_{CS}: Gaussian width of CS in mm/s

δ_{QS}: Gaussian width of QS in mm/s

ρ: correlation of δ_{CS} and δ_{QS}

Table 4.S2:continue

No.	Magnetic site				Background	χ^2	Site proportion (%)		
							Paramagnetic		Magnetic
	CS	δ_{CS}	QS	H			Fe^{3+}	Fe^{2+}	
12 mm/s scale									
A839	0.444(0.047)	1.41(0.12)	0.17(0.09)	22.0(0.9)	1441860(200)	0.59	45.20(0.80)	23.97(0.48)	30.80(1.20)
A840	-0.050(0.210)	2.00(0.80)	0.15(0.11)	28.8(1.1)	2643460(200)	0.56	56.60(1.95)	26.10(1.00)	17.30(2.65)
A841	0.390(0.036)	2.49(0.17)	-0.07(0.10)	19.5(1.3)	1317430(140)	0.59	37.40(0.95)	22.80(0.70)	39.80(1.20)
A843	-0.050(0.330)	2.10(0.95)	-0.04(0.00)	26.0(0.8)	2648090(375)	1.04	61.70(2.55)	28.10(1.40)	10.20(3.20)
A844	-0.210(0.450)	2.70(0.70)	0.10(0.38)	34.2(3.8)	891130(240)	0.64	57.70(2.70)	25.00(1.30)	17.30(3.60)
A846	0.220(0.080)	2.70(0.60)	0.33(0.40)	31.3(3.5)	1290150(295)	0.55	51.00(2.40)	26.60(1.30)	22.40(3.35)
A848	0.244(0.047)	2.40(2.00)	-0.21(0.11)	23.7(1.2)	3048820(270)	1.11	49.50(1.05)	26.50(0.70)	24.00(1.30)
A853	0.296(0.075)	1.89(0.13)	-0.05(0.05)	25.2(0.9)	3591690(180)	0.67	48.40(1.15)	26.60(0.70)	25.00(1.25)
A855	0.167(0.076)	1.71(0.22)	0.13(0.16)	27.1(2.1)	3019520(100)	1.08	54.40(1.45)	28.80(0.95)	16.70(1.75)
A857	0.402(0.022)	2.40(0.04)	-0.32(0.03)	16.7(0.4)	7062640(180)	1.00	28.64(0.41)	20.94(0.36)	50.42(0.43)
A862	0.386(0.041)	1.90(0.08)	-0.26(0.07)	19.5(0.7)	7468790(135)	0.63	37.10(0.80)	20.10(0.65)	42.80(0.90)
A863	0.507(0.043)	2.35(0.15)	0.01(0.11)	16.6(1.2)	3880130(125)	0.6	29.50(0.85)	23.90(0.80)	46.60(1.00)
A867	0.430(0.021)	1.80(0.75)	-0.04(0.12)	29.0(2.0)	3705120(430)	0.57	57.40(1.75)	30.20(1.05)	12.30(2.55)
B402	0.160(0.027)	2.10(0.70)	0.17(0.35)	24.9(2.7)	1675870(115)	0.45	55.80(1.25)	27.00(0.80)	17.20(1.70)
20 mm/s scale									
A840	0.350(0.140)	2.13(0.41)	0.380(0.120)	29.1(1.5)	7941010(105)	0.61	58.10(0.60)	27.12(0.39)	14.80(0.70)
A841	0.333(0.018)	2.24(0.10)	-0.129(0.031)	22.2(0.5)	10721000(155)	0.88	39.30(0.55)	23.78(0.42)	36.90(0.60)
A843	-0.100(0.165)	2.00(0.48)	0.230(0.290)	27.0(0.6)	6161740(120)	0.86	62.50(2.05)	28.10(1.25)	9.40(2.50)
A844	0.070(0.135)	2.30(0.75)	0.140(0.085)	32.2(1.7)	5916010(115)	0.73	57.70(0.95)	26.00(0.80)	16.20(0.90)
A848	0.491(0.048)1	2.23(0.23)	0.040(0.100)	25.5(2.3)	5040870(150)	0.99	51.10(1.50)	27.60(0.12)	21.30(1.75)
A853	0.350(0.060)	2.16(0.38)	-0.040(0.000)	24.2(1.5)	5351640(150)	0.70	48.80(1.45)	25.40(0.95)	25.80(1.65)
A855	0.291(0.029)	2.30(0.37)	0.010(0.140)	26.5(2.1)	5315900(100)	0.79	51.20(2.40)	26.80(0.80)	22.00(1.40)
A857	0.457(0.029)	2.64(0.22)	-0.160(0.110)	16.5(1.1)	5709500(125)	0.82	27.80(0.85)	20.40(0.75)	51.90(0.90)
A863	0.420(0.075)	2.40(0.41)	-0.330(0.390)	17.3(2.7)	2901990(95)	0.55	30.30(2.10)	24.40(2.20)	45.30(2.10)

Uncertainties are in one sigma standard deviation (1σ)
Background: Background in counts
H: hyperfine magnetic field in T
χ^2: Chi square

Table 4.S3: Mössbauer Hyperfine Parameters assumed with $\delta_{\text{CS magnetic site}}$=0

No.	L HWHM	Paramagnetic sites							
		CS(Fe^{3+})	QS(Fe^{3+})	δ_{QS} (Fe^{3+})	CS(Fe^{2+})	δ_{CS} (Fe^{2+})	QS(Fe^{2+})	δ_{QS} (Fe^{2+})	ρ
12 mm/s scale									
A839	0.207(0.033)	0.338(0.014)	1.081(0.020)	0.535(0.014)	1.065(0.018)	0.254(0.021)	1.904(0.028)	0.290(0.060)	0.23(0.01)
A840	0.260(0.019)	0.315(0.004)	1.042(0.011)	0.453(0.009)	1.044(0.005)	0.229(0.010)	1.863(0.017)	0.192(0.022)	0.61(0.05)
A841	0.309(0.022)	0.348(0.009)	1.043(0.017)	0.431(0.015)	1.025(0.009)	0.250(0.018)	1.929(0.022)	0.000(0.060)	0.40(0.03)
A843	0.260(0.024)	0.339(0.008)	1.058(0.017)	0.410(0.012)	1.061(0.023)	0.149(0.025)	1.913(0.033)	0.300(0.050)	0.47(0.13)
A844	0.338(0.004)	0.348(0.001)	0.996(0.015)	0.321(0.005)	1.045(0.015)	0.201(0.004)	2.001(0.003)	0.005(0.012)	0.40(0.04)
A846	0.222(0.042)	0.339(0.017)	1.052(0.033)	0.538(0.019)	1.075(0.033)	0.080(0.005)	1.930(0.050)	0.550(0.060)	0.39(0.22)
A848	0.278(0.018)	0.324(0.003)	1.095(0.005)	0.393(0.013)	1.066(0.003)	0.144(0.008)	1.950(0.009)	0.288(0.014)	0.41(0.46)
A853	0.332(0.036)	0.328(0.012)	1.070(0.025)	0.340(0.027)	1.051(0.023)	0.166(0.030)	1.970(0.400)	0.110(0.070)	0.87(0.27)
A855	0.318(0.007)	0.329(0.018)	1.074(0.005)	0.351(0.007)	1.054(0.018)	0.150(0.039)	1.963(0.005)	0.208(0.009)	0.47(0.34)
A857	0.280(0.006)	0.352(0.019)	1.071(0.037)	0.405(0.027)	1.055(0.025)	0.157(0.033)	1.986(0.041)	0.320(0.007)	0.20(0.12)
A860	0.247(0.003)	0.351(0.026)	1.050(0.006)	0.384(0.035)	1.075(0.039)	0.174(0.038)	1.977(0.011)	0.226(0.007)	0.37(0.40)
A862	0.190(0.170)	0.318(0.028)	1.070(0.030)	0.490(0.090)	1.042(0.015)	0.162(0.028)	2.024(0.030)	0.320(0.055)	0.46(0.14)
A863	0.097(0.007)	0.308(0.028)	0.874(0.006)	0.545(0.006)	0.913(0.006)	0.322(0.047)	2.117(0.013)	0.691(0.008)	0.23(0.29)
20 mm/s scale									
A840	0.262(0.034)	0.336(0.011)	1.077(0.022)	0.488(0.021)	1.079(0.027)	0.234(0.026)	1.939(0.049)	0.270(0.080)	0.36(0.14)
A841	0.349(0.026)	0.348(0.008)	1.111(0.016)	0.397(0.016)	1.067(0.013)	0.161(0.017)	2.009(0.023)	0.264(0.038)	0.38(0.13)
A843	0.266(0.001)	0.340(0.007)	1.058(0.027)	0.445(0.003)	1.065(0.025)	0.152(0.021)	1.910(0.006)	0.302(0.004)	0.39(0.02)
A844	0.305(0.003)	0.345(0.004)	1.069(0.009)	0.484(0.006)	1.090(0.007)	0.143(0.009)	1.975(0.016)	0.380(0.013)	0.22(0.09)
A848	0.370(0.007)	0.341(0.003)	1.128(0.003)	0.328(0.007)	1.115(0.003)	0.144(0.007)	2.030(0.006)	0.107(0.005)	0.78(0.11)
A853	0.350(0.008)	0.348(0.003)	1.110(0.007)	0.392(0.008)	1.095(0.006)	0.161(0.044)	2.019(0.011)	0.108(0.011)	0.66(0.44)
A855	0.313(0.019)	0.348(0.009)	1.122(0.017)	0.420(0.013)	1.116(0.018)	0.164(0.018)	2.023(0.035)	0.266(0.044)	0.31(0.10)
A857	0.310(0.009)	0.377(0.022)	1.138(0.039)	0.414(0.044)	1.101(0.025)	0.167(0.036)	2.119(0.047)	0.330(0.070)	0.19(0.13)
A863	0.330(0.044)	0.350(0.030)	0.916(0.046)	0.330(0.045)	0.968(0.031)	0.130(0.034)	1.990(0.080)	0.390(0.070)	0.37(0.26)

Uncertainties are in one sigma standard deviation (1σ)

L HWHM: Lorentzian half width at half maximum in mm/s

CS: Center shift in mm/s

QS: Quadrupole splitting in mm/s;

δ_{CS}: Gaussian width of CS in mm/s

δ_{QS}: Gaussian width of QS in mm/s

ρ: correlation of δ_{CS} and δ_{QS}

Table 4.S3:continue

No.	Magnetic site				Background	χ^2	Site proportion (%)		
							Paramagnetic		Magnetic
	CS	QS	H	δ_H			Fe^{3+}	Fe^{2+}	
12 mm/s scale									
A839	0.460(0.050)	0.26(0.14)	24.8(4.3)	14.9(3.8)	1441670(8000)	0.59	48.10(2.55)	26.50(1.60)	25.40(3.30)
A840	0.380(0.155)	0.17(0.09)	31.7(1.3)	15.5(1.1)	2643830(225)	0.56	52.80(1.30)	25.80(0.70)	21.40(1.65)
A841	0.385(0.030)	0.02(0.03)	25.1(0.7)	12.9(1.0)	1317500(115)	0.58	38.70(1.40)	25.30(1.00)	36.00(1.70)
A843	0.130)0.050)	0.06(0.17)	27.8(1.9)	9.6(1.5)	2647870(55)	1.02	62.00(1.05)	28.70(0.65)	9.30(1.30)
A844	0.272(0.035)	-0.06(0.03)	39.8(0.3)	11.7(0.3)	891139(10)	0.62	58.97(0.21)	26.05(0.19)	14.98(0.20)
A846	0.310(0.085)	0.12(0.13)	33.2(2.3)	21.3(0.3)	1290590(255)	0.54	44.30(2.35)	24.80(1.40)	30.90(3.00)
A848	0.270(0.015)	-0.02(0.06)	28.4(1.1)	12.3(1.6)	3048780(240)	1.08	50.50(1.50)	28.10(1.00)	21.40(2.00)
A853	0.312(0.046)	0.03(0.04)	28.6(1.3)	8.6(0.6)	3591570(160)	0.64	50.60(1.45)	28.70(1.00)	20.70(1.80)
A855	0.221(0.020)	0.09(0.01)	28.3(0.4)	9.5(1.4)	3019360(65)	1.05	54.45(0.71)	29.28(0.29)	16.27(0.44)
A857	0.374(0.022)	-0.04(0.05)	23.2(1.1)	11.5(1.1)	7063130(275)	0.94	31.50(2.55)	25.60(1.90)	42.90(2.90)
A860	0.461(0.010)	0.06(0.01)	45.9(0.1)	5.36(0.6)	13306050(205)	2.86	52.06(1.20)	39.78(0.13)	8.16(0.09)
A862	0.435(0.045)	-0.24(0.09)	19.2(2.1)	14.0(2.1)	7468970(270)	0.65	28.20(4.60)	17.30(2.95)	54.40(4.90)
A863	0.563(0.016)	0.02(0.13)	23.6(0.3)	9.9(0.1)	3879790(95)	1.2	29.41(2.55)	30.54(0.24)	40.05(0.33)
20 mm/s scale									
A840	0.380(0.100)	0.240(0.155)	30.8(1.6)	15.7(2.6)	7941160(90)	0.61	56.10(1.25)	26.90(0.70)	16.90(1.50)
A841	0.321(0.17)	0.012(0.028)	27.3(0.7)	10.6(0.3)	10721320(160)	0.82	42.50(0.95)	26.70(0.75)	30.80(1.10)
A843	0.380(0.050)	0.170(0.040)	28.9(0.3)	11.2(0.8)	6161641(33)	0.85	62.43(0.85)	28.09(0.09)	9.48(0.03)
A844	0.380(0.075)	0.027(0.041)	36.4(0.6)	11.7(1.7)	5916080(80)	0.71	58.50(0.25)	26.77(0.21)	14.73(0.24)
A848	0.569(0.020)	0.035(0.017)	31.8(0.3)	8.1(0.5)	5040940(65)	0.93	54.58(0.35)	30.15(0.30)	15.27(0.42)
A853	0.299(0.022)	-0.041(0.018)	28.2(0.3)	11.1(0.5)	5351720(80)	0.65	50.38(0.39)	26.65(0.25)	22.97(0.49)
A855	0.309(0.013)	0.012(0.033)	29.4(1.2)	13.8(2.7)	5316030(65)	0.8	50.70(0.60)	27.28(0.46)	22.10(0.70)
A857	0.428(0.038)	0.050(0.060)	24.2(1.7)	11.9(1.4)	5709780(195)	0.81	31.70(3.40)	25.30(2.75)	43.00(3.95)
A863	0.390(0.085)	-0.050(0.070)	24.7(1.4)	10.3(1.3)	2902050(110)	0.53	35.20(2.40)	29.50(2.15)	35.40(2.80)

Uncertainties are in one sigma standard deviation (1σ)

H: hyperfine magnetic field in T — h: Gaussian width of H in T

Background: Background in counts — χ^2: Chi square

Table 4.S4: Mössbauer Hyperfine Parameters for andesitic glasses

No.	L HWHM	Paramagnetic sites							
		CS(Fe^{3+})	QS(Fe^{3+})	δ_{QS} (Fe^{3+})	CS(Fe^{2+})	δ_{CS} (Fe^{2+})	QS(Fe^{2+})	δ_{QS} (Fe^{2+})	ρ
A867	0.226(0.022)	0.339(0.008)	1.029(0.019)	0.477(0.013)	1.047(0.021)	0.229(0.015)	1.902(0.042)	0.148(0.049)	0.54(0.13)
A888	0.321(0.015)	0.347(0.016)	1.017(0.004)	0.345(0.015)	1.122(0.034)	0.181(0.031)	2.040(0.070)	0.200(0.070)	0.46(0.29)
A896	0.235(0.007)	0.334(0.044)	1.098(0.008)	0.466(0.009)	1.058(0.008)	0.199(0.007)	1.933(0.024)	0.244(0.018)	0.40(0.09)
A944	0.196(0.007)	0.333(0.045)	1.173(0.007)	0.489(0.009)	1.074(0.006)	0.231(0.005)	1.999(0.017)	0.249(0.015)	0.26(0.06)
A945	0.322(0.005)	0.369(0.042)	0.985(0.008)	0.422(0.005)	1.035(0.006)	0.247(0.006)	2.025(0.017)	0.057(0.019)	0.35(0.24)
A952	0.180(0.009)	0.332(0.037)	1.106(0.006)	0.407(0.008)	1.071(0.006)	0.159(0.007)	2.000(0.015)	0.312(0.014)	0.40(0.05)
B388	0.263(.0006)	0.330(0.006)	1.192(0.022)	0.432(0.005)	1.074(0.011)	0.196(0.013)	1.996(0.021)	0.199(0.041)	0.40(0.14)
B402	0.270(0.032)	0.352(0.009)	1.026(0.016)	0.439(0.018)	1.031(0.015)	0.192(0.015)	1.969(0.029)	0.241(0.048)	0.04(0.12)
M535	0.207(0.006)	0.342(0.036)	1.184(0.008)	0.458(0.010)	1.089(0.006)	0.210(0.009)	2.043(0.010)	0.179(0.018)	0.40(0.11)
M537	0.226(0.009)	0.337(0.006)	1.157(0.007)	0.406(0.012)	1.094(0.007)	0.150(0.008)	2.064(0.012)	0.301(0.015)	0.33(0.07)
M540	0.236(0.005)	0.328(0.031)	1.179(0.005)	0.397(0.006)	1.082(0.003)	0.195(0.004)	1.992(0.007)	0.145(0.007)	0.61(0.26)
M543	0.275(0.010)	0.344(0.009)	1.195(0.012)	0.516(0.010)	1.079(0.006)	0.241(0.006)	2.057(0.018)	0.133(0.020)	0.40(0.09)
M544	0.186(0.005)	0.334(0.006)	1.166(0.009)	0.494(0.007)	1.080(0.006)	0.272(0.005)	2.013(0.017)	0.156(0.014)	0.38(0.07)
M559	0.180(0.010)	0.349(0.013)	1.189(0.023)	0.485(0.008)	1.105(0.012)	0.229(0.009)	2.213(0.027)	0.168(0.026)	0.40(0.09)
M562	0.188(0.009)	0.348(0.049)	1.201(0.007)	0.462(0.008)	1.102(0.005)	0.165(0.006)	2.096(0.012)	0.329(0.013)	0.27(0.08)
M563	0.175(0.007)	0.339(0.040)	1.170(0.007)	0.498(0.006)	1.102(0.043)	0.231(0.004)	2.088(0.006)	0.248(0.012)	0.31(0.04)
M572	0.186(0.012)	0.343(0.010)	1.138(0.014)	0.560(0.010)	1.108(0.006)	0.231(0.007)	2.165(0.017)	0.227(0.022)	0.40(0.05)
M601	0.221(0.008)	0.346(0.039)	1.185(0.007)	0.408(0.006)	1.108(0.006)	0.148(0.005)	2.100(0.009)	0.296(0.010)	0.34(0.04)
VF1	0.234(0.009)	0.297(0.007)	1.171(0.014)	0.499(0.010)	1.054(0.015)	0.245(0.020)	1.820(0.037)	0.140(0.060)	0.40(0.25)

Uncertainties are in one sigma standard deviation (1σ)
L HWHM: Lorentzian half width at half maximum in mm/s
CS: Center shift in mm/s
QS: Quadrupole splitting in mm/s;
δ_{CS}: Gaussian width of CS in mm/s
δ_{QS}: Gaussian width of QS in mm/s
ρ: correlation of δ_{CS} and δ_{QS}

Table 4.S4:continue

No.	Magnetic site				Background	χ^2	Site proportion (%)		
							Paramagnetic		Magnetic
	CS	QS	H	δ_H			Fe^{3+}	Fe^{2+}	
A888					1632960(75)	0.54	68.20(0.70)	31.80(0.70)	
A896					1884180(75)	0.59	70.10(0.50)	29.90(0.50)	
A944					9807570(205)	1.18	63.73(0.37)	36.27(0.37)	
A945					3167770(75)	0.69	65.28(0.27)	34.72(0.27)	
A952					7392830(195)	1.19	65.78(0.43)	34.22(0.43)	
B388					1855580(75)	0.97	68.19(0.35)	31.81(0.35)	
B402	0.190(0.135)	0.10(0.16)	26.1(3.4)	13.3(4.5)	1675890(180)	0.45	54.40(3.00)	26.80(1.80)	18.90(4.00)
M535					3972960(160)	1.42	59.50(0.47)	40.50(0.47)	
M537					3200280(110)	0.85	59.30(0.55)	40.70(0.55)	
M540	0.418(0.185)	-0.06(0.16)	46.5(0.1)	0.0(5.0)	3756350(85)	0.75	56.53(0.37)	38.88(0.36)	4.59(0.32)
M543					3770380(105)	0.55	60.88(0.47)	39.12(0.47)	
M544					5764070(130)	0.76	60.01(0.42)	39.99(0.42)	
M559					4402960(125)	0.79	53.52(0.50)	46.48(0.50)	
M562					6482170(165)	1.14	54.10(0.50)	45.90(0.50)	
M563	0.339(0.036)	-0.08(0.04)	47.0(0.3)	4.0(0.6)	6107600(295)	0.67	51.04(0.47)	43.22(0.43)	5.70(0.70)
M572					2153890(90)	0.52	52.50(0.65)	47.50(0.65)	
M601	0.378(0.029)	-0.09(0.03)	45.7(0.2)	3.3(0.4)	2658460(155)	1.03	49.08(0.44)	44.51(0.46)	6.41(0.49)
VF1					3056320(85)	0.58	75.30(0.60)	24.70(0.60)	

Uncertainties are in one sigma standard deviation (1σ)

H: hyperfine magnetic field in T — h: Gaussian width of H in T

Background: Background in counts — χ^2: Chi square

Table 4.S5: Fit parameters obtained from pre-edge XANES spectra

Sample Name	Fe^{2+} Intensity*	Fe^{2+} Corrected E_0	Fe^{2+} FWHM#	Fe^{3+} Intensity*	Fe^{3+} Corrected E_0	Fe^{3+} FWHM#
APS						
A867	0.0262(0.0025)	7111.761(0.028)	1.399(0.064)	0.1185(0.0042)	7113.524(0.011)	1.789(0.029)
A888	0.0187(0.0149)	7111.572(0.244)	1.466(0.444)	0.1204(0.0185)	7113.712(0.107)	2.581(0.370)
A896	0.0263(0.0016)	7111.775(0.020)	1.443(0.029)	0.1178(0.0010)	7113.558(0.006)	1.784(0.015)
A944	0.0272(0.0024)	7111.728(0.025)	1.411(0.040)	0.1097(0.0048)	7113.562(0.012)	1.853(0.007)
A945	0.0257(0.0007)	7111.748(0.006)	1.395(0.013)	0.1097(0.0011)	7113.542(0.006)	1.822(0.003)
A952	0.0255(0.0009)	7111.718(0.032)	1.387(0.013)	0.1107(0.0044)	7113.535(0.010)	1.857(0.026)
B388	0.0241(0.0009)	7111.738(0.012)	1.381(0.037)	0.1148(0.0008)	7113.562(0.006)	1.847(0.007)
B402	0.0241(0.0007)	7111.768(0.021)	1.403(0.037)	0.1153(0.0022)	7113.535(0.000)	1.795(0.015)
M537	0.0284(0.0017)	7111.702(0.015)	1.398(0.053)	0.1075(0.0012)	7113.555(0.015)	1.906(0.009)
M540	0.0332(0.0021)	7111.728(0.044)	1.411(0.068)	0.1150(0.0060)	7113.552(0.021)	1.875(0.054)
M543	0.0258(0.0004)	7111.678(0.006)	1.344(0.024)	0.1002(0.0027)	7113.545(0.010)	1.951(0.038)
M544	0.0293(0.0071)	7111.858(0.197)	1.652(0.208)	0.0807(0.0060)	7113.632(0.095)	1.979(0.066)
M559	0.0248(0.0026)	7111.602(0.031)	1.378(0.091)	0.1116(0.0064)	7113.549(0.000)	2.238(0.077)
M562	0.0279(0.0025)	7111.655(0.023)	1.356(0.071)	0.1034(0.0096)	7113.529(0.013)	2.024(0.047)
M572	0.0242(0.0010)	7111.622(0.015)	1.317(0.028)	0.0873(0.0023)	7113.508(0.012)	2.112(0.027)
M601	0.0269(0.0004)	7111.655(0.000)	1.341(0.009)	0.0909(0.0010)	7113.518(0.006)	2.004(0.009)
VF1	0.0274(0.0008)	7111.982(0.023)	1.394(0.002)	0.1406(0.0059)	7113.602(0.006)	1.562(0.016)
NSLS						
A867	0.0273(0.0020)	7111.827(0.054)	1.572(0.055)	0.1186(0.0027)	7113.563(0.026)	1.926(0.028)
A896	0.0290(0.0011)	7111.808(0.026)	1.636(0.020)	0.1232(0.0015)	7113.564(0.012)	1.953(0.011)
A944	0.0301(0.0015)	7111.794(0.012)	1.625(0.054)	0.1099(0.0021)	7113.581(0.010)	1.981(0.008)
A945	0.0303(0.0020)	7111.814(0.051)	1.633(0.053)	0.1112(0.0054)	7113.557(0.017)	1.929(0.042)
A952	0.0306(0.0008)	7111.781(0.006)	1.582(0.025)	0.1241(0.0020)	7113.564(0.007)	2.002(0.017)
B388	0.0286(0.0029)	7111.820(0.078)	1.623(0.067)	0.1165(0.0067)	7113.593(0.022)	1.951(0.064)
B402	0.0282(0.0017)	7111.849(0.022)	1.654(0.061)	0.1185(0.0031)	7113.573(0.005)	1.932(0.026)
M540	0.0348(0.0008)	7111.807(0.022)	1.640(0.041)	0.0997(0.0039)	7113.574(0.012)	1.943(0.038)
M543	0.0325(0.0016)	7111.729(0.029)	1.637(0.045)	0.1070(0.0016)	7113.565(0.019)	2.058(0.024)
M544	0.0255(0.0017)	7111.819(0.067)	1.673(0.035)	0.0747(0.0039)	7113.668(0.053)	2.095(0.081)
M562	0.0276(0.0016)	7111.655(0.018)	1.533(0.026)	0.1014(0.0013)	7113.528(0.013)	2.168(0.017)
M572	0.0256(0.0019)	7111.626(0.032)	1.489(0.043)	0.0876(0.0029)	7113.492(0.020)	2.201(0.056)

*integrated pre-edge intensity
#Full width at half maximum
APS:Advanced Photon Source
NSLS:National Synchrotron Light Source

Bibliography

Abe, Y., and T. Matsui (1986), Early evolution of the earth: Accretion, atmosphere formation, and thermal history, *Journal of Geophysical Research: Solid Earth*, *91*(B13), E291–E302.

Alberto, H. V., J. L. Pinto da Cunha, B. O. Mysen, J. M. Gil, and N. Ayres de Campos (1996), Analysis of Mössbauer spectra of silicate glasses using a two-dimensional gaussian distribution of hyperfine parameters, *Journal of Non-Crystalline Solids*, *194*(1-2), 48–57.

Allwardt, J. R., J. F. Stebbins, B. C. Schmidt, D. J. Frost, A. C. Withers, and M. M. Hirschmann (2005), Aluminum coordination and the densification of high-pressure aluminosilicate glasses, *American Mineralogist*, *90*(7), 1218–1222.

Arculus, R. J. (1985), Oxidation status of the mantle: past and present, *Annual Review of Earth and Planetary Sciences*, *13*, 75–95.

Armstrong, L. S., M. M. Hirschmann, B. D. Stanley, E. G. Falksen, and S. D. Jacobsen (2015), Speciation and solubility of reduced C-O-H-N volatiles in mafic melt: Implications for volcanism, atmospheric evolution, and deep volatile cycles in the terrestrial planets, *Geochimica et Cosmochimica Acta*, *in press*.

Bancroft, M. G., and J. R. Brown (1975), A Mössbauer study of coexisting hornblendes and biotites: quantitative Fe^{3+}/Fe^{2+} ratios, *American Mineralogist*, *60*, 265–272.

Berry, A., H. s. C. ONeill, K. Jayasuriya, S. Campbell, and G. Foran (2003), Xanes calibrations for the oxidation state of iron in a silicate glass, *American Mineralogist*, *88*, 967–977.

Berry, A. J., H. S. C. ONeill, D. R. Scott, G. J. Foran, and J. M. G. Shelley (2006), The effect of composition on Cr^{2+}/Cr^{3+} in silicate melts, *American Mineralogist*, *91*(11-12), 1901–1908.

Berry, A. J., L. V. Danyushevsky, H. S. C. O'Neill, M. Newville, and S. R. Sutton (2008), Oxidation state of iron in komatiitic melt inclusions indicates hot Archaean mantle, *Nature*, *455*(7215), 960–963.

Bertka, C. M., and Y. Fei (1997), Mineralogy of the Martian interior up to core-mantle boundary pressures, *Journal of Geophysical Research: Solid Earth*, *102*(B3), 5251–5264.

Bézos, A., and E. Humler (2005), The $Fe^{3+}/\Sigma Fe$ ratios of MORB glasses and their implications for mantle melting, *Geochimica et Cosmochimica Acta*, *69*(3), 711–725.

Borisov, A., and C. McCammon (2010), The effect of silica on ferric/ferrous ratio in silicate melts: An experimental study using Mössbauer spectroscopy, *American Mineralogist*, *95*(4), 545–555.

Botcharnikov, R. E., J. Koepke, F. Holtz, C. McCammon, and M. Wilke (2005), The effect of water activity on the oxidation and structural state of Fe in a ferro-basaltic melt, *Geochimica et Cosmochimica Acta*, *69*(21), 5071–5085.

Bowles, J. A., J. S. Gee, K. Burgess, and R. F. Cooper (2011), Timing of magnetite formation in basaltic glass: Insights from synthetic analogs and relevance for geomagnetic paleointensity analyses, *Geochemistry, Geophysics, Geosystems*, *12*(2), 5071–5085.

Brearly, M. (1990), Ferric iron in silicate melts in the system Na_2O-Fe_2O_3-SiO_2 at high pressure, *Journal of Geophysical Research: Solid Earth*, *95*(B10), 15,703–15,716.

Campbell, A. J., L. Danielson, K. Righter, C. T. Seagle, Y. Wang, and V. B. Prakapenka (2009), High pressure effects on the ironiron oxide and nickelnickel oxide oxygen fugacity buffers, *Earth and Planetary Science Letters*, *286*(3), 556–564.

Chabot, N. L., D. S. Draper, and C. B. Agee (2005), Conditions of core formation in the earth: Constraints from nickel and cobalt partitioning, *Geochimica et Cosmochimica Acta*, *69*(8), 2141–2151.

Chen, Y.-L., and D.-P. Yang (2007), *Mössbauer effect in lattice dynamics: experimental techniques and applications*, John Wiley and Sons.

Chi, H., R. Dasgupta, M. S. Duncan, and N. Shimizu (2014), Partitioning of carbon between Fe-rich alloy melt and silicate melt in a magma ocean-Implications for the abundance and origin of volatiles in Earth, Mars, and the Moon, *Geochimica et Cosmochimica Acta*, *139*, 447–471.

Christie, D. M., I. S. E. Carmichael, and C. H. Langmuir (1986), Oxidation states of mid-ocean ridge basalt glasses, *Earth and Planetary Science Letters*, *79*(3-4), 397–411.

Cooper, R. F., J. B. Fanselow, and D. B. Poker (1996), The mechanism of oxidation of a basaltic glass: chemical diffusion of network-modifying cations, *Geochimica et Cosmochimica Acta*, *60*(17), 3253–3265.

Corgne, A., S. Keshav, B. J. Wood, W. F. McDonough, and Y. Fei (2008), Metalsilicate partitioning and constraints on core composition and oxygen fugacity during earth accretion, *Geochimica et Cosmochimica Acta*, *72*(2), 574–589.

Cottrell, E., and K. A. Kelley (2011), The oxidation state of Fe in MORB glasses and the oxygen fugacity of the upper mantle, *Earth and Planetary Science Letters*, *305*, 270–282.

Cottrell, E., and K. A. Kelley (2013), Redox heterogeneity in mid-ocean ridge basalts as a function of mantle source, *Science*, *340*(6138), 1314–1317.

Cottrell, E., K. A. Kelley, A. Lanzirotti, and R. A. Fischer (2009), High-precision determination of iron oxidation state in silicate glasses using XANES, *Chemical Geology*, *268*, 167–179.

Dasgupta, R., M. M. Hirschmann, and A. C. Withers (2004), Deep global cycling of carbon constrained by the solidus of anhydrous, carbonated eclogite under upper mantle conditions, *Earth and Planetary Science Letters*, *227*(1-2), 73–85.

Dasgupta, R., H. Chi, N. Shimizu, S. Buono, Antonio, and D. Walker (2013), Carbon solution and partitioning between metallic and silicate melts in a shallow magma ocean: Implications for the origin and distribution of terrestrial carbon, *Geochimica et Cosmochimica Acta*, *102*, 191–212.

Dauphas, N., M. Roskosz, E. Alp, D. Neuville, M. Hu, C. Sio, F. Tissot, J. Zhao, L. Tissandier, E. Medard, and C. Cordier (2014), Magma redox and structural controls on iron isotope variations in earth aposs mantle and crust, *Earth and Planetary Science Letters*, *398*, 127–140.

De Grave, E., and A. Van Alboom (1991), Evaluation of ferrous and ferric Mössbauer fractions, *Physics and Chemistry of Minerals*, *18*, 337–342.

De Grave, E., A. E. Verbeeck, and D. G. Chambaere (1985), Influence of small aluminum substitutions on the hematite lattice, *Physics Letters A*, *107*(4), 181–184.

Dingwell, D. B. (1991), Redox viscometry of some Fe-bearing silicate melts, *American Mineralogist*, *76*, 1560–1562.

Dingwell, D. B., and D. Virgo (1987), The effect of oxidation state on the viscosity of melts in the system Na_2O-FeO-Fe_2O_3-SiO_2, *Geochimica et Cosmochimica Acta*, *51*, 195–205.

Dingwell, D. B., M. Brearley, and J. E. Dickinson Jr (1988), Melt densities in the Na_2O-FeO-Fe_2O_3-SiO_2 system and the partial molar volume of tetrahedrally-coordinated ferric iron in silicate melts, *Geochimica et Cosmochimica Acta*, *52*(10), 2467–2475.

Dunlop, D. J., and Ö. Özdemir (2001), *Rock Magnetism: Fundamentals and Frontiers*, Cambridge University Press.

Dyar, M., D. Agresti, M. Schaefer, C. Grant, and E. Stlute (2006), Mössbauer spectroscopy of earth and planetary materials, *Annual Review of Earth and Planetary Sciences*, *34*, 83–125.

Dyar, M. D. (1985), A review of Mössbauer data on inorganic glasses: the effects of composition on iron valency and coordination., *American Mineralogist*, *70*, 304316.

Dyar, M. D., and M. W. Schaefer (2004), Mössbauer spectroscopy on the surface of Mars: constraints and expectations, *Earth and Planetary Science Letters*, *218*(34), 243–259.

Dyar, M. D., M. T. Naney, and S. E. Swanson (1987), Effects of quench methods on Fe^{3+}/Fe^{2+} ratios: A Mössbauer and wet-chemical study, *American Mineralogist*, *72*, 792–800.

Dyar, M. D., E. A. Breves, E. Emerson, S. W. Bell, M. Nelms, M. V. Ozanne, S. E. Peel, M. L. Carmosino, J. M. Tucker, M. E. Gunter, J. S. Delaney, A. Lanzirotti, and A. B. Woodland (2012), Accurate determination of ferric iron in garnets by bulk Mössbauer spectroscopy and synchrotron micro-XANES, *American Mineralogist*, *97*(10), 1726–1740.

Dyar, M. D., R. L. Klima, A. Fleagle, and S. E. Peel (2013), Fundamental Mössbauer parameters of synthetic Ca-Mg-Fe pyroxenes, *American Mineralogist*, *98*(7), 1172–1186.

Elardo, S. M., D. S. Draper, and C. K. Shearer (2011), Lunar Magma Ocean crystallization revisited: Bulk composition, early cumulate mineralogy, and the source regions of the highlands Mg-suite, *Geochimica et Cosmochimica Acta*, *75*(11), 3024–3045.

Elkins-Tanton, L. (2008), Linked magma ocean solidification and atmospheric growth for Earth and Mars, *Earth and Planetary Science Letters*, *271*(1-4), 181–191.

Fischer, R. A., A. J. Campbell, G. A. Shofner, O. T. Lord, P. Dera, and V. B. Prakapenka (2011), Equation of state and phase diagram of FeO, *Earth and Planetary Science Letters*, *304*, 496–502.

Fox, K. E., T. Furukawa, and W. W.B. (1982), Transition metal ions in silicate melts. Part 2. Iron in sodium disilicate glasses., *Physics and Chemistry of Glasses*, *23*, 169–178.

Frost, D. J., and C. A. McCammon (2008), The redox state of earth's mantle, *Annu. Rev. Earth Planet. Sci.*, *36*, 389–420.

Frost, D. J., C. Liebske, F. Langenhorst, C. A. McCammon, R. G. Trnnes, and D. C. Rubie (2004), Experimental evidence for the existence of iron-rich metal in the Earth's lower mantle, *Nature*, *428*(6981), 409–412.

Funamori, N., T. Yagi, and T. Uchida (1996), High-pressure and high-temperature in situ x-ray diffraction study of iron to above 30 Gpa using MA8-type apparatus, *Geophysical Research Letters*, *23*(9), 953–956.

Gaillard, F., B. Scaillet, and M. Pichavant (2002), Kinetics of iron oxidation-reduction in hydrous silicic melts, *American Mineralogist*, *87*(7), 829–837.

Gaillard, F., M. Pichavant, and B. Scaillet (2003a), Experimental determination of activities of FeO and Fe_2O_3 components in hydrous silicic melts under oxidizing conditions, *Geochimica et Cosmochimica Acta*, *67*(22), 4389–4409.

Gaillard, F., B. Schmidt, S. Mackwell, and C. McCammon (2003b), Rate of hydrogeniron redox exchange in silicate melts and glasses, *Geochimica et Cosmochimica Acta*, *67*(13), 2427–2441.

Ghiorso, M. S. (2004), An equation of state for silicate melts. i. formulation of a general model, *American Journal of Science*, *304*(8-9), 637–678.

Giuli, G., E. Paris, K. Hess, D. Dingwell, M. Cicconi, S. Eeckhout, K. Fehr, and P. Valenti (2011), XAS determination of the Fe local environment and oxidation state in phonolite glasses, *American Mineralogist*, *96*(4).

Govindaraju, K. (1994), 1994 compilation of working values and sample description for 383 geostandards, *Geostandards newsletter*, *18*(S1), 1–158.

Guo, X., R. A. Lange, and Y. Ai (2014), Density and sound speed measurements on model basalt (An-Di-Hd) liquids at one bar: New constraints on the partial molar volume and compressibility of the FeO component, *Earth and Planetary Science Letters*, *388*, 283–292.

Hamada, M., M. Ushioda, T. Fujii, and E. Takahashi (2013), Hydrogen concentration in plagioclase as a hygrometer of arc basaltic melts: Approaches from melt inclusion analyses and hydrous melting experiments, *Earth and Planetary Science Letters*, *365*, 253–262.

Haskel, D. (1999), FLUO: Correcting XANES for self-absorption in fluorescence measurements. www.aps.anl.gov/ haskel/fluo/fluo.ps.

Helgason, Ö., S. Steinthorsson, and S. Mørup (1989), The ferric/ferrous ratio in basalt melts at different oxygen pressures, *Hyperfine Interactions*, *45*(1-4), 287–294.

Hill, R., and P. Roeder (1974), The crystallization of spinel from basaltic liquid as a function of oxygen fugacity, *The Journal of Geology*, *82*, 709–729.

Hirschmann, M. M. (2012), Magma ocean influence on early atmosphere mass and composition, *Earth and Planetary Science Letters*, *341-344*, 4857.

Holland, T. I. M., and R. Powell (2001), Calculation of phase relations involving haplogranitic melts using an internally consistent thermodynamic dataset, *Journal of Petrology*, *42*(4), 673–683.

Holzheid, A., H. Palme, and S. Chakraborty (1997), The activities of nio, coo and feo in silicate melts, *Chemical Geology*, *139*(1), 21–38.

Huebner, J., and M. Sato (1970), The oxygen fugacity-temperature relationships of manganese oxide and nickel oxide buffers, *American Mineralogist*, *55*, 934–952.

Jackson, M., and P. Solheid (2010), On the quantitative analysis and evaluation of magnetic hysteresis data, *Geochemistry, Geophysics, Geosystems*, *11*(4).

Jarosewich, E., J. A. Nelen, and J. A. Norberg (1980), Reference samples for Electron Microprobe Analysis, *Geostandards Newsletter*, *4*(1), 43–47.

Jayasuriya, K. D., H. S. C. ONeill, A. J. Berry, and S. J. Campbell (2004), A Mössbauer study of the oxidation state of Fe in silicate melts, *American Mineralogist*, *89*, 1597–1609.

Jochum, K. P., M. Willbold, I. Raczek, B. Stoll, and K. Herwig (2005), Chemical characterisation of the USGS reference glasses GSA-1G, GSC-1G, GSD-1G, GSE-1G, BCR-2G, BHVO-2G and BIR-1G using EPMA, ID-TIMS, ID-ICP-MS and LA-ICP-MS, *Geostandards and Geoanalytical Research*, *29*(3), 285–302.

Jochum, K. P., B. Stoll, K. Herwig, M. Willbold, A. W. Hofmann, M. Amini, S. Aarburg, W. Abouchami, E. Hellebrand, B. Mocek, I. Raczek, A. Stracke, O. Alard, C. Bouman, S. Becker, M. Dücking, H. Brtz, R. Klemd, D. de Bruin, D. Canil, D. Cornell, C.-J. de Hoog, C. Dalpé, L. Danyushevsky, A. Eisenhauer, Y. Gao, J. E. Snow, N. Groschopf, D. Günther, C. Latkoczy, M. Guillong, E. H. Hauri, H. E. Höfer, Y. Lahaye, K. Horz, D. E. Jacob, S. A. Kasemann, A. J. R. Kent, T. Ludwig, T. Zack, P. R. D. Mason, A. Meixner, M. Rosner, K. Misawa, B. P. Nash, J. Pfänder, W. R. Premo, W. D. Sun, M. Tiepolo, R. Vannucci, T. Vennemann, D. Wayne, and J. D. Woodhead (2006), MPI-DING reference glasses for in situ microanalysis: New reference values for element concentrations and isotope ratios, *Geochemistry, Geophysics, Geosystems*, *7*(2).

Kaufman, L., E. V. Clougherty, and R. J. Weiss (1963), The lattice stability of metalsiii. iron, *Acta Metallurgica*, *11*(5), 323–335.

Kegler, P., A. Holzheid, D. Frost, D. Rubie, R. Dohmen, and H. Palme (2008), New Ni and Co metal-silicate partitioning data and their relevance for an early terrestrial magma ocean, *Earth and Planetary Science Letters*, *268*(1), 28–40.

Kelley, K. A., and E. Cottrell (2009), Water and the oxidation state of subduction zone magmas, *Science*, *325*(5940), 605–607.

Kieffer, S. W. (1979), Thermodynamics and lattice vibrations of minerals: 3. Lattice dynamics and an approximation for minerals with application to simple substances and framework silicates, *Reviews of Geophysics*, *17*(1), 35–59.

Kilinc, A., I. Carmichael, M. Rivers, and R. Sack (1983), The ferric-ferrous ratio of natural silicate liquids equilibrated in air, *Contributions to Mineralogy and Petrology*, *83*(1-2), 136–140.

Knipping, J. L., H. Behrens, M. Wilke, J. Gttlicher, and P. Stabile (2015), Effect of oxygen fugacity on the coordination and oxidation state of iron in alkali bearing silicate melts, *Chemical Geology*, *411*, 143–154.

Komatsu, T., and N. Soga (1980), ESR and Mössbauer studies of crystallization process of sodium iron silicate glass, *The Journal of Chemical Physics*, *72*(3), 1781–1785.

Kraft, S., J. Stmpel, and P. Becker (1996), High resolution xray absorption spectroscopy with absolute energy calibration for the determination of absorption edge energies, *High resolution xray absorption spectroscopy with absolute energy calibration for the determination of absorption edge energies*, *67*(3), 681–687.

Kress, V., and I. Carmichael (1991), The compressibility of silicate liquids containing Fe_2O_3 and the effect of composition, temperature, oxygen fugacity and pressure on their redox states, *Contributions to Mineralogy and Petrology*, *108*, 82–92.

Kress, V. C., and I. S. E. Carmichael (1988), Stoichiometry of the iron oxidation reaction in silicate melts, *American Mineralogist*, *73*(11-12), 1267–1274.

Lagarec, K., and D. G. Rancourt (1997), Extended-Voigt based analytic lineshape method for determining N-dimensional correlated hyperfine parameter distributions in Mössbauer spectroscopy, *Nuclear Instruments and Methods in Physics Research Section B: Beam Interactions with Materials and Atoms*, *129*(2), 266–280.

Lagarec, K., and D. G. Rancourt (1998), Recoil Mössbauer spectral analysis software for windows, *University of Ottawa, Ottawa, ON*.

Lange, R. A., and I. S. E. Carmichael (1987), Densities of Na_2O-K_2O-CaO-MgO-FeO-Fe_2O_3-Al_2O_3-TiO_2-SiO_2 liquids: New measurements and derived partial molar properties, *Geochimica et Cosmochimica Acta*, *51*.

Lange, R. A., and I. S. E. Carmichael (1989), Ferric-ferrous equilibria in Na_2O-FeO-Fe_2O_3 - SiO_2 melts-effects of analytical techniques on derived partial molar volumes, *Geochimica et Cosmochimica Acta*, *53*(9), 2195–2204.

Lécuyer, C., and Y. Ricard (1999), Long-term fluxes and budget of ferric iron: implication for the redox states of the Earth's mantle and atmosphere, *Earth and Planetary Science Letters*, *165*, 197–211.

Li, B., D. Jia, Y. Zhou, Q. Hu, and W. Cai (2006), In situ hybridization to chitosan/magnetite nanocomposite induced by the magnetic field, *Journal of Magnetism and Magnetic Materials*, *306*(2), 223–227.

Li, J., and C. B. Agee (1996), Geochemistry of mantlecore differentiation at high pressure, *Nature*, *381*(6584), 686–689.

Liu, Q., and R. A. Lange (2006), The partial molar volume of Fe_2O_3 in alkali silicate melts: Evidence for an average Fe^{3+} coordination number near five, *American Mineralogist*, *91*(2-3), 385–393.

Magnien, V., D. R. Neuville, L. Cormier, B. O. Mysen, V. Briois, S. Belin, O. Pinet, and P. Richet (2004), Kinetics of iron oxidation in silicate melts: a preliminary XANES study, *Chemical Geology*, *213*(1), 253–263.

Markwardt, C. (2008), Non-linear least squares fitting in idl with mpfit., *Proc. Astronomical Data Analysis Software and Systems XVIII, Quebec, Canada. Astronomical Society of the Pacific, San Francisco*.

Matsui, T., and Y. Abe (1986), Evolution of an impact-induced atmosphere and magma ocean on the accreting earth, *Nature*, *319*(23), 303–305.

McCammon, C. (1997), Ferric iron content of mineral inclusions in diamonds from Säo Luiz: A view into the lower mantle, *Science*, *278*(5337), 434–436.

McCammon, C., and L.-g. Liu (1984), The effects of pressure and temperature on nonstoichiometric wüstite, fexo: The iron-rich phase boundary, *Physics and Chemistry of Minerals*, *10*(3), 106–113.

McCammon, C. C., and M. G. Kopylova (2004), A redox profile of the slave mantle and oxygen fugacity control in the cratonic mantle, *Contributions to Mineralogy and Petrology*, *148*(1), 55–68.

McDonough, W. F., and S. s. Sun (1995), The composition of the earth, *Chemical Geology*, *120*(3-4), 223–253.

Medard, E., C. McCammon, J. Barr, and T. Grove (2008), Oxygen fugacity, temperature reproducibility, and H_2O contents of nominally anhydrous piston-cylinder experiments using graphite capsules, *93*(11-12), 1838–1844.

Métrich, N., J. Susini, E. Foy, F. Farges, and D. Massare (2006), Redox state of iron in peralkaline rhyolitic glass/melt: X-ray absorption micro-spectroscopy experiments at high temperature, *Chemical geology*, *231*, 350–363.

Miller, G. H., E. M. Stolper, and T. J. Ahrens (1991), The equation of state of a molten komatiite: 1 shock wave compression to 36 gpa, *Journal of Geophysical Research: Solid Earth (19782012)*, *96*(B7), 11,831–11,848.

Mo, X., I. S. E. Carmichael, M. Rivers, and J. Stebbins (1982), The partial molar volume of Fe_2O_3 in multicomponent silicate liquids and the pressure dependence of oxygen fugacity in magmas, *Mineral Mag*, *45*, 237–245.

Moore, G., K. Righter, and I. Carmichael (1995), The effect of dissolved water on the oxidation state of iron in natural silicate liquids, *Contributions to Mineralogy and Petrology*, *120*(2), 170–179.

Morup, S., and E. Tronc (1994), Superparamagnetic relaxation of weakly interacting particles, *Physical review letters*, *72*(20), 3278.

Morup, S., H. Topse, and J. Lipka (1976), Modified theory for mössbauer spectra of superparamagnetic particles: application to Fe_3O_4, *Le Journal de Physique Colloques*, *37*(C6), C6–287–C6–290.

Mysen, B. (2006), The structural behavior of ferric and ferrous iron in aluminosilicate glass near meta-aluminosilicate joins, *Geochimica et Cosmochimica Acta*, *70*(9), 2337–2353.

Mysen, B., and P. Richet (2005), Silicate glasses and melts: properties and structure, *Elsevier*, *10*.

Mysen, B., I. Carmichael, and D. Virgo (1985), A comparison of iron redox ratios in silicate glasses determined by wet-chemical and ^{57}Fe mössbauer resonant absorption methods, *Contributions to Mineralogy and Petrology*, *90*(2-3), 101–106.

Mysen, B. O., and E. V. Dubinsky (2004), Melt structural control on olivine/melt element partitioning of Ca and Mn, *Geochimica et Cosmochimica Acta*, *68*(7), 1617–1633.

Mysen, B. O., and D. Virgo (1985), Iron-bearing silicate melts: relations between pressure and redox equilibria, *Physics and Chemistry of Minerals*, *12*(4), 191–200.

Mysen, B. O., and D. Virgo (1986), Volatiles in silicate melts at high pressure and temperature: 1. interaction between oh groups and Si^{4+}, Al^{3+}, Ca^{2+}, Na^{+} and H^{+}, *Chemical Geology*, *57*, 303–331.

Mysen, B. O., D. Virgo, and F. A. Seifert (1982), The structure of silicate melts: implications for chemical and physical properties of natural magma, *Reviews of Geophysics*, *20*(3), 353–383.

Neuville, D. R., P. Courtial, D. B. Dingwell, and P. Richet (1993), Thermodynamic and rheological properties of rhyolite and andesite melts, *Contributions to Mineralogy and Petrology*, *113*(4), 572–581.

Niemantsverdriet, J. W., A. M. Van der Kraan, and W. N. Delgass (1984a), Characterization of surface phases in bimetallic FeRh/SiO_2 catalysts by in situ mössbauer spectroscopy at cryogenic temperatures, *Journal of Catalysis*, *89*(1), 138–149.

Niemantsverdriet, J. W., C. F. J. Flipse, B. Selman, J. J. Van Loef, and A. M. Van Der Kraan (1984b), Influence of particle motion on the mössbauer effect in microcrystals α-FeOOH and α-Fe_2O_3, *Physics Letters A*, *100*(8), 445–447.

Ohtani, E., N. Hirao, T. Kondo, M. Ito, and T. Kikegawa (2005), Iron-water reaction at high pressure and temperature, and hydrogen transport into the core, *Physics and chemistry of minerals*, *32*(1), 77–82.

O'Neill, H. S. (1988), Systems fe-o and cu-o: Thermodynamic data for the equilibria fe-F̈eo,fe-Fe_3O_4,F̈eo-Fe_3O_4,Fe_3O_4-Fe_2O_3, cu-Cu_2O, and Cu_2O-cuo from emf measurements, *73*, 470–486.

O'Neill, H. S. C., and J. Nell (1997), Gibbs free energies of formation of RuO_2, IrO_2, and OsO_2: A high-temperature electrochemical and calorimetric study, *Geochimica Et Cosmochimica Acta*, *61*(24), 5279–5293.

O'Neill, H. S. C., A. J. Berry, C. McCammon, K. D. Jayasuriya, S. J. Campbell, and G. Foran (2006), An experimental determination of the effect of pressure on the $Fe^{3+}/\Sigma Fe$ ratio of an anhydrous silicate melt to 3.0 gpa, *American Mineralogist*, *91*(2-3), 404–412.

Oohata, T., K. Shirahata, T. Toriyama, T. Inamura, K. Yoshino, and H. Iijima (1994), Mössbauer spectroscopy of a semiconductive phosphate glass ($10V_2O_5$-$30Fe_2O_3$-$60P_2O_5$) at low temperature, *Hyperfine Interactions*, *94*(1), 2131–2136.

Osborn, E. F. (1959), Role of oxygen pressure in the crystallization and differentiation of basaltic magma, *American Journal of Science*, *257*, 609–647.

Ottonello, G., R. Moretti, L. Marini, and M. V. Zuccolini (2001), Oxidation state of iron in silicate glasses and melts: a thermochemical model, *Chemical Geology*, *174*, 157–179.

ONeill, H. S. C., C. A. McCammon, D. Canil, D. C. Rubie, and C. R. Ross (1993), Mössbauer spectroscopy of mantle transition zone phases and determination of minimum Fe^{3+} content, *American Mineralogist*, *78*, 456–460.

Partzsch, G. M., D. Lattard, and C. McCammon (2004), Mössbauer spectroscopic determination of Fe^{3+}/Fe^{2+} in synthetic basaltic glass: a test of empirical fO_2 equations under superliquidus and subliquidus conditions, *Contributions to Mineralogy and Petrology*, *147*(5), 565–580.

Pawley, A. R., j. R. Holloway, and P. F. McMillan (1992), The effect of oxygen fugacity on the solubility of carbon-oxygen fluids in basaltic melt, *The effect of oxygen fugacity on the solubility of carbon-oxygen fluids in basaltic melt*, *110*.

PennerHahn, J. E. (2005), Xray Absorption Spectroscopy, *eLS*.

Pick, T., and L. Tauxe (1994), Characteristics of magnetite in submarine basaltic glass, *Geophysical Journal International*, *119*(1), 116–128.

Pound, R. V., and G. A. Rebka Jr (1960), Variation with temperature of the energy of recoil-free gamma rays from solids, *Physical Review Letters*, *4*(6).

Rancourt, D. G., A. M. McDonald, A. E. Lalonde, and J. Y. Ping (1993), Mössbauer absorber thicknesses for accurate site populations in Fe-bearing minerals, *American Mineralogist*, *78*(1-2), 1–7.

Ravel, B., and M. Newville (2005), ATHENA, ARTEMIS, HEPHAESTUS: data analysis for X-ray absorption spectroscopy using IFEFFIT, *Journal of Synchrotron Radiation*, *12*, 537541.

Rigden, S. M., T. J. Ahrens, and E. M. Stolper (1989), Highpressure equation of state of molten anorthite and diopside, *Journal of Geophysical Research: Solid Earth*, *94*(B7), 9508–9522.

Righter, K. (2003), Metal-silicate partitioning of siderophile elements and core formation in the early earth, *Annual Review of Earth and Planetary Sciences*, *31*, 135–174.

Righter, K., and M. Ghiorso (2012a), Redox systematics of a magma ocean with variable pressure-temperature gradients and composition, *Proceedings of the National Academy of Sciences*, *109*(30), 11,955–11,960.

Righter, K., and M. Ghiorso (2012b), Correction for redox systematics of a magma ocean with variable pressure-temperature gradients and composition,, *PROCEEDINGS OF THE NATIONAL ACADEMY OF SCIENCES OF THE UNITED STATES OF AMERICA*, *109*(41), 16,749–16,750.

Righter, K., L. R. Danielson, K. Pando, R. V. Morris, T. G. Graff, D. G. Agresti, A. M. Martin, S. R. Sutton, M. Newville, and A. Lanzirotti (2013), Redox systematics of martian magmas with implications for magnetite stability, *American Mineralogist*, *98*(4), 616–628.

Rivers, M. L., and I. S. E. Carmichael (1987), Ultrasonic studies of silicate melts, *Journal of Geophysical Research: Solid Earth*, *92*(B9), 9247–9270.

Robinson, M., and G. Taylor (2001), Ferrous oxide in mercury's crust and mantle, *Meteoritics & Planetary Science*, *36*(6), 841–847.

Rohrbach, A., C. Ballhaus, U. Schindler, P. Ulmer, V. Kamenetsky, and D. Kuzmin (2007), Metal saturation in the upper mantle, *Nature*, *449*(7161), 456–458.

Roskosz, M., B. O. Mysen, and G. D. Cody (2006), Dual speciation of nitrogen in silicate melts at high pressure and temperature: an experimental study, *Geochimica et Cosmochimica Acta*, *70*(11), 2902–2918.

Roskosz, M., M. J. Toplis, and D. R. Neuville (2008), Quantification of the kinetics of iron oxidation in silicate melts using raman spectroscopy and assessment of the role of oxygen diffusion, *American Mineralogist*, *93*(11-12), 1749–1759.

Rossano, S., E. Balan, G. Morin, J. P. Bauer, G. Calas, and C. Brouder (1999), Fe Mössbauer spectroscopy of tektites, *Physics and Chemistry of Minerals*, *26*, 530–538.

Rossano, S., A. Ramos, J. M. Delaye, and S. Creux (2000), Exafs and molecular dynamics combined study of CaOFeO2SiO$_2$ glass. new insight into site significance in silicate glasses, *Europhysics Letters*, *49*(5), 597–602.

Rossano, S., H. Behrens, and M. Wilke (2008), Advanced analyses of ^{57}Fe Mössbauer data of alumino-silicate glasses, *Physics and Chemistry of Minerals*, *35*, 77–93.

Rubie, D., H. Melosh, J. Reid, C. Liebske, and K. Righter (2003), Mechanisms of metalsilicate equilibration in the terrestrial magma ocean, *Earth and Planetary Science Letters*, *205*(3-4).

Rubie, D., D. Frost, U. Mann, Y. Asahara, F. Nimmo, K. Tsuno, P. Kegler, A. Holzheid, and H. Palme (2011), Heterogeneous accretion, composition and core-mantle differentiation of the earth, *Earth and Planetary Science Letters*, *301*(1-2).

Rubie, D. C., and S. A. Jacobson (2015), Mechanisms and geochemical models of core formation, *arXiv:1504.05417*.

Ruffoni, M., and R. Pettifer (2006), Calibration of xanes spectra from dispersive xas beamline., *J. Synchrotron Radiat*, *13*, 489–493.

Sack, R. O., I. S. E. Carmichael, M. Rivers, and M. S. Ghiorso (1981), Ferric-ferrous equilibria in natural silicate liquids at 1 bar, *Contributions to Mineralogy and Petrology*, *75*(4), 369–376.

Sanloup, C., J. W. E. Drewitt, C. Crpisson, Y. Kono, C. Park, C. McCammon, L. Hennet, S. Brassamin, and A. Bytchkov (2013), Structure and density of molten fayalite at high pressure, *Geochimica et Cosmochimica Acta*, *118*, 118–128.

Sawatzky, G. A., F. Van Der Woude, and A. H. Morrish (1969), Mössbauer study of several ferrimagnetic spinels, *Physical Review*, *187*(2), 747–757.

Schroeder, D. V. (2000), *An Introduction to Thermal Physics*, Addison-Wesley.

Sepelák, V., I. Bergmann, D. Menzel, A. Feldhoff, P. Heitjans, F. J. Litterst, and K. D. Becker (2007), Magnetization enhancement in nanosized $MgFe_2O_4$ prepared by mechanosynthesis, *Journal of Magnetism and Magnetic Materials*, *316*(2), 764–767.

Stanley, B., M. Hirschmann, and A. Withers (2014), Solubility of coh volatiles in graphite-saturated martian basalts, *Geochimica et Cosmochimica Acta*, *129*, 54–76.

Stevenson, D. J. (1977), Hydrogen in the Earth's core, *Nature*, *268*(5616), 130–131.

Stixrude, L., N. de Koker, N. Sun, M. Mookherjee, and B. B. Karki (2009), Thermodynamics of silicate liquids in the deep earth, *Earth and Planetary Science Letters*, *278*(3), 226–232.

Tauxe, L. (1998), *Paleomagnetic Principles and practice*, *Modern Approaches in Geophysics*, vol. 17, Kluwer Academic Publishers.

Thornber, C. R., P. L. Roeder, and J. R. Foster (1980), The effect of composition on the ferric-ferrous ratio in basaltic liquids at atmospheric pressure, *Geochimica et Cosmochimica Acta*, *44*(3), 525–532.

Virgo, D., and B. Mysen (1985), The structural state of iron in oxidized vs. reduced glasses at 1 atm: A ^{57}Fe Mössbauer study, *Physics and Chemistry of Minerals*, *12*, 65–76.

Virgo, D., B. O. Mysen, P. A. Danckwerth, and F. A. Seifert (1982), Speciation of Fe^{3+} in 1-atm Na_2O-SiO_2-FeO melts., *Carnegie Institution of Washington Year Book*, *81*, 349–353.

Virgo, D., B. O. Mysen, and P. A. Danckwerth (1983), Redox equilibria and the anionic structure of $Na_2O.xSiO_2$-FeO melts: effects of oxygen fugacity., *Carnegie Institution of Washington Year Book*, *82*, 305–309.

Volovetskii, M. V., O. A. Lukanin, V. S. Rusakov, and A. A. Kargaltsev (2012), Influence of oxygen fugacity and temperature on the redox state of iron in natural silicic aluminosilicate melts, *Geochemistry International*, *50*(4), 330–343.

Wade, J., and B. Wood (2005), Core formation and the oxidation state of the Earth, *Earth and Planetary Science Letters*, *236*(1-2), 78–95.

Weigel, C., C. McCammon, and H. Keppler (2010), High-temperature mössbauer spectroscopy: A probe for the relaxation time of fe species in silicate melts and glasses, *American Mineralogist*, *95*(11-12), 1701–1707.

Wetzel, D. T., M. J. Rutherford, S. D. Jacobsen, E. H. Hauri, and A. E. Saal (2013), Degassing of reduced carbon from planetary basalts, *Proceedings of the National Academy of Sciences*, *110*(20), 8010–8013.

Wilke, M. (2005), Fe in magma-An overview, *Fe in magma-An overview*, *48*(4/5), 609–617.

Wilke, M., F. Farges, P.-E. Petit, J. Gordon E Brown, and F. Martin (2001), Oxidation state and coordination of Fe in minerals: An Fe K-XANES spectroscopic study, *American Mineralogist*, *86*(5-6), 714–730.

Wilke, M., H. Behrens, D. Burkhard, and S. Rossano (2002), The oxidation state of iron in silicic melt at 500 mpa water pressure, *Chemical Geology*, *189*(1-2), 55–67.

Wilke, M., G. M. Partzsch, R. Bernhardt, and D. Lattard (2005), Determination of the iron oxidation state in basaltic glasses using XANES at the k-edge, *Chemical Geology*, *220*, 143–161.

Wilke, M., C. Schmidt, F. Farges, V. Malavergne, L. Gautron, A. Simionovici, M. Hahn, and P.-E. Petit (2006), Structural environment of iron in hydrous aluminosilicate glass and melt-evidence from x-ray absorption spectroscopy, *Chemical Geology*, *229*(1-3), 144–161.

Wilke, M., F. Farges, and G. Partzsch (2007), Speciation of Fe in silicate glasses and melts by in-situ XANES spectroscopy, *American Mineralogist*, *92*(1), 44–56.

Williams, Q., and R. Jeanloz (1988), Spectroscopic evidence for pressure-induced coordination changes in silicate glasses and melts, *Science*, *239*(4842), 902–905.

Wilson, A. D. (1960), The micro-determination of ferrous iron in silicate minerals by a volumetric and a colorimetric method, *The Analyst*, *85*(1016), 823–827.

Wood, B. J., L. T. Bryndzia, and K. E. Johnson (1990), Mantle oxidation state and its relationship to tectonic environment and fluid speciation, *Science*, *248*(4953), 337–345.

Woodland, A. B., and C. R. Ross II (1994), A crystallographic and mssbauer spectroscopy study of $Fe_3^{2+}Al_2Si_3O_{12}$-$Fe_3^{2+}Fe_2^{3+}Si_3O_{12}$, (almandine-skiagite) and $Ca_3Fe_2^{3+}Si_3O_{12}$-$Fe_3^{2+}Fe_2^{3+}Si_3O_{12}$ (andradite-skiagite) garnet solid solutions, *Physics and Chemistry of Minerals*, *21*(3), 117–132.

Xirouchakis, D., M. M. Hirschmann, and J. A. Simpson (2001), The effect of titanium on the silica content and on mineral-liquid partitioning of mantle-equilibrated melts, *Geochimica et Cosmochimica Acta*, *65*(14), 2201–2217.

Zahnle, K., N. Arndt, C. Cockell, A. Halliday, E. Nisbet, F. Selsis, and N. Sleep (2007), Emergence of a Habitable Planet, *Space Science Reviews*, *129*(1-3), 35–78.

Zhang, H. L., P. A. Solheid, R. A. Lange, A. Von Der Handt, and M. M. Hirschmann (2015), Accurate determination of $Fe^{3+}/\Sigma Fe$ of andesitic glass by mossbauer spectroscopy, *American Mineralogist*, *100*, 1967–1977.